Development of Pulse Shape Discrimination Methods for BEGe Detectors

Heng-Ye Liao

München 2016

Development of Pulse Shape Discrimination Methods for BEGe Detectors

Heng-Ye Liao

Dissertation
an der Fakultät für Physik
der Ludwig–Maximilians–Universität
München

vorgelegt von
Heng-Ye Liao
aus Taichung, Taiwan

München, den 13.04.2016

Zusammenfassung

Bis heute gibt es unbeantwortete, fundamentale Fragen zu Neutrinos, wie z.B. deren absolute Masse oder deren Natur (Dirac- oder Majorana-Teilchen). Neutrinoloser Doppelbetazerfall ($0\nu\beta\beta$-Zerfall) ist ein Prozess, der die Leptonenzahl um zwei Einheiten verletzt. Die Beobachtung des $0\nu\beta\beta$-Zerfalls könnte sowohl Informationen zu der Natur des Neutrinos sowie zur absoluten Massenskala liefern, wenn man annimmt, dass leichte Majorana-Neutrinos die Hauptvermittler des $0\nu\beta\beta$-Zerfalls sind.

Das GERDA-Experiment, das im Laboratori Nazionali del Gran Sasso (LNGS) steht, verwendet hochreine Germanium-Detektoren, welche mit dem Isotop ^{76}Ge angereichert sind. Phase I des Experiments lieferte ein neues Halbwertszeitlimit für den $0\nu\beta\beta$-Zerfall von ^{76}Ge von $T^{0\nu}_{1/2} > 2.1 \cdot 10^{25}$ yr ($90\,\%$ C.L.). Um in GERDA-Phase-II die Sensitivität der Messung der Halbwertszeit zu erhöhen, wurden Broad Energy Germanium Detektoren (BEGe) mit einer erhöhten Effizienz zur Pulsformdiskriminierung (PSD) in den GERDA-Kryostaten eingebaut. Diese neuen Detektoren haben gegenüber den Alten eine bessere Energieauflösung und können Untergründe besser erkennen.

Das Hauptthema dieser Dissertation ist die Entwicklung einer Methode zur PSD, welche auf die Daten von GERDA-Phase-I zur Untergrundunterdrückung angewendet wurde. Eine Methode zur Normalisierung des PSD-Parameters gegen Energie- und Zeitabhängigkeiten wurde entwickelt. Es wurde gezeigt, dass der Algorithmus zuverlässig angewendet werden kann. Der erhaltene PSD-Schnitt entfernt mit einer Effizienz von $(92\pm2)\,\%$ bei der Energie des Q-Wertes des Doppelbetazerfalls $80\,\%$ aller Untergründe der Phase I BEGe Daten. Systematische Studien zur Bestimmung der optimalen Länge eines sich bewegenden mittelnden Filters, welcher für die Glättung der Pulse der Phase-I-BEGe-Ereignisse verwendet wurden, sind durchgeführt worden. Das beste Signal/Untergrund-Verhältnis gelang für eine Länge von $\sim$50 ns. Des Weiteren wurde gezeigt, dass ein alternativer Algorithmus zur Reduktion des Rauschens, welcher auf einem Wavelet-Filter basiert, eine erhöhte Effizienz zur Untergrundidentifizierung erreicht. Bei der Anwendung dieser Filtertechnik auf einen Teil der GERDA-Phase-I-BEGe-Kalibrationsdaten konnte die Effizienz der Untergrunderkennung eines Kalibrationspeaks um $50\,\%$ gesteigert werden. Alle 30 für Phase-II produzierten BEGe-Detektoren durchliefen eine Charakterisierung im Testkryostaten, die mit Hilfe von Kalibrationsquellen durchgeführt wurde. Die Analyse der Kalibrationsmessungen zeigte für die 30 untersuchten BEGe-Detektoren eine Energieauflösung, die die Spezifikationen erfüllt. Des Weiteren ergab die Charakterisierung, dass eine Pulsformanalyse in verlässlicher Weise angewendet werden kann. Während BEGe-Detektoren

eine exzellente PSD-Performance besitzen, weisen sie eine Entartung der Pulsform für den Azimutwinkel auf. Aus diesem Grund können die Topologien der einzelnen Ereignisse und die Position von Strahlungsquellen nicht zuverlässig rekonstruiert werden. Ein neuartiger BEGe-Detektor mit vierfacher Segmentierung wurde vom Max-Planck-Institut für Physik konstruiert und von Canberra, France gebaut. Diese Segmentierung ermöglicht es zusätzliche Informationen zu den Topologien der einzelnen Ereignisse zu erhalten. Bei der ersten Charakterisierung dieses Prototyps konnte gezeigt werden, dass die Simulation die gemessenen Pulsformen sehr gut wiedergibt. Dies wird es ermöglichen einen Algorithmus zur Positionsrekonstruktion zu entwickeln, welcher auf der Basis einer Pulsformbibliothek funktioniert.

Abstract

There are still open fundamental questions about neutrinos such as their absolute mass scale and their nature (Dirac or Majorana particles). Neutrinoless double beta decay ($0\nu\beta\beta$ decay) is a process that violates the lepton number by two units. Observation of $0\nu\beta\beta$ decay could provide information on the nature of neutrinos and it is able to constrain the absolute scale of the neutrino mass assuming light Majorana neutrinos to be the main mediator for $0\nu\beta\beta$ decay.

The GERDA experiment at Laboratori Nazionali del Gran Sasso (LNGS) uses high purity germanium detectors enriched with the isotopes ^{76}Ge. Phase I of the experiment delivered a new limit for the half life of $0\nu\beta\beta$ decay in ^{76}Ge, $T^{0\nu}_{1/2}>2.1\times10^{25}$ yr (90 % C.L.). In order to improve the sensitivity on the half-life of $0\nu\beta\beta$ decay for GERDA Phase II, broad energy germanium detectors (BEGe) with improved pulse shape discrimination (PSD) efficiency resulting in a better background recognition efficiency and a better energy resolution were deployed in the GERDA cryostat.

The main focus of this dissertation is the development of PSD methods applied to Phase I BEGe data to reject background events. The normalization scheme to correct for the PSD dependencies in energy and time was developed. The algorithm was shown to be reliable. The obtained PSD cut rejects $\sim$80 % of background events in Phase I BEGe data at $Q_{\beta\beta}$ with a $0\nu\beta\beta$ decay detection efficiency of (92$\pm$2) %. Systematic studies to determine the optimal window size for the moving average filter used for smoothing the current pulse of Phase I BEGe events were performed. A window size of $\sim$50 ns resulted in the best S/N ratio. It was shown that an alternative de-noising algorithm based on wavelet filters resulted in an improved background identification efficiency. Applying this filtering technique on a subset of Phase I BEGe calibration data resulted in an increase of the background recognition efficiency of a full energy calibration peak by up to 50 %.

For Phase II, in total 30 BEGe detectors were produced. Prior to their delivery to LNGS all 30 detectors have been characterized in vacuum test cryostats using calibration sources. The analysis of the calibration measurements revealed that all 30 BEGe detectors have an energy resolution according to specifications and that pulse shape analysis can be performed reliably.

While BEGe detectors have superior PSD performance, there is a degeneracy of pulse shapes in azimuthal angle. Due to this reason, event topologies and source locations can not be reliably reconstructed. A novel BEGe detector with four-fold segmentation has been designed at Max Planck Institute for Physics and built by Canberra, France. The detector

segmentation allows to extract information on event topologies. A first characterization of this new prototype detector was performed. It was demonstrated that the measured pulse shapes can be well described by simulation. This will allow to develop a position reconstruction algorithm based on a pulse shape library method.

Contents

List of abbreviations

C.I.   Credible Interval

C.L.   Confidence Level

FWHM   Full Width at Half Maximum

GERDA   Germanium Detector Array

HPGe   High Purity Germanium Detectors

BEGe   Broad Energy Germanium Detectors

LAr   Liquid Argon

PSD   Pulse Shape Discrimination

ROI   Region Of Interest

BI   Background Index

SSE   Single-Site Events

MSE   Multi-Site Events

DEP   Double-Escape Peak

SEP   Single-Escape Peak

FEP   Full Energy Peak

A/E   A over E

$\beta\beta$ (decay)   Double beta [decay]

$2\nu\beta\beta$ (decay)   Two-neutrino double beta (decay)

$0\nu\beta\beta$ (decay)   Neutrinoless double beta (decay)

$Q_{\beta\beta}$ Q-value of double beta decay

$T_{1/2}^{2\nu}$ Half-life of $2\nu\beta\beta$ (decay)

$T_{1/2}^{0\nu}$ Half-life of $0\nu\beta\beta$ (decay)

$m_{\beta\beta}$ Effective Majorana neutrino mass

$G_{0\nu}$ Phase space factor

$M_{0\nu}$ Nuclear matrix element

Introduction

In the Standard Model (SM) of elementary particles, neutrinos are massless particles. Neutrino oscillation experiments with solar, atmospheric, and accelerator neutrino sources indicate non-zero neutrino mass and provide information on the differences between the squared masses. The mass scale and the nature of neutrinos (Dirac or Majorana) are still unknown.

For determining the neutrino mass scale, there are three types of experiments: measurement of the neutrino kinematical mass by determining the end point of the (tritium or other isotopes) beta decay spectrum; constraining the sum of neutrino masses from cosmological structure formation; determination of the effective Majorana neutrino mass through neutrinoless double beta decay ($0\nu\beta\beta$).

$0\nu\beta\beta$ is a process in which two neutrons decay into two protons with the emission of two electrons only. It can proceed only if neutrinos are massive Majorana particles. Assuming light Majorana neutrinos to be the dominant source for $0\nu\beta\beta$ decay, information on the effective Majorana mass can be extracted from determining the half-life of the decay. The experimental signature of $0\nu\beta\beta$ decay is a mono-energetic peak at the Q-value of the decay ($Q_{\beta\beta}$). The observation of this process would be a breakthrough discovery. It would reveal that the lepton number is not a good symmetry of nature in the neutrino sector and that neutrinos are their own antiparticles. Lepton number violation plays an important role to explain the generation of the baryon asymmetry of the Universe through the process of leptogenesis. Hence, discovery of the $0\nu\beta\beta$ dacay could be key to understand the evolution of our Universe. An introduction of neutrino physics, $0\nu\beta\beta$ decay process, and experimental efforts for the search of $0\nu\beta\beta$ decay are presented in Chapter 1.

The GERmanium Detector Array (GERDA) was built to search for $0\nu\beta\beta$-decay using the isotope ^{76}Ge. The core of the GERDA setup is an array of high-purity germanium detectors (HPGe) enriched to 86-88 % in the isotope ^{76}Ge. HPGe diodes with excellent energy resolution ($\sim$(0.16-0.24) % at $Q_{\beta\beta}$) are used as source and detector at the same time, which results in a high detection efficiency. The working principle and basic properties of HPGe detectors are described in Chapter 2. The basic principles of the GERDA experiment are described in Chapter 3. The GERDA experiment took data in its first phase (Phase I) between 2011 and 2013 with a total exposure of 21.6 kg·yr. A background index of about 10^{-2} cts/(keV·kg·yr) at $Q_{\beta\beta}$ of ^{76}Ge has been achieved, which is roughly an order of magnitude lower than the measured background levels from previous germanium experiments. A new lower limit of the half-life of $0\nu\beta\beta$ decay, $T_{1/2}^{0\nu}$, ($T_{1/2}^{0\nu}$>2.1·10^{25} yr at

90 % C.L.) was derived. The goal of the GERDA second phase (Phase II) is to improve the sensitivity of $T_{1/2}^{0\nu}$ by another order of magnitude. Additional 20 kg of enriched Broad Energy Germanium detectors (BEGes) with an improved background recognition efficiency and a better energy resolution, plus liquid argon veto instrumentation were deployed in the GERDA Phase II cryostat to achieve the sensitivity goal. Details of Phase I and the current status of Phase II are described in Chapter 3.

One of the main approaches to enhance the experimental sensitivity of $T_{1/2}^{0\nu}$ is to minimize the background at $Q_{\beta\beta}$. The underlying task of this thesis is to improve background rejection efficiencies based on the pulse shape discrimination (PSD) methods for the BEGe detectors. Four enriched BEGe detectors (GD32B, GD32C, GD32D and GD35B) produced for Phase II, were already deployed during Phase I. It was observed that the PSD parameters of the BEGe detectors have both time and energy dependencies which reduce the experimental sensitivity of $T_{1/2}^{0\nu}$. The analysis to correct these dependencies in PSD and the final signal efficiency after the PSD method which are to a large amount a result of this work, are presented in Chapter 4.

In order to enhance the signal recognition efficiency, in the framework of this thesis, a systematic study to find the optimal setting of the Phase I filter was performed. Additionally, an alternative new de-noising technique to improve the signal-to-noise ratio based on the wavelet analysis was developed. The methods for the optimization of the PSD are discussed in Chapter 5.

Before deploying the 30 BEGes to the GERDA Phase II cryostat, a detailed detector characterization was required. Results of these measurements, that were partly taken in the framework of this thesis, are summarized in Chapter 6.

BEGe detector have been demonstrated to have excellent energy resolution and superior PSD rejection efficiency on background events. However, BEGe detectors have a degeneracy in ϕ with respect to pulse shapes. This can lead to a slight decrease of PSD efficiency and a loss of source position reconstruction efficiency. A prototype BEGe detector with 4-fold segmentation has been designed at MPI for Physics and produced by Canberra, France. The additional segmentation facilitates extraction of position information to enable full reconstruction of event topologies. In order to understand this new type of detector, characterization measurements by using a collimated ^{133}Ba source were preformed in the course of this thesis. The basic parameters such as energy resolutions, segment boundaries, temperature dependence of the rise times, as well as the crystal axes were measured. Details are given in Chapter 7.

Chapter 1

Neutrino Physics and Neutrinoless Double Beta Decay

1.1 The Role of $0\nu\beta\beta$ Decay in Neutrino Physics

1.1.1 Neutrinos in the Frame of Standard Model Particle Physics

The Standard Model (SM) of particle physics consistently describes nearly all phenomena observed in experiments. It was developed in the the second half of the 20th century. Neutrinos in the SM are considered as:

- massless,

- left-handed, whereas antineutrinos are right-handed,

- not identical to their antiparticles (Dirac particles),

- to have three flavors: electron neutrinos (ν_e), muon neutrinos (ν_ν), and tau neutrinos (ν_τ).

However, results from the neutrino oscillation experiments showed that neutrinos have a finite mass, indicating new physics beyond the SM.

1.1.2 Neutrino Oscillations

Solar Neutrino Problem

Solar neutrinos were first detected by the Homestake experiment lead by Ray Davis [1] in 1968. The Homestake experiment observed a deficit in the number of solar neutrinos reaching the earth. Only about 1/3 of the expected number of neutrinos was detected as predicted by the Standard Solar Model (SSM) [2]. The experiment consisted of a large tank of liquid C_2Cl_4 located underground. It makes use of the reaction:

$$\nu_e + {}^{37}Cl \rightarrow e^- + {}^{37}Ar \tag{1.1}$$

The deficit of the solar neutrino flux is called "solar neutrino problem". The deficit in the ν_e flux was confirmed by several experiments such as Kamiokande [3], SAGE [4], and GALLEX [5].

Neutrino Oscillations in Theory

The idea of neutrino oscillation was first proposed by B. Pontecorvo [7] in 1957 who suggested that neutrino-antineutrino transitions might occur in analogy with K^0 mixing. No observation of such a process was found but the idea was developed as the nowadays theory of neutrino oscillation. In 1962, Z. Maki, M. Nakagawa, and S. Sakata proposed neutrino flavor oscillations [8].

For the theoretical description of massive neutrinos, their flavor eigenstates $|\nu_\alpha\rangle$ ($\alpha{=}e,\mu,\tau$) can be represented as the superposition of the mass eigenstates $|\nu_i\rangle$ ($i{=}1,2,3$) and vice versa:

$$|\nu_\alpha\rangle = \sum_i U^*_{\alpha i}|\nu_i\rangle \;\; \text{and} \;\; |\nu_i\rangle = \sum_\alpha U_{\alpha i}|\nu_\alpha\rangle, \qquad (1.2)$$

where U is an unitary matrix referred to as the neutrino mixing or Pontecorvo-Maki-Nakagawa-Sakata matrix (PMNS) matrix. A parametrization of the PMNS matrix is:

$$U = \begin{pmatrix} 1 & 0 & 0 \\ 0 & c_{23} & s_{23} \\ 0 & -s_{23} & c_{23} \end{pmatrix} \times \begin{pmatrix} c_{13} & 0 & s_{13}\,e^{-i\delta} \\ 0 & 1 & 0 \\ -s_{13}\,e^{i\delta} & 0 & c_{13} \end{pmatrix} \times \begin{pmatrix} c_{12} & s_{12} & 0 \\ -s_{12} & c_{12} & 0 \\ 0 & 0 & 1 \end{pmatrix} \times \begin{pmatrix} e^{i\alpha_1/2} & 0 & 0 \\ 0 & e^{i\alpha_2/2} & 0 \\ 0 & 0 & 1 \end{pmatrix},$$

$$(1.3)$$

where $c_{ij} \equiv \cos\theta_{ij}$ and $s_{ij} \equiv \sin\theta_{ij}$, θ_{ij} are three mixing angles, and δ, α_1, α_2 are CP-violating phases. The phases α_1 and α_2 are called Majorana phases; they exist only if neutrinos are Majorana particles.

The $\nu_\alpha \rightarrow \nu_\beta$ oscillation probability for a propagating neutrino with energy E at distance L from the source can be calculated as:

$$\begin{aligned} P(\nu_\alpha \rightarrow \nu_\beta) &= |\langle \nu_\beta | \nu_\alpha(t) \rangle|^2 \\[2mm] &= |\sum_{i,\beta} U_{\alpha i} \exp(-ipt)\exp(-\frac{-im_i^2 t}{2E})\, U^\dagger_{\beta i}|^2 \\[2mm] &= \sum_{i,j} U^\dagger_{\alpha i} U_{\beta i} U_{\alpha j} U^\dagger_{\beta j} \exp(-\frac{i\Delta m_{ij}^2 L}{2E}) \\[2mm] &= \delta_{\alpha\beta} - 4\sum_{i>j} \text{Re}(U^\dagger_{\alpha i} U_{\beta i} U_{\alpha j} U^\dagger_{\beta j})\sin^2(\frac{\Delta m_{ij}^2 L}{4E}) \\[2mm] &+ 2\sum_{i>j} \text{Im}(U^\dagger_{\alpha i} U_{\beta i} U_{\alpha j} U^\dagger_{\beta j})\sin(\frac{\Delta m_{ij}^2 L}{2E}), \end{aligned} \qquad (1.4)$$

where $\Delta m_{ij} \equiv m_i^2 - m_j^2$ is the mass-squared difference.

The neutrino oscillation probabilities depend on the 4 mixing parameters θ_{12}, θ_{13}, θ_{23} and δ, and on 2 mass-squared differences Δm_{12}^2 and Δm_{23}^2. The mixing angle θ_{12} and

Parameter	Best fit 1σ
Δm_{12}^2	$(7.50\pm0.20)\times10^{-5}\,\text{eV}^2$
$|\Delta m_{23}^2|$	$(2.32^{+0.12}_{-0.08})\times10^{-3}\,\text{eV}^2$
$\sin^2 2\theta_{12}$	0.857 ± 0.024
$\sin^2 2\theta_{23}$	>0.95
$\sin^2 2\theta_{13}$	0.095 ± 0.010

Table 1.1: Best fit values of the oscillation parameters. Table extracted from [6].

Δm_{12}^2 were measured by solar neutrino and long-baseline reactor neutrino experiments. The mixing angle θ_{23} and Δm_{23}^2 were measured by atmospheric neutrinos and long-baseline accelerator neutrino experiments. The mixing angle θ_{13} was determined by short-baseline reactor neutrino and long-baseline accelerator neutrino experiments. Best fit 1-σ values of the oscillation parameters deduced from the oscillation experiments are summarized in Table 1.1. The sign of Δm_{12}^2 is known from the solar neutrino experiments interpreting neutrino oscillation in matter due to the Mikheyev-Smirnov-Wolfenstein effect (MSW effect) [9]. The atmospheric neutrino oscillation experiments are not sensitive to the sign of Δm_{23}^2, hence, two mass orderings are possible:

- Normal hierarchy (NH):

$$m_1 < m_2 < m_3; \quad \Delta m_{12}^2 \ll \Delta m_{23}^2, \tag{1.5}$$

- Inverted hierarchy (IH):

$$m_3 < m_1 < m_2; \quad \Delta m_{12}^2 \ll |\Delta m_{13}|^2. \tag{1.6}$$

Two questions regarding neutrino masses still remain unanswered from the observations of the neutrino oscillation experiments:

- what is the absolute value of the neutrino mass?

- neutrino mass orderings are normal hierarchy or inverted hierarchy?

1.1.3 Neutrino mass Observables and Experimental Approaches

The neutrino oscillation experiments are not sensitive to the absolute scale of the neutrino mass. There are three experimental approaches to determine the neutrino mass scale with different effective observables:

- kinematical mass

$$m_\beta = \sqrt{\sum_{i=1}^{3} |U_{ei}|^2 \, m_i^2}, \tag{1.7}$$

- sum of neutrino masses

$$m_{\sum} = \sum_i m_i, \tag{1.8}$$

- effective neutrino Majorana mass

$$m_{\beta\beta} = |\sum_{i=1}^{3} U_{ei}^2 \, m_i| \;\; = |e^{i\alpha_1}|U_{e1}^2|m_1 + e^{i\alpha_2}|U_{e2}^2|m_2 + e^{-2i\delta}|U_{e3}^2|m_3|. \tag{1.9}$$

In the kinematical mass approach, the measurements are performed by measuring the end point of the beta decay spectrum which is directly affected by the rest mass of the emitted neutrino. In these experiments β-emitting isotopes with low Q-values are used. The MAINZ, TROITSK, and KATRIN experiment are based on Tritium β-decay with a Q-value of $18.59\,\mathrm{keV}$ using large spectrometers. The MAINZ and TROITSK experiments gave upper limits on the electron neutrino mass of $m_\beta < 2.3\,\mathrm{eV}$ (95 % C.L.) [10] and $m_\beta < 2.1\,\mathrm{eV}$ (95 % C.L.) [11], respectively. The KATRIN experiment with an expected sensitivity of $0.3\,\mathrm{eV}$ is scheduled to start taking data in 2017. Future experiments such as ECHO [12] and HOLMS are based on the measurement of the ^{163}Ho electron capture spectrum with an endpoint of $2.8\,\mathrm{keV}$. These experiments are planed to reach a sensitivity down to sub-eV region.

The second approach is to constrain the sum of neutrino masses from cosmological and astrophysical observations. In the standard model of cosmology, the neutrinos can contribute to the cosmological matter density, Ω, by an amount, $\Omega_\nu h^2 = m_{\sum}/92.5\,eV$, where Ω_ν is the neutrino mass density and h is the Hubble constant (in unit of km/s/Mpc). A recent model dependent limit of $m_{\sum} < 0.17\,eV$ (95 % C.L.), was published by the Planck collaboration [13]. Further large scale experiment like EUCLID [14], which is scheduled for launch in 2020, will be able to probe the neutrino mass hierarchy.

Measurement of $0\nu\beta\beta$ decay can probe $m_{\beta\beta}$ assuming the dominant mediating process being the exchange of a light Majorana neutrino. Fig. 1.1 shows the effective Majorana mass as a function of the lightest neutrino mass. Neutrino oscillation experiments still allow two neutrino mass orderings: normal hierarchy (NH) or inverted hierarchy (IH). The three levels of uncertainties corresponds to 1σ, 2σ, and 3σ of the neutrino oscillation parameters obtained in the global analysis [39]. The horizontal line represents the upper limit of the effective Majorana neutrino mass derived from $0\nu\beta\beta$ decay experiments, whereas the vertical line denotes the upper limit of the lightest neutrino mass that can be derived from beta decay experiments or from cosmological and astrophysical observations. The current most sensitive experiments to derive $m_{\beta\beta}$ upper limits are in the range of $\sim$0.2-0.6 eV (depending on the theoretical calculation of the nuclear matrix elements). GERDA experiment [24] uses ^{76}Ge isotopes and EXO [25] and KAMLAND-ZEN experiment [31] adopt ^{136}Xe isotopes.
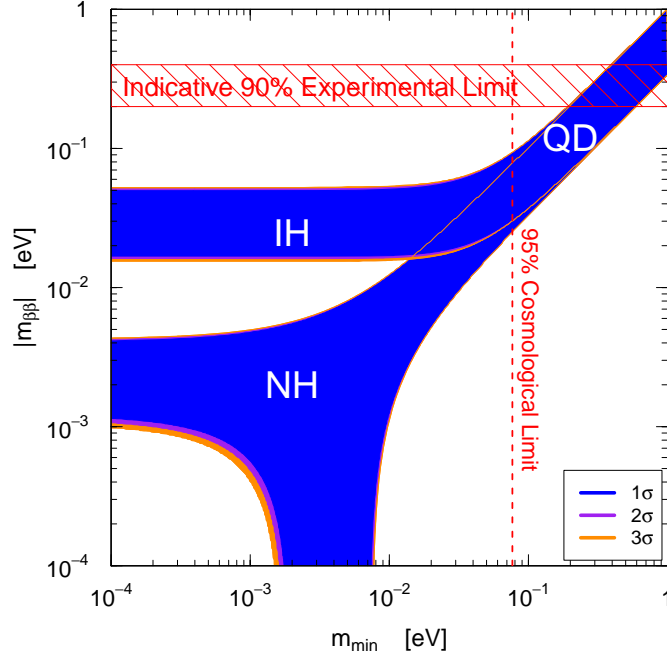
Figure 1.1: Effective Majorana mass as a function of the lightest neutrino mass for the normal hierarchy (NH) and the inverted hierarchy (IH). QD stands for quasi-degeneracy: $m_1^2 \simeq m_2^2 \simeq m_3^2$. Taken from [39].

1.2 Double Beta Decay

Double beta decay $(2\nu\beta\beta)$ is a nuclear process in which two neutrons are converted into two protons under the emission of two electrons and two electron antneutrinos:

$$(2\nu\beta\beta): \; {}^{A}_{Z}X \to {}^{A}_{Z+2}X + 2e^- + 2\bar{\nu}_e, \tag{1.10}$$

where ${}^{A}_{Z}X$ is a nucleus with atomic number Z and atomic mass A.

The $2\nu\beta\beta$ decay process is allowed in the SM and exists due to nuclear pairing interaction that energetically favours the even-even isobars over the odd-odd ones. In the case of ^{76}Ge, the decay to the daughter nucleus, ^{76}As, is energetically forbidden (see Fig. 1.2). Hence, ^{76}Ge can only decay to ^{76}Se. The Feynman diagram of the $2\nu\beta\beta$ process is shown in Fig. 1.3(a). The process is a second-order weak process and hence it has a extremely long half-life $(T_{1/2}^{2\nu})$. The measured half-lives in various isotopes are in the range of 10^{18}-10^{24}
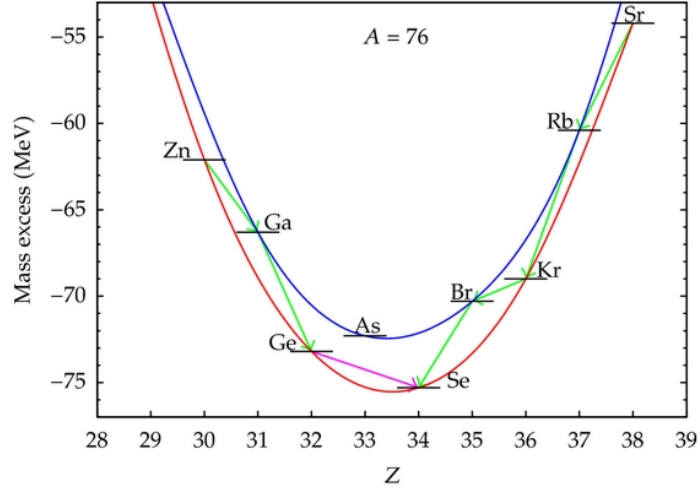
Figure 1.2: Decay scheme of nuclei with A=76. Even-even nuclei are more bound than odd-odd nuclei. The single beta decay from ^{76}Ge to ^{76}As is energetically forbidden. Taken from [15].

yr [16, 17, 18].

For $2\nu\beta\beta$, the total kinetic energy (Q-value of the decay) is shared between the electrons and electron antineutrinos. Therefore, the spectrum of the sum of kinetic energies of electrons is continuous and ends at the Q-value of the decay, as shown in Fig. 1.3(c).

1.3   Neutrinoless Double Beta Decay

In the neutrinoless mode of double-beta Decay ($0\nu\beta\beta$) no neutrinos are emitted,

$$(0\nu\beta\beta): \; {}^A_Z X \rightarrow^A_{Z+2} X + 2e^-. \tag{1.11}$$

The $0\nu\beta\beta$ process was first proposed by Ettore Majorana [20] in 1937. In $0\nu\beta\beta$ decay the lepton number is violated by 2 units. The process is only allowed if neutrinos have Majorana character, i.e. are identical with their own anti-particle. Observation of $0\nu\beta\beta$ would demonstrate physics process beyond the SM. Fig. 1.3(b) shows the Feynman diagram of $0\nu\beta\beta$ decay for the most popular mechanism of exchanging a light Majorana neutrino. There are other beyond SM processes that can contribute to $0\nu\beta\beta$ decay such as right-handed weak currents, R-parity violating SUSY [21, 22], and many other processes.

Fig. 1.3(c) shows the sum spectrum of the kinetic energies of the emitted electrons for $2\nu\beta\beta$ and $0\nu\beta\beta$ decay. The total kinetic energy in $0\nu\beta\beta$ decay is shared between the two emitted electrons and results in a mono-energetic peak at Q-value of the decay, $Q_{\beta\beta}$.

In 1982, Schechter and Valle showed that: any process that allows $0\nu\beta\beta$ to occur requires Majorana neutrinos with non-zero mass [23] (the theorem is called Schechter-

Valle theorem or black box theorem). In summary, the observation of $0\nu\beta\beta$ decay would demonstrate LNV and that neutrinos have Majorana nature, regardless of the mechanisms mediating the process and physics beyond SM.
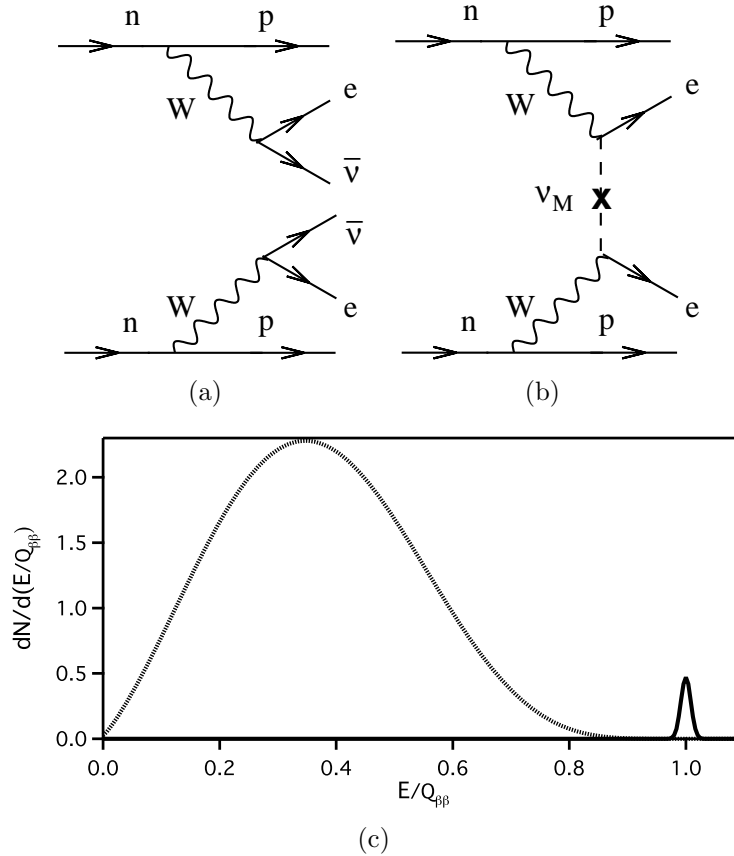

Figure 1.3: (a) Feynman diagram for $2\nu\beta\beta$ decay. (b) Feynman diagram for $0\nu\beta\beta$ decay, assuming the mechanism is the exchange of light Majorana neutrinos. (c) The sum spectrum of the kinetic energies of the emitted electrons for $2\nu\beta\beta$ decay (continuous spectrum) and $0\nu\beta\beta$ decay (mono-energetic peak at $Q_{\beta\beta}$). Figures from [21].

1.4 The Search for Neutrinoless Double Beta Decay

$0\nu\beta\beta$ decay can proceed only if neutrinos are massive Majorana particles. However, the measurement of this decay is challenging due to its long half-life - more than $\sim 10^{25}$ years (limit obtained for ^{76}Ge). The signature is a mono-energetic peak, at 2.039 MeV in the energy spectrum for ^{76}Ge. A very low background rate in the energy region of interest, large exposure with a high fraction of the $0\nu\beta\beta$ decay isotope in the detector target, very good energy resolution and high signal recognition efficiency are the key parameters to

achieve a good sensitivity on the half-life of $0\nu\beta\beta$ decay. The experimental approaches to the $0\nu\beta\beta$ decay is given in this chapter.

1.5 $0\nu\beta\beta$ Signal and Sensitivity

The experimental observable of $0\nu\beta\beta$ decay is the half-life. The number of observed $0\nu\beta\beta$ decay events is related to the $T^{0\nu}_{1/2}$ by:

$$N^{0\nu} = N_A \cdot M \cdot \epsilon \cdot \kappa \cdot (1 - e^{-t\ln 2/T^{0\nu}_{1/2}})/M_A, \tag{1.12}$$

$$\epsilon = f_{76} \cdot f_{av} \cdot \varepsilon_E \cdot \varepsilon_{PSD}, \tag{1.13}$$

where N_A is Advogadros number, M is the total mass of the source material, ϵ is the signal detection efficiency, κ is the mass fraction of the $0\nu\beta\beta$ isotope, t is the measuring time, and M_A is the atomic mass of the isotope. The detection efficiency is composed of several terms, where f_{76} is the fraction of ^{76}Ge atoms, f_{av} is the active volume fraction, ε_E is the energy detection efficiency at $Q_{\beta\beta}$, and ε_{PSD} is the signal acceptance efficiency after pulse shape discrimination cut.

For $T^{0\nu}_{1/2} \gg t$, the relation can be approximately described as:

$$N^{0\nu} = \ln 2 \cdot N_A \cdot M \cdot t \cdot \epsilon \cdot \kappa/(M_A \cdot T^{0\nu}_{1/2}). \tag{1.14}$$

The number of background events in the region of interest around $Q_{\beta\beta}$ is given by:

$$N^{bkg} = M \cdot t \cdot B \cdot \Delta E, \tag{1.15}$$

where B is the background index (usually given in units of cts/(keV·kg·yr)), and ΔE is the width of energy windows, which depends on the energy resolution in the experiment.

In most experimental situations, $N^{bkg} > 0$; in this case the upper limit of $T^{0\nu}_{1/2}$ can be formulated as:

$$T^{0\nu}_{1/2} > \frac{\ln 2}{1.64} \frac{N_A}{M_A} \epsilon \cdot \kappa \sqrt{\frac{M \cdot T}{B \cdot \Delta E}} \quad \text{(at 90\% C.L.)} \tag{1.16}$$

1.6   Experimental Challenges for $0\nu\beta\beta$ Decay

By assuming the dominant mechanism for $0\nu\beta\beta$ decay to be the exchange of light Majorana neutrinos, the decay rate for a given isotope is described by:

$$(T^{0\nu}_{1/2})^{-1} = G^{0\nu}(Q_{\beta\beta}, Z) \cdot |M^{0\nu}|^2 \frac{m^2_{\beta\beta}}{m^2_e}, \tag{1.17}$$

where $G^{0\nu}$ is the phase space factor, $M^{0\nu}$ is the nuclear transition matrix element (NME), $m_{\beta\beta}$ is the effective Majorana neutrino mass, and m_e is the rest mass of the electron.

$G^{0\nu}(Q_{\beta\beta}, Z)$ depends on the $Q_{\beta\beta}$ value and the atomic number Z. $G^{0\nu}(Q_{\beta\beta}, Z)$ is proportional to $Q^5_{\beta\beta}$ [21] and can be reliably calculated. There exist $\sim$35 candidate isotopes

Isotope	$G^{0\nu}$ $[10^{-14}/\text{yr}]$	$Q_{\beta\beta}$ [keV]	Natural abundance [%]	Experiment
^{48}Ca	6.3	4273.7	0.187	CANDLES
^{76}Ge	0.63	2039.1	7.8	GERDA, Majorana Demonstrator
^{82}Se	2.7	2995.5	9.2	SuperNEMO, Lucifer
^{100}Mo	4.4	3035.0	9.6	MOON, AMoRe
^{116}Cd	4.6	2809.1	7.6	Cobra
^{130}Te	4.1	2530.3	34.5	CUORE
^{136}Xe	4.3	2457.8	8.9	EXO, Next, Kamland-Zen
^{150}Nd	19.2	3367.3	5.6	SNO+, DCBA/MTD

Table 1.2: List of $0\nu\beta\beta$ isotopes in the field of $0\nu\beta\beta$ searches and their basic parameters. Table extracted from [35].

that dominantly undergo $2\nu\beta\beta$ decay, the ones with higher $Q_{\beta\beta}$ values are feasible for $0\nu\beta\beta$ decay searches. Only isotopes with $Q_{\beta\beta} \geq 2$ MeV are considered for experimental searches for $0\nu\beta\beta$ decay because above this energy background radiation from natural decay chains is considerably lower. The suitable isotopes in the field of $0\nu\beta\beta$ searches are: ^{76}Ge, ^{136}Xe, ^{130}Te , ^{100}Mo, ^{82}Se, ^{150}Nd, ^{48}Ca, ^{116}Cd, etc. The various isotopes adopted for the experimental searches for $0\nu\beta\beta$ are listed in Table 1.2.

The $M^{0\nu}$ value can be estimated by different approximations, such as: Quasiparticle Random Phase Approximation (QRPA) [36], Interacting Boson Mode (IBM) [37], Generating Coordinate Method (GCM) [38], and other models. Concerning the $0\nu\beta\beta$ sensivity (or $0\nu\beta\beta$ decay rate) per unit mass of isotope, there is no preferred isotope for the $0\nu\beta\beta$ decay searches [34]. There is considerably uncertainty from nuclear physics in the calculation of $M^{0\nu}$. Calculated values for ^{76}Ge differ by up to a factor of $\sim$3. This is a significant uncertainty in converting the measured $0\nu\beta\beta$ decay rate to the effective Majorana neutrino mass. Hence, the experimental result is usually reported by the use of $T^{0\nu}_{1/2}$ value.

Very low background rate in the energy region of interest, large exposure with a high fraction of the $0\nu\beta\beta$ decay isotope, good energy resolution and high signal recognition efficiency are the key parameters to achieve a high sensitivity on the half-life of $0\nu\beta\beta$ decay.

The GERDA experiment uses high purity germanium detectors (HPGe) enriched with the isotopes ^{76}Ge. The detector itself is served as a $0\nu\beta\beta$ source, which results in a high detection efficiency. HPGe detectors have an excellent energy resolution, $\sim$0.2 % in the region of interest, the background due to $2\nu\beta\beta$ decay is hence negligible. HPGe detectors are intrinsically pure, which is very important to the low background experiments. Also, HPGe detectors are industrial produced, i.e. there is lots of experience by suppliers. The drawback of using germanium is that the natural abundance of ^{76}Ge in geramnium is 7.8 %. In order to increase the sensitivity to the $T^{0\nu}_{1/2}$, hence enrichment is required.

1.7   Searching for $0\nu\beta\beta$ Decay

The current most sensitive experiments for the search of $0\nu\beta\beta$ decay are based on the isotopes ^{76}Ge and ^{136}Xe. With combined limit for the effective Majorana mass in a range of 200-600 meV [24, 25].

Previous most sensitive experiments in $0\nu\beta\beta$ decay searches were the Heidelberg-Moscow experiment (HDM) and the international Germanium experiment (IGEX). Both experiments used high purity germanium detectors enriched in ^{76}Ge isotopes. The HDM experiment operated 6 detectors with a total mass of $\sim$11 kg in copper cryostats and surrounded by copper, lead, and polyethylene shielding. An excellent energy resolution of 0.2 % FWHM was achieved. With 35.5 kg·yr data taking in Gran Sasso underground laboratory, the HDM collaboration reported an upper limit of $T_{1/2}^{0\nu}\geq1.3\times10^{25}$ yr (90 %C.L.) and $T_{1/2}^{0\nu}>1.9\times10^{25}$ yr (90 %C.L.), before and after the pulse shape analysis [26].

The IGEX collaboration published their final results with 117 mol·yr of ^{76}Ge data and placed a lower bound for $T_{1/2}^{0\nu}\geq1.57\times10^{25}$ yr (90 %C.L.) [27]. The HDM and IGEX experiment both reached a low background indices of the order of 10^{-1} cts/(keV·kg·yr). A controversial claim for the observation of a ^{76}Ge $0\nu\beta\beta$ decay signal was reported by a subgroup of the HDM collaboration with $T_{1/2}^{0\nu}=1.19^{+0.37}_{-0.23}\times10^{25}$ yr (90 %C.L.) [28], which the announcement raised skepticism in the scientific community [29].

The current experiments using enriched ^{76}Ge isotopes as detectors are GERDA and MAJORANA experiments. The core of the GERDA setup for the search of the $0\nu\beta\beta$ decay is an high purity germanium detector array enriched in ^{76}Ge and operated in ultra-pure liquid argon. In GERDA Phase I, total exposure of 21.6 kg·yr and a low background index of 10^{-2} cts/(keV·kg·yr) have been achieved. A new lower limit of $T_{1/2}^{0\nu}>2.1\times10^{25}$ yr (90 %C.L.) has been set [24] (refer to Chapter 3 for more details.). In combination of the results from GERDA, HDM [26], and IGEX [27], the lower limit of $T_{1/2}^{0\nu}>3.0\times10^{25}$ yr (90 %C.L.) was set. The GERDA Phase I result disfavoured the observation of a ^{76}Ge $0\nu\beta\beta$ decay signal in a model-independent way. For GERDAPhase II, the goal is to explore the $T_{1/2}^{0\nu}$ in the range of 10^{26} yr with the background index $<10^{-3}$ cts/(keV·kg·yr) and an exposure of $\sim$100 kg·yr. The GERDA experiment started Phase II data taking at the end of December of 2015. The MAJORANA experiment [30] aims as a comparable sensitivity as GERDA Phase II and started data taking in 2015. For the MAJORANA experiment, the germanium detectors are assembled into two modular instruments composed of cryostats built from ultra-pure electroformed copper. The Ge detectors are shielded by Cu-, lead-, and polyethylene-shield. The primary goal of the experiment is to demonstrate the feasibility of a next-generation experiment in terms of backgrounds and scalability.

Experiments pursued in searching of $0\nu\beta\beta$ decay in ^{136}Xe isotopes are the KAMLAND-ZEN experiment and the EXO-200 experiment. The KAMLAND-ZEN experiment uses 13 tons of xenon-doped liquid scintillator inside a transparent nylon balloon (mini-balloon) with a diameter of 3 m. The mini-balloon is enclosed in an outer balloon with a diameter of 13 m filled with liquid scintillator which serves as an active shield. The event topology and the energy of the signal events can be reconstructed by the outer PMTs.

Compared to the germanium technology, the energy resolution by using PMTs are limited, an energy resolution of $\sim 3.9\,\%$ (FWHM) at $Q_{\beta\beta}$ of ^{136}Xe was shown. The KAMLAND-ZEN experiment has reached the largest exposure in the field of $0\nu\beta\beta$ decay searches. For KAMLAND-ZEN Phase I, with an exposure of $89.5\,$kg·yr, $T_{1/2}^{0\nu} > 1.9 \times 10^{25}\,$yr (90 %C.L.) was derived [31]. For the KAMLAND-ZEN Phase I, the ^{110m}Ag background contamination limited the first results on upper limit of $T_{1/2}^{0\nu}$. For the current data taking, purification on reducing ^{110m}Ag background was performed and the ^{110m}Ag background was reduced by a factor of ~ 10 at $Q_{\beta\beta}$. With the combined data before and after purification, an upper limit of $T_{1/2}^{0\nu} > 2.6 \times 10^{25}\,$yr (90 %C.L.) was achieved [32]. The EXO-200 experiment was performed by using a liquid xenon time projection chamber (TPC) filled with 175 kg of liquefied xenon. Both the ionization signal and the scintillation light are measured, which allows to have superior energy resolution $3.6\,\%$ at $Q_{\beta\beta}$ of ^{136}Xe. With an exposure of $32.5\,$kg·yr, a result of $T_{1/2}^{0\nu} > 1.6 \times 10^{25}\,$yr (90 %C.L.) was published [33].

Chapter 2

Signal Detection with HPGe Detectors

High purity germanium detectors (HPGe) are widely used in many applications - in spectroscopy, gamma ray tracking, rare event searches like neutrinoless double beta-decay and dark matter searches. They have excellent energy resolution, about 0.1% at 1 MeV, high detection efficiency for α-, β- and γ-radiation, high radio-purity of the detector material and the potential merit of background recognition by pulse shape discrimination (PSD) using the spatial information of charge depositions. These features are applicable to the search for the rare $0\nu\beta\beta$ decay in germanium, discussed in Section 1.4. Good understanding of the detectors and an enhanced pulse shape recognition efficiency between signal-like events and background-like events are crucial to the success of the experiments.
This chapter gives a brief review on the interaction of different types of radiation with matter and how they can be detected using solid-state detectors. The working principle, characteristics of HPGe detectors and the signal formation process are introduced. "Intelligent" detectors, Broad Energy Germanium Detectors (BEGes), used in GERDA Phase II are presented. A powerful PSD technique for BEGe detectors is introduced.

2.1 Interactions of Particles with Matter

The detection of particles happens via their interaction with the material they traverse.

2.1.1 Photons

The three main mechanisms for photons to deposit their energy in matter are: photoelectric absorption, Compton scattering and pair production. The cross sections of photons with matter depends on the atomic number, Z, on the absorber material and the incident photon energy, E_γ. The photoelectric absorption dominates for E_γ up to 140 keV in germanium. Compton scattering is the most important process in the energy range 140 keV $\lesssim E_\gamma \lesssim$ 8.4 MeV. At higher energies, pair production in the electric field of nuclei is the dominant

process.

- **Photoelectric absorption**
  In this process, a photon interacts with the entire atom, not with a free electron. A photon transfers its full energy to a bound electron. The electron is ejected with a kinetic energy, E_e, given by:

$$E_e = E_\gamma \, - \, \varepsilon, \tag{2.1}$$

  where ε is the binding energy of the electron. The cross section of photoelectric absorption, σ_{pa}, can be roughly approximated as [69]:

$$\sigma_{pa} \propto \, Z^n E_\gamma^{-3.5}, \tag{2.2}$$

  where n varies between 4 and 5 over the various photon energies. Hence the effect is strongly enhanced for high-Z materials and is insignificant for photon energies above 1 MeV.

- **Compton scattering**
  The scattering of a photon off a quasi-free electron is called Compton scattering. Its differential scattering cross section per unit solid angle is described by the Klein-Nishina formula [71]. At higher energies ($E_\gamma \gg m_e c^2$), the Compton scattering cross section, σ_{cs}, is given by [72]:

$$\sigma_{cs} = r_e^2 \pi \frac{m_e c^2}{E_\gamma} \left[ln \left(\frac{2E_\gamma}{m_e c^2} \right) + \frac{1}{2} \right]. \tag{2.3}$$

  σ_{cs} decreases with the form of $ln(E_\gamma)/E_\gamma$ and in general Compton scattering is the dominant process from 100 keV to 10 MeV photon energy. Moreover, the process has a well defined kinematic constraint. The maximum energy transfer to an electron is given by 180° backscattering of a photon.

- **Pair production**
  Production of electron-positron pairs in the E-field of a nucleus can occur only for $E_\gamma > 2m_e c^2 = 1.022$ MeV. The pair production cross section, σ_{pp}, rapidly rises above the threshold and is proportional to $Z^2 \, ln E_\gamma$ [73]. It does not decrease with energy. Pair production in germanium dominates for $E_\gamma > 10$ MeV and saturates for $E_\gamma \gtrsim 100$ MeV. After a pair production process, the created electron and positron lose their kinetic energy and the positron subsequently annihilates with another electron and emits two back-to-back 511 keV photons.

The photon cross section per unit mass in matter can be described by the mass attenuation coefficient, μ:

$$\mu = \frac{N_A}{A}(\sigma_{pa} + \sigma_{cs} + \sigma_{pp}). \tag{2.4}$$
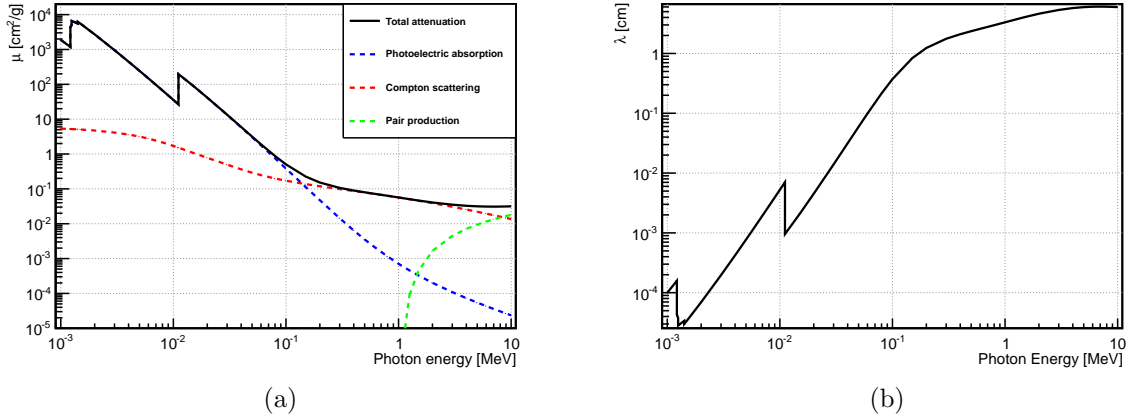
Figure 2.1: (a) Photon mass attenuation coefficient in germanium as a function of incident photon energy. (b) Photon mean free path in germanium. The plots are produced using the NIST photon cross section database [68]. The see-saw structure is due to the absorption edges from different shells.

The mean free path, λ, of photons in matter is described by the inverse of the product of mass attenuation coefficient and absorber density, ρ:

$$\lambda = (\mu\rho)^{-1}. \tag{2.5}$$

The mass attenuation coefficient, μ, and the mean free path, λ, of photons in germanium are shown in Fig. 2.1(a) and Fig. 2.1(b), respectively. For MeV photons in germanium, the mean free path is about a few centimeters.

2.1.2 Electrons, Positrons

The electromagnetic (EM) interaction is the dominant process for sub-GeV charged particles interacting with matter. Electrons and positrons lose their energy in the medium they pass through via ionization and bremsstrahlung. At low electron energies (below few tens of MeVs), the primary process of energy loss of an electron is ionization of the atoms of the medium. Above the critical energy, E_c, energy loss due to bremsstrahlung plays a leading role. E_c depends on the material and can be approximately expressed by the formula [65]:

$$E_c = 800/(Z + 1.2) \; MeV. \tag{2.6}$$

• **Ionization**

The kinetic energy lost per unit distance, dE/dx, of electrons or positrons due to ionization in the target material is given by [66]:

$$-\frac{dE}{dx} = 4\pi N_A r_e^2 m_e c^2 \frac{Z}{A}\frac{1}{\beta^2}\left[ln\left(\frac{\gamma m_e c^2}{2I}\right) - \beta^2 - \frac{\delta^*}{2}\right], \tag{2.7}$$

where N_A is Avogardo's number, r_e is classical electron radius, m_e is electron mass, A, Z is atomic mass and charge of absorber, $\beta = v/c$ is electron velocity, γ is Lorentz factor, I is Mean excitation energy of absorber, which characterizes the stopping properties of a material, and δ^* is Parameter for density effect correction. [1]

- **Bremsstrahlung**
  Electrons or positrons being decelerated or accelerated in the field of a nucleus radiate bremsstrahlung photons. The kinetic energy loss of an electron due to the emission of bremsstrahlung photons can be described using the formula: [66]

$$-\frac{dE}{dx} = 4\alpha r_e^2 \frac{N_A}{A} Z^2 E \; ln \left(\frac{183}{Z^{1/3}} \right), \tag{2.8}$$

  where α is the fine-structure constant and E is the incident electron energy.

The range, R, of an electron or positron in the medium depends on its initial energy and energy loss therein. It can be calculated through the energy loss from initial kinetic energy E_0 down to zero, namely,

$$R = \int_{E_0}^{0} \left(\frac{dE}{dx} \right)^{-1} dE. \tag{2.9}$$

The energy loss, dE/dx, in the range of sub-GeV electrons in germanium is depicted in Fig. 2.2(a). It shows that E_c for electrons in germanium is around 24 MeV. Hence the electrons emitted from $2\nu\beta\beta$ decay of ^{76}Ge lose their energies mainly by the ionization process. Fig. 2.2(b) displays the range of electrons in germanium. The range for 1 MeV electrons or positrons in germanium is about 1 mm.

2.1.3 α-particles

A charged particle is called "heavy" if its rest mass is large compared to the rest mass of an electron. Protons, α-particles, mesons and fission fragments are all heavy charged particles. Heavy charged particles like α-particles ($^4_2$He nuclei) lose their energy via collisions with the electrons and the nucleons in germanium. The dE/dx of heavy charged particles in germanium is dominated by two terms : the nuclear stopping power term and the electronic stopping power term. The nuclear stopping power considers energy transfers from the incident α-particle to the germanium nuclei. The electronic stopping power includes all the processes in which the α-particles transfer their energy to the target electrons. Fig. 2.3 represents dE/dx and the range of α-particles in germanium. The range for 1 MeV α-particles in germanium is about 3 μm, three orders of magnitude less than that for electrons.

---

[1]The transverse E-field of the incident particle leads to the polarization of the absorber. Therefore the energy loss is reduced.
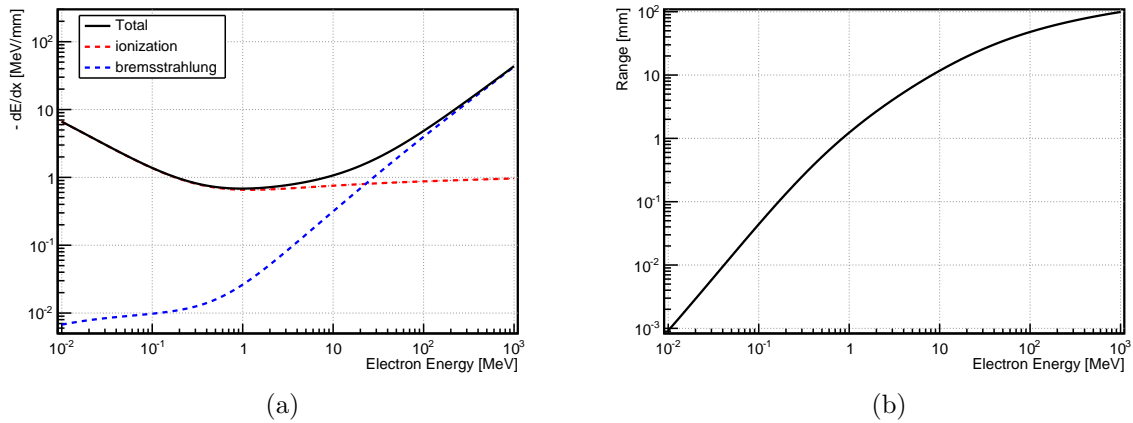
Figure 2.2: (a) Energy loss of electrons in germanium. Below the critical energy, $E_c \approx 24$ MeV, the ionization process dominates. (b) Range of electrons in germanium. The range of MeV electrons in germanium is about few mm. The figures are generated using NIST stopping power and range database for electrons [68].
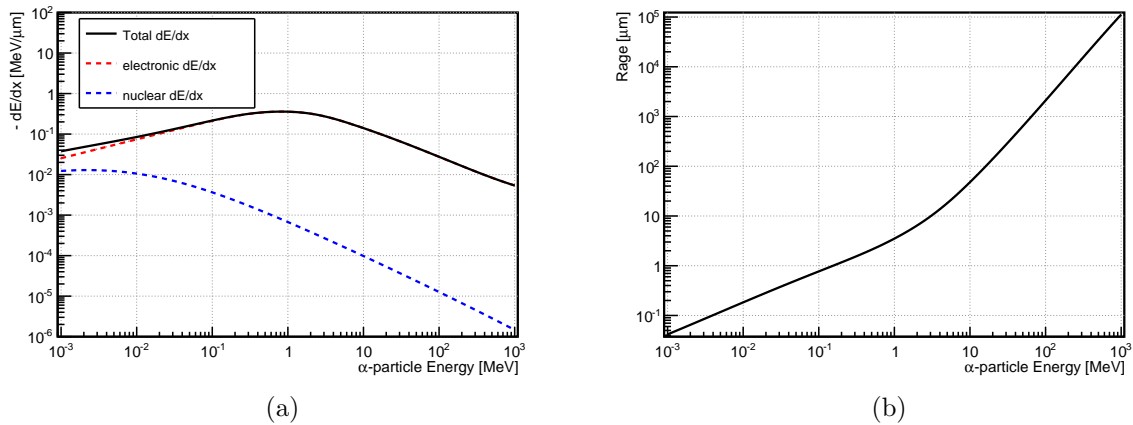

Figure 2.3: Average energy loss and range of an α-particle in germanium. (a) Energy loss of an α-particle in germanium. (b) Range of α-particle in germanium. For a few MeV α-particle in germanium, the range is around few μm. The figures are generated using NIST stopping power and range database for α-particles [68].

2.2 High Purity Germanium Detectors

2.2.1 General Properties

Semiconductor detectors are based on crystalline materials. The basic working principle is the creation of electron-hole pairs in a semiconductor crystal by incoming particles. The charge carriers created by the energy lost of the incoming particles are collected by applying an electric field across a crystal.

The properties of semiconductors can be described by the band theory of solids. In germanium, the band gap, E_g, between the conduction band and the valence band is 0.72 eV. An electron-hole pair is produced when an electron gets promoted from the valence band to the conduction band. The probability of an electron-hole pair being thermally generated is given by:

$$P(T) \propto T^{3/2} \exp\left(\frac{-E_g(T)}{2k_B T}\right),\tag{2.10}$$

where T is absolute temperature, and k_B is Boltzmann constant.

Since $P(T)$ strongly depends on temperature, cooling the material reduces the number of thermal electrons in the conduction band. For this reason, germanium detectors are operated at about 100 K. For the operation mode, the detectors usually sit in a vacuum cryostat with a direct thermal contact to a dewar filled with liquid nitrogen. However, they can be stored at room temperature.

2.2.2 Detector Types

High purity germanium detector technology was developed in the mid-1970s, made possible by the development of zone refining. The electrically active impurity concentration of germanium crystals can be reduced to an extremely low level of $\sim 10^{10}$ atoms per cm^3 [69].

Germanium detectors are fabricated from intrinsic, n-type or p-type crystals. P-type material has more impurities with three valence electrons acting as acceptors. The impurities in N-type materials are dominated by elements with five valence electrons acting as donors. Heavily doped germanium material is labelled as p$^+$ for p-type and n$^+$ for n-type. Heavy doping is used to produce the electrode contacts for detectors via ion implementation (boron) or evaporation (lithium).

A germanium detector is composed of a p-n junction, which is a structure formed by neighbouring materials with p- and n-type materials. Diffusion of donor electrons from n-type material and holes from p-type material across the junction creates a non-conducting depleted region with zero charge carrier density in the conduction and valance bands. If a reverse voltage is applied across the depleted region, electron-hole pairs created by radiation can be drifted to the electrodes. Hence, the depleted region represents the sensitive, i.e. active volume of a detector. To enlarge the active volume, a positive voltage is applied
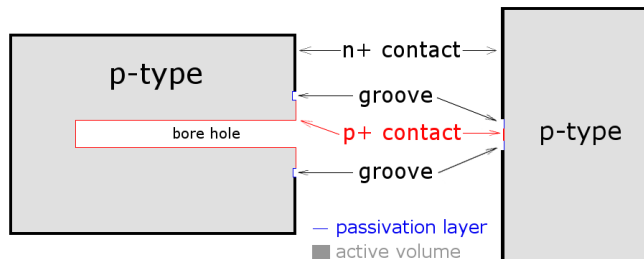
Figure 2.4: Schematic sketch of a closed-end coaxial detector (left) and a point-contact HPGe detector (right). The lithium diffused n^+ layer and the boron implanted p^+ layer are separated by a groove covered by a protective passivation layer.

to the n-type material or a negative voltage is connected to the other side. This operation is called reverse biasing. The voltage needed to deplete the entire detector volume is known as the depletion voltage. The depletion depth is proportional to the square root of the ratio of the reverse bias voltage and the dopant concentration. For high purity germanium, several kilo-volts of depletion voltage allows to deplete several centimetres of germanium. P-type germanium detectors consist of a cylinder of p-type germanium crystal. It has two electrode contacts, p^+ and n^+, on the surface. The n^+ layer on the detector surface serves as a contact and a junction created by lithium diffusion [74]. The p^+ contact is fabricated via boron implantation. Similarly, a n-type germanium detector has a p^+nn^+ structure. The p^+ layer is of the order of μm thick while the n^+ layer has typically about mm. The electrodes are conductive and hence do not contribute to the active volume. The p^+ and n^+ surfaces create *dead layers* with similar thickness. In the *transition layer* the charge collection is incomplete. [75]

Two types of p-type HPGe detectors are discussed in this work: *closed-end coaxial* and *point-contact* detectors, as depicted in Fig. 2.4. In the first type, the crystal has a bore hole for the central contact. In the second one, there is no bore hole in the center but a small point-like contact. Large detection volumes of several hundred cm^3 can be achieved with coaxial geometry. The p^+ electrode is the signal read out contact while n^+ electrode is the HV contact. The n^+ and p^+ contacts are usually separated by a protective layer with high resistivity called a passivation layer.

2.2.3 Detector Performance

Intrinsic Statistical Broadening

The average number of electron-hole pairs being produced, n_{eh}, is proportional to energy deposition of incident particles, E:

$$n_{eh} = \frac{E}{E_{eh}}, \tag{2.11}$$

where E_{eh} is the average energy needed to create electron-hole pairs and it is temperature dependent. In germanium, E_{eh} is 2.96 eV at 77 K. E_{eh} is greater than E_g because part of the energy of incoming particles is dissipated via thermal excitation of the crystal lattice. A 1 MeV photon fully absorbed in the germanium crystal creates about 3.4×10^5 electron-hole pairs. The standard deviation of n_{eh} is given by [76]:

$$\sigma_{eh} = \sqrt{F \cdot n_{eh}}, \tag{2.12}$$

where F is known as Fano factor, which is a parameter to relate the predicted Poission variance to the observed variance. The Fano factor for germanium is of the order of 0.1. [77] The *full width at half maximum* (FWHM) of germanium detectors due to statistical fluctuation of electron-hole pairs is given by:

$$\Delta E_{eh} = 2.35 \; \sigma_{eh} = 2.35 \; \sqrt{F \cdot \frac{E}{E_{eh}}}. \tag{2.13}$$

The factor 2.35 relates the standard deviation to the FWHM. In germanium, $\Delta E_{eh} \approx 1.3 \; \sqrt{E \cdot eV}$. Germanium detectors have very good energy resolution because of the low ionization energy needed to create information charge carriers and the low Fano factor. The intrinsic energy resolution of germanium detectors, $\Delta E_{eh}/E$, is about 0.1 % at 1 MeV.

Electronic Noise

The contribution of electronic noise to the energy resolution can be expressed as a function of shaping time τ by the sum of three terms:

$$\Delta E_{noise} = \sqrt{\frac{S}{\tau} + P \cdot \tau + F}, \tag{2.14}$$

where S, P, and F represent the contributions of series, parallel and flicker noise, respectively.

Series noise is the noise related to current flowing in series with the detector. It dominates at short shaping time. There are many sources contributing to series noise : capacitance of the first preamp stage, the junction field effect transistor (JFET), the capacitance of the detector and the cables, and the shot noise in the JFET [77]. Detectors with a point-contact geometry have low capacitance (at a level of ∼pF) and hence low intrinsic noise. The shot noise originates from random fluctuations of charge carriers in the JFET and depends on the JFET temperature. To minimize the shot noise, the JFET usually stays cold.

Parallel noise dominates at long shaping times. It is noise related to current flowing in parallel with the detector. Several sources contribute to parallel noise: detector leakage current and feedback resistor resistance. The feedback resistor has an intrinsic noise (Johnson noise)[2] associated with it. Johnson noise can be rejected by using a transistor reset preamp.

---

[2]Johnson noise here is generated by thermal agitation of electrons in a feedback resistor.

Flicker noise (known as $1/f$ noise) is low frequency noise whose amplitude varies with a relation of $1/f^{\kappa}$. In most cases, κ is close to 1. The physical origin of Flicker noise can be regarded as low frequency variations of material properties in the devices, including fluctuating configurations of defects in metals and fluctuating occupancies of charge trapping in semiconductors. Flicker noise is independent of shaping time.

The minimum total electronic noise can be reached at $\tau = \sqrt{S/P}$. For point contact germanium detectors, electronic noise at the hundred eV level has been demonstrated.[91]

Energy Resolution

The total energy resolution of a germanium detector can be determined by the combination of three components [66]:

$$\Delta E = \sqrt{\Delta E_{noise}^2 + \Delta E_{eh}^2 + \Delta E_{col}^2}$$
$$= \sqrt{a + b \cdot E + c \cdot E^2}, \tag{2.15}$$

where ΔE_{col} is the contribution from non-uniformity of the charge collection efficiency. The incomplete charge collection, such as charge trapping, reduces the energy resolution. The term depends on the E-field strength and on the position of γ-ray interaction inside the Ge diode. The constants, a, b and c are constants. The first term ΔE_{noise} is from the contribution of electronic noise, which is not correlated with the γ-ray energy and dominates in the low energy region. The electronic noise can be measured by injecting test pulses to the preamp. The second term ΔE_{eh} is proportional to $\sqrt{E}$, as shown in 2.13. The third term ΔE_{col} is linearly proportional to the energy. For the highly segmented HPGe detectors, this term can be improved via analysing the interaction position inside Ge crystal to correct the charge trapping effect.

2.3   Signal Formation in Germanium Detectors

The mechanism of a signal formation in germanium detectors can be described as follows : An incident particle deposits its energy in germanium, creating electron-hole pairs. The reverse bias applied on the electrodes generates an electric field in the bulk of the germanium detector due to which the charge carriers drift towards the respective electrodes. The charges being induced on the readout electrodes change due to the movement of the charge carriers. The induced charges are converted to a voltage pulse using a charge sensitive amplifier. The amplified pulse is digitized with a given sampling frequency by the data acquisition system (DAQ). The time evolution of an event (pulse) can hence be recorded.

2.3.1   Electric Field and Potential

The geometry of HPGe detectors determines the electric field $\vec{E}$ in the bulk of the detector. The E-field can be derived by solving Poisson's equation with the boundary conditions of

the HPGe detector (reverse bias on the electrodes):

$$\nabla \cdot \vec{E} = \frac{\rho}{\epsilon}, \tag{2.16}$$

where ρ is the charge density in the active volume and ϵ is the dielectric constant of germanium.

2.3.2 Charge Carrier Transport

Charge carriers are transported in germanium diodes by several ways: drift in an external E-field and spatial separation owing to thermal diffusion (inhomogeneous expanding of charge cloud in space as time evolves) and self-repulsion.

Drift

Germanium crystals have a face centered cubic (FCC) structure. The main crystallographic axes are $\langle 100 \rangle$, $\langle 010 \rangle$, $\langle 110 \rangle$, $\langle 001 \rangle$ and $\langle 111 \rangle$ by Miller indices [70]. The drift velocity of charge carriers $\vec{v}_{e/h}$ in HPGe detectors is not necessarily parallel to the E-field lines due to the crystal axes in germanium. This phenomenon is due to the *mobility anisotropy*. The relation between the drift velocity of charge carriers, the mobility tensor $\overleftrightarrow{\mu}_{e/h}$ for electrons and holes, and the electric field can be expressed as [69]:

$$\vec{v}_{e/h} = \overleftrightarrow{\mu}_{e/h} \, \vec{E}. \tag{2.17}$$

The longitudinal components of drift velocities along different crystal axes given the same field strength are different. This is called *longitudinal anisotropy*. Similarly, the *traverse anisotropy* refers to the differences between traverse components of drift velocities along different crystal axes.

The drift velocity of charge carriers is parallel to the E-field along the crystal axes because of the symmetry of the crystal lattice. The dependence of $v_{e/h}$ along the $\langle 100 \rangle$- and $\langle 111 \rangle$-axis on the E-field strength can be described using the empirical formula [69, 82, 83]:

$$v_{e/h} = \frac{\mu_0 E}{[1 + (\frac{E}{E_0})^\beta]^{\frac{1}{\beta}}} - \mu_n E, \tag{2.18}$$

where E_0, β are fitting parameters; μ_0, μ_n are low field mobility and high field mobility, respectively.

The parameter μ_0 characterizes the mobility at low E-field. E_0 is associated with the saturation drift velocity $v_{e/h} = \mu_0 E_0$. The term $\mu_n E$ is considered for the field strength above 300 V/mm owing to the Gunn effect [84]. Drift velocities along other directions can then be calculated [85]. Fig. 2.5 demonstrates the longitudinal anisotropy for electrons and holes. A faster carrier drift velocity means a shorter charge collection time in the
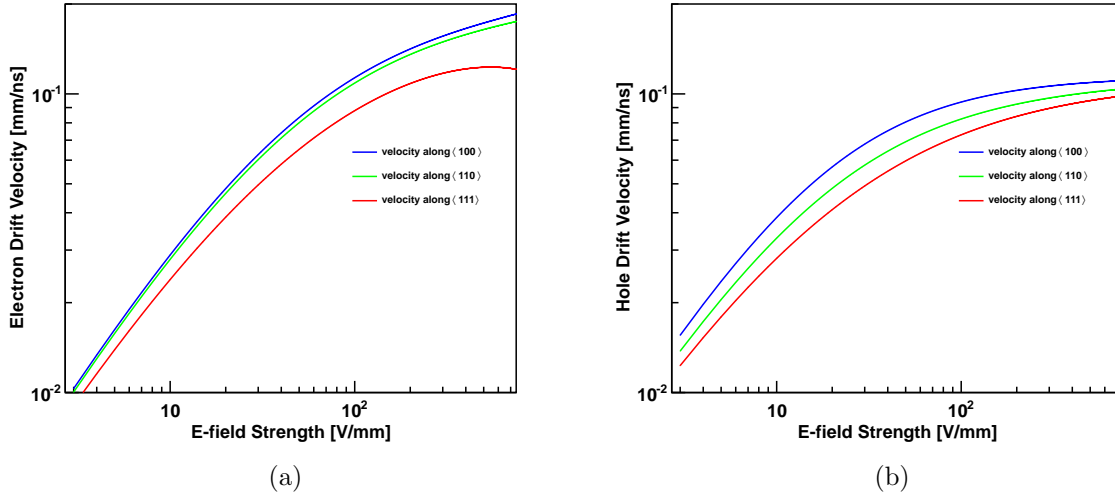
Figure 2.5: Drift velocity along different crystal axes as a function of electric field strength for (a) electrons and (b) holes at 78 K. Fitting parameters along $\langle 100 \rangle$- and $\langle 111 \rangle$-axes were extracted from [82]. Drift velocities along $\langle 110 \rangle$-axes are estimated accordingly.

germanium detector. Therefore, a shorter rise time for the waveform. The characteristics of crystal axes manifests itself along circular faces, as depicted in Fig. 2.6. For the $\langle 100 \rangle$- and $\langle 010 \rangle$-plane, the pattern will repeat every 180°. Features of the $\langle 110 \rangle$-plane would appear every 90°. Each axis has a similar effect on the mobility tensor. So a distinct pattern will repeat every 45°. The $\langle 001 \rangle$-axis is normally aligned with the z axis of a cylindrical germanium detector after the Czochralski pulling procedure. However, the orientation of the $\langle 110 \rangle$-axis is usually unknown after the detector has been processed. This requires a characterization procedure to find the corresponding crystal axes. The details to find crystal axes will be discussed in Section 7.5.

Thermal Diffusion

The point-like charge carrier being produced initially in the detector volume will diffuse as time goes by. The charge carrier density $\rho(\vec{r}, t)$ diffuses according to the diffusion equation:

$$\frac{\partial \rho(\vec{r}, t)}{\partial t} = D_{e/h} \frac{\partial^2 \rho(\vec{r}, t)}{\partial^2 \vec{r}^2}, \tag{2.19}$$

with $D_{e/h}$ being the transverse diffusion coefficient. The Einstein relation relates the transverse diffusion coefficient to the charge carrier carrier mobility [86]:

$$D_{e/h} = \frac{\mu_{e/h} k_B T}{e}, \tag{2.20}$$

where k_B is the Boltzmann constant, T is the absolute temperature, and e is the electric charge.
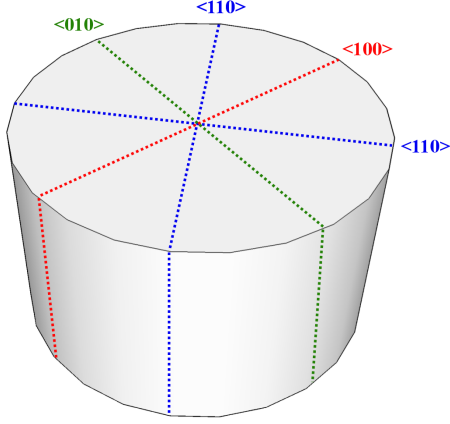
Figure 2.6: Schematic sketch of a germanium crystal labelled with crystal axis planes : $\langle 100\rangle$-, $\langle 010\rangle$-, and $\langle 110\rangle$-plane. The pattern of the $\langle 110\rangle$-plane will appear every $90°$. Features of the $\langle 100\rangle$- and $\langle 010\rangle$-plane repeat every $180°$. Every axis has a similar effect on the mobility tensor. Therefore, the distinct pattern will repeat every $45°$.

The transverse diffusion coefficient constants at 77 K for low transverse component of the E-field are 230 cm^{2}s^{-1} and 210 cm^{2}s^{-1} for holes and electrons, respectively [87]. The width of a Gaussian charge cloud can be described by the formula [69, 88]:

$$\sigma_{e/h}(t) = \sqrt{2D_{e/h}t} = \sqrt{2\frac{\mu_{e/h}k_BT}{e}t}. \tag{2.21}$$

The diffusion process is more pronounced for the charge carriers transport in the low E-field transition layer of p-type HPGe detectors. It is especially important for the energy deposition on the n$^+$ contact, which results in longer rise times of the waveforms. [75, 89]

2.3.3 Signal Formation on the Electrode

The induced charge Q and current I at time t on the readout electrode due to the drift of charge carriers can be approximately described using the Shockley-Ramo Theorem [95, 96, 97]:

$$Q(t) = -q \times [\phi_w(\vec{r}_h(t)) - \phi_w(\vec{r}_e(t))], \tag{2.22}$$

$$I(t) = q \times [\vec{E}_w(\vec{r}_h(t)) \cdot \vec{v}_h(t) - \vec{E}_w(\vec{r}_e(t)) \cdot \vec{v}_e(t)]. \tag{2.23}$$

where:
q: Net electric charge.
$\vec{r}_{e/h}(t)$, $\vec{v}_{e/h}(t)$: Position and velocity of electrons/holes as a function of time, respectively.
$\phi_w(\vec{r}_{e/h}(t))$: Weighting potential at the position $\vec{r}_{e/h}(t)$.
$\vec{E}_w(\vec{r}_{e/h}(t)) = -\nabla\phi_w(\vec{r}_{e/h}(t))$: Weighting field at the position $\vec{r}_{e/h}(t)$.

The theorem is exact if the detector system is electrostatic (i.e. $\partial\vec{E}/\partial t = $ constant) and the dielectric constant does not change with time. The weighting potential can be

calculated by solving Laplace's equation with the boundary conditions :

$$
\begin{cases}
\nabla^2 \phi_w = 0, \\
\phi_w = 1 \text{ for the electrode of interest ; } \phi_w = 0 \text{ for all the other electrodes.}
\end{cases}
\tag{2.24}
$$

The weighting potential for a given readout electrode quantifies the magnitude of the induced mirror charge for a unit charge at given position inside the detector. It depends **only** on the geometry of the detector, but not on the physical voltage applied on the detector. It's range is between 0 and 1. Once the detector geometry is given and the readout electrode is assigned, the induced charge on the electrode as a function of time is known, namely, $Q = \sum_j Q(t_j) = -q \times \sum_j [\phi_w(\vec{r}_h(t_j)) - \phi_w(\vec{r}_e(t_j))]$. The drift path of the charge carriers is determined by the actual E-field lines. After mapping out the trajectory of a carrier as a function of time, the time evolution of induced charge on the electrode of interest can hence be calculated.

Mirror Pulses

In a segmented detector, the charge carriers not only induce charges in the electrodes they drift to, but also in the neighbouring electrodes (or called segments). The pulses induced in the neighbouring electrodes are called *mirror pulses* and the corresponding pulse shapes would return to the baseline.

2.4   Electronics

2.4.1   Response Function

A recorded output signal $S(t)$ in the time domain can be formulated as a convolution of an input signal $I(t)$ and an electronic response function $R(t)$:

$$
S(t) = I(t) * R(t) = \int_{-\infty}^{\infty} R(\tau) \cdot I(t - \tau) d\tau.
\tag{2.25}
$$

The response function can be experimentally measured by injecting a square pulse, $u(t)$, from a pulse generator to the electronics system [99]:

$$
\frac{\partial S(t)}{\partial t} = \frac{\partial}{\partial t}[u(t) * R(t)] = [\frac{\partial u(t)}{\partial t} * R(t)] = \delta(t) * R(t) = R(t),
\tag{2.26}
$$

where $\delta(t)$ is the Dirac delta function.

The time derivative of the recorded output signal is the response function of the electronics system.

2.4.2   Cross-talk

The cross-talk is a signal alternation due to capacitive coupling between detector readout electrodes. It occurs for any segmented detectors. There are two types of cross-talk: the proportional cross-talk and the differential cross-talk. The proportional cross-talk is proportional to the signal amplitude, whereas the differential cross-talk is proportional to the derivative of the signal. The proportional cross-talk is notorious to the energy resolution. The derivative cross-talk takes place only during the rise time for the charge pulses. Moreover, cross-talk can occur in detector pre-amplifier interface. More sophisticated analysis on this type of internal cross-talk can be found in [98].

2.5   Broad Energy Germanium Detector
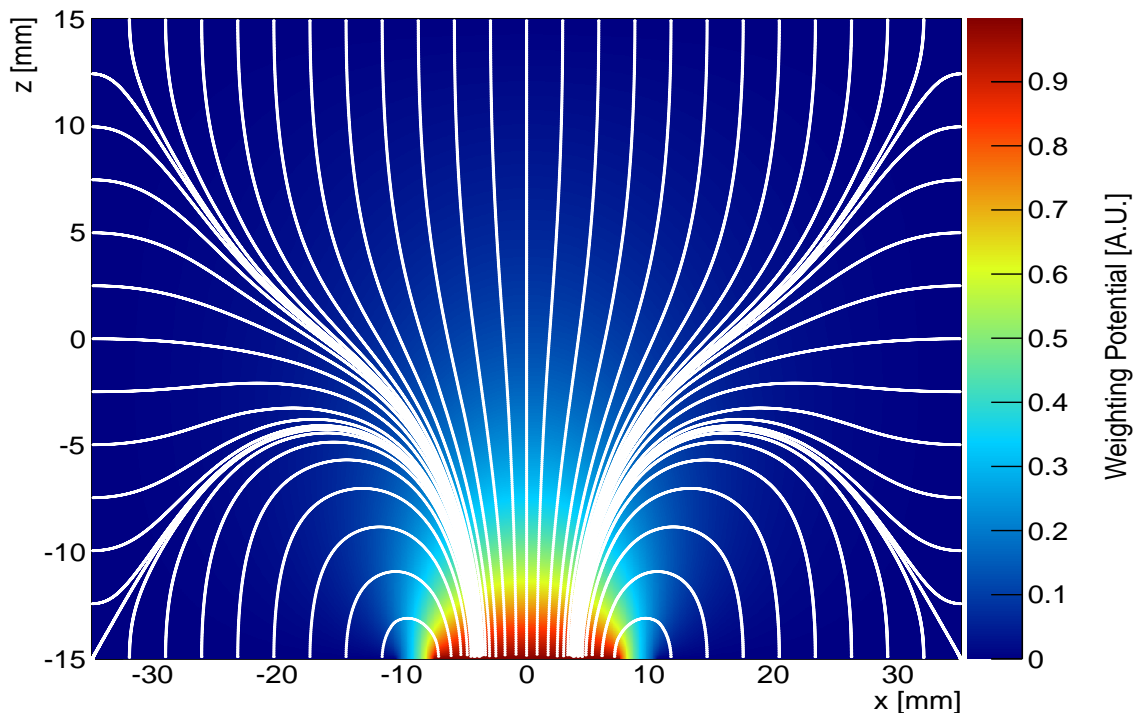
Figure 2.7: Weighting potential and drift paths of charge carriers (indicated in white) for a p-type BEGe detector. A sharp weighting potential close to the p^+ contact can be seen. The field calculation was generated using the software package MAGE [105].

The point-contact geometry of HPGe detectors was first proposed in 1980s, showing that the electronic noise can be significantly reduced by decreasing the size of the central contact to a point contact [90]. In 2007, a p-type HPGe detector of $\mathcal{O}(1\text{kg})$ modular mass plus several hundred eV threshold was proposed [91]. A commercial version of point-contact

HPGe detector produced by CANBERRA is called *Broad Energy Germanium detector* (BEGe) [92]. It covers a wide energy range from 3 keV to few MeV. BEGe detectors are position-sensitive to event location and thus allow to have efficient discrimination between signal-like events and background-like events by pulse shape analysis. Its promising background rejection power has been successfully demonstrated by the GERDA collaboration for the first prototype study [93]. Using this detector type for the second phase of the GERDA experiment may allow to reach the goal of reducing the background index to 10^{-3}cts/(keV·kg·yr) in the energy region of interest.

2.5.1 A/E Pulse Shape Discrimination Method

The specific electrode geometry of a p-type BEGe detector results in a well pronounced weighting field close to the p^+ contact, as shown in Fig. 2.7. Drift paths for charge carriers are also shown. The shown weighting field and charge carrier trajectories were generated using pulse shape generation software [105] based on MAGE - a Geant4-based Monte Carlo software developed by the GERDA and MAJORANA experiments. The internal electric field distribution ensures that holes are always collected along similar paths in the last part of the drift. Thanks to this so called *funnelling effect* and the strongly localized weighting field the induced charge signal always has an uniform shape at the end independent of where the individual energy depositions happen [3]. Hence, the amplitude of the current signal for a single energy deposition is position-independent and depends only on the total charge of the whole cluster [106, 101].

Four typical event topologies in the detector volume shown in Fig. 2.8(a) are : single-site events (SSE), multi-site events (MSE), p^+ surface events, and n^+ surface events. $0\nu\beta\beta$ events are mostly single-site events confined to a scale of about one millimeter [4]. A significant fraction of expected background events in the region of interest (ROI) comes from γ-rays. A 2 MeV photon has a mean free path in germanium of a few centimeters. As the most likely interaction of a photon with this energy is Compton scattering, the photon is likely to deposit its energy at different locations inside the detector. Such events are MSEs.

There is a transition layer in between the n^+ surface and the active volume. The mechanism how charge carriers reach the active volume from the transition layer is diffusion [75]. For an event created on the n^+ surface (n^+ surface event), the holes would take longer time to reach the readout electrode as the characteristic diffusion times are larger than the drift times.

An event being produced near the p^+ contact (in a small volume about 3-6%) is called p^+ surface event. In the very beginning, before any drift happened, the electron and hole pairs are homogeneously distributed so the net charge induced on the p^+ electrode is zero. Subsequently, holes and electrons are separated due to the drift in the E-field. While holes

---

[3]This is the case for most of the detector volume ($\sim$94% - 97%). If an event occurred near p^+ contact, the profile of charge signal in the last part of drift would be different.

[4]A small fraction of events will have bremsstrahlung photons. An event topology like this would not be a SSE.

drift toward the p^+ contact, electrons drift away from it. Therefore, the displacement current is large while both charge carrier types are in the high weighting field region. This leads to a fast rise time.

Pulse shapes of the four typical event topologies are displayed in Fig. 2.8(b). The charge pulses are normalized to one. The integral of current signal is the same for all types of events. MSEs have a bigger width of their charge pulse and therefore have a smaller maximum amplitude of current signal compared to SSEs. For p^+ surface events, it has a sharp rise in the beginning and the maximum current amplitude is higher. For n^+ surface events, due to the surface effect, it has a slower charge signal and the maximum amplitude of the current pulse is smaller. A pulse shape discrimination (PSD) method was devised to efficiently differentiate signal-like events from background-like events, exploiting the ratio of the maximum amplitude of the current signal (A) over the energy from the amplitude of the charge signal (E) - the A/E parameter. For a given energy, MSE and n^+ surface events have lower A/E values, while p^+ surface events have larger A/E values, in comparison to signal-like SSEs.

The thickness of the dead layers/transition layers is different for p^+ and n^+ contacts. The n^+ layer is typically $\sim$ mm thick whereas the p^+ layer thickness is of the order of μm. α-particles with energies in between 4 MeV to 9 MeV are relevant to the GERDA experiment. The range of 4 - 9 MeV α-particles is 14 - 41 μm in Ge and 34 - 113 μm in LAr [68]. α-emitting isotopes in liquid argon can contribute to the background **only** if its decay takes place within a few μm from the detector surface. Specifically, only decays in the vicinity of the p^+ electrode or groove surface can deposit energy to the detector active volume. α-particles depositing $\sim$MeV in the detector active volume can only result from decay of α-emitting isotopes close to the p^+ contact. They hence have higher A/E values.

MeV β-particles in germanium have an attenuation length of the order of millimeters. They can reach the detector active volume if the decay happens close to both the p^+ and the n^+ contact. Energy deposition of surface MeV β-particles is well localized within a few millimeters. If MeV β-particles deposit their energy on the n^+ surface, they have lower A/E values. These background candidates can be identified efficiently using a single A/E parameter. The data analysis on A/E PSD method will be discussed in Chapter 4.

2.5.2 PSD Calibration Method

γ Calibration Scheme

^{228}Th calibration spectra are used to determine the A/E cut values for the distinction of event topologies and for the determination of SSE/MSE recognition efficiencies. It is essential to build SSE- and MSE-abundant samples to study, improve, and monitor the PSD performance.

The events in the double-escape peak (DEP, at 1592.5 keV) of the 2614.5 keV photons from ^{208}Tl decay are proxies for SSEs. DEP events are created when the photons interact in the BEGe detector via pair-production and the two 511 keV photons from the positron
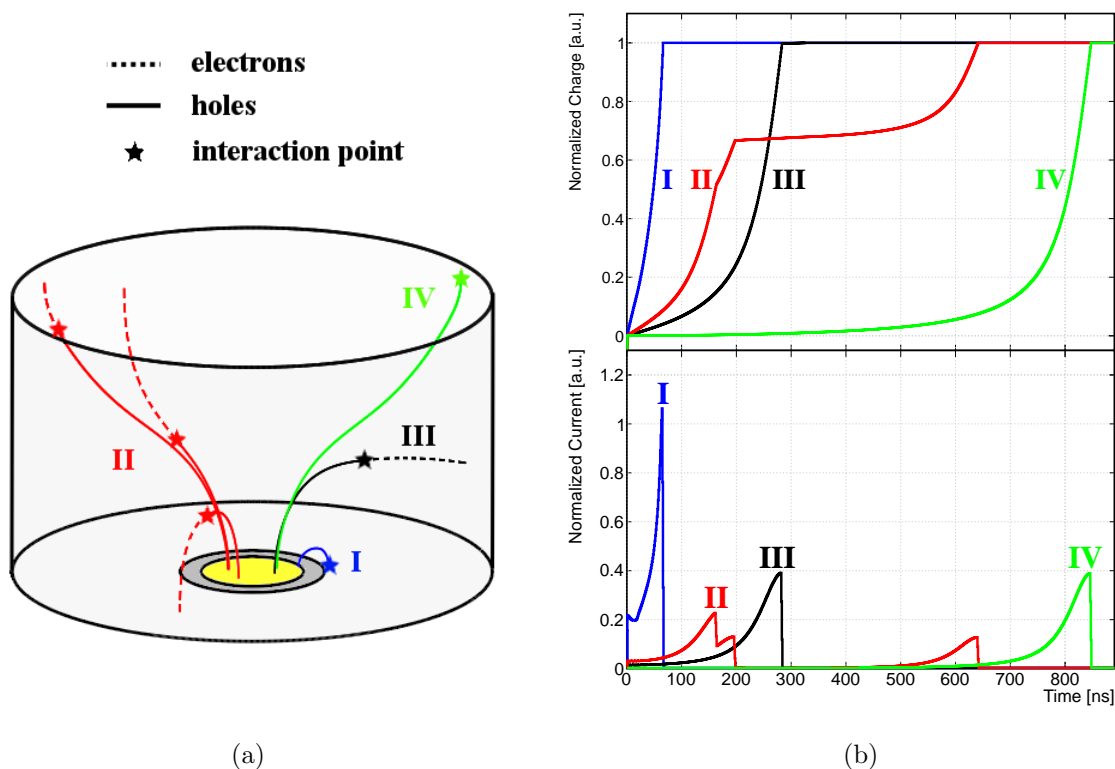
Figure 2.8: Classification of the event topologies in a BEGe detector. Type I shows a p+ surface event. Type II displays a MSE event. Type III represents a SSE event. Type IV event illustrates a n+ surface event without diffusion effect. (a) Drift path for each type of event. Hole drift paths are represented in solid lines, while electron drift paths are shown with dashed lines. The star symbols denote the interaction positions in the detector volume. (b) The corresponding charge wave forms on the top figure and current pulses on the bottom figure. $0\nu\beta\beta$-like events can be disentangled by using the A/E PSD method.

annihilation escape the detector. The electrons and positrons mostly have well-localized energy depositions and result in SSEs. However, DEP events are not perfect samples for $0\nu\beta\beta$ events. The energy of DEP events is 1592.5 keV while the energy for $0\nu\beta\beta$ events is expected to be 2039 keV in Ge. The distribution of DEP events is not homogeneous in the detector volume as it is for the expected $0\nu\beta\beta$ signal. Because two 511 keV photons escape the detector, the interaction point has higher probability to be located close to the detector surfaces. These systematic uncertainties have to be taken into account [109].

For events in the single-escape peak (SEP, at 2103.5 keV) only one 511 keV photon escapes and the other photon mainly interacts through multiple Compton scatterings in the detector. Hence SEP events provide MSE-dominant samples. Similarly, the events in the full energy peak (FEP, 1620.7 keV from ^{212}Bi decay) are mostly due to Compton scattered photons. They also represent MSE-dominant samples. As a benchmark, to evaluate the

performance of the GERDA phase II BEGe detectors, the A/E cut value is artificially set to cut 90% of DEP events after background subtraction on the left and right side of the DEP peak. The survival fractions in the SEP and FEP are treated as indicators of PSD capabilities. To have quality controls on PSD performances, the calibration on the phase II BEGe detectors are performed every one or two weeks.

β Calibration Scheme for the Surface Events

Calibration schemes of A/E method on the n^+ and p^+ surface events for the BEGe detector have been studied in previous measurements. The β-emitting sources (^{90}Sr and ^{106}Ru) were used to scan the n^+ surfaces of different BEGe detectors with different dead layer thickness in vacuum cryostats [111]. The A/E cut values are all calibrated to accept 90% of the DEP events from ^{228}Th measurements prior to the ^{90}Sr and ^{106}Ru measurements. The survival fractions of the n^+ surface events from 1 MeV to 1.6 MeV after A/E cut were demonstrated to be $\lesssim 1\%$ for all ^{90}Sr measurements . The survival probability after PSD cut at $Q_{\beta\beta}$ in the ^{106}Ru measurement is estimated to be $< 1.6\%$ at 95% C.I..

To study the A/E response for the ^{42}K (daughter product of ^{42}Ar) surface events in a similar setup like GERDA, measurements were performed in LArGe [115]. LArGe is a GERDA low-background test facility in LNGS to study novel background suppression methods, for future application in the GERDA experiment. The measurements were taken using a bare BEGe detector immersed directly in liquid argon. The estimated ^{42}Ar activity in LArGe liquid argon is (65.6 ± 14.0) μBq/kg [112]. To enhance the ^{42}Ar concentration, newly produced ^{42}Ar with activity of (5.18 ± 0.91) Bq, relevant to PSA, was added into the LArGe cryostat [113, 114]. 98.7% of the surface events (on both n^+ and p^+ side) around $Q_{\beta\beta}$ (1989 - 2089 keV) are rejected using an A/E cut on both low and high side of the A/E parameter where the cut value is determined by accepting 88% of the DEP events calculated from the ^{228}Th measurement. Background components such as ^{228}Th, ^{68}Ga, and ^{214}Bi that contribute to the SSE band leads to underestimation of the suppression factor. By considering these background components, the suppression factor on surface events using the A/E PSD method is enhanced to be in the range of 98.6% - 99.8%.

α Calibration Scheme on the p^+ Surface Events

To calibrate the A/E response on the p^+ electrode and groove surface events, measurements using a collimated ^{241}Am α source scanning along a diameter of the BEGe detector in steps of 1.5 mm from one side of the groove to the other side had been made in a shallow underground lab in Technische Universität München [107]. The surface α events are positioned above the SSE band of A/E distribution and their energies are between 2.6 MeV and 4.3 MeV. Although placing the A/E cut value to a higher side was sufficient to reject surface α events, the low side A/E cut was applied as well to reduce the contribution from muon-induced background. The survival fraction of p^+ surface α events after A/E cut was shown to be $\lesssim 1\%$ at 95% C.I. with calibrated 89% acceptance of the DEP events from the ^{228}Th measurement.

Chapter 3

The GERDA Experiment

The GERmanium Detector Array (GERDA) experiment is built to search for neutrinoless double beta-decay in ^{76}Ge. Data taking of the GERDA experiment is divided into two phases. For the first Phase (Phase I), detectors enriched in ^{76}Ge inherited from HdM and IGEX experiments were used. The goal for GERDA Phase I was to reach a background index of 10^{-2} cts/(keV·kg·yr) with an exposure of 20 kg·yr, sufficient to improve limits for the half-life of $0\nu\beta\beta$-decay in ^{76}Ge and capable to test the positive claim of a $0\nu\beta\beta$ signal from the results of the HdM experiment [42]. The design of Phase I, data taking parameters, detector performances, the blinding procedure, background decomposition, pulse shape discrimination efficiency, and the final result regarding neutrinoless double beta decay are discussed in the main part of this chapter. For Phase II, the physics goal is to further improve the sensitivity to half life by a factor of 5. This is achieved by increasing the detector mass by 20 kg using BEGe detectors and by improving the background recognition efficiency with help of LAr instrumentation. Liquid argon instrumentations can reduce background index to 10^{-3} cts/(keV·kg·yr). The efforts toward the second phase (Phase II) are discussed in the rest part of this chapter.

3.1   Design and Facility

The GERDA collaboration comprises about 100 research scientists from major institutions/universities in Germany, Italy, Poland, Switzerland, Belgium, and Russia. Details about the technical infrastructure can be found elsewhere in [110]. The GERDA (GERmanium Detector Array) experiment was proposed in 2004 [47] and its construction was completed in 2010. The collaboration initiated commissioning started in July 2010.

The underground location and ultra-low-background materials used allow the GERDA experiment to reduce various background sources with respect to previous experiments. As depicted in Fig. 3.1(a), the experiment is located in Hall A of the Laboratori Nazionale del Gran Sasso (LNGS), Italy. 1.4 km of rock overburden (3500 m.w.e.) reduce the cosmic muon flux by a factor of $\sim 10^6$ compared to the surface.

The core of the setup is an array of HPGe detectors enriched to 86-88 % in ^{76}Ge isotope.
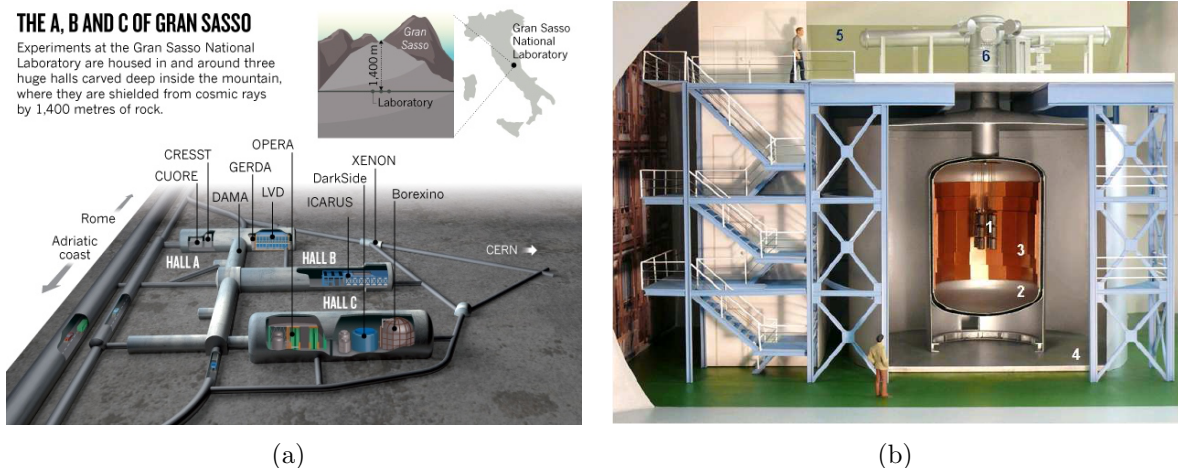
Figure 3.1: (a) The GERDA experiment is located in Hall A of the LNGS, Italy. The overburden of the laboratory is about 3800 m.w.e. The sketch is taken from [48]. (b) Schematic view of the GERDA experiment (not to scale). The HPGe array (1) is submerged in to the LAr cryostat (2). The LAr cryostat with linings made of electroformed copper (3) is placed in a water tank (4) equipped with PMTs to detect Čhrenkov light emitted by the muons passing through the tank. The supporting structure around the water tank holds the extended infrastructure of the experiment. On the top of the system is the clean room (5) and the lock system (6) through which detectors are deployed to the LAr. The figure is taken from [49]

High purity germanium diodes with excellent energy resolution ($\sim$0.2 % in the region of interest) are used as source and detector at the same time, which results in a very good detection efficiency. Holders made from a minimum amount of screened ultra-pure materials are used to support the detectors.

The main design concept of the GERDA experiment is to immerse HPGe detectors directly into a cryogenic liquid, which serves as a cooling medium as well as a shield against external radiations [50]. Cryogenic liquids, such as liquid argon (LAr), due to their production process, can be produced in an extremely clean way [52]. Moreover, LAr scintillation light with 128 nm wavelength can be used as an anti-Compton veto to further suppress background events [53, 54].

A schematic view of the GERDA experiment is shown in Fig. 3.1(b). Bare HPGe detectors mounted on strings are suspended in the LAr cryostat. The cryostat is about 4 m in diameter and 6 m in height. The cryostat material is carefully selected low-background stainless steel [51] with additional electroformed copper linings. The radio-pure copper lining shields the γ-radiations from the steel vessel. The LAr cryostat is embedded into a tank filled with ultra-pure water. The water tank has dimensions of about 10 m in diameter and 9 m in height. The water tank with 630 m^3 ultra-pure water shields against neutrons coming mostly from natural radioactivity from the rocks in the environment and against external γ-backgrounds. It is instrumented with 66 photomultiplier tubes (PMTs) which

detect Čhrenkov light emitted by the muons passing through the tank. To increase the light collection efficiency, the inner surface of the water tank is covered with a commercial high reflecting wave-length shifting foil. A support structure around the water tank houses the extended infrastructure of the experiment. On the top, there is a clean room. The HPGe detectors are mounted and deployed into to the LAr cryostat through a lock system located in the clean room. To complete the coverage of the cosmic muon veto, an array of plastic scintillators with dimensions of $(220 \times 50 \times 3)\,\mathrm{cm}^3$ equipped with PMTs are installed on the top of the clean room. The GERDA muon-veto system has a high muon rejection efficiency of better than $99\,\%$ estimated from comparison of Monte Carlo simulation and measurements [55, 56].

3.2 Phase I Detectors and Data Taking

3.2.1 Phase I Detectors

The Phase I detector array includes 3 coaxial detector strings and 1 string used for employing different detectors in different periods. The array setup for Phase I is listed in Table 3.2. In Phase I, two types of p-type HPGe detectors enriched in ^{76}Ge, closed-end coaxial HPGe detector (^{enr}Ge-coax) and BEGe detector were used for $0\nu\beta\beta$ search. Additionally, closed-end coaxial HPGe detectors with natural isotopic abundance (^{nat}Ge-coax) were used as reference detectors. Details of the detector types have been described in Section 2.2.2. Five ^{enr}Ge-coax detectors (ANG1-5) were inherited from the HDM experiment [40] and three ^{enr}Ge-coax detectors (RG1-3) were taken from the IGEX experiment [41]. Before deployment to the GERDA LAr cryostat, these detectors had been reprocessed [44, 45] at CANBERRA Semiconductor NV, Olen. Three ^{nat}Ge-coax low background detectors (GTF32, GTF45, and GTF112) were taken from the *Genius Test Facility* experiment (GENIUS-TF) [43]. Five newly made BEGe detectors (GD32B, GD32C, GD32D, GD35B, and GD35C) [92], designed for Phase II, were added later to the cryostat. Point-contact type HPGe detectors were used in this field of research for the first time.

The main parameters for all detectors, such as enrichment fraction f_{76}, total mass M, active mass M_{act}, active volume fraction f_{AV}, and the thickness of the n$^+$ dead layer d_{dl}, are listed in Table 3.1. During data taking the detectors ANG1 and RG3 had developed high leakage currents and hence were not taken into account to the data analysis. The detector RG2 was switched off due to the increase of leakage current after ~ 1 year of data taking. Five BEGe detectors were inserted to the cryostat in July, 2012. They replaced the two low background ^{nat}Ge-coax detectors, GTF32 and GTF45. During Phase I data taking, one of the BEGe detectors, GD35C, was unstable and therefore was not used for the Phase I analysis.

Table 3.1: Main parameters of the HPGe detectors used in GERDA commissioning and Phase I: enrichment fraction of ^{76}Ge (f_{76}), total mass (M), active mass (M_{act}), active volume fraction (f_{AV}) and effective thickness of the n$^+$ dead layer (d_{dl}). The numbers quoted in parentheses represent the 1σ uncertainties. The symbol [†] denotes detectors that are not taken into account in the Phase I analysis. Table adapted from [46].

Detector	f_{76} (δf_{76})	M [g]	M_{act} (δM_{act}) [g]	f_{AV} (δf_{AV})	$\delta f_{AV,u}$	$\delta f_{AV,c}$	d_{dl} [mm]
Enriched closed-end coaxial detectors							
ANG1[†]	0.859 (29)	958	795 (50)	0.830 (52)	0.045	0.027	1.8 (5)
ANG2	0.866 (25)	2833	2468 (145)	0.871 (51)	0.043	0.028	2.3 (7)
ANG3	0.883 (26)	2391	2070 (136)	0.866 (57)	0.049	0.028	1.9 (7)
ANG4	0.863 (13)	2372	2136 (135)	0.901 (57)	0.049	0.029	1.4 (7)
ANG5	0.856 (13)	2746	2281 (132)	0.831 (48)	0.040	0.027	2.6 (6)
RG1	0.855 (15)	2110	1908 (125)	0.904 (59)	0.052	0.029	1.5 (7)
RG2	0.855 (15)	2166	1800 (115)	0.831 (53)	0.046	0.027	2.3 (7)
RG3[†]	0.855 (15)	2087	1868 (113)	0.895 (54)	0.046	0.029	1.4 (7)
Enriched BEGe detectors							
GD32B	0.877 (13)	717	638 (19)	0.890 (27)			1.0 (2)
GD32C	0.877 (13)	743	677 (22)	0.911 (30)			0.8 (3)
GD32D	0.877 (13)	723	667 (19)	0.923 (26)			0.7 (2)
GD35B	0.877 (13)	812	742 (24)	0.914 (29)			0.8 (3)
GD35C[†]	0.877 (13)	635	575 (20)	0.906 (32)			0.8 (3)
Natural closed-end coaxial detectors							
GTF32[†]	0.078 (1)	2321	2251 (116)	0.97 (5)			0.4 (8)
GTF45[†]	0.078 (1)	2312					
GTF112	0.078 (1)	2965					
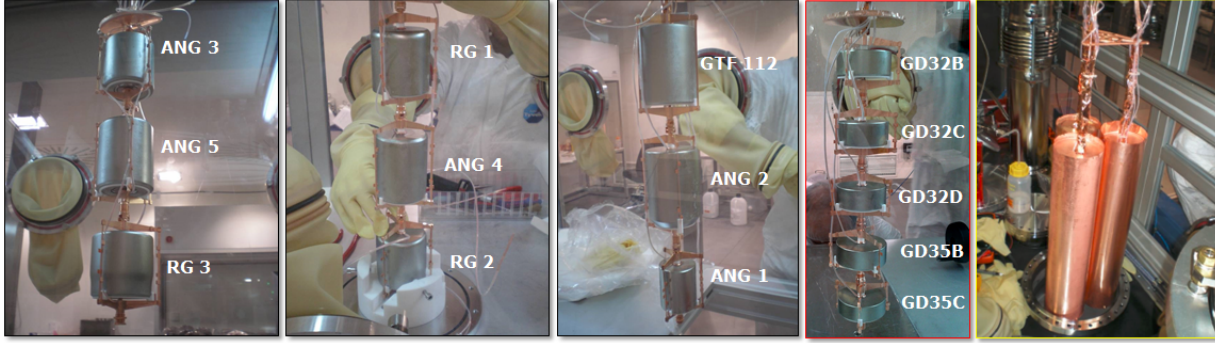
Figure 3.2: GERDA Phase I detectors mounted in the strings. Figure from left to right represents different detectors mounted in different strings. The closed-end coaxial HPGe detectors were mounted in the first three strings; all the BEGe detectors were mounted in a single string. The right most figure shows that each string was enclosed by a radiopure copper mini-shroud to mitigate ^{42}K background (see Section 3.3).

String	Detectors (top-bottom)	Data taking period	Run number	High voltage [V] (top-bottom)
1 $^{\times A}$	GTF45, GTF32	09/11/2011-21/05/2013	25-32	-3000 for all
1 $^{\cup D}$	GD32B, GD32C, GD32D, GD35B, GD35C[†]	08/07/2015 -21/05/2013	35-46	3500 for all except GD35C
2 $^{\cup D}$	GTF112, ANG2, ANG1[†]	09/11/2011		3000, 3500, 0
3 $^{\cup D}$	RG1, ANG4, RG2	-	25-46	4500, 3500, 4000
4 $^{\cup D}$	ANG3, ANG5, RG3[†]	21/05/2013		3500, 2500, 0

Table 3.2: Summary of setup of strings. The entire data taking period of Phase I is from 09/11/2011 to 21/05/2013 (Run number 25 to 46). The high voltages of ANG1 and RG3 were gradually decreased and eventually were switched off due to the high leakage currents. The high voltage of GD35C was switched off because of the instability. The notations $\bigcup$ and $\times$ represent with and without copper mini-shrouds, respectively. The superscripts, D and A, stand for DC and AC coupled readout mode, correspondingly. The symbol [†] denotes the detector that is not taken into account in the Phase I analysis.

3.2.2 Off-line Signal Processing and Data Quality Cuts

The off-line digital signal processing for the FADC traces were performed within the software framework GELATIO (GErda LAyouT for Input/Output) [118, 119]. This C++/ROOT based framework was tailor-made for the GERDA data management and analysis. The basic idea underlying GELATIO is its modular design, with each module being in charge of it's own task. The built-in library contains abundant modules commonly used for the data analysis, such as pile up rejection, pole zero cancellation, waveform decay

correction, trapezoidal filter for energy reconstruction, pulse shaping filters for de-noising, etc. The input traces are processed along a chain of modules and the characteristic information of waveforms are obtained. This includes rise time, maximum amplitude, pulse peaking time, trigger timing, root-mean-square (RMS) of baseline, etc. After processing the raw data by GELATIO, the information from raw traces is extracted and the data size is immensely reduced.

A series of quality cuts is applied on raw data to remove non-physical and pileup events:

- **Non-physical events**
  This type of events can originate from e.g., discharges, pick-up noise events, and potential fluctuations. They usually have anomalous pulse shapes. Their characteristics can be easily tagged and hence rejected by PSD cuts using parameters like the position of the leading edge, maximum amplitude after Gaussian filter [1], the 10%-90% rise time (for pulses inconsistent with the detector charge collection time) and the charge pulse height (for traces that exceed the dynamic range of FADC).

- **Pile-up events**
  This type of waveform is generated by the superposition of multiple physical pulses. They can be vetoed using pulse shape parameters such as baseline slope, the position of the main leading edge, and the number of off-line triggers within the pulse. In the Phase I calibration run with a rate of about 100 events/sec above 500 keV, the fraction of pile-up events can rise up to 15 %. However, in the Phase I physics run with extremely low event rate of about 10^{-2} events/s above ~30 keV, the pile-up event rate is negligible.

The efficiency of the data quality cuts is better than 99.9 % for energies above 1 MeV.
To monitor the data taking performance and to have better control on the data quality, the key parameters concerning event rates, noise levels, gain stability of electronics, etc., were checked daily [120, 121]. The event rates of HPGe detectors (~2 mHz above threshold [2] per detector) and cosmic muon events (~0.5 counts/day per detector) are expected to be approximately constants over time with stable data taking conditions. A considerable deviation on the averaged event rate indicates problems in the performance of the data taking system.

To monitor the stability of the electronics, pulses with fixed amplitude (test pulses) were regularly injected to all pre-amplifiers. The rate of test pulses was 0.1 Hz in the first period and 0.05 Hz in the last period of Phase I. Several relevant parameters were monitored over time to check the stabilities of electronics and DAQ system : the pedestal and the RMS of the baseline, and the amplitude and width of the test pulse. Drifts or fluctuations in the baseline position reveal changes in the detector leakage currents or in the gain of the electronic chain. The standard deviation of the baseline with respect to the baseline pedestal denotes the noise level of the electronic chain. Instabilities or rapid

---

[1] A shaping filter results in a Gaussian-like pulse shape, see details in Section 4.1.1
[2] Thresholds are in the energy range between 50 and 100 keV, detector dependet.

shifts are indications that operating conditions of the electronic system changed. The amplitude of test pulses is designed to have a fixed height. A time fluctuation of test pulse amplitude manifests a change of the global response of the electronic system, such as gain shift, system capacitance changes, etc. Variations of the width of test pulses are related to the noise of the electronics.

By monitoring the long term stability of parameters in Phase I, data taken under unstable conditions can be excluded and hence guarantees the quality of data being analyzed.

3.2.3 Data Taking Parameters

The Phase I data taking lasted from November 2011 to May 2013. The key parameters of the considered data in Phase I are described in details in [62]. The Phase I data set used for the $0\nu\beta\beta$ analysis covers Run 25 to Run 46, excluding Run 33. The duty factor of GERDA Phase I, the ratio of DAQ running time to the total time, is 88.1%. The DAQ running time is 492.3 days. The live time of Phase I is established via monitoring the trigger efficiency from test pulses. Table 3.3 lists the live times and the exposures calculated for the total mass M ($\mathcal{E} = M \cdot t$), the active mass $M_{act} = M \cdot f_{AV}$ ($\mathcal{E}_{AV} = M \cdot t \cdot f_{AV}$) and the ^{76}Ge active mass $M_{76} = M_{act} \cdot f_{76}$ ($\mathcal{E}_{76} = M \cdot t \cdot f_{AV} \cdot f_{76}$), for each detector. The operation conditions can differ for each detector and hence the live time can differ for individual detectors.

Fig. 3.3 shows the live time fraction (left axis) and total exposure, $\mathcal{E}$, (right axis) for the ^{enr}Ge detectors as a function of time for the full Phase I data taking. The total exposure is 21.6 kg·yr. The total exposure for *coax* and *BEGe* data sets is 19.2 kg·yr. and 2.4 kg·yr, respectively. The interruptions in the live time are due to the regular calibration measurements of the detectors. Calibration measurements were performed using ^{228}Th radioactive sources every one or two weeks. Both energy and PSD performance were calibrated. The Phase I data taking was stable during most of the time. However, there are noticeable interruptions along Phase I data taking. At the end of May 2012, there was a considerable interruption due to temperature instabilities in the GERDA clean room. The other interruption in July 2012 was due to the deployment of the BEGe detectors into the GERDA cryostat. The indicated time intervals in Fig. 3.3 are related to the data analysis strategy, which is discussed in Section 3.2.4.

The gain shift of the 2615 keV γ-line for successive calibrations in terms of energy was stable for the close-ended detectors during Phase I data taking. Fig. 3.4(a) shows the 2615 keV peak position stability for the BEGe detectors in Phase I. It was stable most of the time with typical gain fluctuations between calibrations of $\sim 0.05\%$ for detectors GD32B, GD32C, and GD32D. The overall gain shift was about 0.05% at 2615 keV, which is small compared to FWHM $\sim 0.2\%$ at $Q_{\beta\beta}$. The energy resolution of ^{enr}Ge-coax detectors at $Q_{\beta\beta}$ as a reference of time was stable among the entire Phase I data taking. The exposure-weighted average FWHM at $Q_{\beta\beta}$ for the *coax* data set was (4.8 ± 0.2) keV.

Data affected by the instabilities were excluded in the data analysis. Fig. 3.4(b) depicts the long term behavior of the energy resolution for BEGe detectors at $Q_{\beta\beta}$ in Phase I. All BEGe detectors had stable energy resolution along data taking period. The averaged
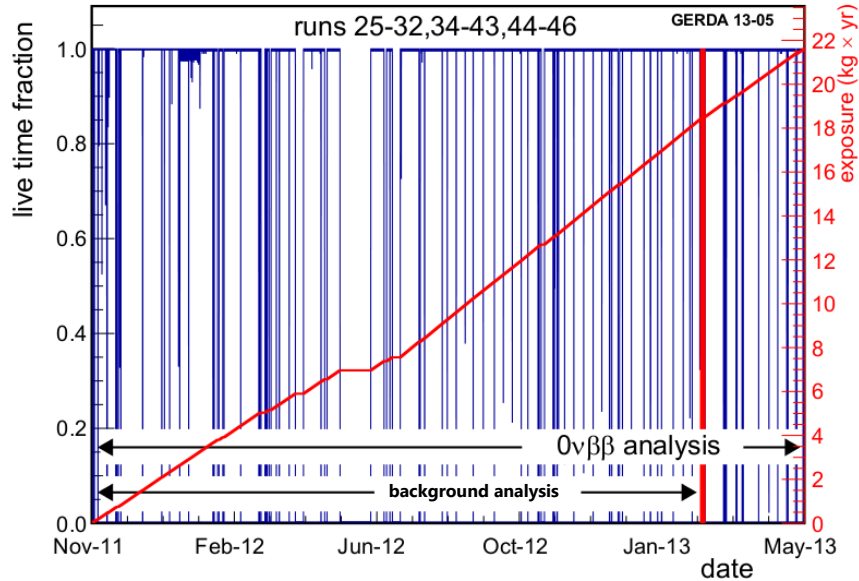
Figure 3.3: Phase I live time fraction and the accumulated exposure as a function of time for the ^{enr}Ge detectors. Data taking during most of time in Phase I was stable. Reasons for the interruptions as refer to the content [46].

energy resolution of the BEGe detectors was in the range of 2.8 to 3.0 keV for GD32B, GD32C, and GD32D; while for GD35B, it was ~3.6 keV. The BEGe detectors operated in the GERDA LAr cryostat have 30 % degraded energy resolutions compared with their performances in the vacuum cryostats. This is most likely due to the length of the signal cable, which was ~30 cm longer between the read-out electrode and the FET compared with that in vacuum cryostat [116]. Off-line semi-Gaussian filtering was used for Phase I energy reconstruction, details are discussed in Section 4.1.1. A new software algorithm for energy reconstruction, the ZAC filter, was demonstrated to have better energy resolution [117] compared to performance of the algorithm used in Phase I analysis. The new software algorithm will be tested in the GERDA Phase II. The exposure-weighted average FWHM at $Q_{\beta\beta}$ was (3.2 ± 0.2) keV for the Phase I *BEGe* data sets.

3.2.4 Blind Analysis

To eliminate the experimenter's bias, the GERDA collaboration used a blind analysis technique in Phase I. This was the first analysis performed using blind analysis in the field of $0\nu\beta\beta$ search.

A representation of energy spectra for definition of the energy windows used in the blind analysis is depicted in Fig. 3.5. During data taking, the events in the $(Q_{\beta\beta} \pm 20)$ keV energy region were saved but did not enter the data analysis pipeline before all analysis parameters were fixed. The unblinding procedure was carried out in two steps:

Detector	t	$\mathcal{E}$	$\mathcal{E}_{AV}$	$\mathcal{E}_{76}$	$\mathcal{E}_{76}$
	[days]	[kg·yr]	[kg$_{AV}$ yr]	[kg$_{76}$ yr]	[mol yr]
Enriched closed-end coaxial detectors					
ANG2	490.9	3.81	3.32	2.88	37.9
ANG3	490.9	3.21	2.78	2.46	32.4
ANG4	490.9	3.19	2.87	2.49	32.7
ANG5	490.9	3.69	3.07	2.63	34.7
RG1	490.9	2.84	2.56	2.20	29.0
RG2	417.2	2.47	2.06	1.76	23.2
sum ^{enr}Ge-coax		19.21			
Natural closed-end coaxial detector					
GTF112	490.9	3.98			
Enriched BEGe detectors					
GD32B	280.0	0.55	0.49	0.43	5.7
GD32C	303.4	0.62	0.56	0.49	6.5
GD32D	284.0	0.56	0.52	0.46	6.0
GD35B	303.4	0.67	0.62	0.54	7.1
sum BEGe		2.40			

Table 3.3: Summary of Phase I live time t and exposures. Exposures calculated in relation to the total mass M ($\mathcal{E}$), the active mass M_{act} ($\mathcal{E}_{AV}$) and the ^{76}Ge active mass M_{76} ($\mathcal{E}_{76}$) of the individual detectors [62].

- Evaluation of run parameters, background model, and PSD using energy region outside the blinding window: After evaluation of run parameters, PSD cut values and development of the background model, the window was partially unblinded while keeping the central ROI still blinded.

- Complete unblinding after consistency check: Only once all parameters were checked for consistency and all parameters were fixed, the energy window around $Q_{\beta\beta}$ was unblinded. The central blinding window size for ^{enr}Ge-coax detectors is $Q_{\beta\beta} \pm 5\,\text{keV}$; $Q_{\beta\beta} \pm 4\,\text{keV}$ for BEGe detectors [3].

3.2.5 Signal Read-out and Data Acquisition

Most HPGe detectors were operated in the direct coupling scheme (DC mode), where the HV is applied on the n$^+$ electrode and the p$^+$ electrode is grounded and is connected to the charge sensitive preamplifier. Two detectors, GTF45 and GTF32, were working in alternative coupling scheme (AC mode), in which the n$^+$ contact is grounded and the

---

[3]Smaller window size is because of better energy resolutions of BEGe detectors

signal is readout from p$^+$ contact but coupled with a low background HV capacitor to the preamplifier [58].

The analog signals from the HPGe detectors were read out by an electronics and data acquisition systems [59, 60] based on 4-channel, 100 MHz sampling rate, 14-bit Flash Analog-to-Digital-Convertor (FADC) modules. The readout allows full recording of all the relevant waveform and timing information after the initial trigger. Two HPGe traces for each event were recorded to disk for off-line data analysis: a high-frequency-short (HFS) trace, 4 μs long with 100 MHz sampling rate; and a low-frequency-long (LFL) trace, 160 μs long with 15 MHz sampling rate [61]. The HFS trace has high time-resolution and was used for the pulse shape analysis, while the LFL trace was used for analyzing the trigger, baseline, and the reconstruction of energy.

3.3 GERDA Phase I Background

3.3.1 Event Selection Cuts

Events uncorrelated with the muon veto cut and anti-coincidence cut are candidates for $0\nu\beta\beta$ signal events. In the data analysis step, event selection cuts were applied to the physics data:

- **Muon veto cut**
  Muon-induced background events can be recognized by coincidence of an HPGe detector event within 8 μs with a hit in a muon detector. The muon-induced events are rejected, reducing the background in the ROI by 7 %.

- **Anti-coincidence cut**
  Further background events can be rejected by requiring that energy is only deposited in one detector. Events with energy depositions > 20 keV in more than one detector were not considered. The background reduction around $Q_{\beta\beta}$ is ∼15 %. Because $0\nu\beta\beta$ events are mostly single site events, the survival probability after anti-coincidence cut is ∼95 %.

3.3.2 Phase I Energy Spectrum: Main Structures

A good understanding of the background components estimates the expected number of events in the ROI due to contaminations. The background sources, in the Phase I, could be identified by the observation of their characteristic γ lines or by other features in the measured energy spectrum. Fig. 3.6 shows the Phase I energy spectrum from 100 keV to 7.5 MeV for ^{enr}Ge-coax (16.7 kg·yr), BEGe (1.8 kg·yr), and ^{nat}Ge detectors (3.13 kg·yr), respectively. The green cover the blinded regions and the horizontal bar in each plot represents the energy region at $Q_{\beta\beta} \pm 200$ keV used for determining the background index.

The effect of enrichment in ^{76}Ge yields a characteristic bell-shape distribution in the energy spectra. Compared the enriched detectors with the natural detector in between 600

and 1500 keV, the enriched detectors manifest an enhanced continuous spectrum originated from neutrino accompanied double beta decay of ^{76}Ge.

The low energy region up to 565 keV is dominated by the β-decay of cosmogenic ^{39}Ar. ^{39}Ar is a β-emitting isotope with $T_{1/2}=$ 269 yr and $Q_{\beta} = 565$ keV. Its activity was determined to be (1.15 ± 0.11) Bq/kg [108], consistent with the values reported in literature [136].

A prominent peak-like structure at 5.3 MeV with a tail towards lower energies can be identified in the energy spectrum of the enriched closed-end coaxial detectors. It is due to ^{210}Po α decays ($T_{1/2}=$138.4 d) on the detector p$^+$ surfaces.

Another prominent line at 1525 keV γ-line is due to ^{42}K (Q_{β}=3.5 MeV, $T_{1/2}$=12.3 h). ^{42}K is the daughter isotope of long lived ^{42}Ar (Q_{β}=600 keV, $T_{1/2}$=32.9 yr). ^{42}Ar is an isotope, created mostly in cosmic-ray induced spallation reactions. ^{42}K being positively ionized after the ^{42}Ar decay, can get attracted by the E-fields generated by the detector high voltages. In order to protect the detectors against ^{42}K ions, the individual string was enclosed by a 60 μm thick cylindrical copper foil with 113 mm in diameter, as displayed in Fig. 3.2. The copper foil, called mini-shroud, demonstrated to efficiently suppress the ^{42}K background.

Several γ-lines from decay of the isotopes ^{40}K, ^{208}Tl, ^{214}Bi, and ^{60}Co could be identified.

3.3.3   Phase I Background Modelling

The energy region from 570 keV to 7.5 MeV, excluding the blinded region at $Q_{\beta\beta}\pm20$ keV, was considered for developing a background model. In order to avoid uncertainties due to n$^+$ deadlayer thickness and the theoretical shape of beta decay spectrum, ^{39}Ar decay was not taken into account to the background modelling. In addition to the isotopes that could be identified in the energy spectra, contaminations identified by screening of materials were taken into account.
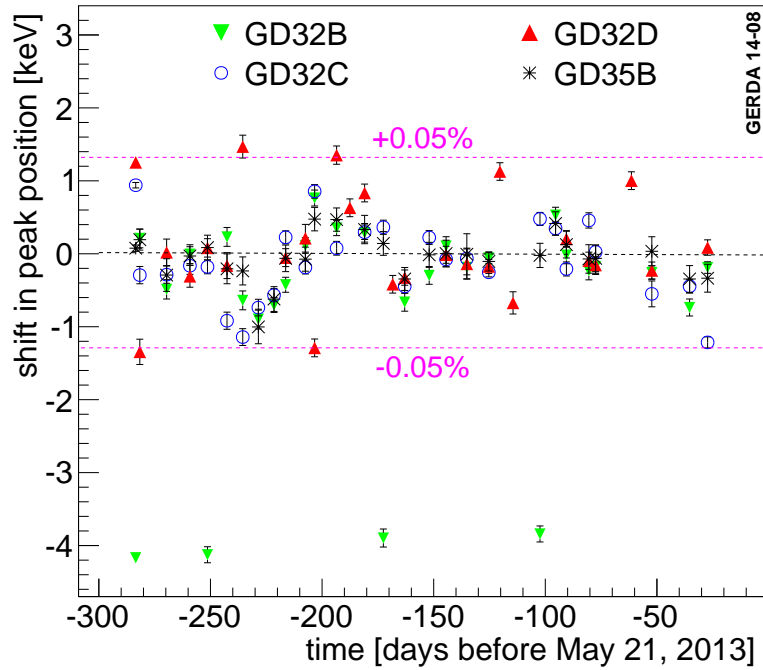
(a)
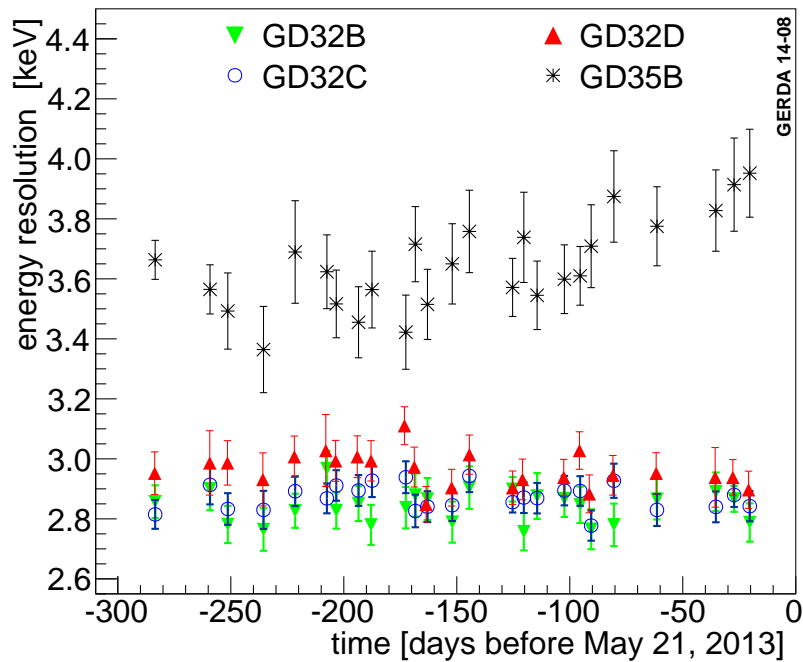
(b)

Figure 3.4: (a) Shift of $2615\,\mathrm{keV}$ γ-line for BEGe detectors between subsequent calibration measurements for Phase I data taking. The shifts are within $0.05\,\%$ for most of the time. (b) Energy resolution for BEGe detectors at $Q_{\beta\beta}$ as a function of time. Taken from [116].
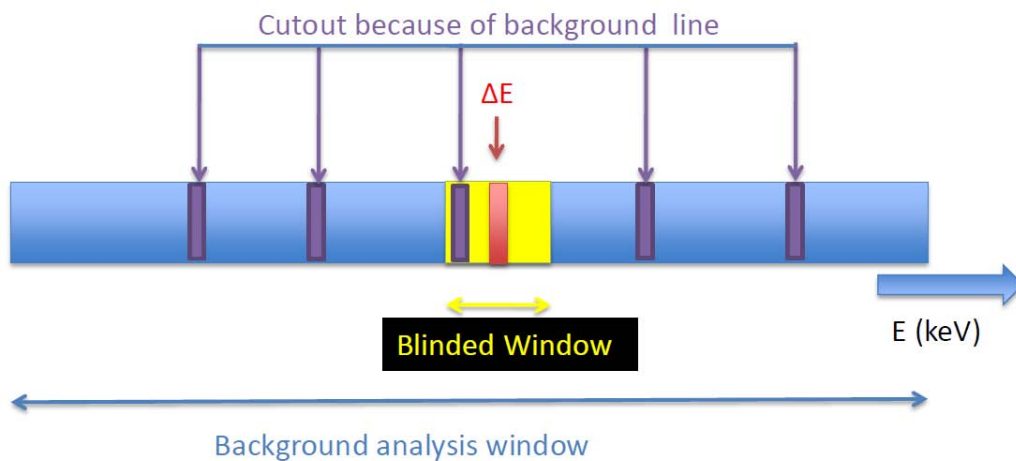
Figure 3.5: Energy windows performed in the blinding procedure. The energy region in $Q_{\beta\beta} \pm 20\,\mathrm{keV}$ (yellow region) is blinded. Energy region except $Q_{\beta\beta} \pm 20\,\mathrm{keV}$ (blue region) is used for the evaluation of run parameters, developing background models, and developing pulse shape discrimination methods. More details on Phase I blinding strategy, as refer to the text. Taken from [46].
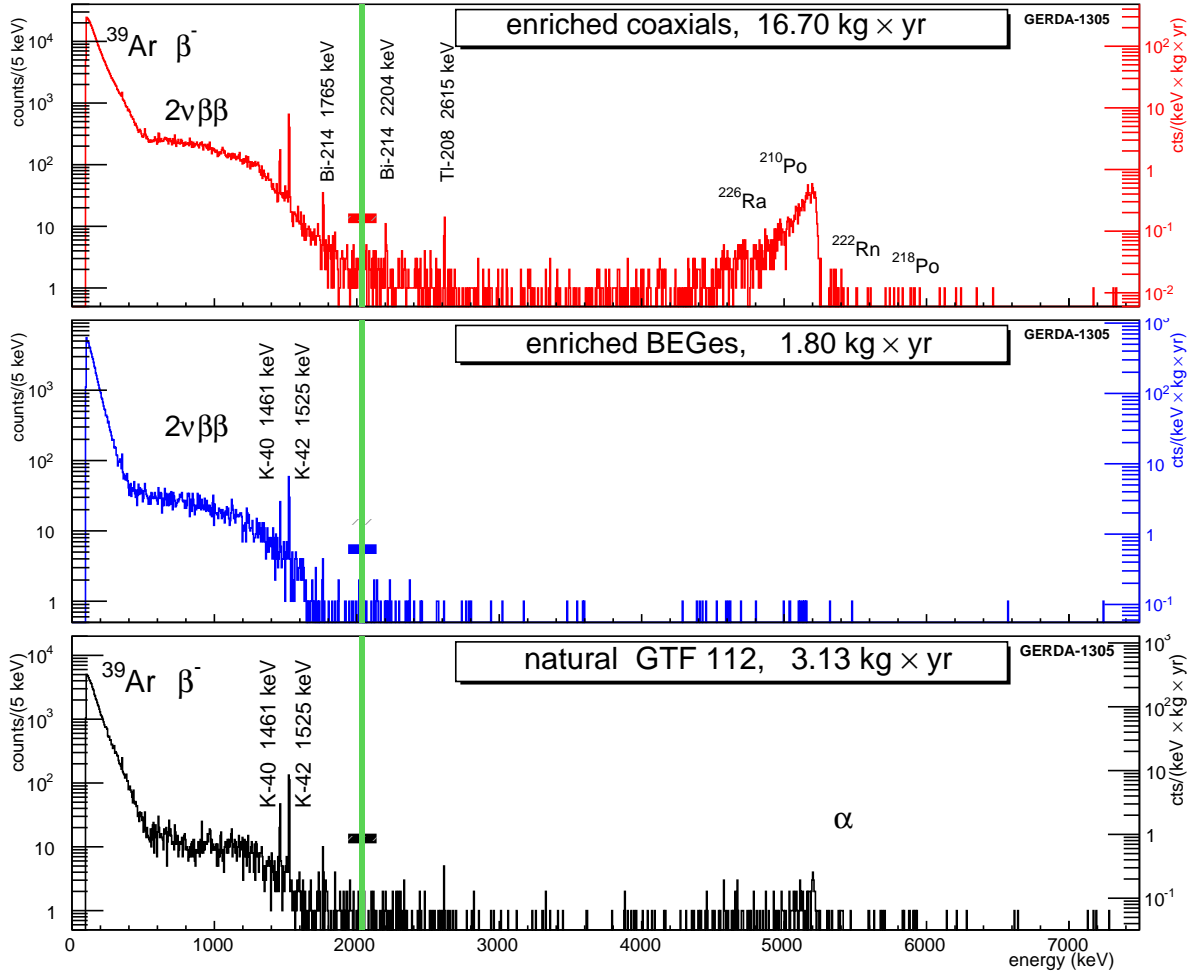
Figure 3.6: Phase I energy spectrum for ^{enr}Ge-coax, BEGe, and ^{nat}Ge detectors, respectively. The green lines represent blind regions. The various horizontal bars in the plots stand for the energy region for background level at $Q_{\beta\beta}$ (in energy region at $Q_{\beta\beta} \pm 200\,\mathrm{keV}$). Low energy region up to $565\,\mathrm{keV}$ in all spectra is dominated by the cosmogenic ^{39}Ar β decay. The bell-shape distributions from $600\,\mathrm{keV}$ to $1500\,\mathrm{keV}$ in enriched detectors come from $2\nu\beta\beta$-decay; whereas in natural diode shows a rather flat distribution. α events from ^{226}Ra, ^{222}Rn, and ^{210}Po decay result in peak-like distribution above $4\,\mathrm{MeV}$. The $1525\,\mathrm{keV}$ peak originates from ^{42}K β-decay. The various γ-lines at 1461 and $2614\,\mathrm{keV}$ are from ^{40}K and ^{208}Tl, respectively. The γ-peaks at 1765 and $2204\,\mathrm{keV}$ come from ^{214}Bi decay. Taken from [46].
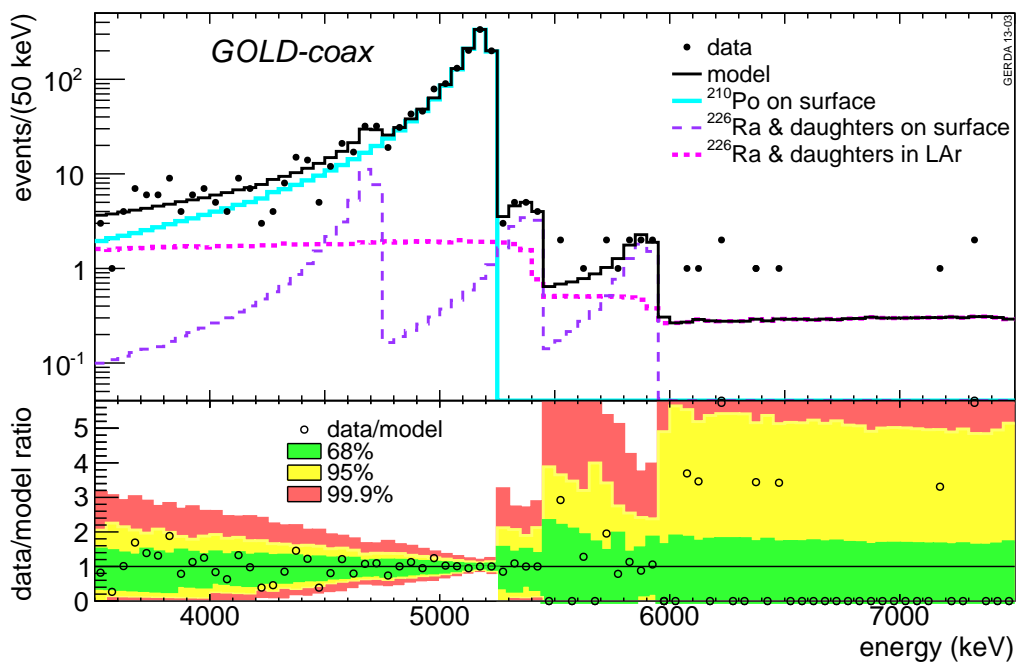
Figure 3.7: Measured spectrum (black markers) with the best α fit model (black line) for the *golden coaxial data set*. The lower panel depicts the ratio between data and model with the smallest intervals of 68% (green region), 95% (yellow region) and 99.9% (red region) C.I. for the model expectation. Taken from [46].

Analysis of background had been performed by fitting simulated to measured spectra in binned distribution, calculating posterior probabilities given by Bayes. The spectral shapes of individual components for different source locations were generated by using Geant4 Monte Carlo simulations [138] and were compared to the measured spectra [46, 108]. The energy range above the Q-value of ^{42}K, between 3.5 and 7.5 MeV, was analyzed first, giving the best fit for the α induced spectra. Fig. 3.7 shows the observed spectrum with the best fit model and the individual background contributions considered in the α fit, for the *golden coaxial data set*. The lower panel shows the ratio between data and model together with the smallest intervals of 68 %, 95 % and 99.9 % probability for the model expectation.

Two background models were developed to account for the observed energy spectra of the closed-end coaxial detectors. A minimum model (see Fig. 3.8(a)) was established by using the minimum amount of sources to reasonably describe the measured energy spectrum. The components used in the minimum model are: ^{214}Bi decays in the holders and on the p$^+$ surface, ^{228}Th decays in the holders, ^{228}Ac decays in the holders, ^{42}K decays homogeneous in LAr, ^{60}Co decays in the holders and in Ge, best-fit α model from ^{210}Po and from ^{226}Ra sub-chain, ^{40}K in the holders, and ^{76}Ge $2\nu\beta\beta$ decays. In the maximum model plausible sources expected from the results of material screening and the activation histories were added. On the top of the minimum model components, the extra allowing components were considered: ^{42}K decays on the p$^+$ and the n$^+$ surfaces, ^{214}Bi decays in LAr close to the p$^+$ surface and in the Rn shroud, ^{228}Ac decays in the Rn shroud, and ^{228}Th decays in the Rn shroud and in the heat exchanger.

To describe the measured spectra of the BEGe detectors, the minimum model components with two additional contributions, intrinsic ^{68}Ge decay and ^{42}K decays on the n$^+$ surface, were considered (see Fig. 3.8(b)).

Background contamination from ^{68}Ge decays in Ge is expected for the newly produced BEGe detectors due to the cosmogenic activation above ground. The contribution of ^{68}Ge with half life of 270.8 d to the background of the closed-end coaxial detectors is negligible since the detectors have been stored underground for many years.

The contribution from ^{42}K decays on the n$^+$ surface is more pronounced in the BEGe detectors with respect to that in the closed-end coaxial detectors due to the thinner n$^+$ surfaces of the BEGe detectors [4].

For the closed-end coaxial detectors, the main sources contributing to background are mainly located close-by at $Q_{\beta\beta}$ are [5]: ^{214}Bi in the detector assembly, ^{228}Th in the detector assembly, ^{42}K decays homogeneous distributed in the LAr and α events on the p$^+$ surface. The background index and individual contribution to $Q_{\beta\beta}$ for the BEGe detectors is listed in Table 3.4. The dominant background at $Q_{\beta\beta}$ for BEGe detectors is due to ^{42}K decays on the n$^+$ surface (54.6 % of the total events in the ROI, background index (BI)=2.08×10^{-2} cts/(keV·kg·yr)).

---

[4]Thickness of n$^+$ surface is about 2 mm and ≈ 1 mm for the closed-end coaxial detectors and the BEGe detectors, respectively.

[5]Decomposition using minimum model.

component location	$SUM - BEGe$ minimum model + n^+ BI (10^{-3}cts/(keV·kg·yr))
^{42}K n^+ surface	20.8 [6.8, 23.7]
^{214}Bi detector assembly	5.1 [3.1, 6.9]
^{228}Th detector assembly	4.2 [1.8, 8.4]
^{42}K LAr homogeneous	2.0 [1.8, 2.3]
α model p^+ surface	1.5 [1.2, 1.8]
^{60}Co in Ge	1.0 [0.3, 1.0]
^{214}Bi p^+ surface	0.7 [0.1, 1.3]
^{68}Ge in Ge	1.5 (<6.7)
^{60}Co detector assembly	<4.7
Total	38.1 [37.5, 38.7]

Table 3.4: Total background index and individual contributions in $Q_{\beta\beta}\pm 4$ keV for the BEGe data sets estimated from Phase I background model. The values in the table were presented with the uncertainty intervals [upper, lower limit] obtained as the smallest 68 % interval of the marginalized distributions. Table extracted from [46].

The data available after partial unblinding are shown in Fig. 3.9. The background seen in the central window was in a good agreement with the prediction from the background model. No peaks were predicted in the blinded region. The best fit models predicted the spectral shapes were flat around $Q_{\beta\beta}$, as shown in Fig. 3.9. That made it feasible to interpolate the background by a constant in the BI evaluation windows. The energy window used to determine the BI was from 1930 keV to 2190 keV, excluding all the expected peak regions and ROI, with a total width of 200 keV. The BI before applying any pulse shape discrimination method at $Q_{\beta\beta}$ are $(1.75^{+0.26}_{-0.24})\times 10^{-2}$ cts/(keV·kg·yr) (68% C.I.) and $(3.6^{+1.3}_{-1.0})\times 10^{-2}$ cts/(keV·kg·yr) (68 % C.I.) [6] for the closed-end coaxial detectors and the BEGe detectors, respectively [46, 108].

3.4   Phase I Pulse Shape Discrimination

$0\nu\beta\beta$ events are mostly SSEs while a significant fraction of background events in the ROI are MSEs. The experimental sensitivity can be improved via analysing the pulse shape of the detector signals to recognize signal-like events and veto background-like events.

Different techniques were used for the BEGe detectors and the closed-end coaxial detectors because of their distinct geometries that result in different weighting fields inside Ge diodes. For the BEGe detectors, a mono-parametric A/E PSD method was used. The basics of the A/E method are discussed in Section 2.5.1. The signal efficiency after the

---

[6]Predicted background indices for the closed-end coaxial and the BEGe detectors were estimated via interpolation.

A/E PSD cut was (92±2)% while 82.5% of the background events at $Q_{\beta\beta}$ were rejected. For $2\nu\beta\beta$ events, the signal recognition efficiency after PSD cut was (91±5)%. Details of the pulse shape analysis of the BEGe detectors will be discussed in Chapter 4.

For the closed-end coaxial detectors, three different PSD analyses were performed. The main PSD approach was using artificial neural network (ANN). About 45% of the background events at $Q_{\beta\beta}$ were rejected with a signal recognition efficiency of $(90^{+5}_{-9})\%$. $2\nu\beta\beta$ efficiency was (85±2)% after ANN cut. The result of ANN method was in agreement with the results from two other PSD methods : likelihood approach trained on Compton edge events and two pulse shape parameters method.

3.5 New Limits on the Half-life of Neutrinoless Double Beta Decay

The combined energy spectrum of all the enriched Ge detectors around $Q_{\beta\beta}$ after data unblinding is shown in Fig. 3.10. The open and filled histograms shows the energy spectrum before and after PSD cut, respectively. After data unblinding, no excess of events was found above the expected background.

Two approaches were performed to derive the lower limit of $T^{0\nu}_{1/2}$, the frequentist analysis and the Bayes analysis. The primary method is the frequentist analysis where a profile likelihood method was performed to fit the data sets with a common $(T^{0\nu}_{1/2})^{-1}$. The best-fit value of $N_{0\nu}$ is zero and an upper limit of $N_{0\nu}$ is 3.5 counts (90 % C.L.) was obtained. The lower limit of $T^{0\nu}_{1/2}$ was then derived, $T^{0\nu}_{1/2}>2.1\times10^{25}$ yr (90 %C.L.). The Bayes analysis was performed by using a flat prior on $(T^{0\nu}_{1/2})^{-1}$ in the range of 0-10^{-24} yr^{-1}. The best-fit was zero counts as well and the corresponding lower limit is $T^{0\nu}_{1/2}>1.9\times10^{25}$ yr (90 %C.I.). This is the current best limit of $T^{0\nu}_{1/2}$ using ^{76}Ge isotopes [24]. By combining the results from GERDA, HDM [26], and IGEX [27], the lower limit of $T^{0\nu}_{1/2}>3.0\times10^{25}$ yr (90 %C.L.) was set.

A hypothesis test was performed to compare the GERDA Phase I result with the signal claim as reported by a subgroup of the HDM collaboration. The expected number of events for the null hypothesis (background only), H_0, is 2.0±0.3 (see the blue line in Fig. 3.10). The expected number of events for the alternative hypothesis (signal plus background), H_1, is 5.9±1.4, corresponding to a $T^{0\nu}_{1/2}$=1.19×10^{25} yr (see the red-dash line in Fig. 3.10). The number of the observed events is 3. Assuming the model H_1 is true, the probability to obtain $N_{0\nu}$=0 is 0.01 (frequestist p-value method). The result can be tested as well by using the Bayes factor. The ratio of the probabilities of the two models $P(H_1)/P(H_0)$ is 0.024. The combination of the results from GERDA, HDM, and IGEX, the derived Bayes factor is 2.0×10^{-4}. Hence, the long standing claim is strongly disfavored.

3.6 Phase II Upgrade

The goal of the second phase (Phase II) of the GERDA experiment is to improve the sensitivity of $T_{1/2}^{0\nu}$ by another order of magnitude. In order to achieve the increase in sensitivity, additionally to the Phase I closed-end detectors a total of 20 kg in form of 30 BEGe detectors with improved PSD efficiencies and energy resolutions were deployed. The discrimination method of the BEGe detectors is described in Section 2.5.1 and the data analysis method used for the Phase I BEGe detectors is presented in Chapter 4. The detector production and the characterization are described in Chapter 6.

Additionally in Phase II the liquid argon (LAr) instrumentation is used to identify background events with energy deposition simultaneously in HPGe detectors and the surrounding LAr. The LAr veto system consists of two parts: 16 3" PMTs in total on the top and bottom of the array and a curtain surrounding the detector array, which consists of scintillating fibers read out by Si-PMTs. Taking advantage of LAr veto instrumentation allows to reach a background index of $\sim 10^{-3}$cts/(keV·kg·yr). Fig. 3.11(a) shows the setup of the Phase II detector system.

Fig. 3.11(b) shows the sensitivity of $T_{1/2}^{0\nu}$ as a function of exposure. With an exposure of 100 kg·yr ($\sim$5 yrs data taking), a sensitivity to the $0\nu\beta\beta$ half-life of ^{76}Ge in the range of 10^{26} year is expected. GERDA Phase II has started data taking at the end of December 2015.
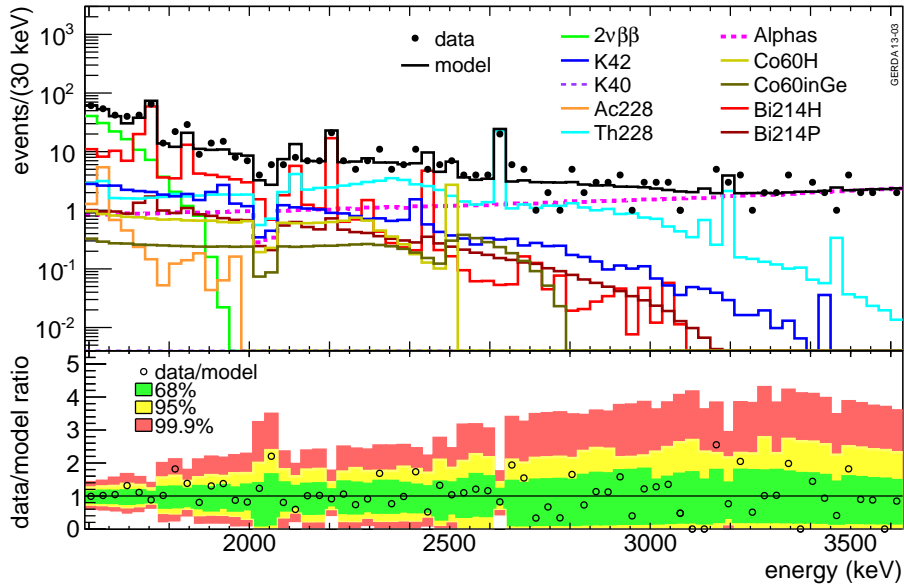
(a)
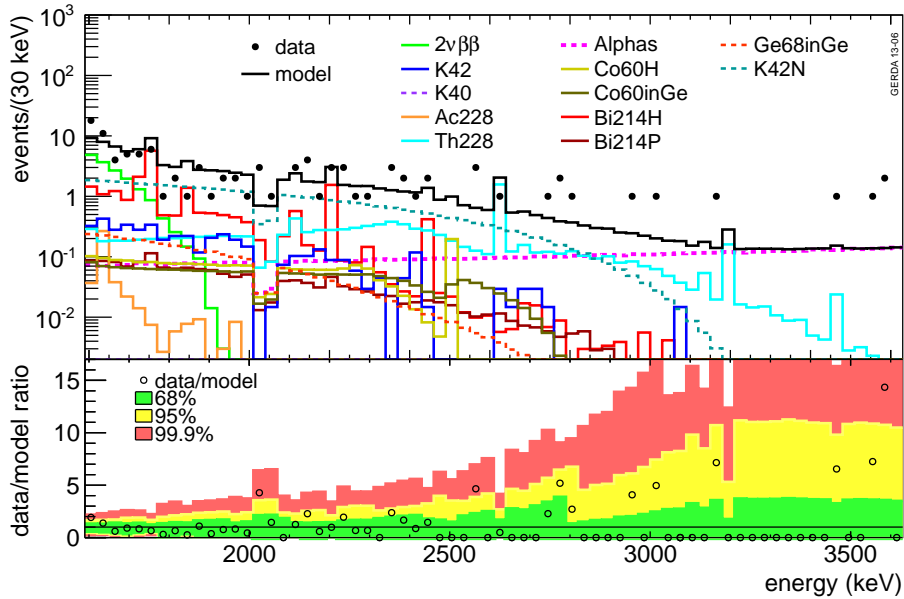
(b)

Figure 3.8: Measured spectrum (markers) in the medium energy region with the best fit minimum model (black line) as well as individual background compositions for (a) *golden coaxial data set* and (b) *BEGe data set*. The abbreviations in the legend "inGe", "H" and "P", refer to the decays in the germanium detectors, the holders and the p^+ surface, respectively. The bottom panels depicts the ratio between data and model, together with the 68 %, 95 % and 99.9 % probabilities for the ratios by the best fit parameters. Taken from [46].
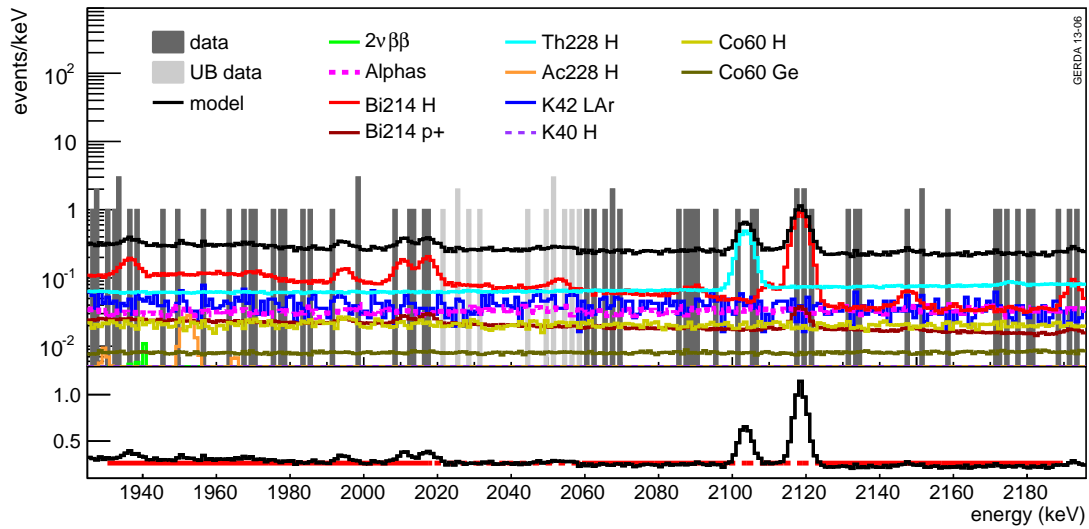
(a)
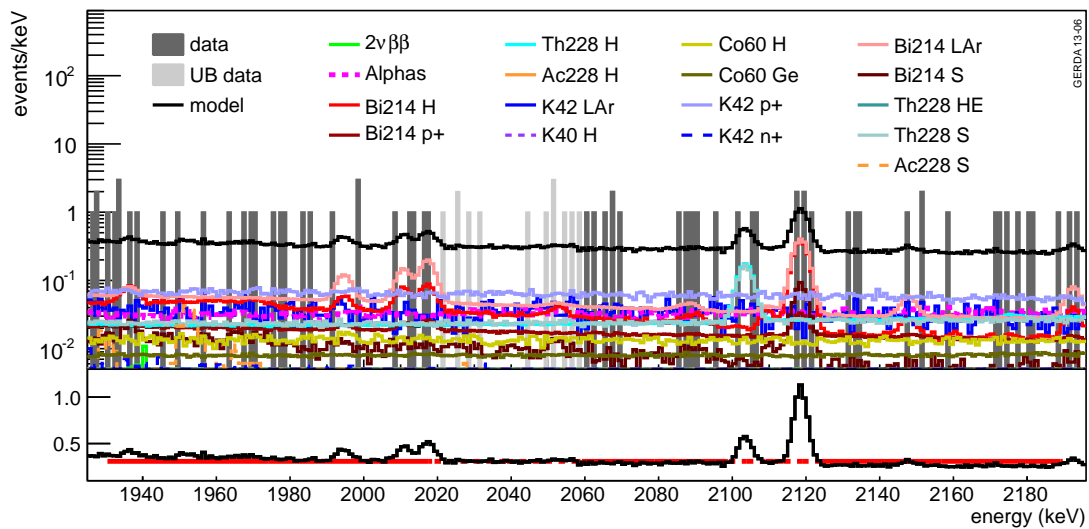
(b)

Figure 3.9: The measured spectrum spectrum between 1930 and 2190 keV of the *golden coaxial data set* with (a) Minimum mode and (b) Maximum model accompanied with their individual background compositions. The light grey histogram refers to the partially unblinded data, which was not used for the background modelling. The abbreviations in the legend are : H (detector holders), LAr (uniformly distributed in LAr), Ge (inside Ge diode), p+ (in p^+ contact), n+ (in n^+ contact), S (randon shroud) and HE (heat exchanger). Around $Q_{\beta\beta}$, no peaks were expected for both models and the predicted spectral shapes are flat. The bottom panel of each figure shows the model fitted with a constant. Taken from [46].
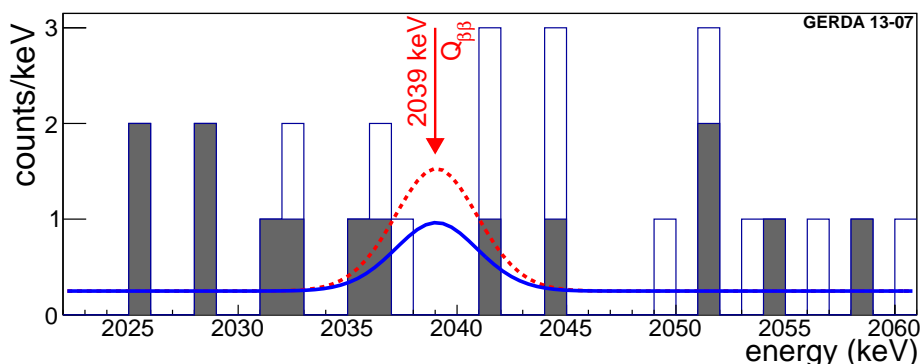
Figure 3.10: Combined spectrum after unblinding around the ROI. The spectrum before and after PSD cut is shown with a open histogram and a filled histogram, respectively. The 90 % C.L. upper limit derived from the GERDA result is shown in blue, whereas the red-dashed line shows the expected signal claim from [28] (normalized to the GERDA exposure).
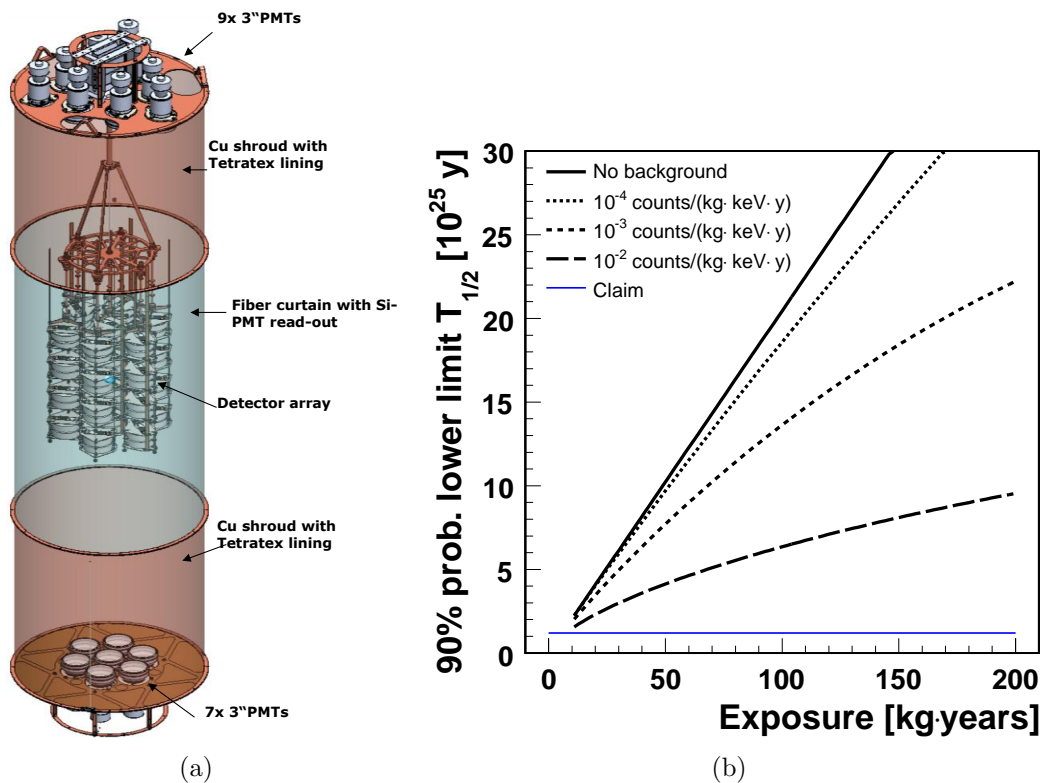
Figure 3.11: (a) Sketch of the whole Phase II setup [63]. (b) $T_{1/2}^{0\nu}$ sensitivity as a function of exposure. Figure from [64].

Chapter 4

BEGe Pulse Shape Analysis

To improve on the limit for the half life of neutrinoless double beta decay, the enhancement of background recognition efficiency and the reduction of the background index are crucial. BEGe detectors have the potential to improve background recognition efficiency by pulse shape analysis, exploiting the ratio of the maximum amplitude of the current signal (A) over the energy of the charge signal (E) - the A/E parameter. Four enriched BEGe detectors produced for Phase II, GD32B, GD32C, GD32D and GD35B were already deployed during Phase I. The entire data analysis procedure could be well-established. This chapter focuses on the Phase I BEGe PSD method and the Phase I results obtained with the BEGe detectors.

4.1 PSD Algorithm for the BEGe Detectors

4.1.1 Off-line Energy Reconstruction

The amplitude of the charge pulse is proportional to the energy deposition. An off-line semi-Gaussian filter was used for the Phase I energy reconstruction of BEGe detectors [118]. The semi-Gaussian filter transforms an input waveform to a pseudo-Gaussian shape using a CR-RC^n algorithm. The CR filter serves as a differentiator which passes the high frequency component of input waveforms and reduces its low frequency component by differentiation. The subsequent recursive algorithm, RC^n filter, performs as a low-pass filter (integrator) which attenuates the high frequency component by recursively integrating the input signal for n times.

The CR-RC^n filter can be expressed as follows:

$$
\begin{aligned}
&\text{CR filter: } \mathfrak{D}_i \equiv\ P_i - P_{i-L}, \\
&\text{RC}^n \text{ filter: } \mathfrak{I}_i{}^n \equiv\ \begin{cases} (\frac{1}{L}\ \sum_{k=i-L}^{k=i}\ P_k)^n & \text{if i} < \text{L} \\ 0 & \text{if i} \ge \text{L}, \end{cases}
\end{aligned} \tag{4.1}
$$

where P_i is the amplitude of the charge pulse at the ith time bin, $\mathfrak{D}_i$ is the time derivative of

the charge pulse between the ith and $(i - L)$th time bin, and $\mathfrak{I}_i$ is the averaged amplitude of a pulse at the ith bin averaged over nearby bins. The index n denotes the number of recursion(s).

$\mathfrak{I}_i$ is also called the **moving average filter** (**MA**), which is the most common filter in digital signal processing for denoising. For Phase I BEGe detectors, the widths of the CR and RC filter were set to $5\,\mu s$ (L=500) and the number of recursions of the RC filter was set to 24 (n=24). Fig. 4.1 shows an input charge waveform and its transforms after the CR-RC^n filter step by step. The energy deposition is proportional to the maximum amplitude of the output pseudo-Gaussian shape waveform after the CR-RC^{24} shaping filter.

(a)   (b)
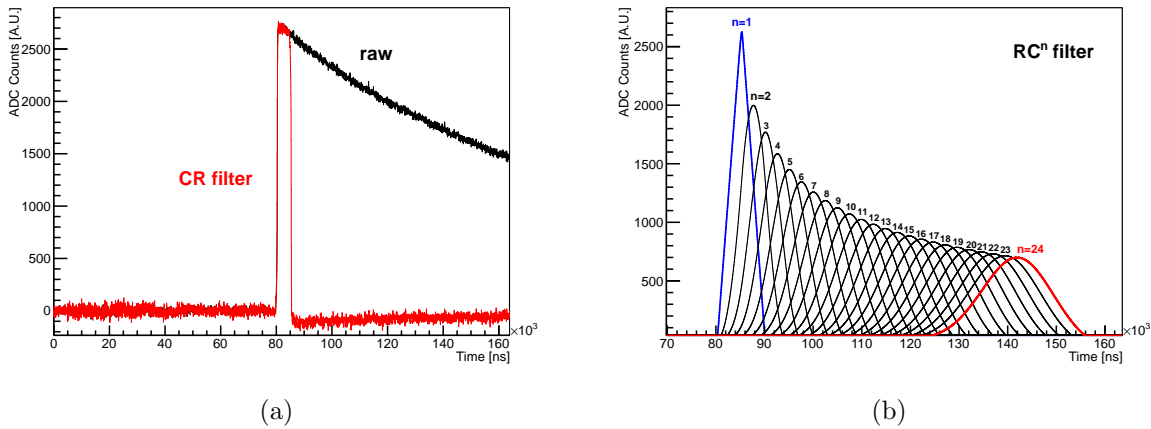
Figure 4.1: GERDA Phase I energy reconstruction for the BEGe detectors using semi-Gaussian filtering. (a) The raw charge pulse and the pulse after CR filtering. (b) The successive pulses after recursive RC filtering. The number n stands for the number of recursions of the RC filter. The output pulse with pseudo-Gaussian shape is displayed (in red). The deposited energy is proportional to the maximum amplitude of the output waveform.

4.1.2   Maximum Amplitude Determination of Current Pulse

The de-noising algorithm used for the off-line reconstruction of maximum amplitude of the current pulse is mainly based on the **MA** algorithm defined in Section 4.1.1. The charge pulse transforms to the current pulse by several filtering steps, which are shown in Fig. 4.2. The charge pulse is de-noised by MA filters with $50\,ns$ window size (L=5) recursively 3 times. The current pulse is then calculated by differentiating the charge pulse with $10\,ns$ bin width. The output current pulse is smoothed in advance to increase 10 times resolution by a linear interpolation.

(a)   (b)
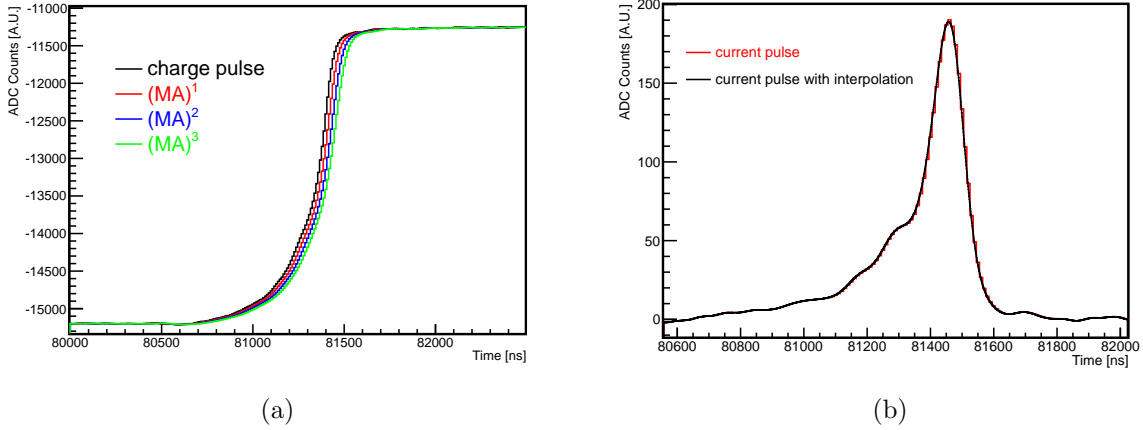
Figure 4.2: GERDA Phase I maximum amplitude determination from current waveform of the BEGe detector using MA filtering. (a) The raw charge pulse and the pulses after recursive MA filters. (b) The subsequent pulse from the derivative of the charge pulse and the waveform after smoothing applying interpolation.

4.1.3 Parametrization of the A/E Distribution

Modelling A/E Distributions

A typical A/E distribution, $f(A/E)$, at a given energy for events from a ^{228}Th calibration is shown in Fig. 4.3. The distribution can be well described by an empirical function [102]:

$$f(A/E) = s(A/E) + m(A/E),$$
$$s(A/E) = \frac{\alpha}{\sigma_{A/E}\ \sqrt{2\pi}}\ \exp[\frac{-(E - \mu_{A/E})^2}{2\ (\sigma_{A/E})^2}],$$
$$m(A/E) = \beta \cdot \{\kappa + \exp[\xi \cdot (E - \nu)]\} \cdot \left\{1 + \exp[\frac{(E - \nu)}{\zeta}]\right\}^{-1}.$$

(4.2)

The SSE term, $s(A/E)$, is given by a single Gaussian with mean value $\mu_{A/E}$, standard deviation $\sigma_{A/E}$ and amplitude α. The MSE term, $m(A/E)$, which describes the asymmetric A/E distribution for MSEs, is parametrized with free parameters β, ξ, ν, κ and ζ. Note that the MSE term depends on source location and type.

A/E Resolution

The FWHM of the SSE component of the A/E distribution at a given energy, $b_{A/E}=2.35 \cdot \sigma_{A/E}$, is an index to determine the pulse shape discrimination power of a BEGe detector only in combination with the reduction power for a FEP[1].

---

[1]One can always design a filter which has an excellent A/E resolution but with a poor discrimination power of MSEs. See more examples in 5.1.1.
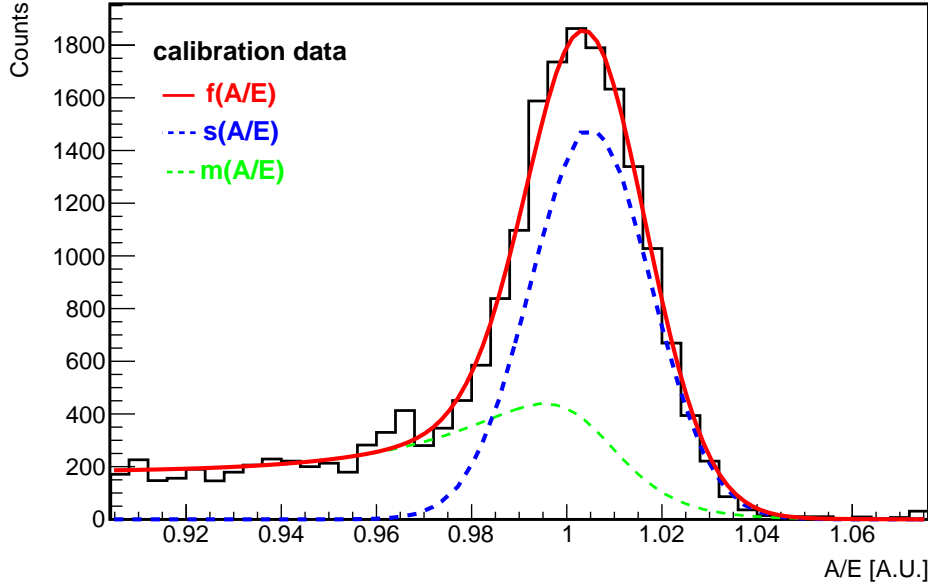
Figure 4.3: A/E distribution using a ^{228}Th source. The distribution can be well described using an empirical fit function, $f(A/E)$ (red curve in the figure), as shown in Eq.4.2. The blue dashed histogram represents the SSE component and the MSE contribution is shown in green.

At low energies, $\sigma_{A/E}$ is dominated by the electronic noise on the current pulse, which is energy dependent, namely, $\sigma_{A/E} \propto \sigma_A/E \propto 1/E$. In the MeV region, the contribution due to the intrinsic statistical broadening of energy peaks contributes only with $\sim 1\%$ of $\sigma_{A/E}$, hence is negligible. Therefore, similar to Eq.2.15, $\sigma_{A/E}$ as a function of E can be described approximately as:

$$\sigma_{A/E}(E) = \sqrt{\frac{c0}{E^2} + c1}, \tag{4.3}$$

where c0 and c1 are constants.

4.2 PSD Normalization Procedure for Phase I BEGe Detectors

The A/E PSD method is sensitive to the stability of the amplitude of a current/charge pulse. Calibrations using a ^{228}Th source allow to monitor the stability of the A/E parameter over time. As mentioned in 2.5.2, the ^{228}Th source provides abundant samples of signal-like and background-like events. DEP events of the ^{208}Tl line at 2614.5 keV are proxies of $0\nu\beta\beta$ events. SEP and FEP events are samples for MSE. Also, the Compton continuum
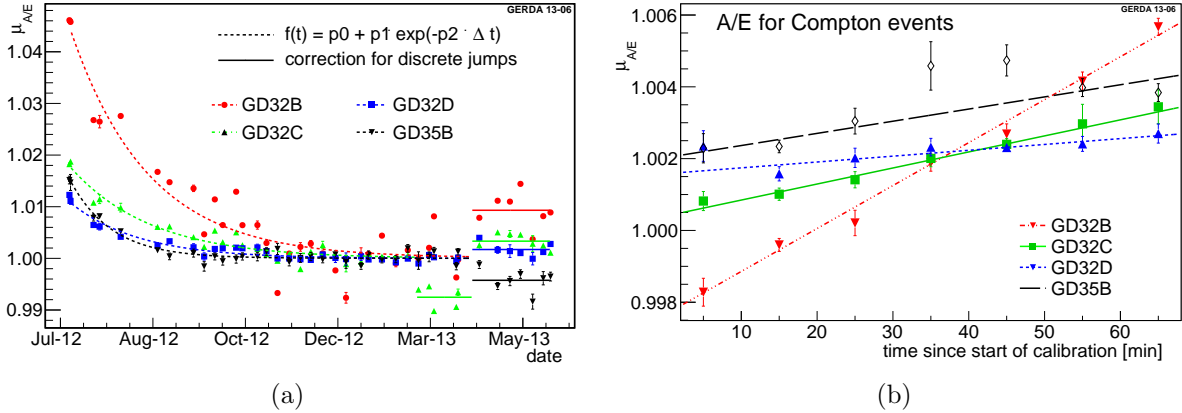
Figure 4.4: (a)Time distribution of $\mu_{A/E}$ for DEP events for each ^{228}Th calibration. Before the occurrence of jumps, the data points can be described by fitting a polynomial plus a constant. While during the period of jumps, different constants for $\mu_{A/E}$ were estimated via averaging $\mu_{A/E}$ over the periods. Each distribution was normalized to one with respect to it's own steady plateau. (b)$\mu_{A/E}$ as a function of time for Compton events between 1 and 1.3 MeV since the beginning of calibration runs. Time scale of the drift lasted about an hour for each detector. The effect can be corrected by fitting a linear function to each calibration data. Taken from [103].

of ^{208}Tl contains a considerable fraction of SSEs ($\sim$40 %) which can be used to check PSD at different energies.

The A/E value was observed to have time and energy dependence during Phase I data taking. The process to correct these effects is referred to as normalization. To compare the A/E PSD performances between individual BEGe detectors, a normalization scheme on PSD was investigated.

4.2.1   Time Dependence Normalization

Long Term Drift Correction

The stability of the A/E PSD method was monitored using DEP events. As shown in Fig. 4.4(a) the Gaussian mean A/E, $\mu_{A/E}$ (definition refer to the formula 4.2), decreased quasi-exponentially by about 1 % to 5 %, depending on the detector, in a time scale of approximately a month after the detector deployment in July 2012. In a period close to the end of data taking a power failure occurred which resulted in a jump of the $\mu_{A/E}$ values. The long term drift behaviour of $\mu_{A/E}$ can be fitted with an exponential plus a constant before the jump. After the jump, $\mu_{A/E}$ can be described by a constant. All the data points for each detector can be normalized to the fitted function shown in Fig. 4.4(a). The long term drift normalization as a function of time was applied to the background data.

Short Term Drift During Calibration

Additionally a drift of the PSD parameters during calibration was observed. The development of $\mu_{A/E}$ as a function of time for all BEGe detectors is shown in Fig. 4.4(b). Due to the limited statistics of the DEP events, the events in the Compton region between 1 and 1.3 MeV were used for correcting the additional A/E drift. During calibration runs, the A/E parameter shifted slightly to higher values by $\sim 0.8\%$ within 70 minutes. After calibration, $\mu_{A/E}$ dropped to the normal value within a day. The time scale is short compared to the one week interval between calibration runs. The increase of $\mu_{A/E}$ during calibration is well described by a linear function. The short term drift correction was **only** applied on the calibration data.

The origin of the A/E drift over time is possibly due to the accumulation of electric charges from LAr on the detector groove surface. This phenomenon was observed in the GERDA Detector Laboratory (GDL) [45]. Also, pulse shape simulation results showed that extra space charges on the groove have considerable effect on the A/E PSD parameter [139].

4.2.2   Energy Dependence Normalization

Scatter plots of A/E versus E of the BEGe detectors after time drift normalization are shown in Fig. 4.5. A slight energy dependence of normalized A/E can be observed. The reason of the non-zero slope of A/E versus E might be due to the different size of charge clouds in the low and high energy region [2].

The dependence was determined by fitting a Gaussian with mean A/E to the SSE component in different energy bins in the ^{228}Th Compton continuum between 600 and 2300 keV [3]. The algorithm is listed as follows:

- Exclude peak regions.
  Since the $\mu_{A/E}$ values in the Compton and peak regions are different, 99.9 % of the peak area of every energy peak in the data was not considered in the procedure.

- Bin the data.
  Energy bin size was set to 5 keV for the calibration data.

- Project onto A/E-axis.

- Fit the A/E distribution on each energy bin using the function 4.2.

- Determine A/E peak positions.

---

[2]For high energy, the size of the charge cloud is bigger than that for lower energies. The drift time of charge carriers at high energy is longer, so the corresponding A/E has a smaller value.

[3]Due to the high contamination of the surface events from ^{39}Ar β decay ($T_{1/2}$=269 d, Q_{β^-}=565 keV, as mentioned in 3.3.2), the energy below 600 keV was not considered in the procedure.
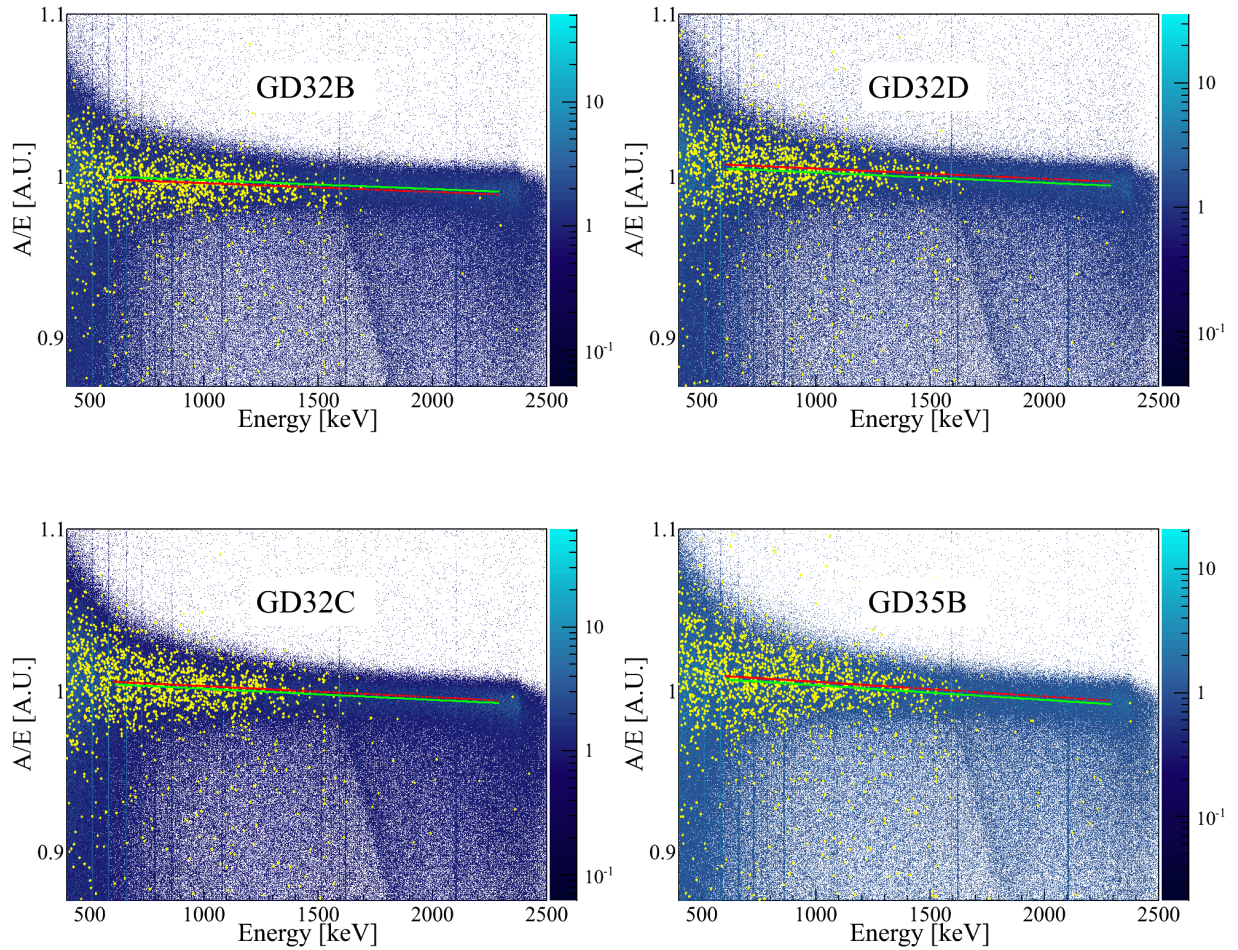
Figure 4.5: Scatter plots of A/E versus energy for each BEGe detector in Phase I. ^{228}Th calibration data are shown in blue. Background data (mainly from $2\nu\beta\beta$) are depicted with yellow points. The A/E energy dependence was determined by fitting a Gaussian with mean A/E of the SSE component at different energies in the ^{228}Th Compton continuum. The energy dependence can be well described by a linear function. The fitted functions are shown in green and red for the calibration and background data, respectively.

- The $\mu_{A/E}$ value as a function of energy, $\mu_{A/E}(E)$, can be well determined by a linear fit function $\eta + \lambda \cdot E$ [4]. Where η and λ are constants.

The scatter plot of A/E versus energy of the background data (dominated by events from $2\nu\beta\beta$ decay) is shown together with the calibration data in Fig. 4.5. Due to the limited statistics of the background data, the parameters used in the energy dependence procedure were slightly different than those used in the calibration data. The fit range

---

[4]If the fit function was chosen to include a quadratic term, its value (p2) was around 10^{-11} for each BEGe detector indicating a linear A/E energy dependence.

Detectors	Fitting results of $\mu_{A/E}(E)$ [A.U.]			
	η		λ (x10^{-7})	
	^{228}Th calibration	background data	^{228}Th calibration	background data
GD32B	1.0030±0.0001	1.0012±0.0005	-5.46±0.06	-5.46±0.06
GD32C	1.0081±0.0001	1.0097±0.0005	-6.86±0.05	-6.86±0.05
GD32D	1.0085±0.0001	1.0110±0.0006	-6.28±0.07	-6.28±0.07
GD35B	1.0124±0.0002	1.0145±0.0006	-9.02±0.09	-9.02±0.09

Table 4.1: Summary of the fit results for $\mu_{A/E}(E)$. The linear functions were fitted on the calibration and background data. The fit functions of background data were derived leaving the constant terms η free. The fit values, including the offset η and the slope λ, are presented with 1σ statistical uncertainties.

of the background data was from 600 keV to 1.4 MeV with 100 keV binning. For the determination of the A/E peak positions the $2\nu\beta\beta$ continuum was fitted with the same function, leaving the constant term η free (using λ from the calibration data). In the final step for the normalization, the BEGe data were normalized to the Gaussian mean of A/E of the DEP events.

4.2.3 Deviations Between the Background and the Calibration Data

For normalized data, the deviation of $\mu_{A/E}(E)$ between $2\nu\beta\beta$ events in the energy region 1.0-1.3 MeV and the SSEs of the calibration data, $\Delta\mu_{A/E}(2\nu\beta\beta, \text{ Compton})$, is defined as:

$$\Delta\mu_{A/E}(2\nu\beta\beta, \text{ Compton}) \equiv \mu_{A/E}(2\nu\beta\beta) - \mu_{A/E}(\text{Compton}). \tag{4.4}$$

$\Delta\mu_{A/E}(2\nu\beta\beta, \text{ Compton})$ was small compared to the width of the A/E SSE component, as shown in Table 4.2 [5]. Hence, $\mu_{A/E}(E)$ of the calibration and the background data are in agreement with each other. Similarly, deviation of $\mu_{A/E}(E)$ between $2\nu\beta\beta$ decay and DEP events from the calibration data can be defined as:

$$\Delta\mu_{A/E}(2\nu\beta\beta, \text{ DEP}) \equiv \mu_{A/E}(2\nu\beta\beta) - \mu_{A/E}(\text{DEP}). \tag{4.5}$$

$\Delta\mu_{A/E}(2\nu\beta\beta, \text{ DEP})$ was smaller than the width $\sigma_{A/E}(\text{Compton})$ as well. The deviations as reported were taken into account as systematic uncertainty in the determination of the $0\nu\beta\beta$ PSD cut efficiency.

---

[5] Due to different bin size, the values listed are slightly different than what has been quoted in [103]

Detector	$\Delta\mu_{A/E}(2\nu\beta\beta,\text{ DEP})$	$\Delta\mu_{A/E}(2\nu\beta\beta,\text{ Compton})$	$\sigma_{A/E}(2\nu\beta\beta)$	$\sigma_{A/E}(\text{Compton})$
	($\times10^{-2}$ [A.U.])		($\times10^{-2}$ [A.U.])	
GD32B	-0.20±0.06	-0.19±0.01	0.70±0.05	0.93±0.01
GD32C	0.18±0.09	0.16±0.01	0.74±0.07	0.95±0.01
GD32D	0.40±0.07	0.24±0.01	1.07±0.09	0.96±0.01
GD35B	0.28±0.06	0.22±0.02	0.79±0.05	1.10±0.01

Table 4.2: Comparison of the $\mu_{A/E}$ value and the A/E width of the SSE component from the normalized background data (1.0 - 1.3 MeV, dominated by $2\nu\beta\beta$ decay) and the normalized calibration data (1.0 - 1.3 MeV and the DEP events).

4.3 Application of PSD on the Phase I Background Data

4.3.1 PSD Cut Value Determination

The width of the A/E SSE component, $\sigma_{A/E}$, in the ^{228}Th Compton region versus energy using the fit function in formula 4.3 is shown in Fig. 4.6 for the BEGe detectors used in the analysis. The fit results of $\sigma_{A/E}(E)$ are summarized in Table 4.3. To determine the cut values, $\sigma_{A/E}(E)$ of the GD35B detector was used to make a global PSD cut. The choice is conservative since the detector had the largest $\sigma_{A/E}(E)$ value among the BEGe detectors.

The A/E cut value was chosen to optimize the sensitivity of the $0\nu\beta\beta$ analysis. A greater than ~99.99 % quantile of the A/E SSE component at DEP can be covered. By setting the cut position to $\sigma_{A/E}$=0.035 (i.e. in the range of $\mu_{A/E}$=1±0.035). The cut value together with its systematic uncertainty of the DEP events [6] is also shown in Fig. 4.6. It can be seen that by placing the cut position at $\sigma_{A/E}$=0.035, the energy dependence of the cut is negligible above ~1 MeV since the cut value is far away from the 99 % quantile of the A/E SSE component. For the same reason, the survival fraction after the PSD cut by the same cut value is essentially independent of energy above 1 MeV. Hence, a constant A/E cut at all energies is used. However, the cut is not valid below 1 MeV due to the increase of the A/E width of the SSE component. Therefore, the efficiency estimation is restricted to energies above 1 MeV.

4.3.2 Normalized Background Data and A/E PSD Cut

Fig. 4.7 shows the combined scatter plot of A/E versus energy for the normalized background data with 2.4 kg·yr exposure plus the acceptance of the PSD cut. The signal events are inside the horizontal A/E SSE band. The SSE band between 1 and 1.45 MeV is domi-

---

[6]The uncertainty for the cut position at DEP is mainly from the normalization procedure. The statistical uncertainty of the DEP events, $\frac{\sigma_{A/E}(DEP)}{\sqrt{N(DEP)}}$, is very small, about 0.2 % of the one at $\sigma_{A/E}$=0.035.

Detectors	Fitting results of $\sigma_{A/E}(E)$ [A.U.]	
	c_0	c_1 (x10^{-5})
GD32B	90.86±1.04	1.67±0.07
GD32C	106.70±1.18	0.93±0.07
GD32D	108.03±1.56	1.03±0.09
GD35B	139.13±2.29	1.52±0.14

Table 4.3: Summary of the fit results for $\sigma_{A/E}(E)$. The fit values are presented with 1σ uncertainty. The fit parameters, c_0 and c_1, correspond to the variables as defined in Eq.4.3.
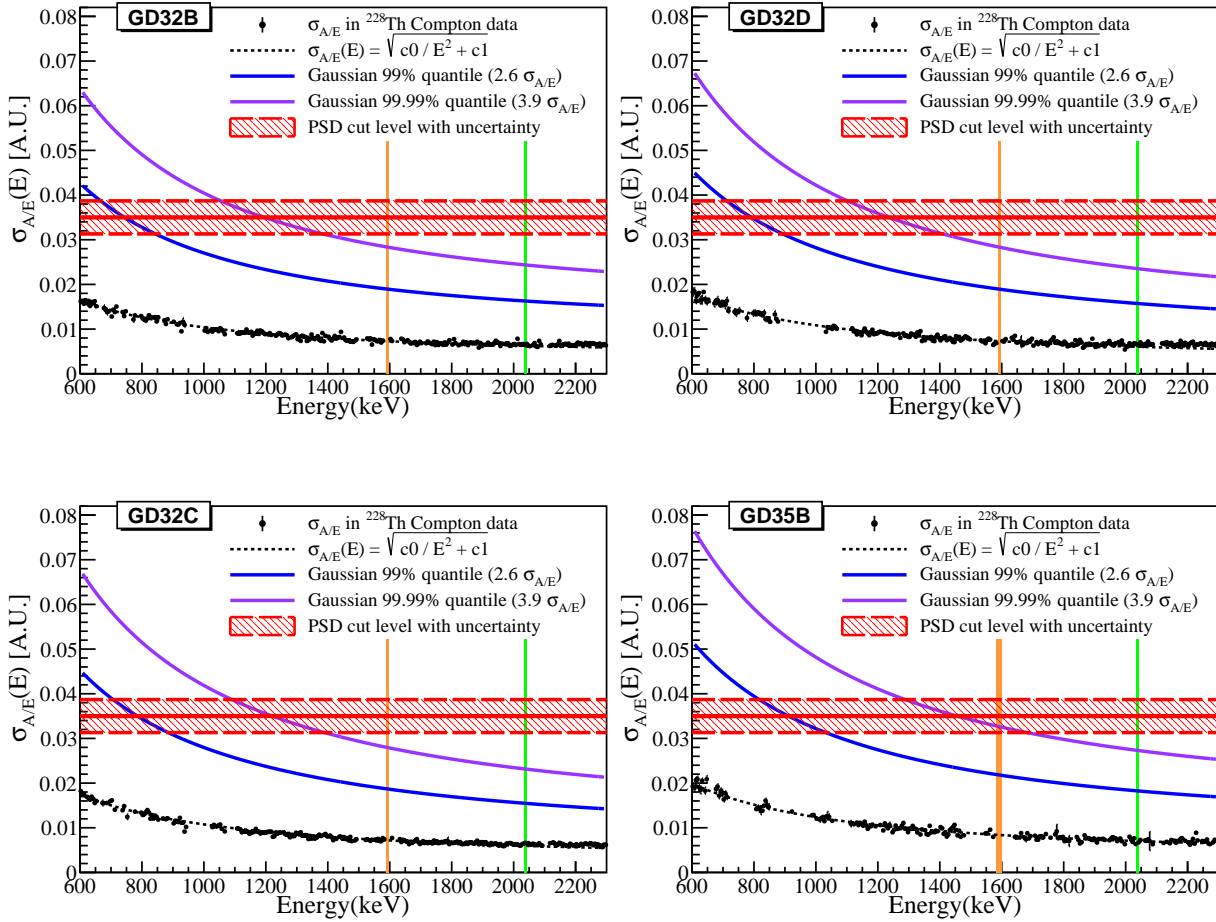
Figure 4.6: $\sigma_{A/E}$ in the Compton region versus energy for the BEGe detectors in Phase I. The data points were fitted using formula 4.3 (black dashed lines). The 99 % quantile of the Gaussians (2.6 $\sigma_{A/E}$) are shown in blue lines. The 3.9 $\sigma_{A/E}$ of the Gaussians (99.99 %) are shown in magenta lines. The red horizontal lines represent constant A/E cut values together with systematic uncertainties. Vertical lines are DEP ($E\pm2.5$ σ_E, shown with orange lines) and blinded regions (green lines).
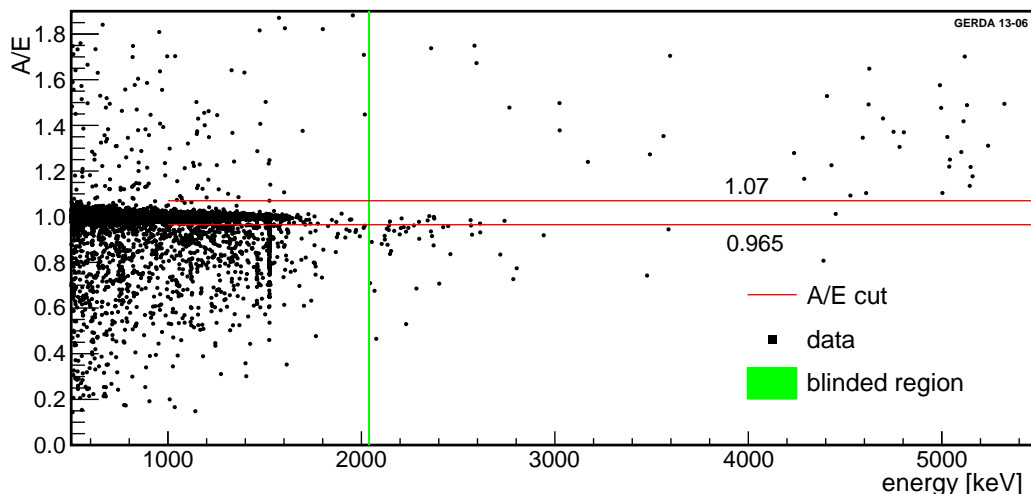
Figure 4.7: Scatter plot of A/E versus energy of the combined background data with 2.4 kg·yr exposure. Two horizontal red lines represent the low and high A/E cut. The blinded region is depicted by the green band. Taken from [103].

nated by events from $2\nu\beta\beta$ decay. Events below or above the SSE band are considered as background events. The vertical line structure at 1524.7 keV originates from the ^{42}K γ-line. As indicted by the Phase I background model, the events with energies above 4 MeV are mainly resulting from the decays of α-emitting isotopes around the p$^+$ electrode or groove surface. It is confirmed by this pulse shape analysis that the α-induced events occurred in the high A/E region, as shown in the top-right region in Fig. 4.7.

The cut value was designed to have high probability to have zero background events at $Q_{\beta\beta}$ (see Fig. 4.7) with high signal efficiency ($\geq 4.5 \ \sigma_{A/E}$ at $Q_{\beta\beta}$, as shown in Fig. 4.6). Background events can be rejected by A/E < 0.965 (low A/E cut, reject MSEs and n$^+$ surface events) and by A/E > 1.07 (high A/E cut, reject p$^+$ electrode events). Due to the much lower occurrence and the better separation of the p$^+$ electrode events in the A/E distribution, the width of the high A/E cut was set twice as wide as the low side one.

4.3.3 Survival Fractions After A/E PSD Cut

The survival fractions of various study samples after an A/E PSD cut are tabulated in Table 4.4. The survival fraction of the DEP events from the ^{228}Th calibration data was (93.1 ± 0.3) %. The suppression factors of MSE-dominant samples, FEP and SEP from the ^{228}Th calibration data, were better than 77 % and 82 %, respectively.

The suppression factor of the 1524.7 keV ^{42}K γ-line in the background data was in agreement with the one of the FEP at 1620.7 keV from ^{212}Bi of the ^{228}Th calibration data. α-induced p$^+$ surface candidates, 33 out of 35 events, were effectively vetoed by the high A/E cut. The background index at $Q_{\beta\beta}\pm200$ keV ($Q_{\beta\beta}\pm4$ keV excluded) of the combined background data with 2.4 kg·yr exposure after PSD cut was reduced from $(4.2\pm0.7)\times10^{-2}$

region	survival fraction (in %)		
	SSE acceptance 0.965<A/E<1.07	low A/E cut A/E<0.965	high A/E cut A/E>1.07
^{228}Th calibration			
DEP 1592.5 keV	93.1±0.3	5.4±0.3	1.5±0.1
FEP 1620.7 keV	22.0±0.8	77.1±0.8	0.9±0.2
SEP 2103.5 keV	16.5±0.5	82.5±0.5	1.1±0.1
background data			
FEP 1524.7 keV	29±5	69±5	2.7±1.5
1000-1450 keV	74.8±1.1	23.0±1.1	2.2±0.4
1839-2239 keV	7/40	30/40	3/40
>4 MeV (α at p+)	1/35	1/35	33/35

Table 4.4: Survival probabilities after low A/E cut, high A/E cut and SSE acceptance region of the combined background data and the total ^{228}Th calibration data. The physics data was with 2.4 kg·yr exposure. Table adopted from [103].

to $(0.7^{+0.4}_{-0.2}) \times 10^{-2}$ cts/(keV·kg·yr) , i.e. better than 80 % suppression. The events between 1 and 1.45 MeV are dominated by $2\nu\beta\beta$ decays. The energy region used to derive $2\nu\beta\beta$ efficiency excluded the peaks at 1461 keV γ-line from ^{40}K and 1525 keV γ-line from ^{42}K. The survival fraction in the interval of 1-1.45 MeV after the PSD cut was (74.8±1.1) % which can be used to cross check the $2\nu\beta\beta$ efficiency; details will be given in Section 4.3.4.

4.3.4 $0\nu\beta\beta$ Detection Efficiency of the Phase I BEGe Detectors

Estimation of $0\nu\beta\beta$ Detection Efficiency and its Systematics

As mentioned in Section 2.5.2, the topologies of $0\nu\beta\beta$ events and DEP events are slightly different. As a result the $0\nu\beta\beta$ events are expected to be homogeneously distributed in the detector volume, while DEP events have higher probabilities to be located close to the detector surfaces. The deviations in the A/E distribution of DEP events and $0\nu\beta\beta$ events was taken into account in the systematics. This systematic effect was studied by pulse shape simulation [106]. The derived survival fraction of $0\nu\beta\beta$ decay after the same PSD cut was 92 % [7].

The total systematic uncertainty of the $0\nu\beta\beta$ event detection efficiency was derived by combination of the individual contributions in quadrature:

- systematic uncertainty due to the difference between the survival fraction from the simulated $0\nu\beta\beta$ decay and the one from measured DEP events: ±1.8 % (dominant

---

[7]The influence of the transition layer on the A/E distribution for simulated $0\nu\beta\beta$ events was considered already. The survival fractions in the low A/E region (A/E<0.965) for the DEP events and the $0\nu\beta\beta$ events are equivalent within uncertainties. The rejected fraction by low A/E cut was 5.4 %. The removed fraction of simulated $0\nu\beta\beta$ events by high A/E cut (A/E>1.07) was 2.5 %.

contribution)

- uncertainty due to the difference in $\mu_{A/E}$ between the background and the calibration data: $\pm 0.4\,\%$

- statistical uncertainty of the DEP survival fraction (in Table 4.4): $\pm 0.3\,\%$

- uncertainty from the A/E energy dependence normalization: $\pm 0.008\,\%$

Therefore the $0\nu\beta\beta$ signal detection efficiency, $\epsilon_{0\nu\beta\beta}=(92\pm2)\,\%$ was derived.

Cross Check with the $2\nu\beta\beta$ Detection Efficiency

The derived $\epsilon_{0\nu\beta\beta}$ can be cross checked with the survival fraction of $2\nu\beta\beta$ events after the PSD cut between 1 and 1.45 MeV, $\epsilon_{2\nu\beta\beta}$. By knowing the fraction of each background component and the survival fraction after PSD cut in this energy region, $\epsilon_{2\nu\beta\beta}$ can be estimated accordingly. $\epsilon_{2\nu\beta\beta}$ can be formulated as:

$$\epsilon_{2\nu\beta\beta} = \frac{1}{f_{2\nu\beta\beta}} \cdot \left(\epsilon_{data} - \sum_i f_i \cdot \epsilon_i \right). \qquad (4.6)$$

where:
$\epsilon_{2\nu\beta\beta}$: survival fraction after the PSD cut of $2\nu\beta\beta$ events between 1 and 1.45 MeV.
$f_{2\nu\beta\beta}$: fraction of $2\nu\beta\beta$ events in the spectrum between 1 and 1.45 MeV.
ϵ_{data}: survival fraction after PSD cut between 1 and 1.45 MeV.
f_i, ϵ_i: fraction and survival fraction after PSD cut of the individual background component (listed in Table 4.5) between 1 and 1.45 MeV, respectively.

The value of $f_{2\nu\beta\beta}$ was $(66\pm3)\,\%$, derived from the Phase I background model [46]. The f_i together with ϵ_i were listed in Table 4.5. $\epsilon_{2\nu\beta\beta}=(90\pm5)\,\%$ was hence calculated. However, the $\epsilon_{2\nu\beta\beta}$ derived from Eq.4.6 did not fold in the effect of the transition layer. By taking into account this effect, the $\epsilon_{2\nu\beta\beta}$ was scaled by a factor of 0.985. Hence, the estimated $\epsilon_{2\nu\beta\beta}$ was $(91\pm5)\,\%$, and agrees well with $\epsilon_{0\nu\beta\beta}$.

4.3.5 Background at $Q_{\beta\beta}\pm200$ keV

Fig. 4.8 shows the observed A/E distribution of the background data at $Q_{\beta\beta}\pm200\,\text{keV}$ together with distributions from different background sources. The background data shows a peak at about 0.94, which is consistent with the simulated A/E distribution from ^{42}K decays close to the n$^+$ surface. This confirms the result of the Phase I background model that the dominant background of the BEGe detectors at $Q_{\beta\beta}$ comes from ^{42}K decaying on the n$^+$ surface. Compared to signal events, n$^+$ surface events have a lower A/E value and can be rejected efficiently by a low A/E cut. The remaining distribution is consistent within statistical uncertainty with the ones from other expected background sources.

component	f_i	ϵ_i
^{40}K	3.2±0.9	56±3
^{42}K in LAr	18.7±2.2	49±5
^{42}K at n$^+$ surface	3.0±1.7	30±4
^{60}Co	1.3±1.3	29±2
^{60}Co intrinsic	0.2±0.1	21±2
^{68}Ga intrinsic	0.7±0.7	33±2
^{214}Bi	3.6±1.4	41±2
^{228}Th	0.3±0.2	54±3
p$^+$ events	0.3±0.2	2±2
other	2.4±2.4	45±45

Table 4.5: Background decompositions and their survival fraction (in %) after the PSD cut between 1 and 1.45 MeV. The fraction of each component f_i and its PSD survival fraction ϵ_i. Table adopted from [103].
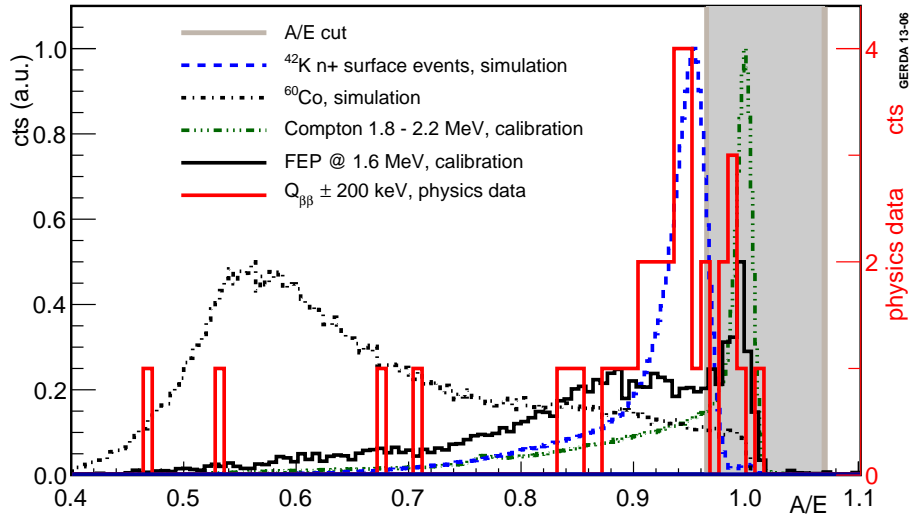
Figure 4.8: The observed A/E distribution of the background data at $Q_{\beta\beta}\pm200$ keV (red histogram). The dominant contribution is consistent with the A/E distribution of the expected background source from ^{42}K decaying on the n$^+$ surface (blue histogram, generated from simulation). The grey region shows the acceptance of the PSD cut. The n$^+$ surface events can be rejected efficiently by the low A/E cut. The remaining distribution is consistent with the other expected background sources. Adopted from [103].

4.4   Summary on the PSD of the BEGe Detectors

The experimental sensitivity of germanium detectors can be improved by analyzing the detector pulse shapes. BEGe detectors have enhanced signal recognition efficiency and thus the suppression factor of background events can be significantly improved with respect to closed-end HPGe detectors.

A single-parametric A/E method, the ratio of maximum amplitude of current pulse over the energy of the charge pulse, was performed for GERDA Phase I BEGe PSD analysis. The BEGe detectors were calibrated using ^{228}Th sources every one or two weeks to have quality control of the PSD performance. The A/E parameter has been observed to have time and energy dependence in Phase I. A normalization procedure was implemented to correct for these dependencies. The method was shown to be achievable.

The determined A/E PSD cut rejects about 80 % of the background events at $(Q_{\beta\beta}\pm200)$ keV with a $0\nu\beta\beta$ signal detection efficiency of (92 ± 2) %. The $2\nu\beta\beta$ signal detection efficiency was shown to be (91 ± 5) %, which is in good agreement with the derived $0\nu\beta\beta$ efficiency. The background index after applying the A/E PSD cut is reduced to $(7^{+4}_{-2})\cdot10^{-3}$ cts/(keV·kg·yr) with a total exposure of 2.4 kg·yr in Phase I. The dominant A/E distribution at $(Q_{\beta\beta}\pm200)$ keV in the observed spectra is consistent with the expected A/E distribution from ^{42}K decayed on the n$^+$ surface as predicted from the Phase I background model.

Chapter 5

Investigation of PSD Methods on Phase I data

The A/E method used for the BEGe detectors is based on the maximum of the current pulse amplitude normalized to the amplitude of the charge pulse. It is hence sensitive to the amplitude-to-noise ratio. In GERDA Phase I, the distance between the preamp and DAQ is about 10 m. The additional noise fluctuations induced by the extra length reduce the signal-to-noise ratio. Hence, the performance of the pulse shape discrimination method is deteriorated. In order to enhance the signal recognition efficiency, a systematic study of the Phase I MA filters was performed. The performance of a wavelet de-noising technique applied to Phase I calibration data will be discussed.

5.1 Systematic studies on Phase I MA Filter

In previous Phase I analysis, the window size of the MA filter, Δt_{MA}, for smoothing the charge pulses was set to 50 ns [93, 103, 106]. Δt_{MA}=50 ns was used for the digital signal processing of Phase I BEGe detectors. While the performance of PSD with this window size proved to be good, no systematic study of the optimal window size has been performed. In this analysis a systematic study of the effect of the window size on the PSD performance is done in order to determine the optimal MA filters for the Phase I BEGe data set.

5.1.1 MA Filter Survey in a Small Scale

In order to verify that the choice of Δt_{MA} can have a significant effect, a quick analysis was performed, using a small data sample (GD76C BEGe detector, data taking using ^{228}Th source) from the HADES underground facility [141].

The standard GERDA algorithm used to derive the amplitude from the current pulse and the energy from the charge pulse discussed in Section 4.1.2 and Section 4.1.1 was used.

A flow chart of the analysis steps is shown in Fig. 5.1. The main processes are:

(A) derivation of the A/E distribution,

(B) normalization the A/E distribution,

(C) comparison of the filter performance.

The first process is the derivation of the A/E distributions by applying MA filters with different window sizes. The steps to derived the maximum amplitude of the current pulses were carried out as follows:

(a) set filter parameters,

(b) calculate current pulses after filter,

(c) derive maximum amplitudes of the current pulses.

The raw charge pulse is smoothed by applying MA filter with N ns window size recursively by 3 times. The current pulse is derived by 10 ns differentiation of the charge pulse. The maximum amplitude of the current pulse can be derived. The calculation is done event-by-event. Δt_{MA} is scanned from 10 ns to 400 ns, where the default size is 50 ns.

The second process is E-dependence normalization, refer to Section 4.2.2 for details. The last process is the evaluation of the filter performances. A standard GERDA figure of merit (FOM) has been used to determine the performance of the filters. A constant A/E cut is applied where the cut value is determined by fixing 90% of the events in the Compton background subtracted DEP. The FOM of each filter parameter is calculated by evaluating the rejected fraction of the FEP events (2103.5 keV) after the A/E PSD cut.

The rejected fraction of the FEP events as a function of Δt_{MA} is shown in Fig. 5.3. Note that the uncertainties are highly correlated. As the window size increases beyond 50 ns, the PSD power to the background events decreases. It should be noted that the FWHM of the A/E distribution can be improved significantly by increasing Δt_{MA} (see Fig. 5.2). Even though increasing Δt_{MA} can improve the A/E resolution significantly, the details of the current pulse also disappear leading to a degradation of the PSD rejection power. The optimal window size in this small data set as shown in Fig. 5.3 is 50 ns. Scanning within a range of 100 ns should be able to determine the optimal Δt_{MA} for the total Phase I BEGe data.
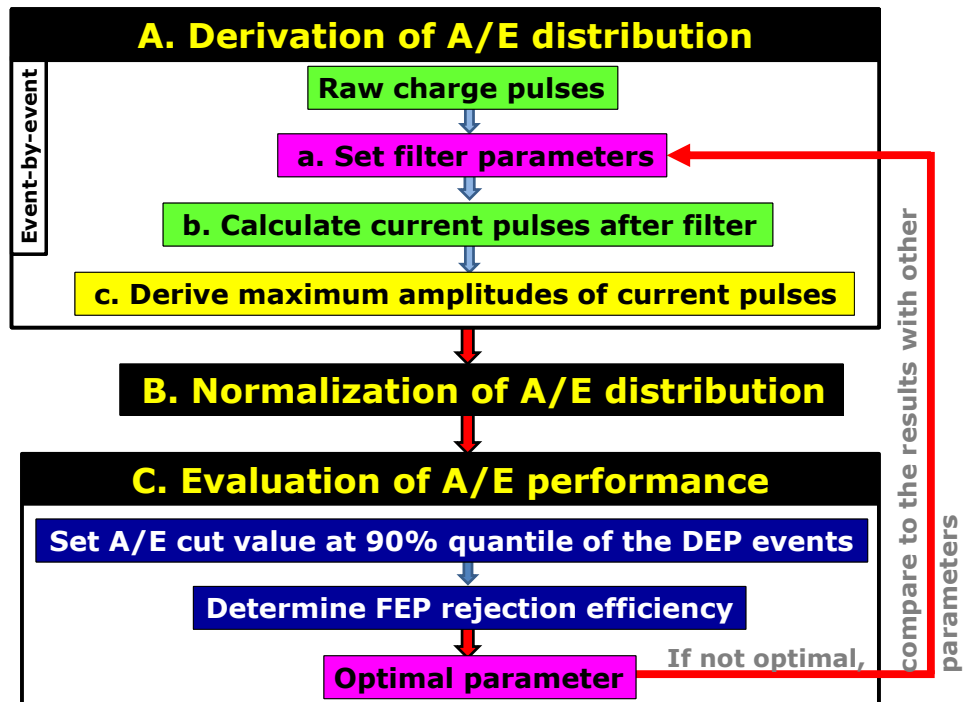
Figure 5.1: Flow chart of the filter optimization.
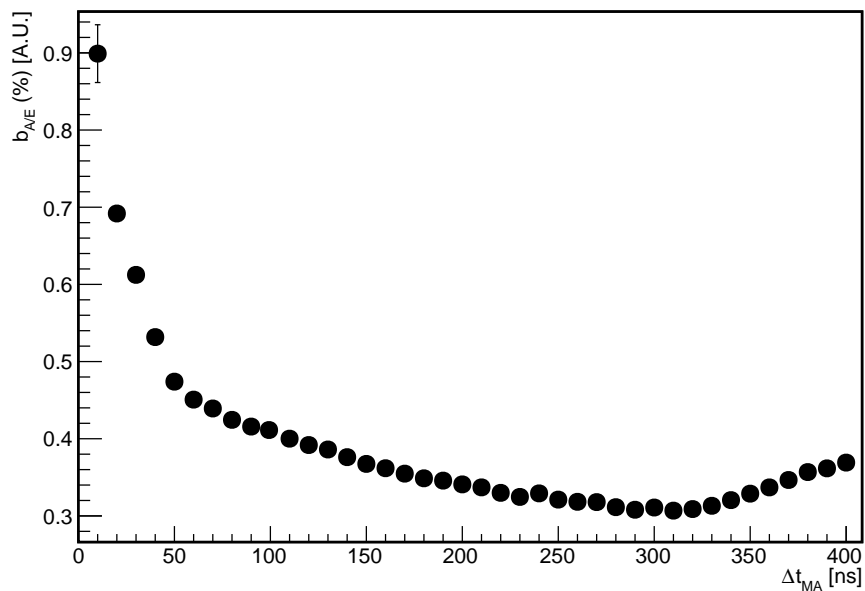
Figure 5.2: $b_{A/E}$ at 1593 keV as a function of Δt_{MA}.
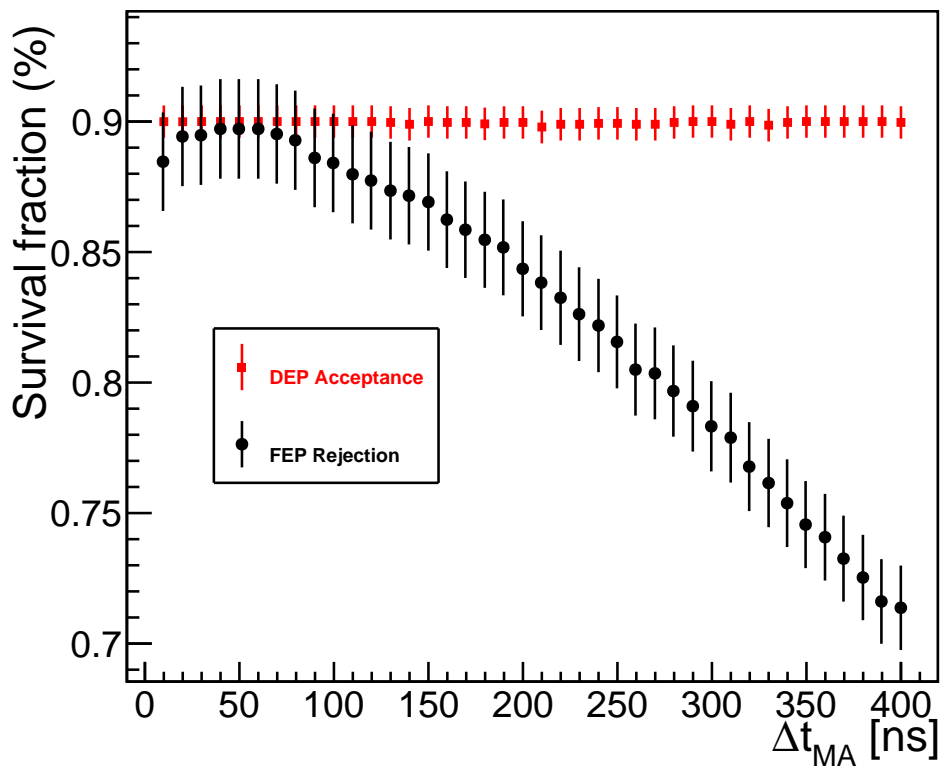
Figure 5.3: The rejected fraction of FEP after PSD as a function of Δt_{MA}. The A/E cut positions are always set at the 90 % quantile of the DEP events.

5.1.2 Phase I Normalization Procedure for MA Filters

As discussed in Chapter 4, the A/E parameter in Phase I exhibits both time and energy dependencies. A normalization procedure is necessary to correct for these dependencies. In order to compare the performance of BEGe detectors using MA filters with different window sizes, the normalization procedure is performed.

Long Term Drift Correction

In order to increase the statistics for the correction, the SSE events between 600 keV and 2.3 MeV (excluding peaks) are used [1]. The stabilities of η and λ of the A/E-versus-E as a function of time, using MA filter with different window sizes, are shown in Fig. 5.4 and Fig. 5.5, respectively. The descriptions of parameters, refer to Section 4.2.2 for details. The time dependences of the η values ($\eta(t)$) and the λ values ($\lambda(t)$) of all the data points can be parametrized using the fit functions shown in Fig. 5.4 and Fig. 5.5. The A/E value can be normalized by dividing $\eta(t)$.

Short Term Drift Correction

The SSE events between 1.0 and 1.5 MeV are used for the correction. The $\mu_{A/E}$ values of the SSE events in 1.0-1.5 MeV after applying different MA filters, since the beginning of the calibration runs, are shown in Fig. 5.6. The normalized A/E for the short term drift correction is defined as follows:

$$\begin{cases} \dfrac{A/E}{\eta_b + \lambda_b \cdot t} \cdot \eta_b & t < T_c \\ \dfrac{A/E}{\eta_a} \cdot \eta_b & t \geq T_c. \end{cases} \tag{5.1}$$

where:
t: time since the beginning of the calibration.
T_c: time when the A/E value stabilizes.
λ_b, η_b: slope and offset of the linear fit of $\mu_{A/E}$ for $t < T_c$.
η_a: constant fit of $\mu_{A/E}$ for $t \geq T_c$.

---

[1]The ratio of the number of DEP events, the events between 1.0-1.3 MeV, and the events in 600-2300 keV (excluding peaks) is about 1:10:50.
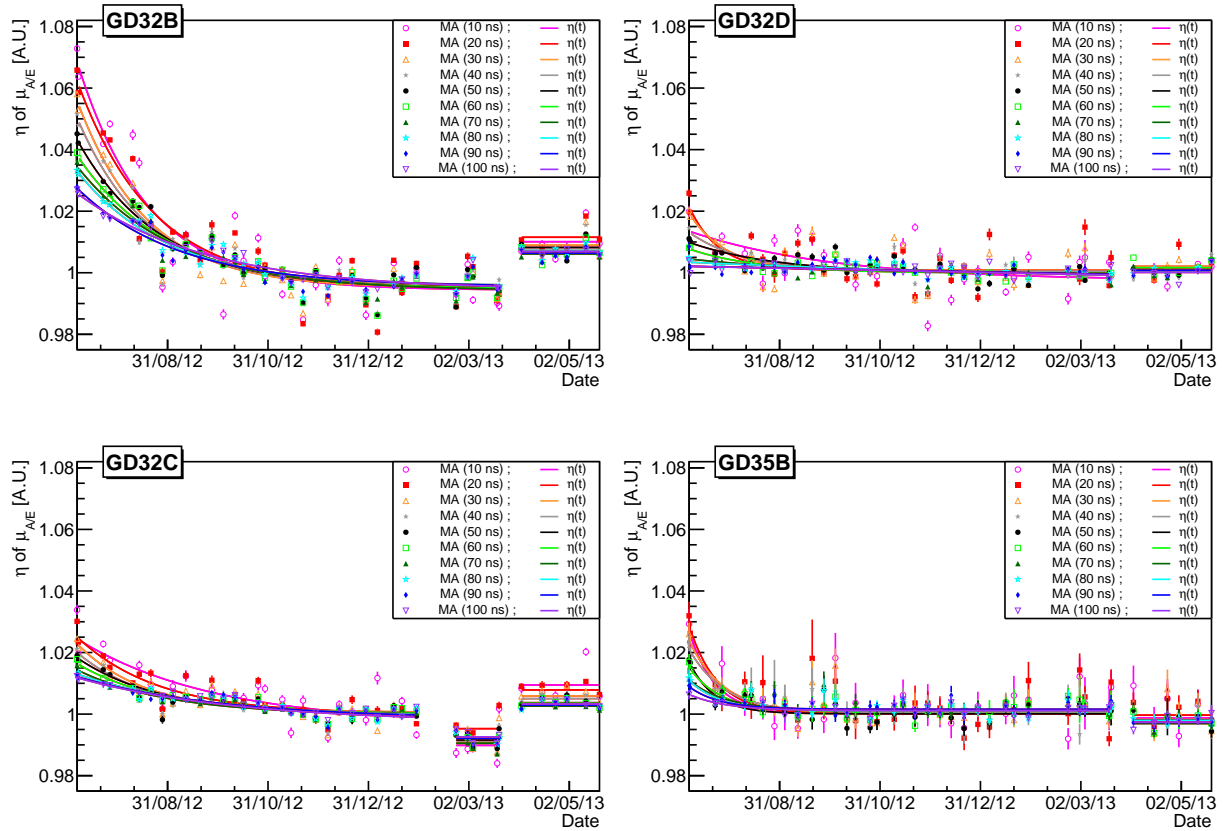
Figure 5.4: Offset of $\mu_{A/E}$ as a function of time by applying different MA filters. The proxy to derive $\mu_{A/E}$ is from the SSE events between 600 and 2300 keV, excluding peaks. The window size of the MA filter is scanned from 10 ns to 100 ns.

The T_c is 70 min for all the detectors, except for GD32D where T_c=130 min. The additional short term drift correction for $t \geq T_c$ has not been applied before. It can slightly improve the A/E resolution by about 1-3 % in this step compared to the standard Phase I normalization algorithm.

Fig. 5.7 demonstrates an example of the A/E distributions with Δt_{MA}=50 ns between 1 and 1.3 MeV for the GD32B before and after the time dependent correction.
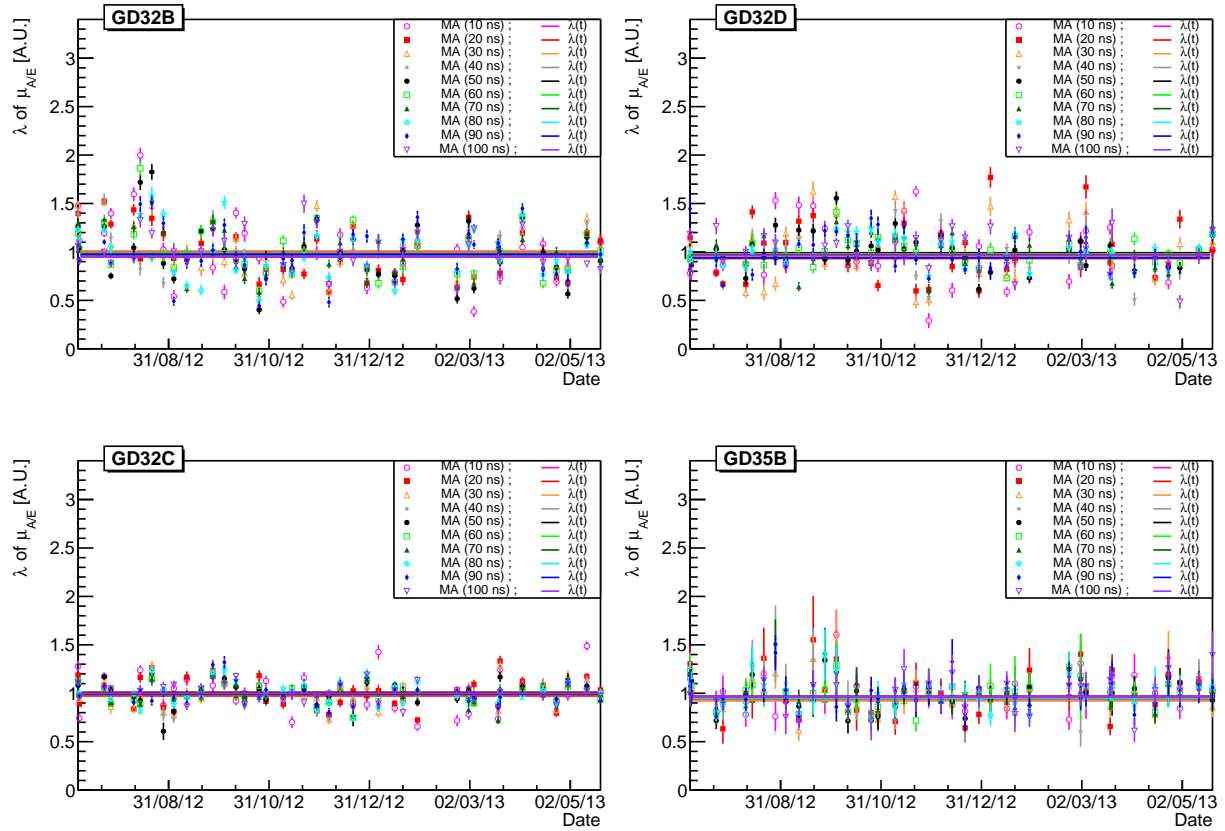
Figure 5.5: Slope of $\mu_{A/E}$ versus time with different MA filters. The proxy to derive $\mu_{A/E}$ is from the SSE events between 600 and 2300 keV, excluding peaks. The window size of the MA filter is scanned from 10 ns to 100 ns.
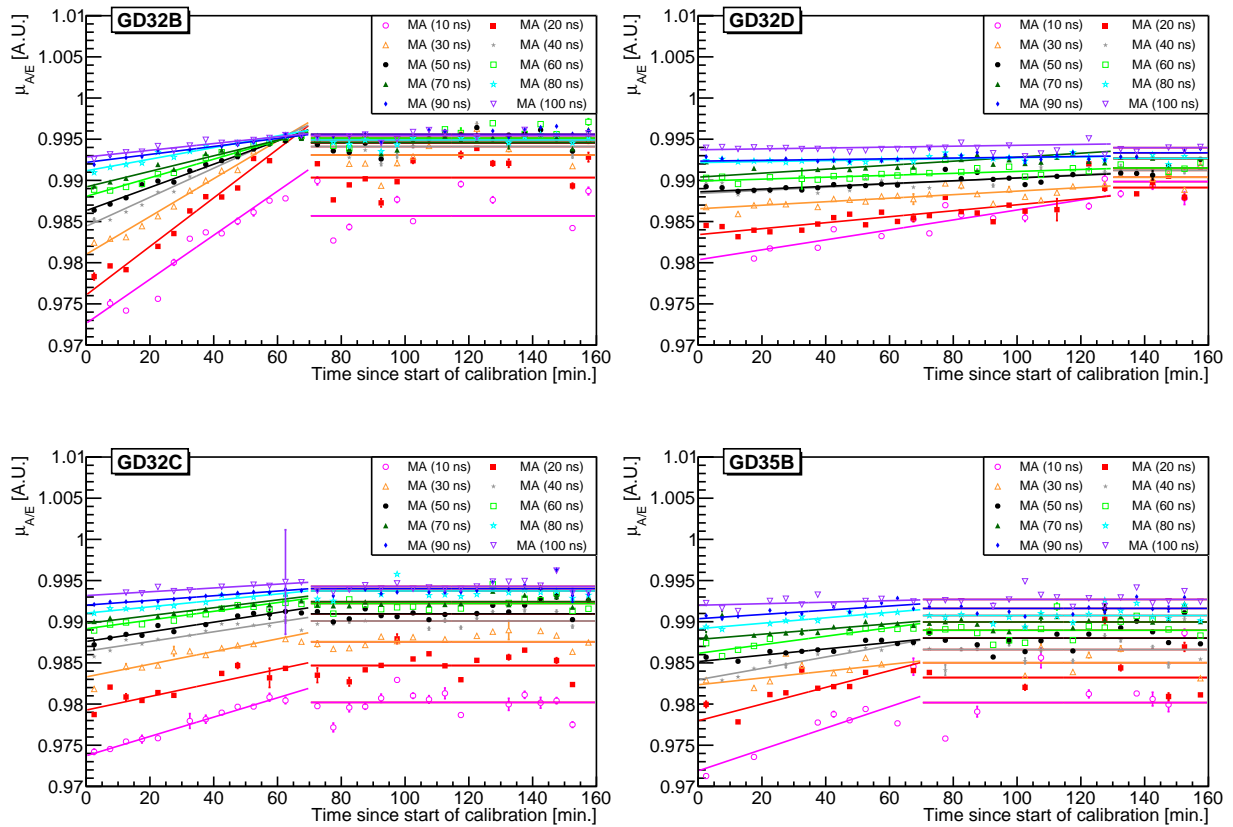
Figure 5.6: $\mu_{A/E}$ as a function of time for different MA filters. The proxy to derive $\mu_{A/E}$ is from the SSE events between 1.0 and 1.5 MeV, excluding peaks.
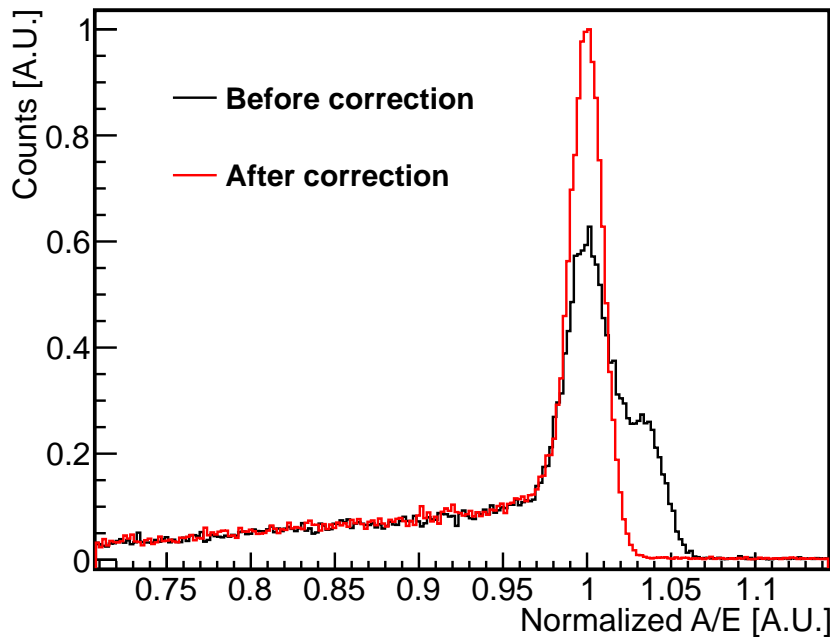
Figure 5.7: A/E distributions in the 1-1.3 MeV range before (black) and after (red) time dependency correction for GD32B detector. The distributions have been normalized with respect to the $\mu_{A/E}$ value. A Δt_{MA}=50 ns is used.

Energy Dependence Correction

Fig. 5.8 shows the scatter plots of the normalized A/E versus energy distributions of both the calibration and the background data applying MA filters with different lengths, for the GD32D. The E-dependent normalizations of the other BEGes are shown in Appendix A.

Fig. 5.9 shows the $\sigma_{A/E}$ as a function of energy using MA filters with different window sizes. It can be observed that:

- larger Δt_{MA} have better A/E resolution,

- A/E resolution improves as energy increases,

- the normalization scheme has similar performance compared to the standard Phase I normalization.

Nevertheless, one should note that a long window size reduces the PSD recognition efficiencies for the signal-like and the background-like events due to the degradation of the PSD performance, as shown in 5.3.
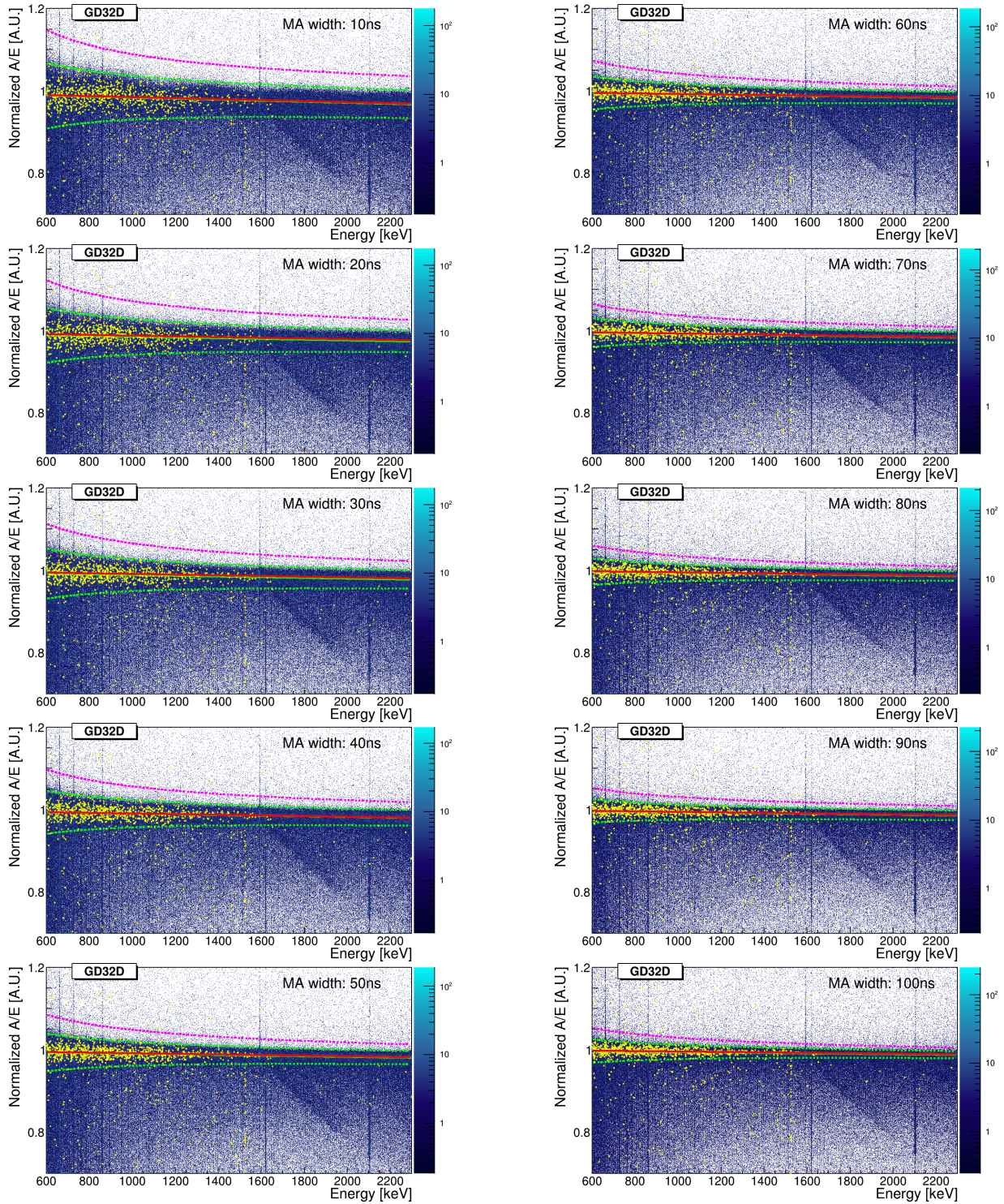
Figure 5.8: Scatter plots of the normalized A/E versus E for the GD32D detector after applying MA filters with different window sizes. Each figure shows the ^{228}Th calibration data (blue) and the background data (yellow) with the linear fits for the energy dependence correction (green line for calibration data and red line for the background data). The green and pink dash-lines represent the cut values in $\mu_{A/E} \pm 2.6\ \sigma_{A/E}$ and $\mu_{A/E} + 5.2\ \sigma_{A/E}$, respectively.
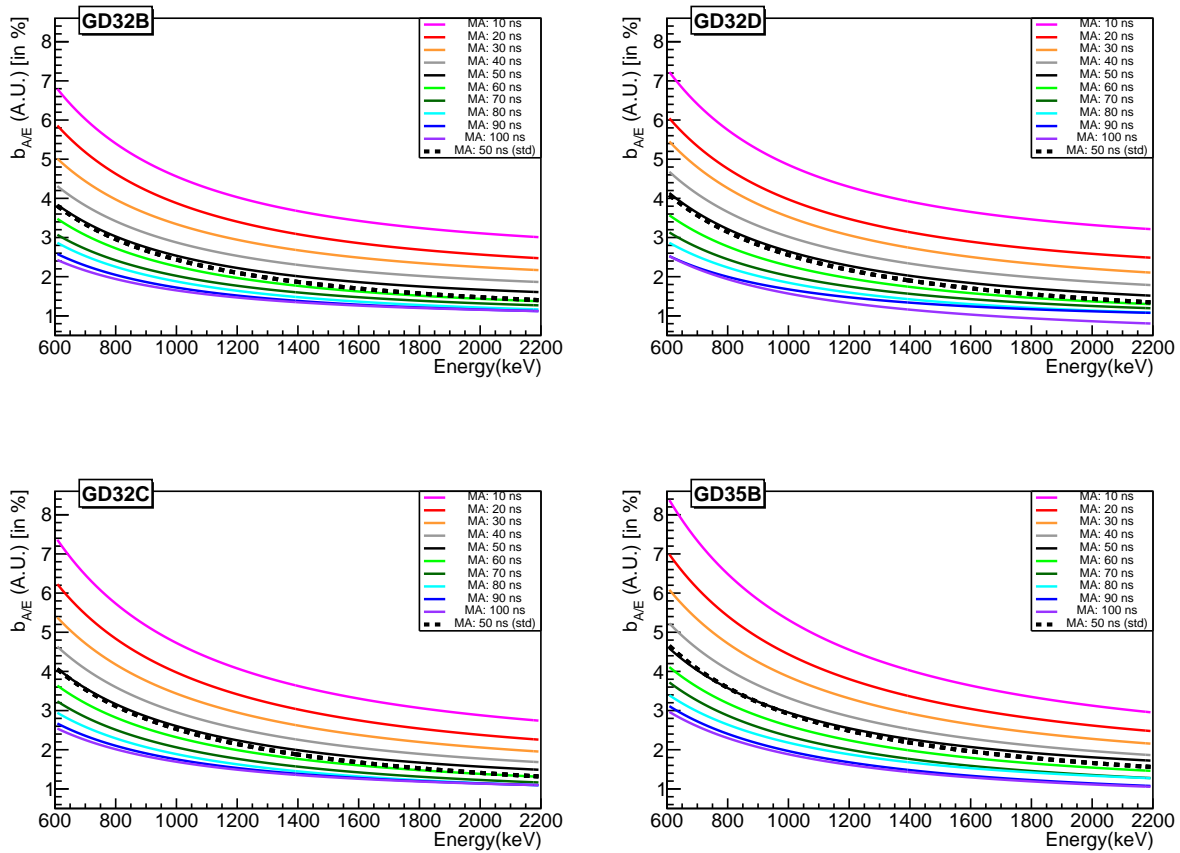
Figure 5.9: $b_{A/E}$ of the individual BEGe detectors as a function of energy for MA filters with different lengths.

5.1.3   Survival Fractions after A/E PSD using MA Filters

Three regions are defined for each BEGe detector after the energy dependent PSD cut : the high (hAE), the SSE (sAE), and the low A/E region (lAE). The cut regions are defined as (also see Fig. 5.8):

$$
\begin{cases}
\mu_{A/E} \geq 1 + 2 \cdot \sigma_{A/E} & \text{high A/E region (hAE)} \\
\mu_{A/E} \leq 1 - \sigma_{A/E} & \text{low A/E region (lAE)} \\
\text{else} & \text{SSE region (sAE)}
\end{cases}
\tag{5.2}
$$

Due to the lower occurrence of events close to the p^+ electrode and the resulting lower statistics hence higher uncertainty, the cut value at hAE region is set twice as wide as the one from the lAE region. The survival fractions after the E-dependent PSD cut, using the combined calibration data, as a function of MA window length are listed in Table 5.1. The results of the combined background data are listed in Table 5.2.

The systematic uncertainties of the survival fractions after E-dependent PSD cuts come from:

- uncertainty due to the A/E normalization procedure (dominant contribution),

- uncertainty due to the A/E cut values.
  The uncertainty due to the A/E cut value is less than about 0.5% compared to the uncertainty from the A/E normalization (hence negligible).

As listed in Table 5.1 and Table 5.2, the main contribution to the total uncertainty arises from the statistical uncertainty.

Fig. 5.10(a) shows the survival fractions from calibrations of DEP (1592.5 keV), FEP (1620.7 keV), and SEP (2103.5 keV) in the sAE region as a function of Δt_{MA}. ϵ_{DEP}^{sAE}, ϵ_{SEP}^{sAE}, and ϵ_{FEP}^{sAE} stand for the survival fraction of the DEP, SEP, and FEP events in the sAE region, respectively. Similarly, ϵ_{DEP}^{lAE}, ϵ_{SEP}^{lAE}, and ϵ_{FEP}^{lAE} represent the survival fraction of the DEP, SEP, and FEP events in the sAE region, correspondingly. The DEP events are mostly SSEs, the survival fractions in the sAE region are about 92% and the survival fraction as a function of Δt_{MA} is flat. As the window size is increased, the survival fractions of FEP and SEP in the sAE region increase by about 3%. In the lAE region, the survival fractions of FEP and SEP decrease also about 3% as the window size is increased, as shown in Fig. 5.10(b). It is evident that the background-like events leak to the signal region as the window size increases. From calibration data, a clear trend can be seen. The optimal MA window size ranges between $\sim$20 ns and 60 ns.

Fig. 5.10(c) shows the survival fractions of the signal-like events in background data between 1 and 1.45 MeV (dominated by the $2\nu\beta\beta$ decay), and the background-like events at 1524.7 keV γ-line (mainly from ^{42}K FEP) in the sAE region. Fig. 5.10(d) shows the survival fractions in the $Q_{\beta\beta}\pm200$ keV region and the region above 4 MeV (dominated by

the α-induced events) in the sAE region. Due to the limited statistics of the background data, it is not possible to determine the optimal window size of the MA filter.
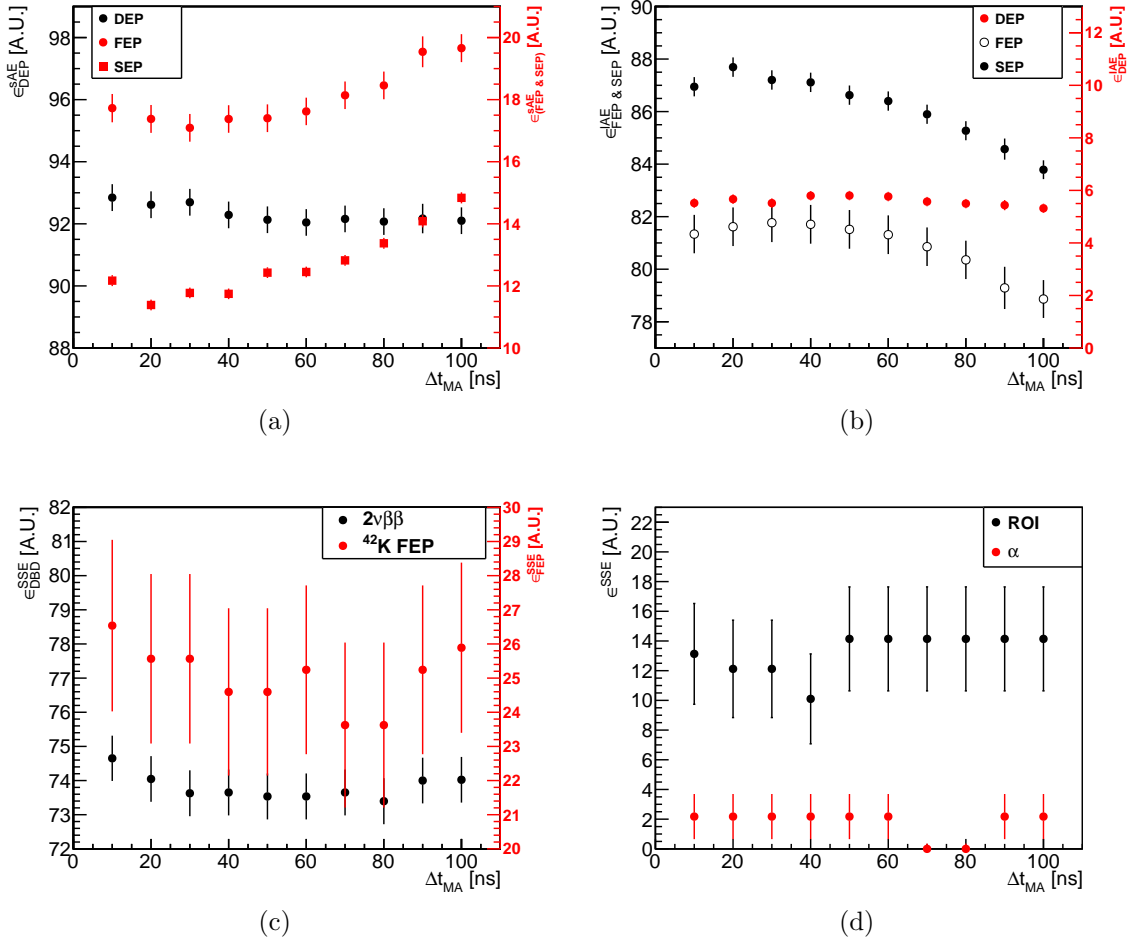
Figure 5.10: (a) Survival fractions of DEP, FEP and SEP in the sAE region as a function of MA window size. (b) Survival fractions of DEP, FEP and SEP in the lAE region as a function of Δt_{MA}. (c) Survival fractions in the sAE region of the background events from $2\nu\beta\beta$ dominated region (1.0-1.45 MeV) and at 1524.7 keV γ-line (contributed from ^{42}K decay) as a function of Δt_{MA}. (d) Survival fractions in the sAE region of the background events in the $Q_{\beta\beta}\pm200$ keV region (ROI) and >4 MeV region (dominated by the α events) against Δt_{MA}. Note that the uncertainties are highly correlated.

cut	proxy	Window length of Moving Averaging Filter [ns]									
		10	20	30	40	50	60	70	80	90	100
lAE	DEP	$5.52^{\pm0.18}_{\pm0.02}$	$5.67^{\pm0.18}_{\pm0.02}$	$5.52^{\pm0.18}_{\pm0.01}$	$5.80^{\pm0.18}_{\pm0.01}$	$5.80^{\pm0.18}_{\pm0.01}$	$5.77^{\pm0.18}_{\pm0.01}$	$5.57^{\pm0.18}_{\pm0.01}$	$5.50^{\pm0.18}_{\pm0.02}$	$5.44^{\pm0.19}_{\pm0.02}$	$5.32^{\pm0.18}_{\pm0.02}$
	FEP	$81.34^{\pm0.73}_{\pm0.06}$	$81.62^{\pm0.73}_{\pm0.04}$	$81.77^{\pm0.74}_{\pm0.03}$	$81.71^{\pm0.74}_{\pm0.03}$	$81.52^{\pm0.74}_{\pm0.04}$	$81.31^{\pm0.74}_{\pm0.03}$	$80.86^{\pm0.73}_{\pm0.04}$	$80.35^{\pm0.73}_{\pm0.05}$	$79.29^{\pm0.80}_{\pm0.08}$	$78.86^{\pm0.72}_{\pm0.08}$
	SEP	$86.95^{\pm0.37}_{\pm0.04}$	$87.69^{\pm0.37}_{\pm0.03}$	$87.20^{\pm0.37}_{\pm0.02}$	$87.11^{\pm0.37}_{\pm0.02}$	$86.63^{\pm0.37}_{\pm0.02}$	$86.40^{\pm0.37}_{\pm0.02}$	$85.90^{\pm0.37}_{\pm0.02}$	$85.27^{\pm0.36}_{\pm0.03}$	$84.57^{\pm0.40}_{\pm0.05}$	$83.79^{\pm0.36}_{\pm0.04}$
sAE	DEP	$92.84^{\pm0.43}_{\pm0.02}$	$92.61^{\pm0.43}_{\pm0.02}$	$92.69^{\pm0.43}_{\pm0.01}$	$92.29^{\pm0.43}_{\pm0.01}$	$92.13^{\pm0.43}_{\pm0.01}$	$92.04^{\pm0.43}_{\pm0.01}$	$92.16^{\pm0.43}_{\pm0.01}$	$92.07^{\pm0.43}_{\pm0.02}$	$92.17^{\pm0.47}_{\pm0.02}$	$92.10^{\pm0.43}_{\pm0.03}$
	FEP	$17.73^{\pm0.46}_{\pm0.06}$	$17.38^{\pm0.45}_{\pm0.04}$	$17.09^{\pm0.45}_{\pm0.03}$	$17.38^{\pm0.44}_{\pm0.03}$	$17.40^{\pm0.45}_{\pm0.04}$	$17.62^{\pm0.44}_{\pm0.03}$	$18.14^{\pm0.44}_{\pm0.04}$	$18.46^{\pm0.45}_{\pm0.05}$	$19.54^{\pm0.50}_{\pm0.08}$	$19.66^{\pm0.45}_{\pm0.08}$
	SEP	$12.17^{\pm0.18}_{\pm0.04}$	$11.39^{\pm0.17}_{\pm0.03}$	$11.77^{\pm0.17}_{\pm0.02}$	$11.74^{\pm0.17}_{\pm0.02}$	$12.43^{\pm0.17}_{\pm0.02}$	$12.45^{\pm0.17}_{\pm0.02}$	$12.82^{\pm0.17}_{\pm0.02}$	$13.37^{\pm0.17}_{\pm0.03}$	$14.08^{\pm0.20}_{\pm0.05}$	$14.84^{\pm0.18}_{\pm0.04}$
hAE	DEP	$1.64^{\pm0.041}_{\pm0.010}$	$1.72^{\pm0.042}_{\pm0.002}$	$1.79^{\pm0.044}_{\pm0.006}$	$1.92^{\pm0.045}_{\pm0.005}$	$2.07^{\pm0.046}_{\pm0.003}$	$2.19^{\pm0.048}_{\pm0.007}$	$2.27^{\pm0.049}_{\pm0.003}$	$2.43^{\pm0.050}_{\pm0.009}$	$2.39^{\pm0.056}_{\pm0.012}$	$2.58^{\pm0.052}_{\pm0.013}$
	FEP	$0.94^{\pm0.075}_{\pm0.009}$	$1.00^{\pm0.089}_{\pm0.007}$	$1.14^{\pm0.091}_{\pm0.005}$	$0.91^{\pm0.093}_{\pm0.011}$	$1.08^{\pm0.085}_{\pm0.002}$	$1.07^{\pm0.098}_{\pm0.003}$	$1.00^{\pm0.099}_{\pm0.006}$	$1.19^{\pm0.101}_{\pm0.009}$	$1.17^{\pm0.114}_{\pm0.013}$	$1.48^{\pm0.106}_{\pm0.014}$
	SEP	$0.88^{\pm0.034}_{\pm0.001}$	$0.92^{\pm0.035}_{\pm0.005}$	$1.02^{\pm0.040}_{\pm0.003}$	$1.14^{\pm0.041}_{\pm0.001}$	$0.95^{\pm0.038}_{\pm0.003}$	$1.15^{\pm0.042}_{\pm0.002}$	$1.28^{\pm0.043}_{\pm0.002}$	$1.36^{\pm0.044}_{\pm0.004}$	$1.34^{\pm0.049}_{\pm0.007}$	$1.38^{\pm0.046}_{\pm0.006}$

Table 5.1: Survival fraction of calibration data after energy dependent A/E cut, applying Δt_{MA} from 10 ns to 100 ns. The upper/lower script in the content shows the statistical/systematic uncertainty.

region	target	Window length of Moving Averaging Filter [ns]									
		10	20	30	40	50	60	70	80	90	100
lAE	FEP	72.17±2.55 / ±0.78	72.82±2.53 / ±0.72	72.82±2.53 / ±0.32	72.82±2.53 / ±0.11	72.82±2.53 / ±0.56	72.17±2.55 / ±0.32	73.79±2.50 / ±1.01	73.79±2.50 / ±1.18	72.17±2.55 / ±1.05	71.52±2.57 / ±1.05
	DBD	23.86±0.65 / ±0.19	24.33±0.65 / ±0.14	24.60±0.66 / ±0.14	24.44±0.66 / ±0.12	24.51±0.66 / ±0.14	24.42±0.66 / ±0.12	24.14±0.65 / ±0.11	24.40±0.65 / ±0.14	23.60±0.65 / ±0.15	23.53±0.65 / ±0.15
	ROI	83.84±3.70 / ±2.40	84.85±3.60 / ±2.58	84.85±3.60 / ±2.58	86.87±3.39 / ±2.74	82.83±3.79 / ±1.41	82.83±3.79 / ±0.33	82.83±3.79 / ±0.33	82.83±3.79 / ±1.41	82.83±3.79 / ±1.41	82.83±3.79 / ±1.41
	α	1.09±1.08 / ±0.36	1.09±1.08 / ±0.36	1.09±1.08 / ±0.36	1.09±1.08 / ±0.36	1.09±1.08 / ±0.36	1.09±1.08 / ±0.36	1.09±1.08 / ±0.36	1.09±1.08 / ±0.36	1.09±1.08 / ±0.36	1.09±1.08 / ±0.36
sAE	FEP	26.54±2.51 / ±0.78	25.57±2.48 / ±0.72	25.57±2.48 / ±0.32	24.60±2.45 / ±0.11	24.60±2.45 / ±0.56	25.24±2.47 / ±0.32	23.62±2.42 / ±1.01	23.62±2.42 / ±1.18	25.24±2.47 / ±1.05	25.89±2.49 / ±1.05
	DBD	74.65±0.66 / ±0.19	74.05±0.67 / ±0.14	73.63±0.67 / ±0.15	73.65±0.67 / ±0.13	73.53±0.67 / ±0.14	73.53±0.67 / ±0.12	73.65±0.67 / ±0.12	73.40±0.67 / ±0.14	74.00±0.67 / ±0.16	74.02±0.67 / ±0.16
	ROI	13.13±3.39 / ±2.40	12.12±3.28 / ±2.58	12.12±3.28 / ±2.58	10.10±3.03 / ±2.74	14.14±3.50 / ±1.41	14.14±3.50 / ±0.33	14.14±3.50 / ±0.33	14.14±3.50 / ±1.41	14.14±3.50 / ±1.41	14.14±3.50 / ±1.41
	α	2.17±1.52 / ±0.36	2.17±1.52 / ±0.36	2.17±1.52 / ±0.36	2.17±1.52 / ±0.36	2.17±1.52 / ±0.36	2.17±1.52 / ±0.36	$0.00^{+0.36}_{-0.00}$ / $^{+0.36}_{-0.00}$	$0.00^{+0.36}_{-0.00}$ / $^{+0.36}_{-0.00}$	2.17±1.52 / ±0.36	2.17±1.52 / ±0.36
hAE	FEP	1.29±0.64 / ±0.11	1.62±0.72 / ±0.11	1.62±0.72 / ±0.11	2.59±0.90 / ±0.11	2.59±0.90 / ±0.11	2.59±0.90 / ±0.11	2.59±0.90 / ±0.11	2.59±0.90 / ±0.11	2.59±0.90 / ±0.11	2.59±0.90 / ±0.11
	DBD	1.49±0.18 / ±0.03	1.63±0.19 / ±0.01	1.77±0.20 / ±0.05	1.91±0.21 / ±0.04	1.95±0.21 / ±0.01	2.05±0.22 / ±0.02	2.21±0.22 / ±0.05	2.21±0.22 / ±0.01	2.40±0.23 / ±0.05	2.44±0.24 / ±0.05
	ROI	3.03±1.72 / ±0.33	3.03±1.72 / ±0.33	3.03±1.72 / ±0.33	3.03±1.72 / ±0.33	3.03±1.72 / ±0.33	3.03±1.72 / ±0.33	3.03±1.72 / ±0.33	3.03±1.72 / ±0.33	3.03±1.72 / ±0.33	3.03±1.72 / ±0.33
	α	96.74±1.85 / ±0.36	96.74±1.85 / ±0.36	96.74±1.85 / ±0.36	96.74±1.85 / ±0.36	96.74±1.85 / ±0.36	96.74±1.85 / ±0.36	98.91±1.08 / ±1.52	98.91±1.08 / ±0.36	96.74±1.85 / ±1.52	96.74±1.85 / ±0.36

Table 5.2: Survival fraction of background events after energy dependent A/E cut, applying Δt_{MA} from 10 ns to 100 ns. The upper/lower script in the content shows the statistical/systematic uncertainty. The low/high A/E region is labeled as lAE/hAE. The abbreviations of FEP, DBD, ROI, and α are the energy peak at 1524.7 keV (^{42}K γ-line), region in 1.0-1.45 MeV (dominated by $2\nu\beta\beta$ decay), $Q_{\beta\beta}\pm200$ keV region, and the region for energy >4 MeV, respectively.

Figure-of-Merit of MA Filter

To determine the optimal window size of the MA filter for the Phase I data, one can define a test statistic to quantify the performance from calibration data:

$$Ts\,(\text{cali}) \equiv \frac{\epsilon_{DEP}^{sAE}}{\sqrt{1 - \epsilon_{FEP}^{sAE}}}, \tag{5.3}$$

where ϵ_{DEP}^{sAE} represents the survival fraction of the DEP events (1592.5 keV) in the sAE region and ϵ_{FEP}^{sAE} is the survival fraction of the FEP events (1620.7 keV) in the sAE region. The DEP events are used as a sample of signal-like events and the FEP events serve as a background-like sample. For a perfect filter, Ts is equal to 1 (with $\epsilon_{DEP}^{sAE}=1$ and $\epsilon_{FEP}^{sAE}=0$). Fig. 5.11(a) shows the test statistic using the clean sample from the calibration data, as a function of Δt_{MA}. The test statistic has a minimum value at 50 ns.

Similarly, the test statistic using the background data can be defined as:

$$Ts\,(\text{bkg}) \equiv \frac{\epsilon_{data}^{sAE}}{\sqrt{1 - \epsilon_{FEP}^{sAE}\,(\text{bkg})}}, \tag{5.4}$$

where ϵ_{data}^{sAE} is the survival fraction of the events between 1 and 1.45 MeV (dominated by $2\nu\beta\beta$ decay) in the sAE region; $\epsilon_{FEP}^{sAE}\,(\text{bkg})$ stands for the survival fraction at 1524.7 keV γ-line (mainly from ^{42}K decay) in the sAE region. Fig. 5.11(b) shows the test statistic as a function Δt_{MA} using the test samples given by the background data. Using the test sample in 1-1.45 MeV as a signal proxy, distribution of the test statistic in Fig. 5.11(b) shifts to the lower value. This may be due to other background components as listed in Table 4.5.

The test statistic can relate to the MA window size by the following equation:

$$Ts = \tau_0 + \tau_1 \cdot (\Delta t_{MA} - \tau_{opt})^2, \tag{5.5}$$

where τ_0, τ_1, and τ_{opt} are fitting parameters and τ_{opt} characterizes the optimal window size.

The best-fit results with 1σ uncertainties of the test statistic derived from the calibration data and from the background data are summarized in Table 5.3. The optimal window size derived from the ^{228}Th calibration data is 49.1±6.1 ns. The one determined from the background data is 61.2±10.9 ns [2]. The derived optimal window size with best-fit 2σ uncertainties for the calibration and the background data are shown in Fig. 5.11(a) and Fig. 5.11(b), respectively. The optimal window sizes using test statistic derived from the ^{228}Th calibration data and from the background are in agreement within ±2 σ uncertainties.

As a result of the systematic investigation of optimal MA window length, it can be stated that 50 ns used for Phase I data analysis was a good choice and that the sensitivity of the analysis can not be significantly improved by the systematic optimization.

---

[2]The best-fit 1σ uncertainties of Δt_{MA} for the calibration and the background data are derived by calculating the square root of the relevant diagonal elements of the covariance matrix [126]

Test data set	Parameters for test statistic		
	τ_0	τ_1	τ_{opt}
	[A.U.]	$(\times 10^6)$ [ns^{-2}]	[ns]
^{228}Th calibration	1.015±0.003	5.6±2.4	49.1±6.1
background data	0.844±0.008	9.6±7.4	61.2±10.9

Table 5.3: Summary of the fitting results of the test statistic derived from the calibration data and the background data.
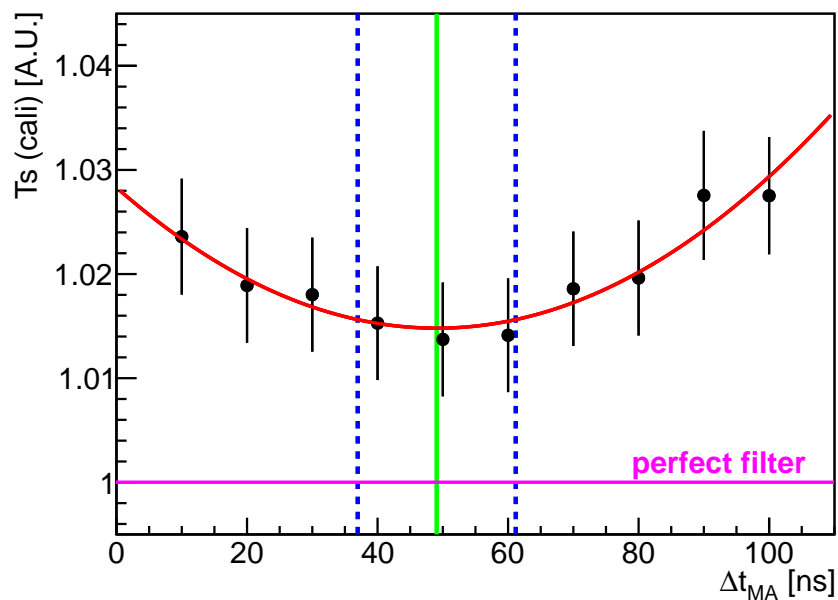
(a)
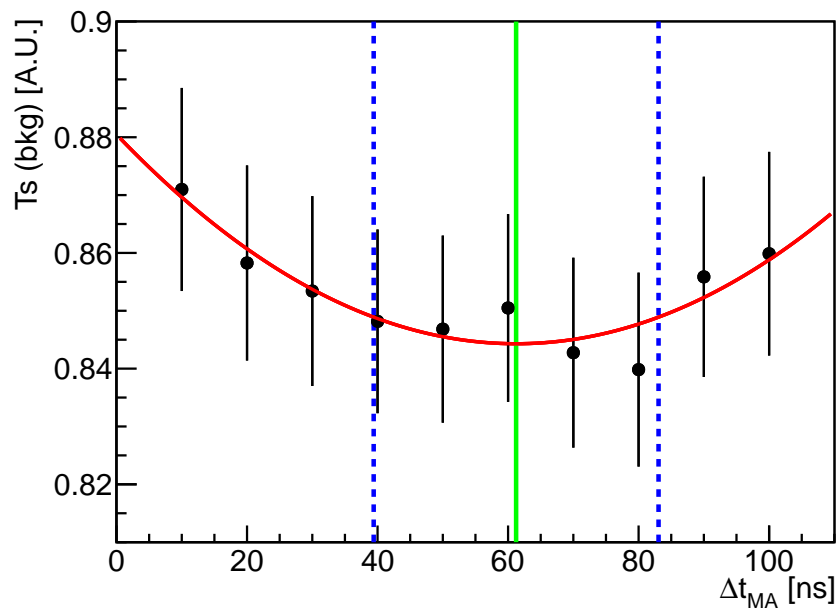
(b)

Figure 5.11: (a) Test statistic as a function of Δt_{MA} using the combined ^{228}Th calibration data. DEP and FEP events are used as samples for the signal-like and the background-like events. (b) Test statistic against Δt_{MA} using the combined background data. The events between 1.0 and 1.45 MeV (dominated by the $2\nu\beta\beta$ decays) are used as a proxy for the signal-like events. The events at 1524.7 keV γ-line (dominated by ^{42}K decays) serve as the background-like events. The optimal window size (green line) with $\pm 2\,\sigma$ uncertainty (blue-dash lines) are shown in each plot.

5.2   R&D on PSD using Wavelet De-noising Technique

The noise reduction method used for the GERDA Phase I analysis is based on a low-pass filter algorithm. A new de-noising algorithm for PSD using the wavelet based de-noising techniques is implemented. A comparison between the Phase I MA filter and the new wavelet based de-noising algorithms has been made and discussed in this section.

5.2.1   Wavelet De-noising and Multi-Resolution Analysis

Wavelet analysis is commonly applied for signal processing - noise reduction, data compression[3], feature extraction, edge detection, and fast numerical analysis. In digital signal processing, the wavelet transform decomposes an input signal into a group of oscillated bases (wavelets). The coefficients of the wavelets can be used for further analysis.

A signal in time domain, $f(t)$, can be decomposed with the combination of biorthogonal functions [4], the scaling function ϕ and the wavelet function ψ: [147]

$$f(t) = \sum_{j, \ k} C_{jk}\phi_{jk}(t) + \sum_{j, \ k} D_{jk}\psi_{jk}(t) \ , \tag{5.6}$$

where j and k are integers. The dual bases are obtained by the translation and dilation from the mother wavelets [5]:

$$
\begin{aligned}
\phi_{jk}(t) &\equiv 2^{-j/2}\phi(2^j t - k)\\
\psi_{jk}(t) &\equiv 2^{-j/2}\psi(2^j t - k).
\end{aligned}
\tag{5.7}
$$

The scaling function ϕ has an integrating property. It smooths the details of the input signal and hence can be used as a low-pass filter. The wavelet function ψ has a differentiating character. It reveals the details of the input signal and therefore serves as a high-pass filter. The scaling coefficient C_{jk} and the wavelet coefficient D_{jk} can be derived via the inner products of $f(t)$ with the dual basis functions.

A decomposition tree of a discrete wavelet transform is shown in Fig. 5.12. The V_0 is the space span by the original signal, whereas the V_n are the subspaces span by the original signal at successively lower resolution and the difference is kept in the wavelet spaces W_n. The original signal V_0 can be decomposed into certain resolution levels [143]. For each level, the signals are down-sampled by a factor of 2 compared to the previous level. The blocks labelled with V_n stand for the low frequency components at a decomposition level n, while W_n represent the high frequency components for the transitions from decomposition level n to n+1. If a signal contains 2^N samples, it can be decomposed to N+1 levels, including the signal itself. The signal can be reconstructed by the inverse discrete wavelet transform.

---

[3]The same technique is used for fingerprint compression for FBI. Also, another successful application of the wavelet is the image compression standard called JPEG2000.

[4]Biorthogonal bases refer to [149] for details.

[5]Here only concerning the discrete wavelet transform and using biorthogonal bases.
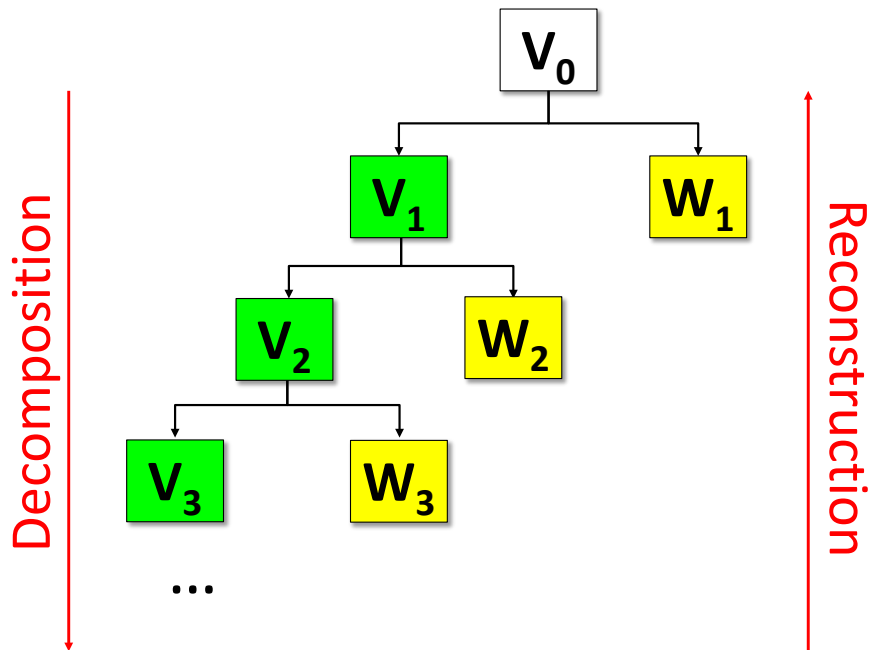
Figure 5.12: Wavelet decomposition tree. A signal can be decomposed into approximate components (green blocks) and detail components (yellow blocks), recursively. The signal can be analyzed by studying the decomposed scaling coefficients and the wavelet coefficients. The signal can be reconstructed by inverse wavelet transformation.

The high frequency components contain high frequency information of the original signal and they are considered as noise drawn to a certain frequency. Hence noise can be suppressed via subtracting (or diminishing) the wavelet coefficients. The method of attenuating the wavelet coefficients is called thresholding. Two methods of thresholding are frequently used in the digital signal processing. The algorithms are:

- hard-thresholding,

- soft-thresholding.

Hard-thresholding algorithms set any wavelet coefficient less than the threshold value to zero. Soft-thresholding algorithms attenuate each wavelet coefficient using a smooth function.

The steps of a wavelet de-noising algorithm are as follows:

- select a basis,

- perform a transformation to a decomposition level n to derive n groups of scaling coefficients and wavelet coefficients,

- apply thresholding to the wavelet coefficients,

- reconstruction of the signal by inverse wavelet transformation.

5.2.2 Applying Wavelet De-noising Algorithm to Phase I Data

The goal is to study possible de-noising algorithms aiming to improve the A/E performance. Data from single Phase I ^{228}Th calibration run of the GD32C BEGe detector was used. Since the A/E PSD method is sensitive to the amplitude of the current pulse, the de-noising procedure studied here mainly focuses on the noise reduction of the current pulse. The standard semi-Gaussian filter for the charge pulse is applied (see Section 4.1.1). The de-noising procedure to calculate the amplitude of each current pulse, deriving from the raw charge pulse, is shown as follows:

1. increasing the sampling rate of the charge pulse,

2. phase locking of the timing of 50% maximum amplitude of the charge pulse,

3. differentiation to derive the current pulse,

4. de-noising using wavelet filter,

5. calculation of maximum amplitude from the de-noised current pulse.

In the first step, the charge pulse is smoothed by cubic spline wavelet interpolation [144] to increase the sampling rate by a factor of 16 (see Fig. 5.14(a)). Details of the phase locking algorithm will be discussed later. The current pulse is obtained by differentiation of the charge pulse. The C++ package Blitzwave [145] was used for the wavelet analysis. The discrete wavelet transformation is performed by using the lifting scheme algorithm [148, 149] to increase the computation speed. The current pulse is denoised by using a CDF(4,2) wavelet class, a sub-branch of the Cohen-Daubechies-Feauveau (CDF) wavelets [147] (see Fig. 5.13). 8-level decomposition is performed. The values of the wavelet coefficients is shown in Fig. 5.15 as a function of the decomposition level. Soft-thresholding is used in this analysis by applying a Sigmoid function [150]. The equation that relates the attenuated and the original coefficients is:

$$D_s = \frac{D_0}{1 + e^{[s \cdot (1 - \frac{|D_0|}{T_h})]^{-1}}} \; , \tag{5.8}$$

where:
D_s : attenuated wavelet coefficient.
D_0 : original wavelet coefficient.
s : softness parameter.
T_h : global threshold cut.

In this analysis, the softness parameter s is empirically set to 0.2. The value of the global threshold cut T_h is scanned from 0 to 2 with a step size of 0.05. After applying

a global threshold cut (i.e., set a constant cut on the y-axis in Fig. 5.15), the de-noised current pulse can be reconstructed via an inverse wavelet transform using the attenuated wavelet coefficients. Fig. 5.14(b) shows a current pulse before and after wavelet de-noising. The noise reduction power by using wavelet de-noising is clearly visible.

Fig. 5.16(a) shows the A/E versus energy distribution after the wavelet de-noising. A ripple structure on the A/E versus E distribution can be seen. The phenomenon appears due to the wavelet coefficients being sensitive to the position of the onset of the signal. Hence, setting a global threshold cut would have a different effect on the reconstructed current pulse because the trigger position of each pulse is different.

The phase locking algorithm is performed before the wavelet de-noising (see the flow chart of the de-noising algorithm). To eliminate the noise effect on determining the pulse position, a low-pass MA filter with 200 ns length is used to determine the timing of the 50 % of the maximum amplitude of the charge pulse (t_{50}), as shown in Fig. 5.14(a). For each event, t_{50} is aligned. The sub-sample of the charge pulse in the range of $t_{50}\pm1.28\,\mu$s is used to derive the current pulse. The A/E versus E distribution after the phase locking algorithm is shown in Fig. 5.16(b). After applying the phase locking method, the ripple structure on the A/E versus E distribution is absent.
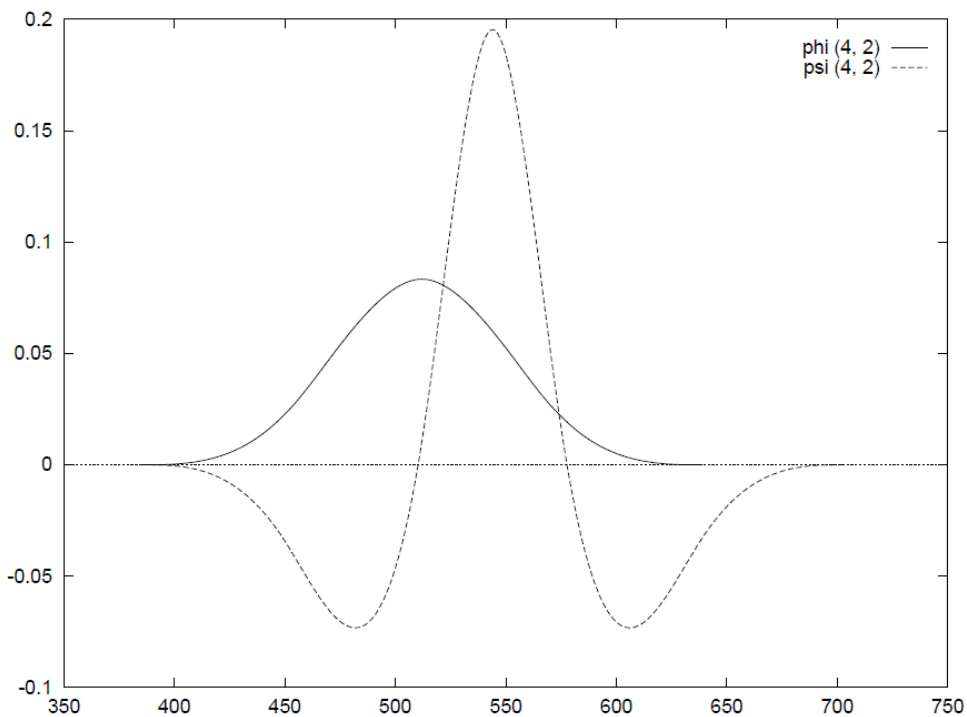
Figure 5.13: Mother wavelets of the CDF(4,2) class for the scaling function ϕ (solid line) and the wavelet function ψ (dash line). Figure from [146].
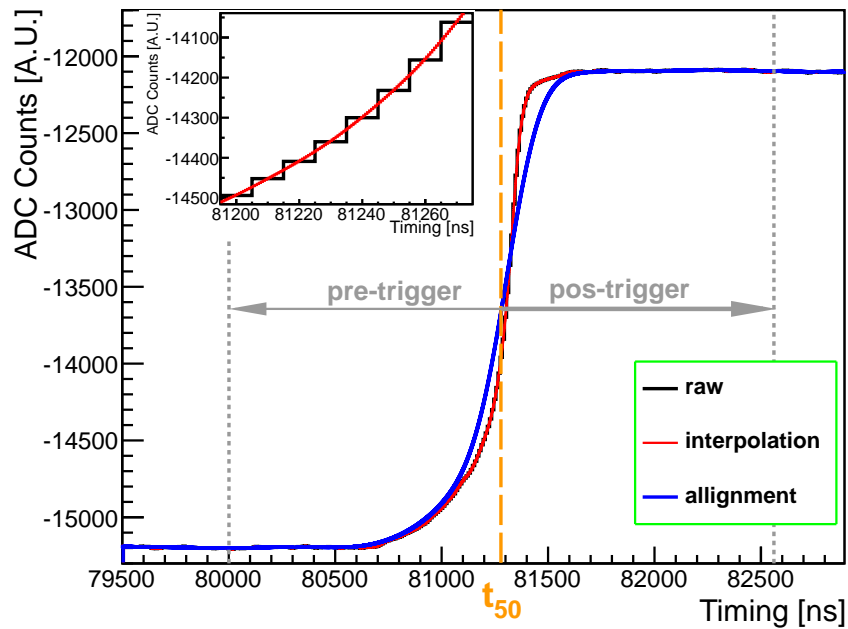
(a)
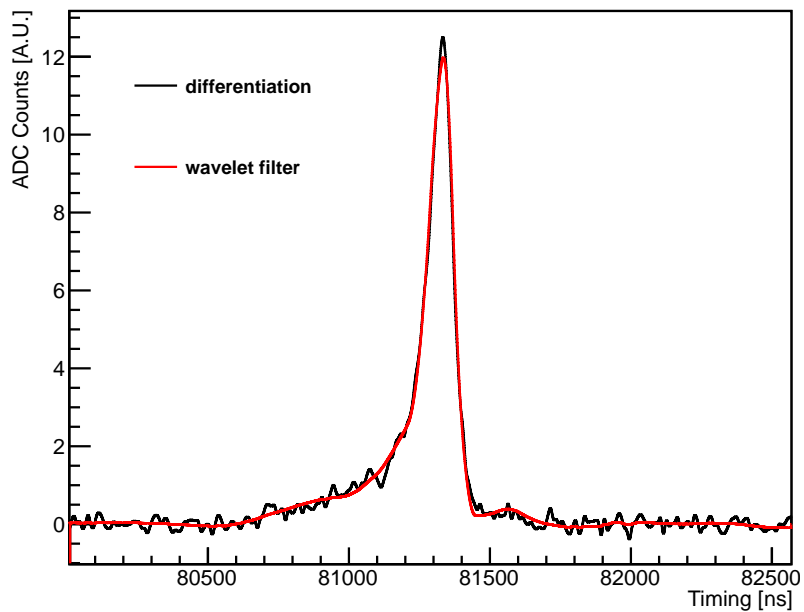
(b)

Figure 5.14: (a) Digital signal processing for the charge pulse. The raw charge pulse (black) after interpolation (red) and phase locking processing using MA filter. The pulses in the inlet show the effect before and after using the cubic spline interpolation. The phase locking procedure is implemented to solve the position dependence problem of the discrete wavelet transform. Refer to the text for the details. (b) The current pulse before and after wavelet filtering.
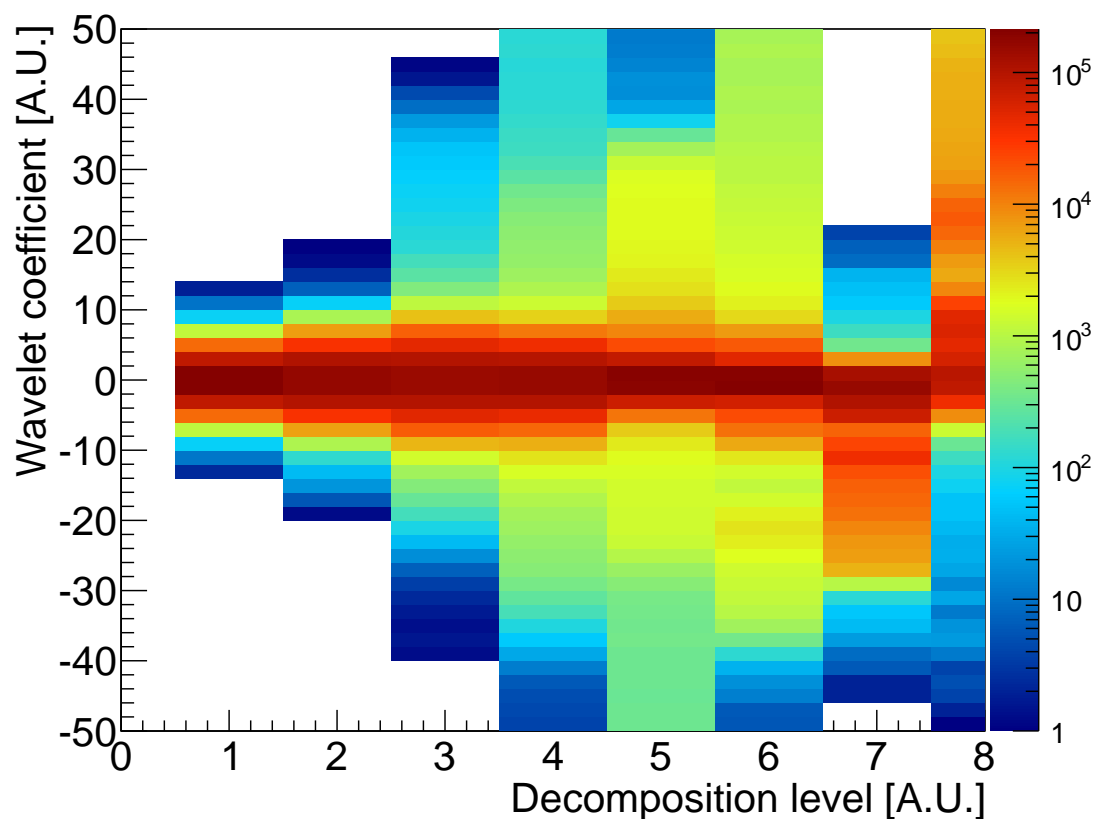
Figure 5.15: Wavelet coefficient versus decomposition level. The decomposition level is set to 8. Noise reduction is via thresholding on the wavelet coefficients.
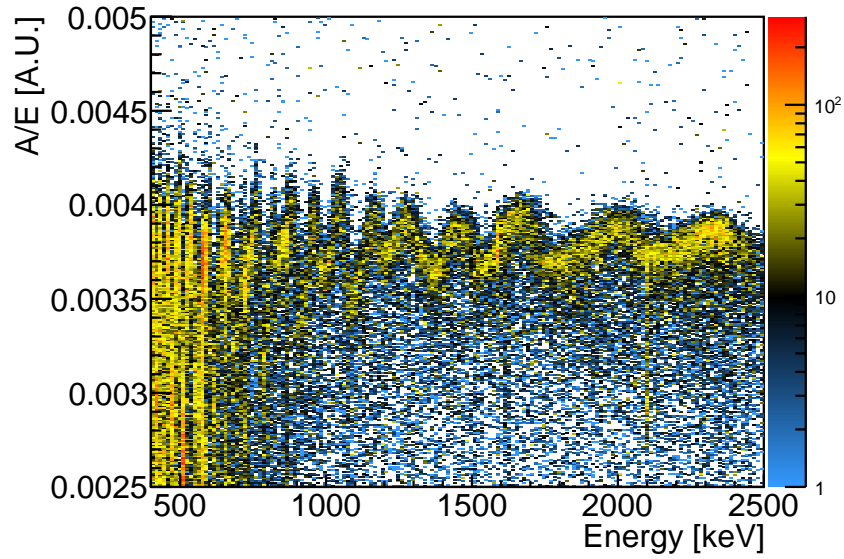
(a)
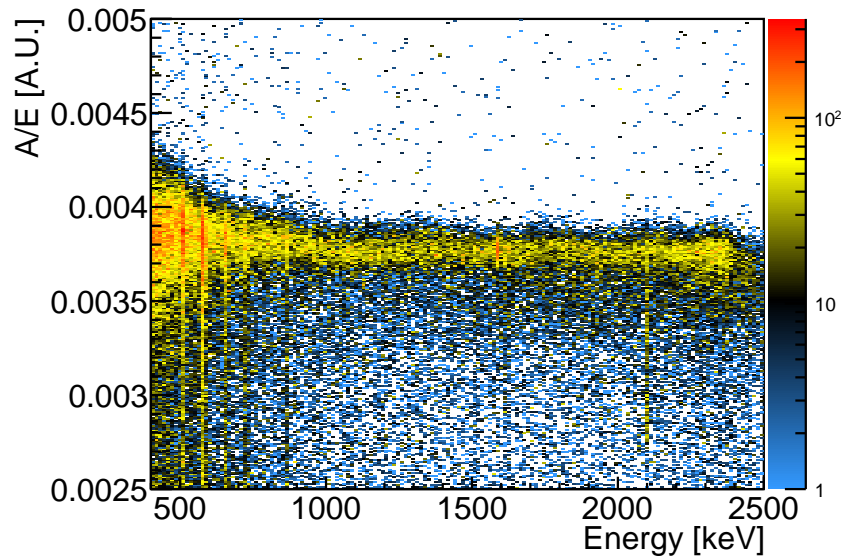
(b)

Figure 5.16: (a) Scatter plot of A/E versus energy without phase locking correction. (b) Scatter plot of A/E versus energy after applying phase locking correction.
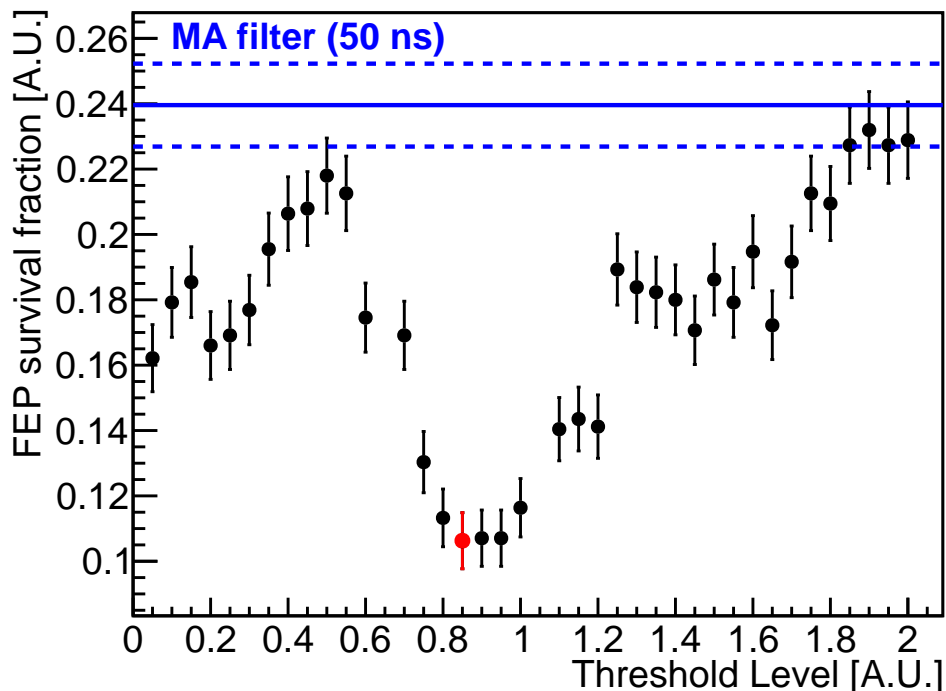
Figure 5.17: Survival fraction of FEP (1620 keV) as a function of global threshold level using wavelet filter together with the result using standard MA filter (50 ns) (blue). The blue-dashed lines show the uncertainty of the results from MA filter.

5.2.3 Figure-of-Merit of Wavelet De-Noising Method

A PSD figure of merit (FOM) is used to determine the performance of the wavelet filter of applying different global threshold cuts. A constant A/E cut is applied to the calibration data where the cut position is determined by fixing 90 % quantile of the DEP events. The FOM value is calculated by evaluating the FEP (1620 keV) survival fraction after the A/E PSD cut.

In order to find the optimal value of the global threshold cut, the value is scanned from 0 to 2 with a step size of 0.05. The FEP survival fraction as a function of the global threshold level is shown in Fig. 5.17. The optimal value of the threshold cut is at 0.85 where the FEP survival fraction has a minimum value. Using the optimal setting of the wavelet filter, the background events at FEP can be suppressed further by about a factor of ~50 % compared to the result using the standard MA filter with 50 ns window size.

5.3   Summary and Outlook

For the Phase I BEGe detectors, a moving averaging (MA) algorithm is applied on current pulses. Systematic studies for determination of the optimal window size of the MA filter in Phase I background BEGe data were performed. An analysis framework for the evaluation of the PSD performance was developed. The framework included the derivation of A/E distribution, the normalization of A/E distribution, and the evaluation of A/E performance. The window size of the MA filter was scanned from $10\,\mathrm{ns}$ to $100\,\mathrm{ns}$ for both ^{228}Th calibration data and background data. The window sizes with the best signal-to-background ratio were determined to be $(49.1\pm6.1)\,\mathrm{ns}$ and $(61.2\pm10.9)\,\mathrm{ns}$, for the ^{228}Th calibration data and background data, respectively. The results from both calibration and background data sets are in good agreement within $\pm2\,\sigma$. As a result of the systematic investigation, it can be stated that $50\,\mathrm{ns}$ used for Phase I data analysis was a good choice and that the sensitivity of the analysis can not be significantly improved by the further optimization of the window size.

An alternative wavelet-denoising algorithm, based on CDF(4,2) wavelets, was developed. The method was applied to a subset of the Phase I ^{228}Th calibration data. The background-like events at FEP can be further suppressed by $\sim50\,\%$ using the wavelet-denoising method compared to the result using a standard MA filter. A phase locking correction is developed to solve the problem of the ripple structure in the A/E versus energy distribution. The major ripple structure is significantly suppressed. A minor ripple structure of the A/E versus E distribution still remained. To eliminate the remaining ripple structure, one could perform a position-dependent threshold cut, a dedicated phase locking correction, or using continuous wavelet transform which can increase the resolutions of the wavelet coefficients.

Chapter 6

Phase II BEGe Detector Characterization

In order to increase the sensitivity, 30 new enriched BEGe detectors with superior pulse shape discrimination power and energy resolution were deployed to fulfill the sensitivity goal of GERDA Phase II. The total mass of the BEGe detectors is about 20 kg. Detector parameters such as depletion voltage, energy resolution, active volume fraction, dead layer thickness, background rejection performance, and other parameters have to be known precisely since they have direct influences on the sensitivity to $T_{1/2}^{0\nu}$. Hence, a variety of measurements on all new BEGe detectors were carried out in the HADES underground laboratory for detector characterizations. The energy resolution and the background rejection power are the benchmark parameters for the BEGe detectors. The characterization results of the 30 BEGe detectors are summarized in this chapter.

6.1   Phase II BEGe Detector Production

37.5 kg of germanium enriched in the isotope ^{76}Ge to $\sim$88 % in form of GeO_2 powder was produced at ECP, Zelenogorsk in Russia [151]. The germanium oxide powder was reduced and zone-refined to 35.5 kg 6N electronic grade (99.9999 %) material in the shape metallic bars by PPM, Langelsheim in Germany [152].

Further zone refinement and crystal pulling for producing crystal slices for the BEGe detectors was carried out by Canberra Oak Ridge, TN, USA [153]. In total 9 crystal ingots were produced and were cut into 30 slices. Up to 4 slices per crystal (named AA, BB, CC, and DD slice) were cut for Phase II BEGe detector production. Pictures of GeO_2, zone-refined bars, Czochralski growth, and crystal ingot are shown in Fig. 6.1. The average dimension of the 30 slices are 73.3±2.8 mm in diameter and 29.7±3.1 mm in height. The total mass of the 30 slices is 20.0 kg after detector production and the individual masses are in a range of 0.390-0.835 kg after BEGe production. The mass yield is 53.3 % from the original germanium oxide.

The Phase II BEGe diodes have have different shapes. 22 diodes have a cylindrical
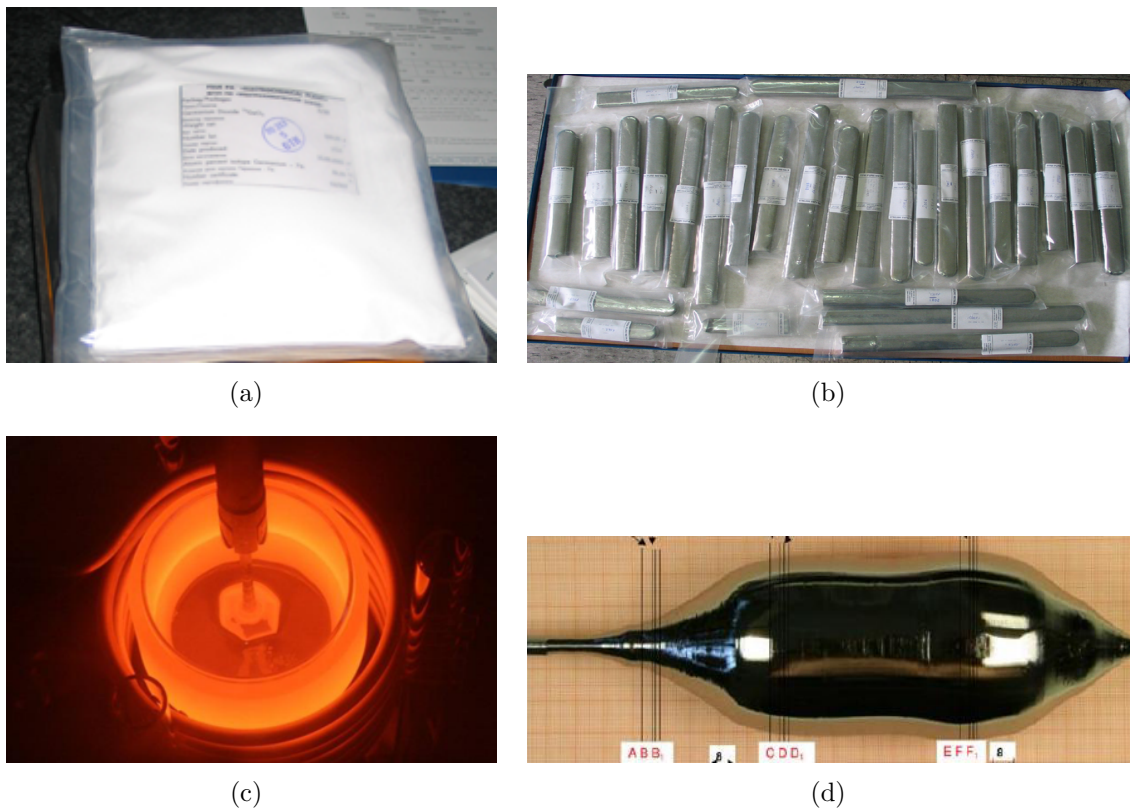
Figure 6.1: BEGe diode processing. (a) GeO$_2$ powder. (b) Germanium metallic bars. (c) Crystal pulling process. (d) Germanium ingot. Taken from [63].

shape, whereas 8 diodes are conical. Typical shapes of the Phase II BEGe diodes are shown in Fig. 6.2. All the diodes were converted to operational BEGe detectors at Canberra Semiconductors N.V., Olen, Belgium [154].

6.2   Cosmic Activation

Long-lived cosmogenic ioisotopes produced in germanium such as ^{60}Co ($T_{1/2} = 5.27$ yr) and ^{68}Ge ($T_{1/2} = 270.8$ d) via spallation processes are critical backgrounds for the $0\nu\beta\beta$ decay, since Q-values in their decay chains are above $Q_{\beta\beta} = 2039$ keV of ^{76}Ge and their long half-lives.

The logistics were optimized to minimize the exposure of cosmic activation during the diode production chain: minimization of exposure during transportation in a shielding container, underground storage close to the manufacturer site, and BEGe characterization measurements in the underground lab. During transportation from one processing site to another, the germanium was protected by a 70 cm steel- and 70 cm salt water-shields. The expected suppression factor of cosmic activation using the shielding container was in the range of 15 and 10 for ^{60}Co and ^{68}Ge, respectively according to simulations [132]. While the

(a)   (b)   (c)
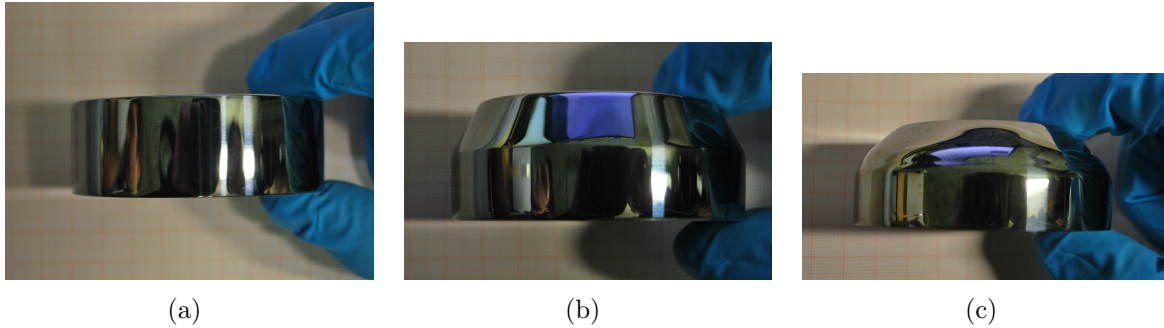
Figure 6.2: Typical shapes of the Phase II BEGe diodes. (a) A cylindrical shape (GD02C). (b) A conical shape (GD02A). (c) A double conical shape (GD00A). Figures from [63].

shipping across the Atlantic ocean, the container was loaded to the bottom most place of the container ship to further reduce cosmic activation. During times of the material that was not processed, the germanium was always stored in underground site, in Cherokee Caverns close to Canberra Oak Ridge and HADES underground lab near Canberra Olen site. Precise tracking of each Ge diode above ground was recorded and saved to a central database. The activity of the intrinsic ^{60}Co and ^{68}Ge in the newly produced BEGe detectors can be predicted using the assumed cosmogenic activation rate [132], the known histories of exposure to cosmic rays of the individual detectors at September 1st, 2014, only 21.4 ^{60}Co nuclei and 4.9 ^{68}Ge nuclei were expected per kg of germanium [116].

6.3   HADES **Underground Facility**

After diode production all enriched BEGe detectors were characterized in vacuum cryostats in the screening facility HEROICA at HADES [141]. HADES is a semi-deep underground laboratory with overburden of 223 m of clay, corresponding to $\sim$500 m of water equivalent (m.w.e.). The HADES (High Activity Disposal Experimental Site) underground facility is at the Belgian nuclear research center SCK·CEN (Studiecentrum voor Kernenergie · Centre d'Etude de l'Energie Nucléaire) in Mol, Belgium. The location of the facility is close to the diode manufacturer, Canberra Olen (about 25 km in between). The HERO-ICA (Hades Experimental Research Of Intrinsic Crystal Appliances) screening facility was built at the HADES underground laboratory in 2012 for acceptance tests, characterization measurements, and for the storage of the enriched germanium diodes.

<div align="center">(a)   (b)</div>
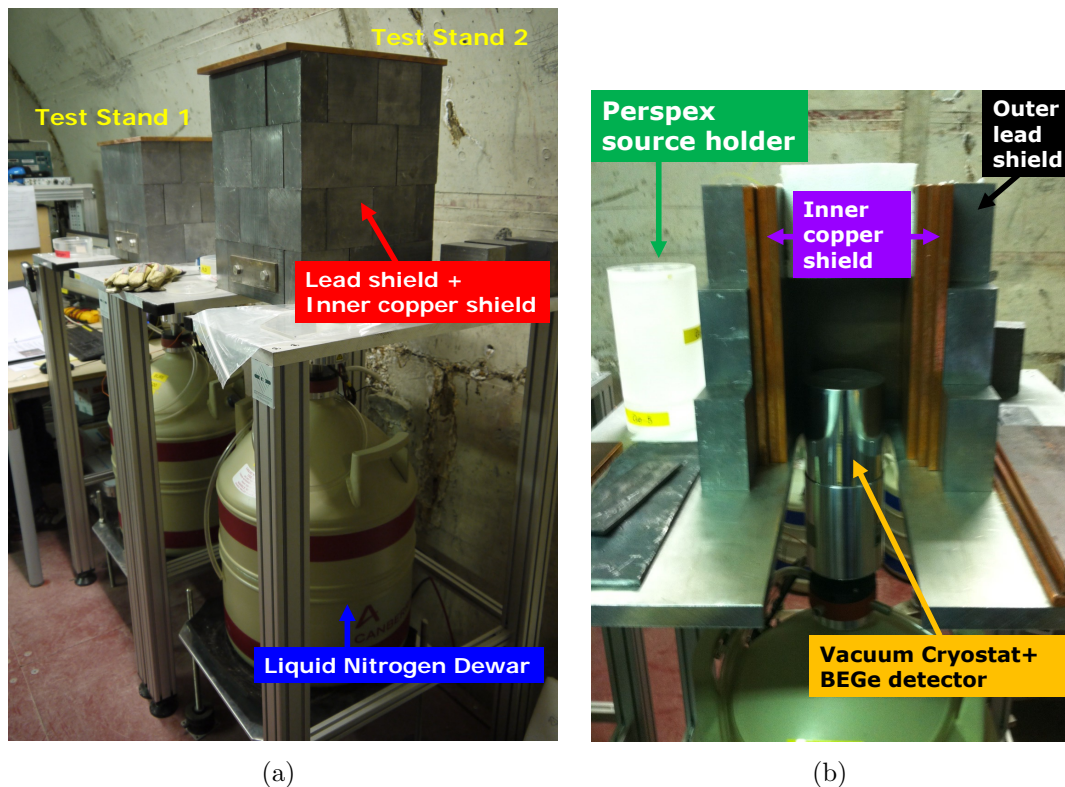
Figure 6.3: (a) Front view of the two test stands for the ^{228}Th measurements in the HADES underground laboratory. (b) A cross section of the shield and the support stand [63]. The BEGe detector is shielded by a copper shield and covered by a lead shield. The LN$_2$ Dewar is below the vacuum cryostat.

6.4 Phase II BEGe Characterizations

6.4.1 Experimental Setup

Test Stands and Calibration Sources

Two test stands shown in Fig. 6.3(a) were used for the characterization. The BEGe detectors were enclosed by passive shielding materials, as shown in Fig. 6.3(b). The shields provide attenuation to the external gamma background, and are made up of, inside out, 3 cm thickness of copper plates, and 5 cm thickness of lead bricks. Another 1 cm thickness of copper plate was employed on the top. The dimensions of the shielding castle is 30 cm^3.

Uncollimated ^{228}Th sources were used to determine the background rejection efficiency of the new BEGe detectors. Fig. 6.4 shows the layout of the ^{228}Th source setup. The ^{228}Th source is encapsulated in a ceramic and is embedded in the middle of a circular holder. Customized source holders made of acrylic glass with the same inner radius (4.35 cm) but different heights were used in the measurements: the holders, PL1, has a height of 4 cm and another holder, PL4, has a height of 16 cm. PL1 and PL4 can be exchanged. A

plexiglass base, PL0, which fits on the end-cap of the vacuum cryostat, has a height of 3.8 cm. To minimize the systematics due to the setting of the source position, the circular holder is always placed on PL1 or PL4 and combined with the PL0 base module which fits the end-cap of the vacuum cryostat.

The activities of the ^{228}Th sources, HS6, HS7, and HS8 used in the measurements are listed in Table 6.1.

Heroica ID	Reference Activity [kBq]	Reference Date day/month/year	Activity [kBq] 01/09/2012	Activity Uncertainty [%]
HS6	8.71	07/02/2006	0.80	20
HS7	13.60	20/03/2012	11.33	7
HS8	15.20	01/04/2012	13.06	7

Table 6.1: Activities of the ^{228}Th sources used in the Hades underground laboratory.

Data Taking Configuration

Measuring time and live time of the ^{228}Th measurement for each BEGe detector are listed in Table 6.2. Most of the measurements have high live time fractions. Some measurements have low live time fractions which affect the statistical uncertainty in the analysis. One detector, GD32D, was reprocessed after initial Hades measurements, denoted as GD32D-I. Hades data taken after reprocessing is denoted as GD32D-II.

Electronics and Data Acquisition System

The front-end signal of the BEGe detectors is amplified by a charge sensitive pre-amp (with cold FETs) [155]. The output signal is read out by parallel data acquisition (DAQ) systems including 6-channel analyzer modules (MCA) [156] and Struck FADCs. The Struck FADC is based on a 8-channel, 100 MHz sampling rate, 14-bit Flash Analog-to-Digital-Convertor (FADC) module [157]. The readout allows a full recording of all the relevant charge pulses with maximum trace-lengths up to 1.28 ms. For the ^{228}Th measurements, the FADC trace-length was set to 40 μs. The 6-channel MCA modules were used to save the measured energy spectrum.

Figure 6.4: Layout of the ^{228}Th source setup (unit in the figure: mm) [63]. The PL0 holder (green) fits the end-cap of the cryostat (grey). The PL1 holder (blue) is placed on the top of the PL0 holder. The height of the PL0 and PL1 holder is 3.8 cm and 4 cm, respectively. The ^{228}Th source is a embedded in a circular holder (yellow) and is placed on the top of the PL1 holder. Another PL4 holder (not shown in the figure) can be exchanged with PL1 holder.

detector	source ID	source position	data taking time [hour]	live time fraction [%]
GD32A	HS6	PL0+PL1	14.0	100.0
GD32B	HS6	PL0+PL1	7.0	100.0
GD32C	HS6	PL0+PL1	5.0	100.0
GD32D-I	HS6	PL0+PL1	12.0	22.5
GD32D-II	HS8	PL0+PL1	10.0	90.3
GD35A	HS6	PL0+PL1	18.0	100.0
GD35B	HS6	PL0+PL1	8.0	100.0
GD35C	HS6	PL0+PL1	8.0	100.0
GD61A	HS7	PL0+PL1	10.0	89.2
GD61B	HS8	PL0+PL1	10.0	100.0
GD61C	HS7	PL0+PL1	8.0	88.5
GD89A	HS8	PL0+PL1	8.0	88.3
GD89B	HS7	PL0+PL1	10.0	100.0
GD89C	HS7	PL0+PL1	10.0	87.3
GD89D	HS7	PL0+PL1	8.0	29.2
GD76B	HS8	PL0+PL1	8.0	33.8
GD76C	HS8	PL0+PL4	12.0	100.0
GD79B	HS7	PL0+PL1	8.0	100.0
GD79C	HS7	PL0+PL1	12.0	100.0
GD91A	HS7	PL0+PL1	8.0	88.3
GD91B	HS8	PL0+PL1	10.0	72.1
GD91C	HS7	PL0+PL1	8.0	100.0
GD91D	HS7	PL0+PL1	10.0	72.1
GD00A	HS8	PL0+PL1	10.0	100.0
GD00B	HS7	PL0+PL1	8.0	46.6
GD00C	HS8	PL0+PL1	10.0	87.3
GD00D	HS8	PL0+PL1	12.0	100.0
GD02A	HS7	PL0+PL1	12.0	100.0
GD02B	HS8	PL0+PL1	8.0	67.8
GD02C	HS8	PL0+PL1	8.0	88.5
GD02D	HS7	PL0+PL1	8.0	23.0

Table 6.2: Data taking conditions for the ^{228}Th measurements in HADES underground laboratory.

6.4.2   Parametrization of the A/E Distribution

Modeling Double-peak A/E Distribution

In the measurements, it was found that some BEGe detectors have a double-peak structure in the A/E distribution. A typical A/E distribution with double-peak structure, at a given energy for the events from a ^{228}Th calibration is shown in Fig. 6.5. The A/E distribution with double A/E structure can be described by a superposition of two distributions with:

$$f(A/E) = \sum_{j=1}^{2} s_j(A/E) + m_j(A/E), \tag{6.1}$$

where $s_j(A/E)$ and $m_j(A/E)$ are SSE component and MSE component of the jth A/E distribution, respectively. The parametrization of each A/E distribution is defined in Eq.4.2.
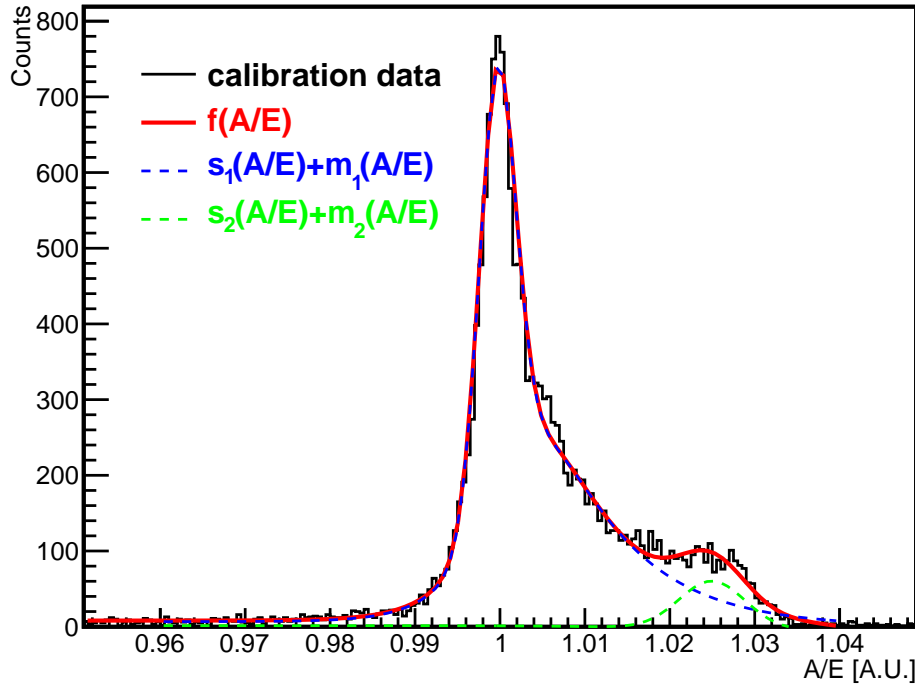
Figure 6.5: A/E distribution for a BEGe detector with double-peak structure (GD35A). The double-peak structure can be described using the fit function, $f(A/E)$ (red curve in the figure), given in Eq.6.1. The two distinct distributions are shown in blue and green.

It is hence necessary to extend the definition of the A/E FWHM $b_{A/E}$. In order to be able to describe the A/E distribution:

$$b_{A/E} = \begin{cases} 2.35 \cdot \sigma_{A/E} & \text{if only single-peak structure} \\ \Delta\mu_{A/E}(2,1) + 2.35 \cdot \langle\sigma_{A/E}\rangle & \text{if double-peak structure} \end{cases} \quad (6.2)$$

where :
$\Delta\mu_{A/E}(2,1)=\mu_{A/E}(2)-\mu_{A/E}(1)$: Deviations between the means of A/E Gaussian peaks
$\langle\sigma_{A/E}\rangle=[\sigma_{A/E}(1)+\sigma_{A/E}(2)]/2$: Average width of two A/E Gaussian peaks

6.4.3   Evaluation of Detector Performance

Data Analysis Procedure and A/E Normalization

Evaluation of the PSD performance follows the standard algorithm (see flow chart of the data analysis in Fig. 5.1). The MA filter with 50 ns window size is used.

Fig. 6.6, Fig. 6.7, and Fig. 6.8 show the scatter plots of the A/E as a function of energy after normalization. Note that the normalization procedure is performed on the first A/E peak for the case of A/E double-peak structure occurs. The horizontal line in red shows the PSD cut value at 90 % quantile of the DEP events. The various vertical lines show the selected peaks for calculating the survival fractions. The MSE samples for calculating the survival fractions after PSD cut are SEP at 2104 keV, FEP at 2615 keV, FEP at 1620 keV, and the ROI (2004-2074 keV) [1].

---

[1]No background subtraction for the FEP (2615 keV) and the ROI (2004-2074 keV) for the calculation of the survival fraction after PSD cut.

(a) GD32B

(b) GD02C

(c) GD35B

(d) GD35C

(e) GD89A

(f) GD79B

(g) GD91C

(h) GD00D

(i) GD02A

(j) GD02B

(k) GD61A

(l) GD00A

(m) GD61B

(n) GD89D

(o) GD89B
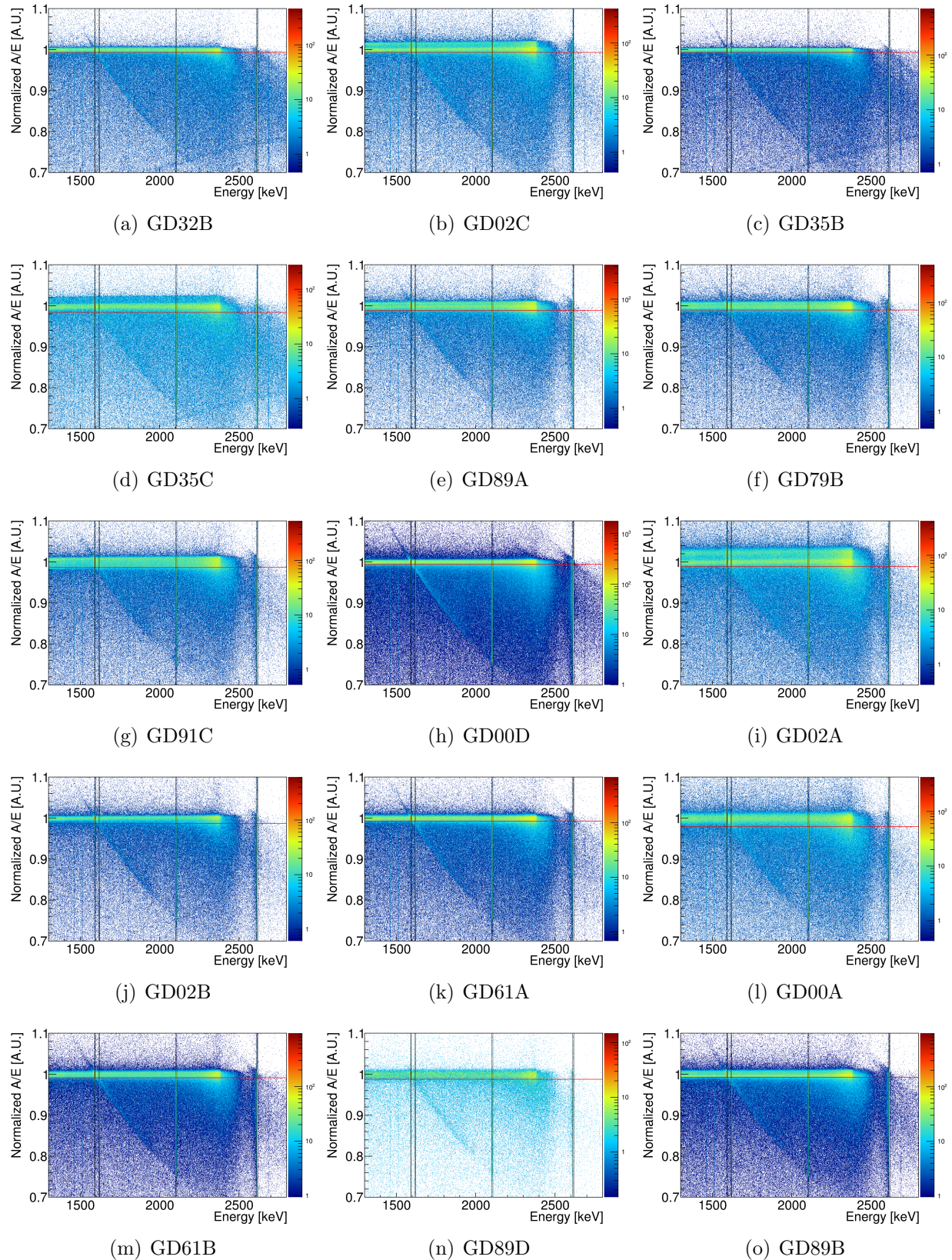
Figure 6.6: Scatter plot of the Normalized A/E as a function of energy (part-I). The horizontal line (red) shows the PSD cut value at 90% quantile of the DEP events. The various vertical lines represent the relative peaks for the analysis.

(a) GD00B

(b) GD89C

(c) GD02D

(d) GD91B

(e) GD91A

(f) GD76B

(g) GD91D

(h) GD32D-II

(i) GD32A
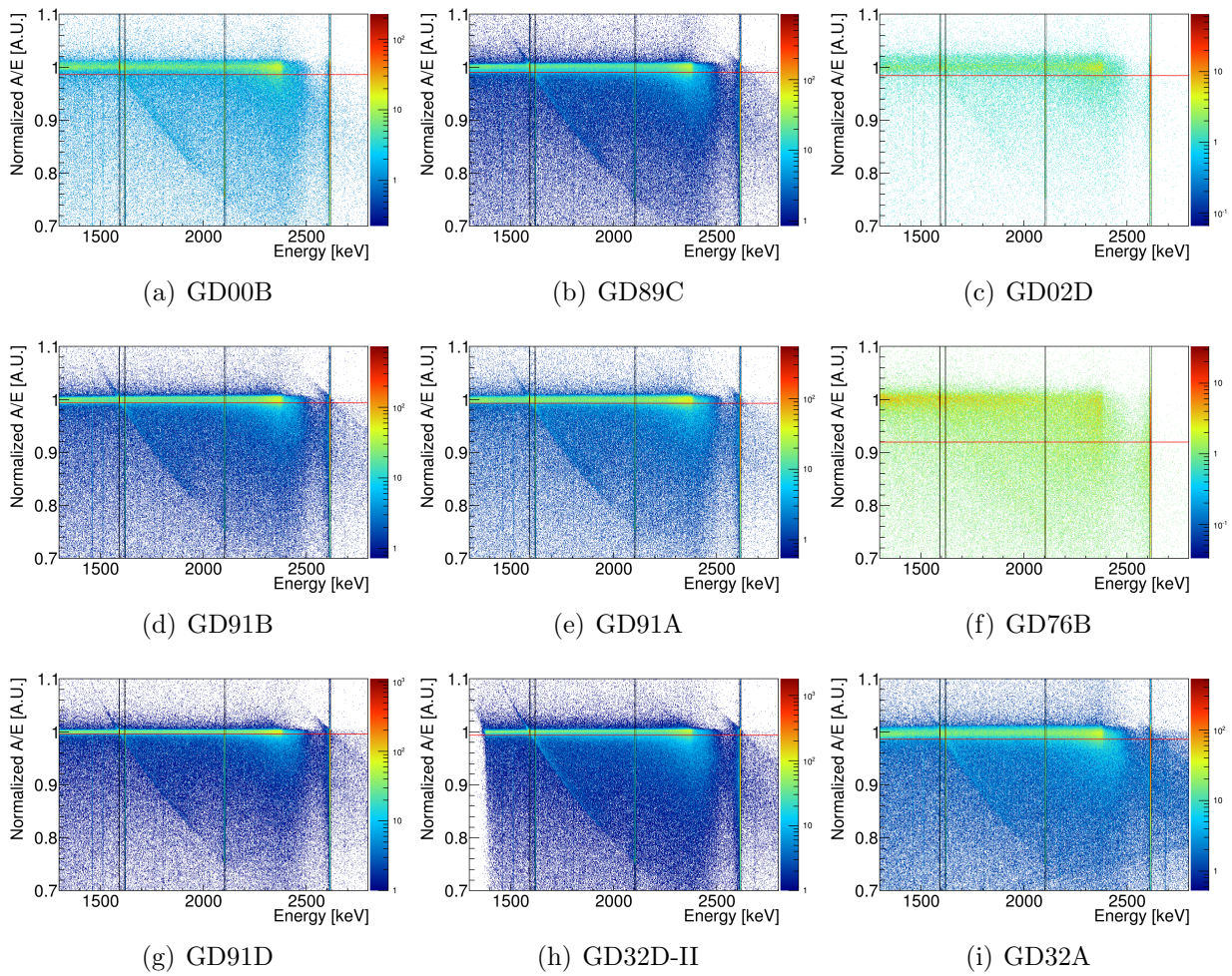
Figure 6.7: Scatter plot of the Normalized A/E against energy (part-II).

(a) GD76C

(b) GD32C-I

(c) GD00C

(d) GD79C

(e) GD61C

(f) GD35A

(g) GD32D-I
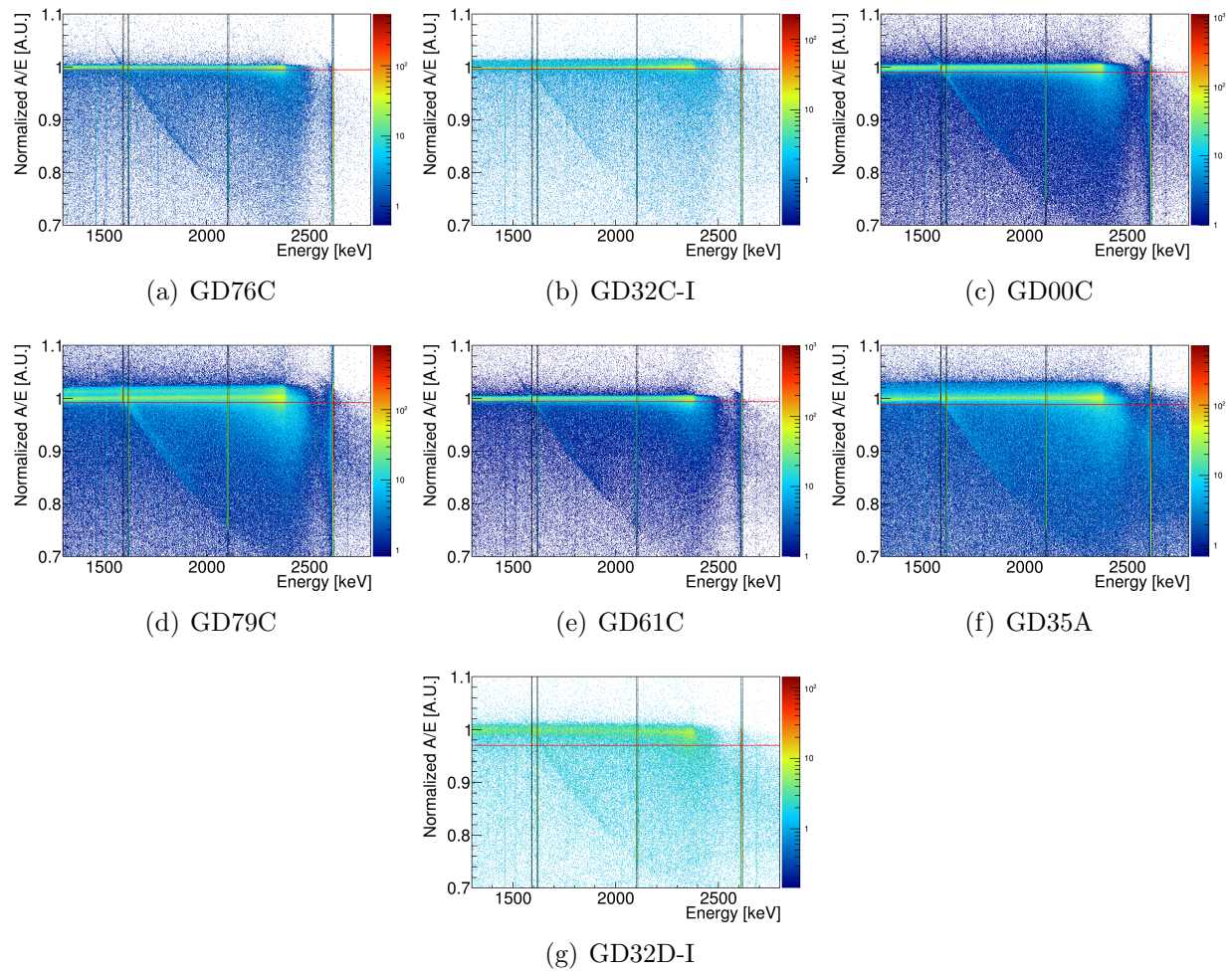
Figure 6.8: Scatter plot of the Normalized A/E versus energy (part-III).

Detector Characterizations

A better $b_{A/E}$ leads to an improved background rejection power using the same MA window size. The $b_{A/E}$ values at DEP are in a range of about 0 to 4 % for the Phase II detectors (Fig. 6.9-Fig. 6.11). 12 out of the 30 BEGe detectors have very good A/E resolutions ($b_{A/E}$ <1 %), as shown in Fig. 6.9. Another 40 % of the detectors have acceptable A/E resolutions, ($1 \leq b_{A/E}$ <2 %) (see Fig. 6.10). Another 20 % of the detectors have double-peak A/E structures ($b_{A/E} \geq 2$ %), as displayed in Fig. 6.11.

Table 6.3 summarizes the survival probabilities of DEP, SEP, FEPs, and the ROI, together with the energy resolutions at DEP. The uncertainties registered include statistical and systematic contributions (refer to Section 6.4.3 for more details). The survival probabilities of the SEP, 2615 keV and 1620 keV FEPs, and ROI, are in a range of (5-21) %, (6-35) %, (9-23) %, and (32-56) % (central value), respectively. The PSD performance of the detector GD32D got improved after reprocessing by Canberra. The GD02D detector which has the worst background rejection power (see Table 6.3), turned out to have an unsatisfactory impurity concentration. The detector can not be fully depleted and hence has a deteriorated charge collection efficiency. Thus leading to a degraded background rejection power. This detector will still be used for the Phase II. However, whether to include this detector in the data analysis or not will be decided after the deployment in Phase II.

All the detectors satisfied the specified requirements for Phase II: the leakage current was less than 50 pA at operational voltages (≤ 4 kV) [116] and the FWHMs at DEP for the 30 BEGe detectors were in a range of 1.76 and 2.08 keV (Table 6.3). Other dedicated measurements like determinations of active volume and dead layer thickness are discussed elsewhere [161, 162].

Systematic Uncertainties of the Survival Fractions

The total uncertainty of the survival fraction given in Table 6.3 is calculated by combining the following contributions in quadrature:

- statistical uncertainty after the A/E PSD cut (δ_{stat})

- systematic uncertainty due to the A/E normalization (δ_{norm}, the dominant contribution in most of the detectors)

- systematic uncertainty due to the finite number of the DEP events (δ_{dep})

The details of each contribution are summarized in Table 6.4. For most of the detectors, δ_{norm} is the dominant uncertainty of the survival fractions of SEP and FEPs. Data taking time of some of the detectors, such as GD32D-I, GD76B, and GD02D, were short (1.8 hr-2.7 hr) compared to others. The major uncertainty of these detectors is due to δ_{stat}.

For the majority of the detectors, the main uncertainty on the survival fraction at the ROI is δ_{dep}. This is due to the lower statistics of the ROI compared to the peak regions.
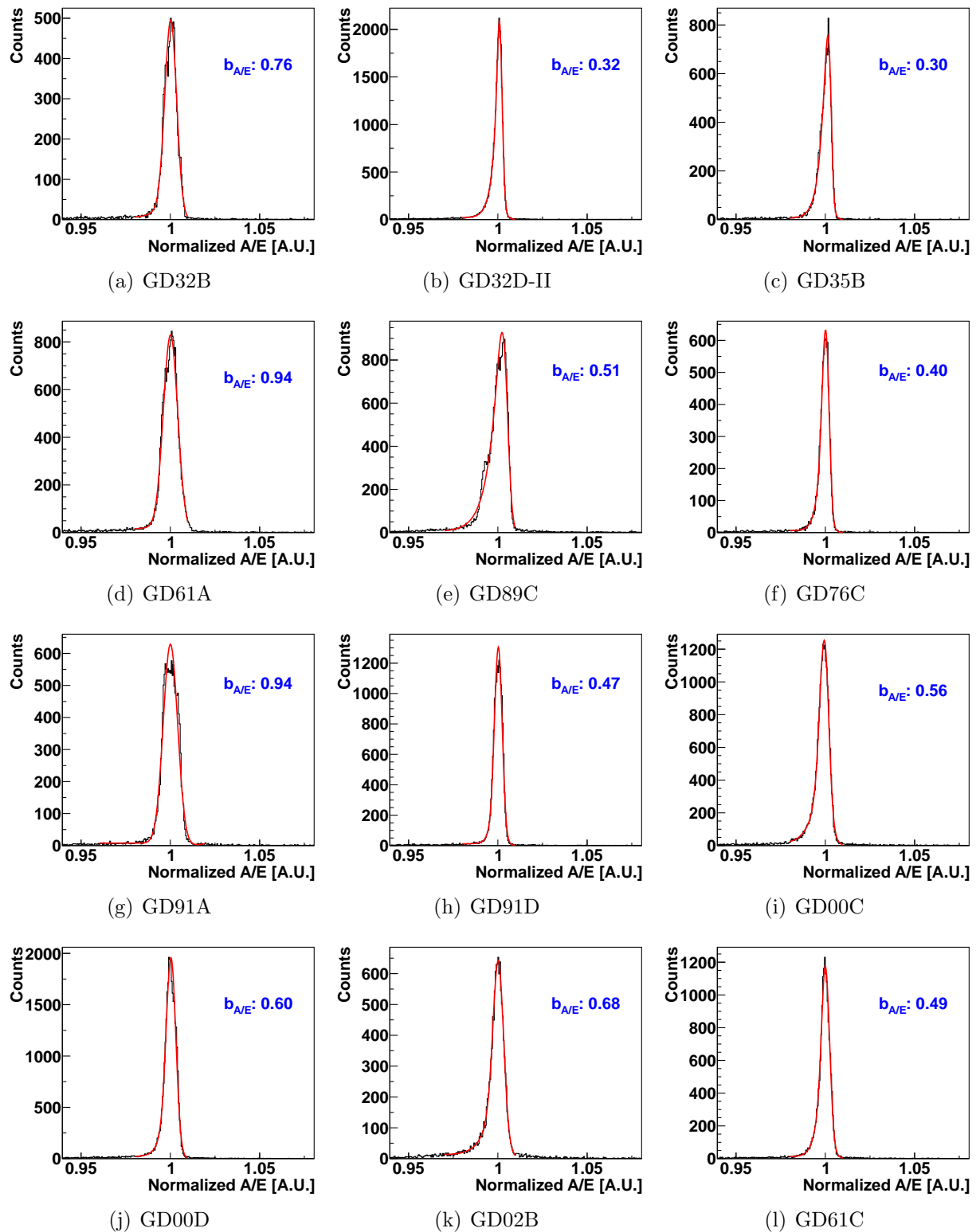
Figure 6.9: Normalized A/E distributions at DEP for $b_{A/E} \leq 1\%$. The measured data (black) and the fitted functions (red) are shown.
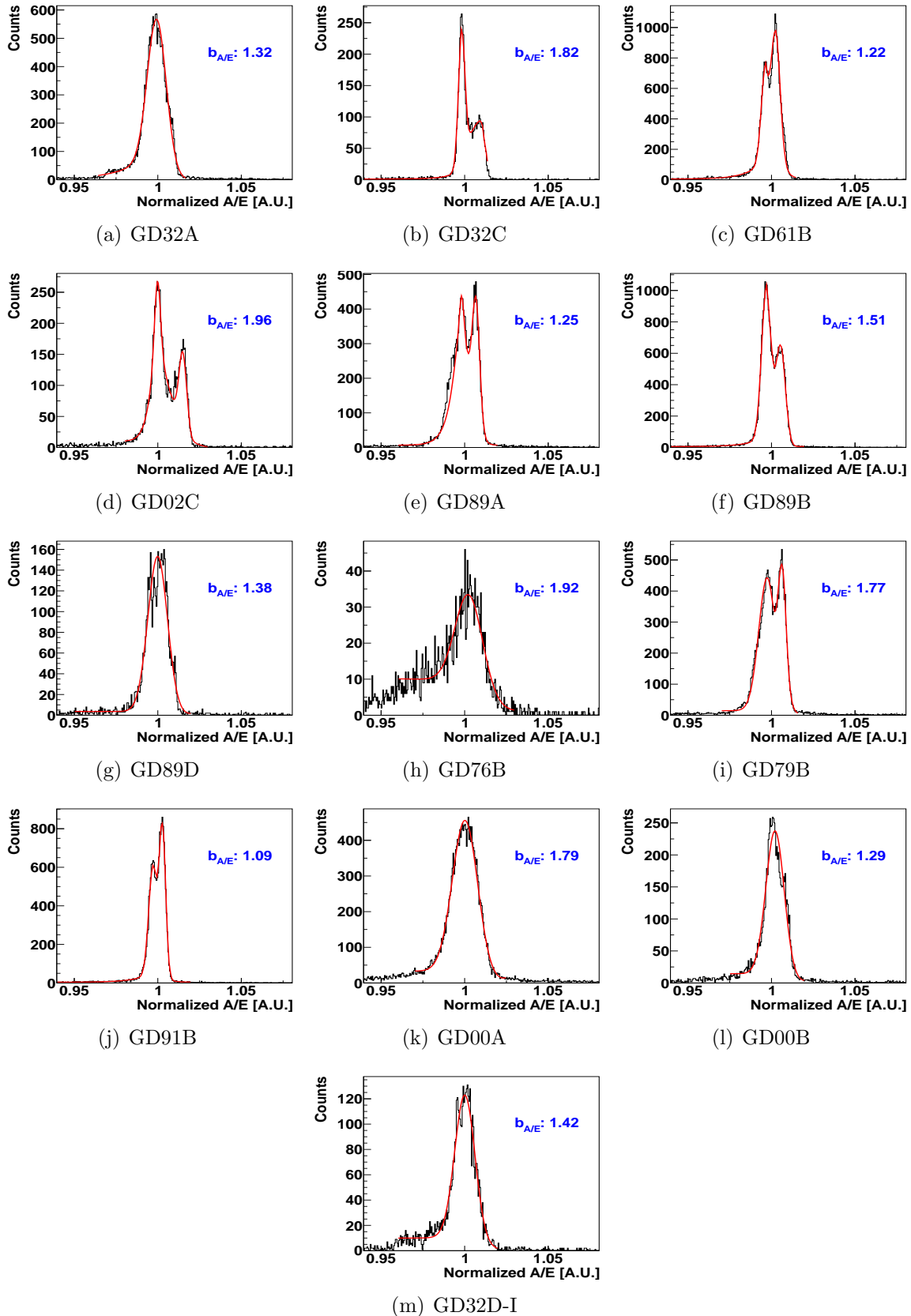
Figure 6.10: Normalized A/E distributions at DEP for $1 < b_{A/E} \leq 2\,\%$. The measured data (black) and the fitted functions (red) are shown.

(a) GD35A   (b) GD35C   (c) GD79C

(d) GD91C   (e) GD02A   (f) GD02D
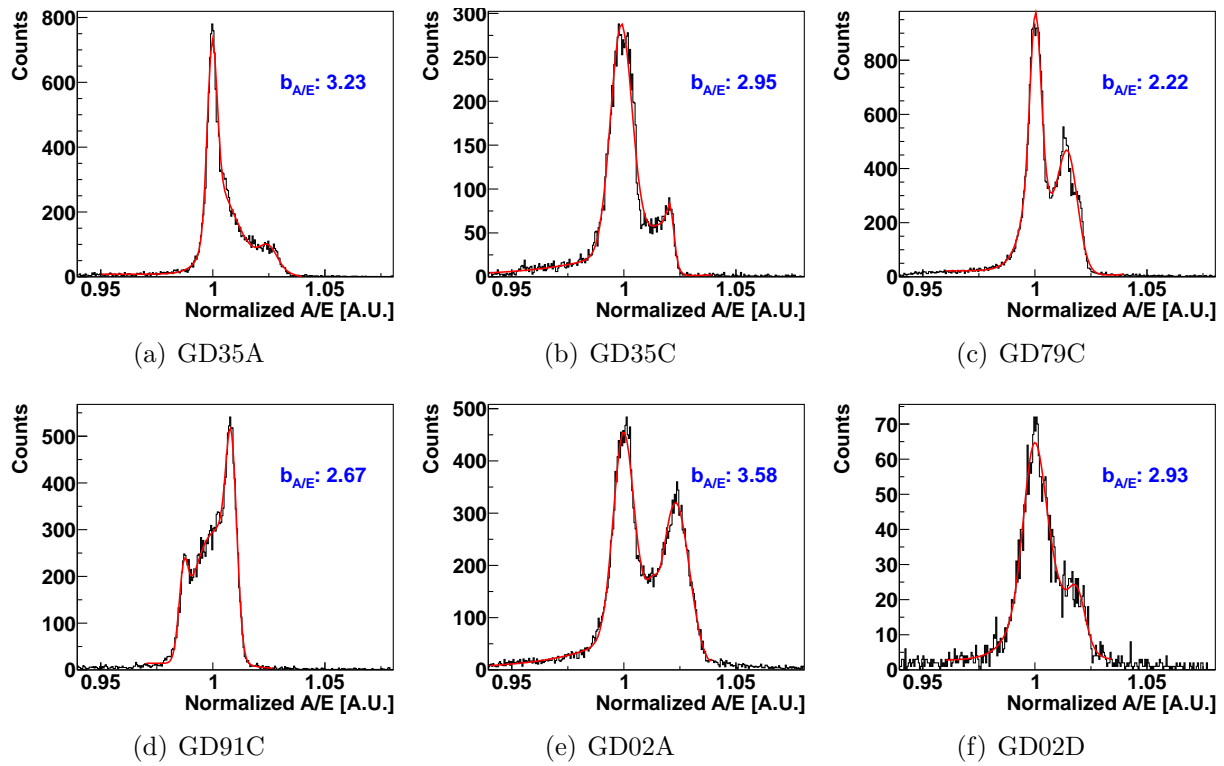
Figure 6.11: Normalized A/E distributions at DEP for $b_{A/E} > 2\%$. The measured data (black) and the fitted functions (red) are shown. The multiple peak structures of A/E distributions are clearly seen.

Correlation Among Parameters

Fig. 6.12 shows the correlation between the SEP survival probability and the A/E resolution. The two parameters have a positive correlation. A linear fit with best-fit 1σ uncertainty is performed using data points with single A/E structure with $b_{A/E} <2\,\%$. It can be seen that for detectors with single A/E peak, there is a correlation between $b_{A/E}$ and PSD performance. The detectors below the band have a rather broaden A/E peak or a double-peak structure in the A/E distribution. The data points above the band have a rather degraded PSD power compared to those in the band with the same $b_{A/E}$ value.

There is no strong correlation between the survival fraction and different slices of ingots, as shown in Fig. 6.12. Also, no correlations between the survival fractions and other parameters such as impurity concentrations, geometry of detectors, ingot IDs were found [2]. Similar studies on searching for the correlations among parameters among 7 BEGe detectors have been reported earlier [116]. However, no correlations among parameters were found. Even if two detectors have exactly the same geometry, the differences in impurity concentration would result in different E-field distributions in the bulks [85]. Hence, the PSD performances would also be different. To conclude, due to the fact that some detectors show A/E double-peak structures, using a single parameter $b_{A/E}$ to estimate the background rejection power among detectors is not reliable.

---

[2]Details of impurity concentrations, geometry of the 30 detectors have not been made public yet.
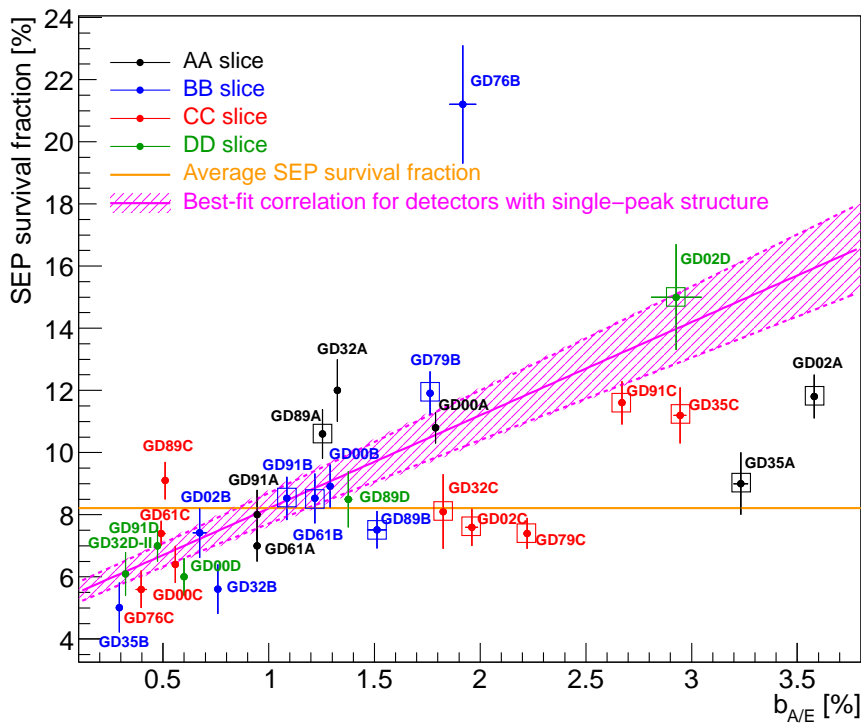
Figure 6.12: SEP survival fraction versus $b_{A/E}$ plot. The linear function with a best-fit 1σ uncertainty is performed using A/E single-peak structure. The A/E distribution which has a visible double-peak structure is labeled with a rectangular box. The total uncertainty is quoted for each data point.

detector	DEP 1593 keV	SEP at 2104 keV	FEP at 2615 keV	FEP 1620 keV	ROI (2004-2074) keV	$b_{A/E}$ [%]	FWHM at DEP [keV]
GD32A	90.0±0.9	12.0±1.0	16.8±0.7	17.8±1.2	43.4±0.4	1.32±0.01	1.87±0.02
GD32B	90.0±1.3	5.6±0.8	8.0±0.7	10.0±0.9	32.3±0.6	0.76±0.01	1.86±0.03
GD32C	90.0±2.0	8.1±1.2	13.8±0.7	11.6±1.6	42.4±0.7	1.82±0.01	1.92±0.04
GD32D-I	90.0±0.3	11.8±1.6	17.4±0.9	18.6±1.7	43.9±0.6	1.42±0.03	1.74±0.05
GD32D-II	90.0±0.9	6.1±0.7	8.7±0.5	9.0±0.9	39.6±0.4	0.32±0.01	1.96±0.03
GD35A	90.0±0.3	9.0±1.0	13.3±0.7	12.9±1.2	36.9±0.5	3.23±0.03	1.77±0.02
GD35B	90.0±1.2	5.0±0.8	6.4±0.6	9.9±1.1	32.3±0.6	0.30±0.01	1.81±0.03
GD35C	90.0±0.6	11.2±0.9	16.3±0.6	16.0±1.0	41.7±0.4	2.95±0.03	1.76±0.03
GD61A	90.0±0.7	7.0±0.5	9.9±0.4	11.5±0.9	39.8±0.4	0.94±0.01	2.08±0.03
GD61B	90.0±0.8	8.5±0.8	13.7±0.5	13.5±0.9	45.4±0.3	1.22±0.01	1.90±0.02
GD61C	90.0±0.3	7.4±0.4	10.2±0.3	12.4±0.7	41.4±0.4	0.49±0.02	1.90±0.02
GD89A	90.0±0.9	10.6±0.8	17.0±0.5	16.5±1.0	48.5±0.3	1.25±0.01	1.86±0.03
GD89B	90.0±1.1	7.5±0.6	12.4±0.4	12.3±0.8	43.8±0.3	1.51±0.04	1.86±0.03
GD89C	90.0±0.9	9.1±0.6	13.2±0.4	14.3±1.0	46.3±0.3	0.51±0.00	1.91±0.02
GD89D	90.0±0.5	8.5±0.9	14.8±0.9	16.4±2.1	47.4±0.6	1.38±0.02	1.85±0.04
GD76B	90.0±1.0	21.2±1.9	34.7±1.1	21.9±2.7	48.6±0.5	1.92±0.06	1.88±0.08
GD76C	90.0±0.8	5.6±0.6	7.0±0.6	8.9±1.0	37.1±0.7	0.40±0.03	1.91±0.04
GD79B	90.0±1.0	11.9±0.7	16.4±0.4	17.7±0.7	48.4±0.3	1.77±0.02	1.83±0.02
GD79C	90.0±0.6	7.4±0.5	12.8±0.3	13.0±0.6	44.8±0.2	2.22±0.02	1.98±0.02
GD91A	90.0±1.1	8.0±0.8	11.9±0.5	11.9±0.7	43.3±0.4	0.94±0.01	1.84±0.02
GD91B	90.0±0.8	8.5±0.7	12.2±0.4	13.3±0.9	43.8±0.3	1.09±0.02	1.88±0.03
GD91C	90.0±1.1	11.6±0.6	17.4±0.4	17.8±0.8	49.5±0.2	2.67±0.01	1.84±0.03
GD91D	90.0±0.4	7.0±0.5	10.6±0.3	11.7±0.7	42.4±0.3	0.47±0.01	1.87±0.03
GD00A	90.0±0.6	10.8±0.5	16.9±0.4	16.6±0.9	49.7±0.2	1.79±0.01	1.90±0.02
GD00B	90.0±0.9	8.9±0.7	12.5±0.6	11.0±1.2	44.1±0.5	1.29±0.02	2.00±0.04
GD00C	90.0±0.8	6.4±0.6	10.0±0.4	10.3±0.6	41.0±0.4	0.56±0.01	1.94±0.02
GD00D	90.0±0.8	6.0±0.6	9.1±0.4	9.9±0.7	38.9±0.4	0.60±0.01	1.87±0.02
GD02A	90.0±0.5	11.8±0.7	18.6±0.4	18.4±0.8	49.9±0.2	3.58±0.01	1.92±0.02
GD02B	90.0±0.7	7.4±0.8	13.8±0.6	11.4±0.9	45.8±0.4	0.68±0.03	1.97±0.03
GD02C	90.0±0.9	7.6±0.6	11.2±0.4	11.9±1.0	42.3±0.4	1.96±0.03	1.79±0.07
GD02D	90.0±0.7	15.0±1.7	27.6±1.1	23.2±2.5	56.1±0.8	2.93±0.12	1.95±0.05

Table 6.3: Gammy-ray background survival fractions (in percentages), $b_{A/E}$ at DEP, and energy resolution at DEP for the thirty enriched BEGe detectors operated in vacuum cryostat. In the case of the detector GD32D, the pulse shape performance was measured before (I) and after (II) reprocessing. For detectors showing no A/E double-peak structures, $b_{A/E}$ is correlated with the PSD performance. The uncertainty of the survival fraction includes the statistical and the systematic uncertainty.

Detector	DEP (1593 keV) δ_{norm}	δ_{stat}	SEP (2104 keV) δ_{norm}	δ_{dep}	FEP (2615 keV) δ_{stat}	δ_{norm}	δ_{dep}	FEP (1620 keV) δ_{stat}	δ_{norm}	δ_{dep}	ROI (2004-2074 keV) δ_{stat}	δ_{norm}	δ_{dep}
GD32A	± 0.94	± 0.26	± 0.84	± 0.54	± 0.11	± 0.60	± 0.37	± 0.41	± 0.85	± 0.69	± 0.22	± 0.28	± 0.19
GD32B	± 1.32	± 0.22	± 0.64	± 0.44	± 0.09	± 0.54	± 0.40	± 0.36	± 0.66	± 0.5	± 0.26	± 0.47	± 0.36
GD32C	± 1.98	± 0.42	± 0.91	± 0.70	± 0.18	± 0.56	± 0.33	± 0.66	± 1.11	± 0.91	± 0.44	± 0.41	± 0.26
GD32D-I	± 0.31	± 0.43	± 0.17	± 1.48	± 0.19	± 0.20	± 0.82	± 0.65	± 0.27	± 1.51	± 0.39	± 0.10	± 0.41
GD32D-II	± 0.87	± 0.15	± 0.55	± 0.33	± 0.07	± 0.39	± 0.24	± 0.27	± 0.66	± 0.54	± 0.20	± 0.30	± 0.18
GD35A	± 0.34	± 0.17	± 0.39	± 0.88	± 0.07	± 0.26	± 0.59	± 0.28	± 0.43	± 1.09	± 0.17	± 0.19	± 0.42
GD35B	± 1.15	± 0.19	± 0.54	± 0.52	± 0.08	± 0.48	± 0.34	± 0.33	± 0.86	± 0.63	± 0.25	± 0.45	± 0.35
GD35C	± 0.60	± 0.32	± 0.43	± 0.67	± 0.14	± 0.37	± 0.49	± 0.45	± 0.54	± 0.71	± 0.27	± 0.20	± 0.28
GD61A	± 0.69	± 0.18	± 0.32	± 0.30	± 0.08	± 0.31	± 0.26	± 0.32	± 0.63	± 0.61	± 0.22	± 0.24	± 0.22
GD61B	± 0.79	± 0.20	± 0.60	± 0.42	± 0.09	± 0.37	± 0.25	± 0.37	± 0.60	± 0.53	± 0.21	± 0.19	± 0.13
GD61C	± 0.33	± 0.21	± 0.16	± 0.35	± 0.09	± 0.15	± 0.29	± 0.44	± 0.28	± 0.51	± 0.25	± 0.11	± 0.23
GD89A	± 0.92	± 0.27	± 0.58	± 0.46	± 0.12	± 0.37	± 0.29	± 0.48	± 0.67	± 0.61	± 0.27	± 0.11	± 0.08
GD89B	± 1.15	± 0.16	± 0.50	± 0.22	± 0.08	± 0.37	± 0.18	± 0.30	± 0.70	± 0.34	± 0.20	± 0.23	± 0.11
GD89C	± 0.89	± 0.23	± 0.49	± 0.28	± 0.10	± 0.35	± 0.24	± 0.41	± 0.71	± 0.52	± 0.23	± 0.16	± 0.11
GD89D	± 0.52	± 0.48	± 0.48	± 0.61	± 0.24	± 0.49	± 0.73	± 1.02	± 1.24	± 1.31	± 0.50	± 0.17	± 0.28
GD76B	± 1.01	± 1.12	± 0.38	± 1.49	± 0.43	± 0.36	± 0.99	± 1.46	± 0.55	2.25	± 0.41	± 0.08	± 0.24
GD76C	± 0.84	± 0.24	± 0.40	± 0.37	± 0.10	± 0.37	± 0.24	± 0.46	± 0.49	± 0.81	± 0.34	± 0.36	± 0.42
GD79B	± 1.00	± 0.27	± 0.55	± 0.33	± 0.11	± 0.35	± 0.22	± 0.46	± 0.37	± 0.30	± 0.25	± 0.11	± 0.07
GD79C	± 0.57	± 0.15	± 0.39	± 0.32	± 0.07	± 0.25	± 0.21	± 0.27	± 0.40	± 0.37	± 0.17	± 0.12	± 0.11
GD91A	± 1.06	± 0.22	± 0.57	± 0.45	± 0.10	± 0.39	± 0.26	± 0.45	± 0.48	± 0.00	± 0.25	± 0.24	± 0.17
GD91B	± 0.84	± 0.22	± 0.49	± 0.37	± 0.10	± 0.34	± 0.26	± 0.40	± 0.62	± 0.51	± 0.24	± 0.19	± 0.15
GD91C	± 1.10	± 0.25	± 0.50	± 0.33	± 0.11	± 0.31	± 0.17	± 0.43	± 0.57	± 0.33	± 0.24	± 0.05	± 0.03
GD91D	± 0.37	± 0.20	± 0.25	± 0.42	± 0.09	± 0.15	± 0.25	± 0.37	± 0.27	± 0.55	± 0.25	± 0.09	± 0.17
GD00A	± 0.56	± 0.24	± 0.33	± 0.35	± 0.11	± 0.29	± 0.30	± 0.43	± 0.54	± 0.60	± 0.23	± 0.03	± 0.04
GD00B	± 0.91	± 0.33	± 0.36	± 0.57	± 0.14	± 0.35	± 0.50	± 0.54	± 0.35	± 1.02	± 0.35	± 0.19	± 0.30
GD00C	± 0.80	± 0.16	± 0.45	± 0.36	± 0.07	± 0.34	± 0.27	± 0.28	± 0.42	± 0.38	± 0.20	± 0.25	± 0.20
GD00D	± 0.83	± 0.13	± 0.49	± 0.29	± 0.06	± 0.34	± 0.21	± 0.24	± 0.54	± 0.41	± 0.17	± 0.28	± 0.19
GD02A	± 0.53	± 0.22	± 0.42	± 0.46	± 0.10	± 0.27	± 0.26	± 0.39	± 0.48	± 0.58	± 0.20	± 0.01	± 0.02
GD02B	± 0.67	± 0.24	± 0.46	± 0.58	± 0.12	± 0.38	± 0.42	± 0.45	± 0.41	± 0.66	± 0.18	± 0.18	± 0.20
GD02C	± 0.91	± 0.26	± 0.48	± 0.32	± 0.10	± 0.30	± 0.24	± 0.41	± 0.64	± 0.60	± 0.24	± 0.23	± 0.19
GD02D	± 0.73	± 0.80	± 0.33	± 1.44	± 0.39	± 0.47	± 0.87	± 1.52	± 0.77	± 1.88	± 0.63	± 0.20	± 0.48

Table 6.4: The statistical and systematic uncertainties of the survival fractions for various samples. δ_{stat} represents the systematic uncertainty from statistical uncertainty after the A/E PSD cut. δ_{norm} describes the systematic uncertainty due to the A/E normalization procedure. δ_{dep} is the systematic uncertainty due to the statistical uncertainty of the DEP events.

Chapter 7

The Segmented Broad Energy Germanium Detector

BEGe detectors are used in neutrinoless double beta-decay [24] and dark matter searches [125]. They have excellent energy resolution and notable pulse shape discrimination in distinguishing SSEs and MSEs. The disadvantage of the BEGe detectors is the degeneracy in angular direction. Detector segmentation can provide additional spatial information, useful to efficiently disentangle different event topologies [163, 164, 165].

A novel BEGe detector with four-fold segmentation design has been built, which allows to break the degeneracy in azimuthal direction with a minimum number of contacts. Results of the characterizations and the sensitivity of the position reconstructions performed with this new type of detector are presented in this chapter.

7.1 Experimental Setup

7.1.1 Segmented BEGe Detector, Test Cryostat, and DAQ

The segmented BEGe detector is a high purity n-type BEGe detector with four-fold segmentations in the azimuthal angle ϕ. The detector geometry and the segmentation scheme are shown in Fig. 7.1. It was designed by the GEDET group and made by Canberra, France. The germanium diode has dimensions of 75 mm in diameter and 40 mm in height. The total mass is 940 g. The operation voltage is +4500 volt and is applied on the n^+ core contact. The measured energy resolutions as provided by the manufacturer are summarized in Table 7.1.

The detector was operated in K1 conventional vacuum test cryostat [169]. It was produced from Canberra, France for the characterization of segmented HPGe detectors. K1 test stand is shown in Fig. 7.2. The K1 consists of a two-walled aluminum cryostat with a combined thickness of 6 mm. The detector in K1 is cooled down by a copper cooling finger submerged in a 60 l liquid nitrogen dewar. A Pt100 resistor, installed close to the cooling finger, is used to monitor the temperature of the coldest part of the cooling finger, like this

Energy [keV]	core	segment 1	segment 2	segment 3	mantle
122	1.0	1.9	2.0	2.1	3.7
1173	4.1	3.6	3.6	3.8	5.2
1332	4.4	3.7	3.8	4.2	5.5

Table 7.1: Measured FWHMs of individual channels provided by manufacturer.

giving information on the temperature of the detector itself. The operational temperature is in a range between 94-109 K. The cryostat can be pumped to about 10^{-6} mbar. The K1 test stand is situated in a room with stable controlled condition of temperature and humidity.

The schematic diagram of the front-end electronics of the segmented BEGe detector is given in Fig. 7.3(a). The signals from core and segments were both read out using PSC-823C charge-sensitive pre-amplifiers with a decay time of 50 μs and a bandwidth of about 10 MHz [158]. A junction gate field-effect transistor (JFET) for the core signal is located in the cryostat close the detector. The high voltage bias to the detector is decoupled with a charge resistor (1 GΩ) and a decoupling capacitor (1.2 nF) to the JFET source node in the cryostat. The FETs for the segments and the mantle are integrated in the pre-amplifiers outside. The cold FET of the core pre-amplifier is AC coupled while all segments and the mantle are DC coupled. The croystat has 4 feed-throughs. The layout of the feed-throughs of the detector cryostat is shown in Fig. 7.3(b). A 9-channel feed-through and the high-voltage feed-through are on one side of the cryostat. The other two 7-channel feed-throughs are located on the opposite site. The cryostat holds two copper ears designed at Max-Planck-Institut für Physik to house the pre-amplifiers.

The output signals were recorded by a 75 MHz DGF Pixie-4 data acquisition system with two four-channel modules [159]. For each event, the time stamp, energy, and pulse shape from each channel can be recorded. The trace-length of the charge pulse of each channel was set to 13.6 μs. The DAQ system is triggered by core signals above $\sim$20 keV.
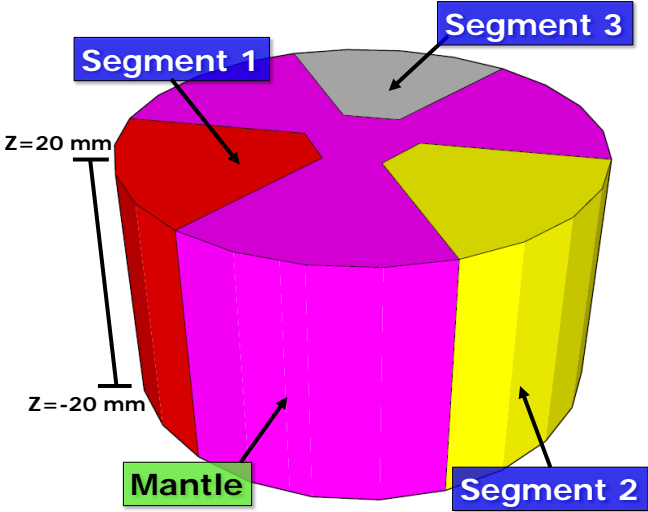
(a)
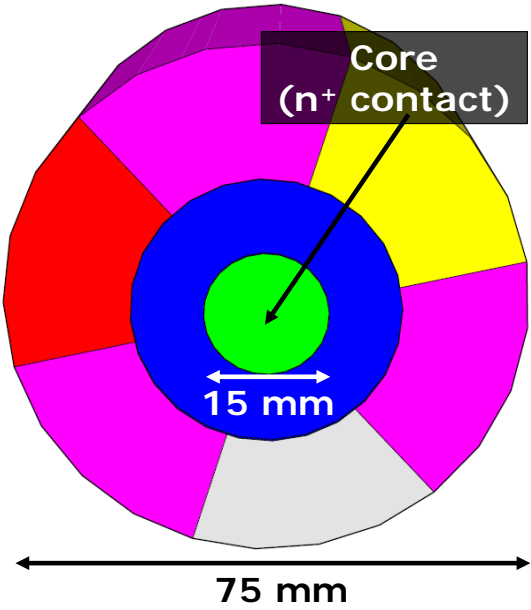
(b)

Figure 7.1: Geometry of the 4 segments of the n-type BEGe detector with the detector dimensions. (a) Top view. (b) Bottom view.
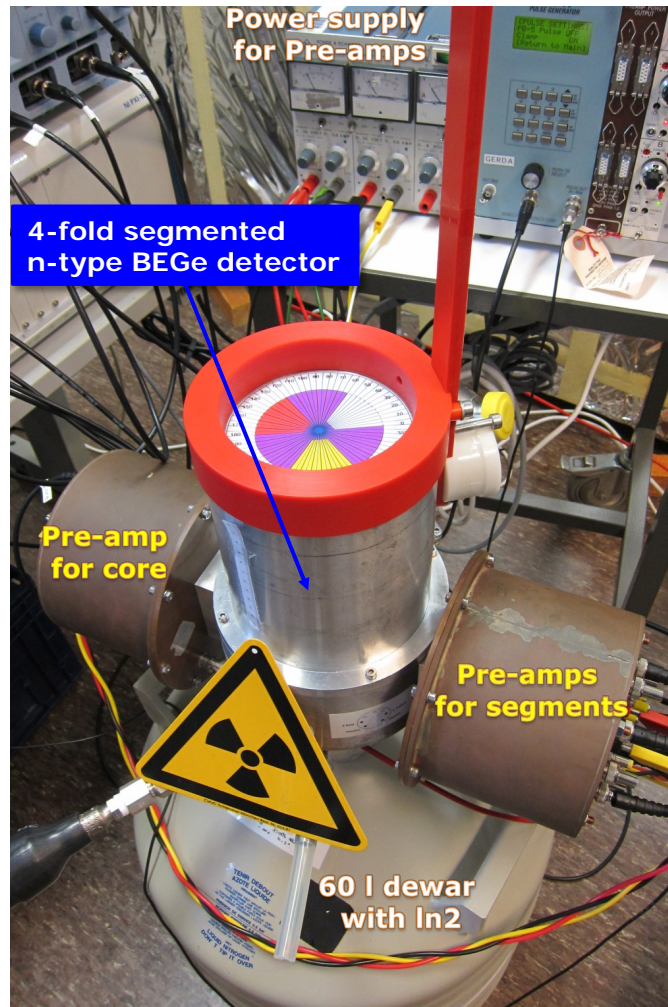
Figure 7.2: The K1 test stand with source pointing system on top of the end-cap of K1. The segmented BEGe detector in K1 is cooled down by a copper cooling finger submerged in a 60 l liquid nitrogen dewar.
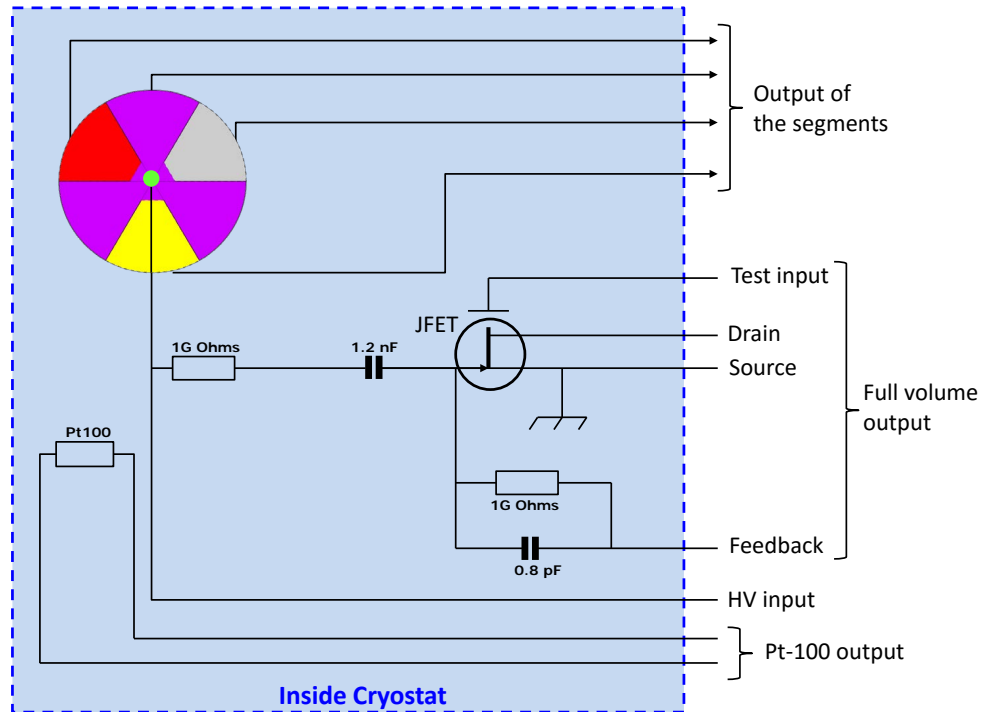
(a) Schematic drawing inside cryostat
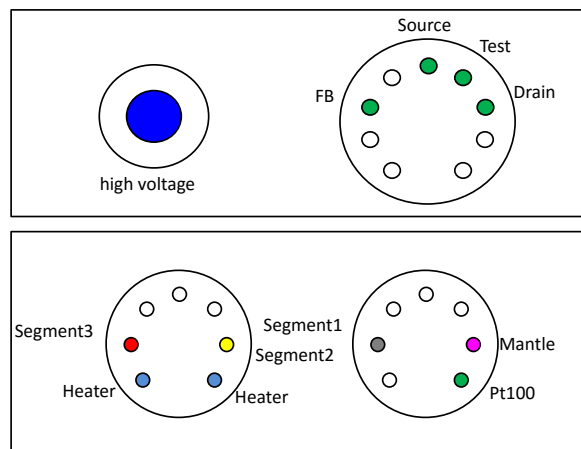
(b) Feed-throughs

Figure 7.3: (a) Schematics of the front-end electronics of the segmented BEGe detector. The FETs for the segments and the mantle are integrated in the PSC-823C pre-amplifiers outside the K1. (b) Layout of the feed-throughs of the detector cryostat.

Energy [keV]	branching ratio (%)
30.625	34.99
30.973	64.52
34.987	11.63
80.997	34.06
276.398	7.16
302.853	18.33
356.017	62.05
383.851	8.94

Table 7.2: List of major γ-lines of ^{133}Ba. The rest γ-lines refer to [160] for more details.
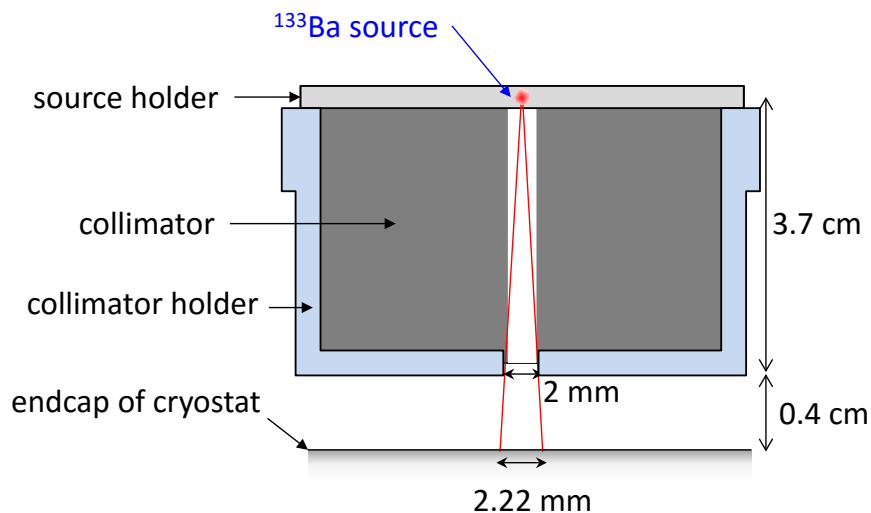
Figure 7.4: Schematic diagram of the Tungsten collimator and the ^{133}Ba source.

7.1.2 Characterization using Collimated ^{133}Ba Source

A ^{133}Ba source with activity of 37 kBq was used for the detector characterizations. Table 7.2 summarizes the major γ-lines from the ^{133}Ba decay that are used for energy calibrations.

The schematic diagram of the source and the collimator is shown in Fig. 7.4. The ^{133}Ba source was mounted on the top of a Tungsten collimator to ensure that the beam spot size is well-controlled. The collimator has a bore hole with 3 mm in diameter at the center. The beam spot size on the end-cap of cryostat is about 2.22 mm.

Spatial Distribution of Energy Deposition

The spatial distributions of energy depositions inside the detector caused by 356 keV, 81 keV, and 31 keV γs were studied by Monte Carlo simulation using MaGe [105]. Photon

calibration beams were simulated from the top (r=0 mm, Z=20 mm) of the end-cap. The center-of-energy-deposition along the z-direction is calculated for each event as:

$$Z_c = \frac{\sum_j E_j Z_j}{\sum_j E_j} \; , \tag{7.1}$$

where j is the number of the hits, E_j is the individual energy deposition, Z_j is the hit position in Z, and the sum runs over all individual energy depositions in the Ge diode.

The Z_c distributions of 356 keV, 81 keV, and 31 keV photons are shown in Fig. 7.5. It can be observed that the 356 keV photons can deposit their energies in a rather broad range in the crystal, whereas 81 keV and 31 keV photons deposit their energies only in a localized region. The distance of the averaged energy barycenter, with respect to the detector surface, for the 356 keV, 81 keV, and 31 keV γs are 16.78 mm, 2.42 mm, and 0.15 mm, respectively. In order to keep the characteristic feature of the core and segment pulses, the 81 keV and 31 keV γ-peaks were used as samples for characterizations [1].
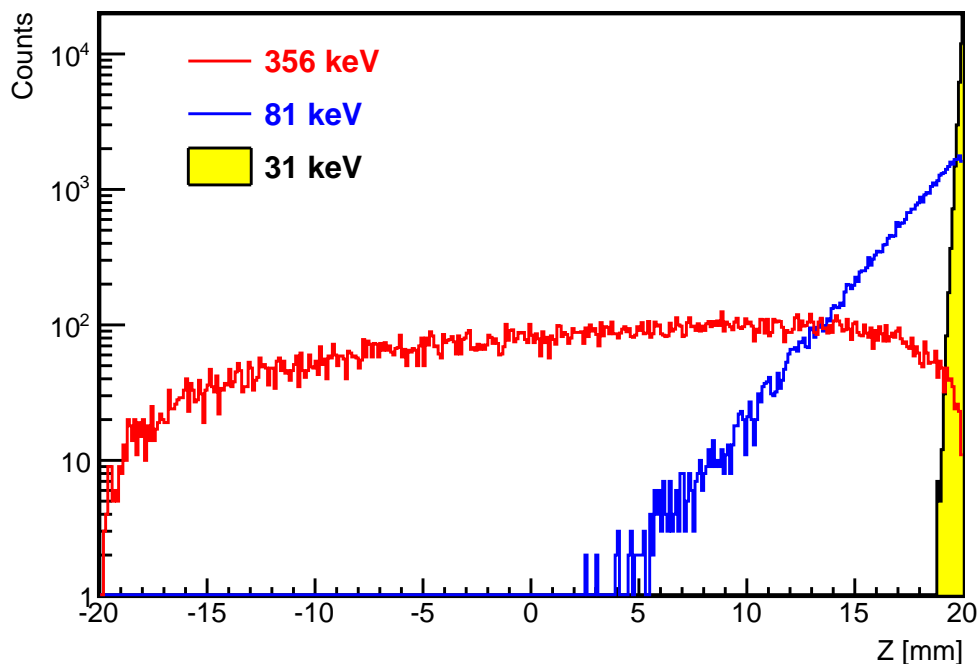
Figure 7.5: Simulated enegy-weighted distributions along Z-direction for mono energetic photon beams at 356 keV, 81 keV, and 31 keV. The photons are entering from the top of the end-cap (r=0 mm, Z=20 mm).

---

[1]It is especially important for the mirror pulses since the polarities of the mirror pulses depend on the locations of energy depositions.

7.1.3   Measurements and Data Sets

Three main sets of scan measurements using collimated ^{133}Ba source were performed. The top-scan measurements were carried out on the top of the end-cap of the K1 cryostat. The measurements were performed by scanning with equal radius of 25 mm with respect to the center of the end-cap and a 5 degree in azimuth angle ϕ between each scanning position (see Fig. 7.6(a)). In the case of the measurements, it was discovered that the holder for Ge crystal is tilted. This was confirmed by visual inspection, when the cryostat was opened for service. The center of the end-cap does not align to the center of the detector (discentralization). Hence, the measured scanning positions need to be corrected. All the measured positions presented in this work were converted to represent the position with respect to the center of the detector.

A side-scan measurement was performed at Z=0 mm (see Fig. 7.1(a)), scanning with 5 degree displacement in ϕ between individual measurements, as seen in Fig. 7.6(b).

Additionally, r-scan measurements were performed with constant azimuth angle but varying radius, as shown in Fig. 7.6(c). The source-pointed azimuth angles are 341°, 299°, 285°, 272°, 258°, 215°, 170°, 121°, 105°, 88°, 72°, and 26°.

For each measured data point, there were 64000 events in total with ∼20 minutes data taking time.

(a)

(b)

(c)
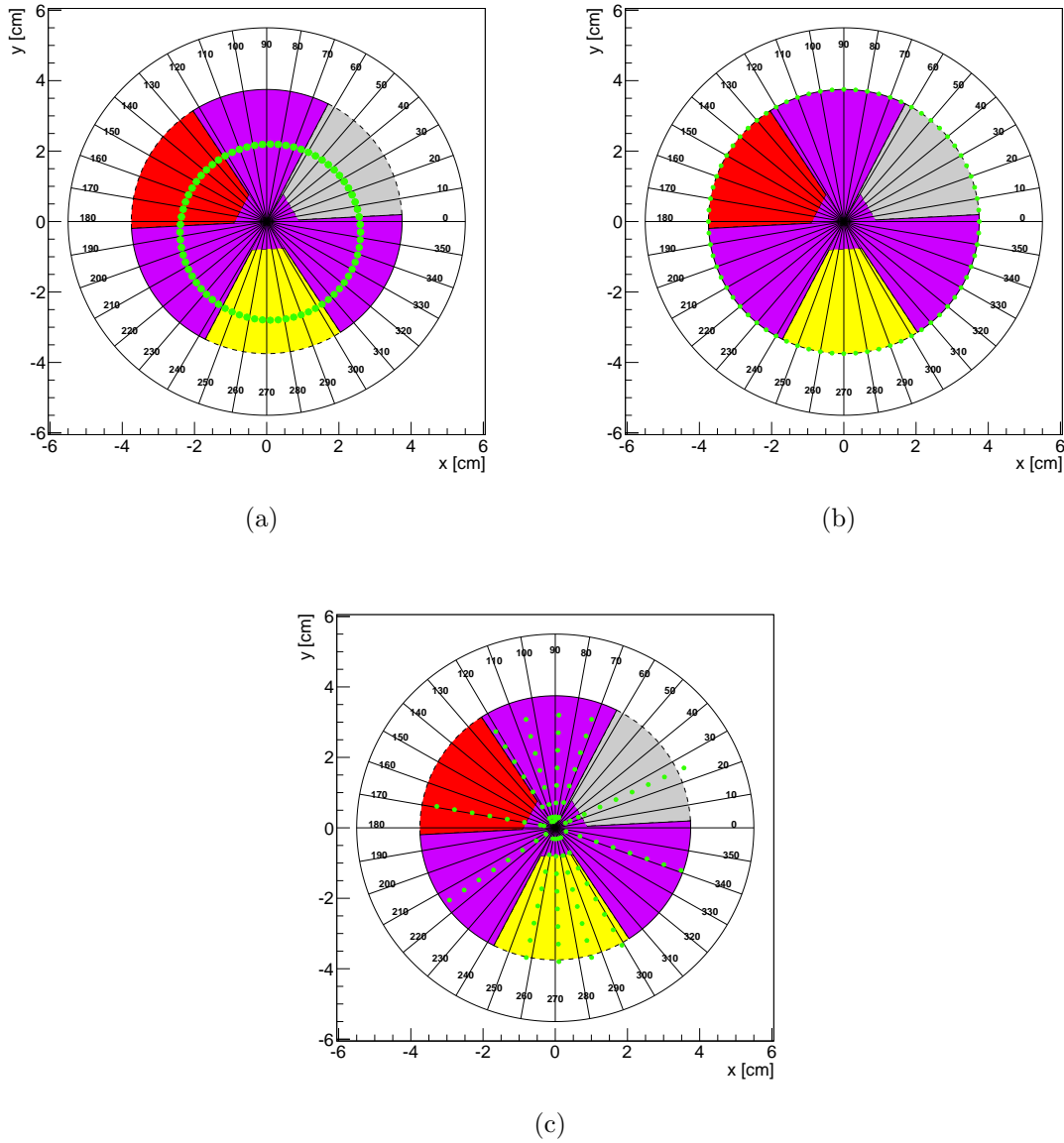
Figure 7.6: Sketch of positions where measurements were taken using a collimated ^{133}Ba source (top view). The diameter of the beam spot is presented in an actual diameter in half. (a) Top-scans with the same radius but different azimuth angles ϕ. (b) Side-scans with Z=0 mm along different azimuth angles ϕ. (c) R-scans with fixed ϕ along different radius.

channel	pre-amplifier decay constant [μs]
core	53.32±0.002
segment 1	49.17±0.010
segment 2	50.62±0.010
segment 3	49.51±0.010
mantle	61.40±0.014

Table 7.3: Measured decay constants for all the channels of the segmented BEGe detector.

7.2   Energy Calibration and Cross-talk Correction

7.2.1   Off-line Energy Reconstruction

It was found that the DGF Pixie-4 can not correctly handle the pulses with long rise time ($>1\,\mu$s), the energies of all channels were reconstructed off-line. In the beginning, a commonly used trapezoidal filter with a rise time of $5.547\,\mu$s and a flat top of $2.027\,\mu$s was applied to the recorded charge pulses, and the maximal output value is taken as the uncalibrated energy. However, this method gives the wrong energy calculations for the mirror pulses, since it takes the maximum output value of the energy filter. Hence, a new energy reconstruction method is needed.

For each charge pulse, the energy reconstruction was performed in the following way:

- pre-amplifier decay time correction,

- baseline subtraction,

- amplitude calculation.

Before performing the energy reconstruction, the decay time from the pre-amplifier RC circuit is corrected (τ-correction), so the reconstructed pulse height does not depend on the pulse rise time. The τ-correction is applied for each channel. The measured preamp decay constants are summarized in Table 7.3 (refer to Appendix B for details of τ-correction.).

In the second step, the baseline is set to zero by subtracting the average value of the first 337 bins (4.493 μs). In the last step, the uncalibrated energy is calculated as the average value of the last 497 bins (6.627 μs) subtracting the average value of the baseline. Without looking for the maximum values, the new reconstruction method is not affected by mirror pulses. An example of energy reconstruction with baseline subtraction after τ-decay correction is shown in Fig. 7.7.
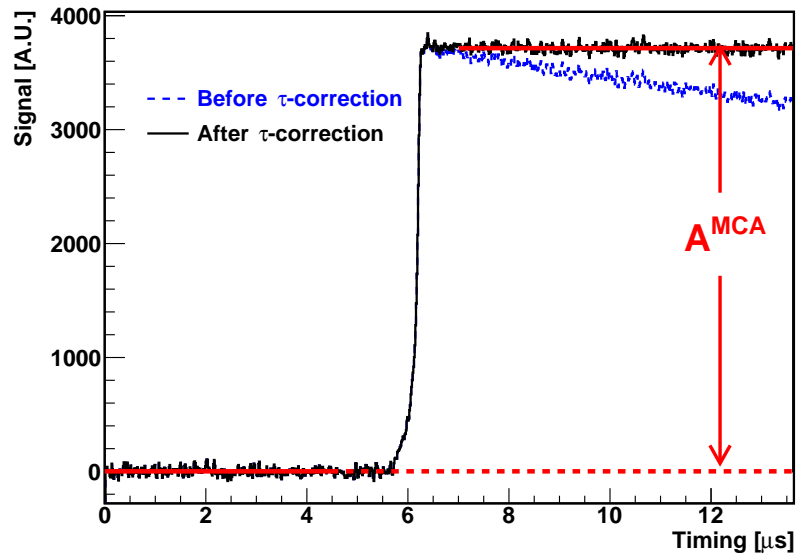
Figure 7.7: Charge pulse of the core channel before (blue) and after (black) τ-correction, as well as the calculation of the pulse height. The uncalibrated energy (A_{MCA}) is derived from the subtraction of average values from the last $6.627\,\mu$s and the first $4.493\,\mu$s.

7.2.2 Cross-talk Correction and Energy Calibration

After the off-line reconstruction of the pulse height, the cross-talk correction and energy calibration are performed. Only cross-talks among the segments and the mantle have been observed. There is no significant cross-talk from the core to segments and mantle or vice versa. Hence the core energy can be calibrated independently. The cross-talk among the three segments is $\sim$ -0.15 %, the one from the segment to the mantle is $\sim$0.5 %, and the one from the mantle to segments is $\sim$5 %.

The procedure of cross-talk correction and energy calibration is given as follows :

- core energy calibration,

- segment-to-segment cross-talk correction using single segment events,

- calibration of segment energy using a ratio method.

In the first step, the core energy is calibrated by using the 7 major γ-lines from the ^{133}Ba source listed in Table 7.2. The first two γ-lines are averaged to a single one with 30.851 keV energy. The uncalibrated core pulse height relates to the known energy by a linear dependence:

$$E_{core} = \lambda_{core} \; A_{core}^{MCA} \; , \tag{7.2}$$

where E_{core} is the calibrated core energy, λ_{core} is the core energy scale, and A_{core}^{MCA} is the uncalibrated core pulse height.

The second step is to perform cross-talk corrections among segments. The relation before and after the cross-talk correction, presented in a matrix form, is given by:

$$\overrightarrow{A}^{MCA} = \overleftrightarrow{C} \; \overrightarrow{A}$$

$$\begin{pmatrix} A_1^{MCA} \\ A_2^{MCA} \\ A_3^{MCA} \\ A_4^{MCA} \end{pmatrix} = \begin{pmatrix} C_{11} & C_{12} & C_{13} & C_{14} \\ C_{21} & C_{22} & C_{23} & C_{24} \\ C_{31} & C_{32} & C_{33} & C_{34} \\ C_{41} & C_{42} & C_{43} & C_{44} \end{pmatrix} \begin{pmatrix} A_1 \\ A_2 \\ A_3 \\ A_4 \end{pmatrix} \; , \tag{7.3}$$

where:
A_i^{MCA}: the segment i pulse height before cross-talk correction
C_{ij}: the cross-talk coefficient contributed from the segment j to the segment i [2]
A_i: the segment i pulse height after cross-talk correction
index i, j: 1-3 for segment 1-3 and 4 for the mantle

The cross-talk matrix elements in $\overleftrightarrow{C}$ can be disentangled by selecting single segment events [3]. Hence, the cross-talk coefficient element $C_{jk} = A_j^{MCA}/A_k^{MCA}$ can be calculated [4].

The process for the cross-talk correction can be summarized as follows:

---

[2]If $i=j$, $C_{ij}=1$ since no cross-talk comes from the segment itself. (the second order cross-talk correction is not considered since the coefficient is small in our system.)

[3]Single segment events are the events with full energy depositions in only one segment.

[4]By definition, choosing single-segment-k events means $A_k^{MCA}=A_k$ and $A_{j \neq k}=0$.

- selection of pure single-segment events,

- estimation of the cross-talk coefficient from pure single segment events to other segments,

- performing inverse transformation of the cross-talk matrix.

The first step of cross-talk correction is done by requiring a single-segment cut. Pure single-segment-k events are selected by requiring:

$$A_k^{MCA} > A_{th} \ , \tag{7.4}$$

where A_k^{MCA} is the segment k pulse height and A_{th} is the threshold of the pulse height. A_{th} is set to 500 for each single-segment event selection, which corresponds to $\sim$50 keV.

In the second step of cross-talk correction, the ratio of A_j^{MCA}/A_k^{MCA} ($j \neq k$) is fitted with a Gaussian fit where the centroid of the Gaussian represents the cross-talk coefficient C_{jk}. A typical ratio plot to derive cross-talk coefficients is shown in Fig. 7.8. A typical cross-talk matrix is given as follows [5]:

$$\begin{pmatrix} 1 & -0.00114 & -0.00113 & 0.07151 \\ -0.00133 & 1 & -0.00102 & 0.07386 \\ -0.00188 & -0.00138 & 1 & 0.07660 \\ 0.00748 & 0.00466 & 0.00630 & 1 \end{pmatrix}$$

The uncalibrated segment energies after cross-talk correction can be derived by the inverse transformation, namely, $\overrightarrow{A} = \overleftrightarrow{C}^{-1} \overrightarrow{A}^{MCA}$.

The last step is the segment energy calibration. After cross-talk correction, the segment energy is performed by using the ratio of the segment pulse height to the core pulse height:

$$E_j = \lambda_j \, A_j \ ,$$
$$\lambda_j = \lambda_{core} \cdot \left(\frac{A_{core}}{A_j} \right) \ , \tag{7.5}$$

where E_j is the calibrated segment j energy , λ_j is the segment j energy scale, and A_j is the segment j pulse height after cross-talk correction.

The advantage of using this calibration method is that no energy peaks from the segment energy spectrum are required to do the calibration. Hence the method is applicable for the segments that are not facing the collimated ^{133}Ba source.

Fig. 7.9(a) shows the scatter plot of the segment 1 pulse height (A_1^{MCA}) as a function of the core pulse height (A_{core}^{MCA}) before cross-talk correction at scan position (r=25 mm, ϕ=212°) from the top-scan. The source pointed on the mantle. It can be seen that the upper band corresponds to the single-segment 1 events, whereas the lower band represents the cross-talk events from mantle to segment 1. Fig. 7.9(b) shows segment 1 energy (E_1) versus core energy (E_{core}) after cross-talk correction and energy calibration. The cross-talk correction is applied to each individual bin of the pulses. The reconstructed energy of the cross-talk events were zero.

---

[5]At source position of (r=25 mm, ϕ=212°) from top scan.
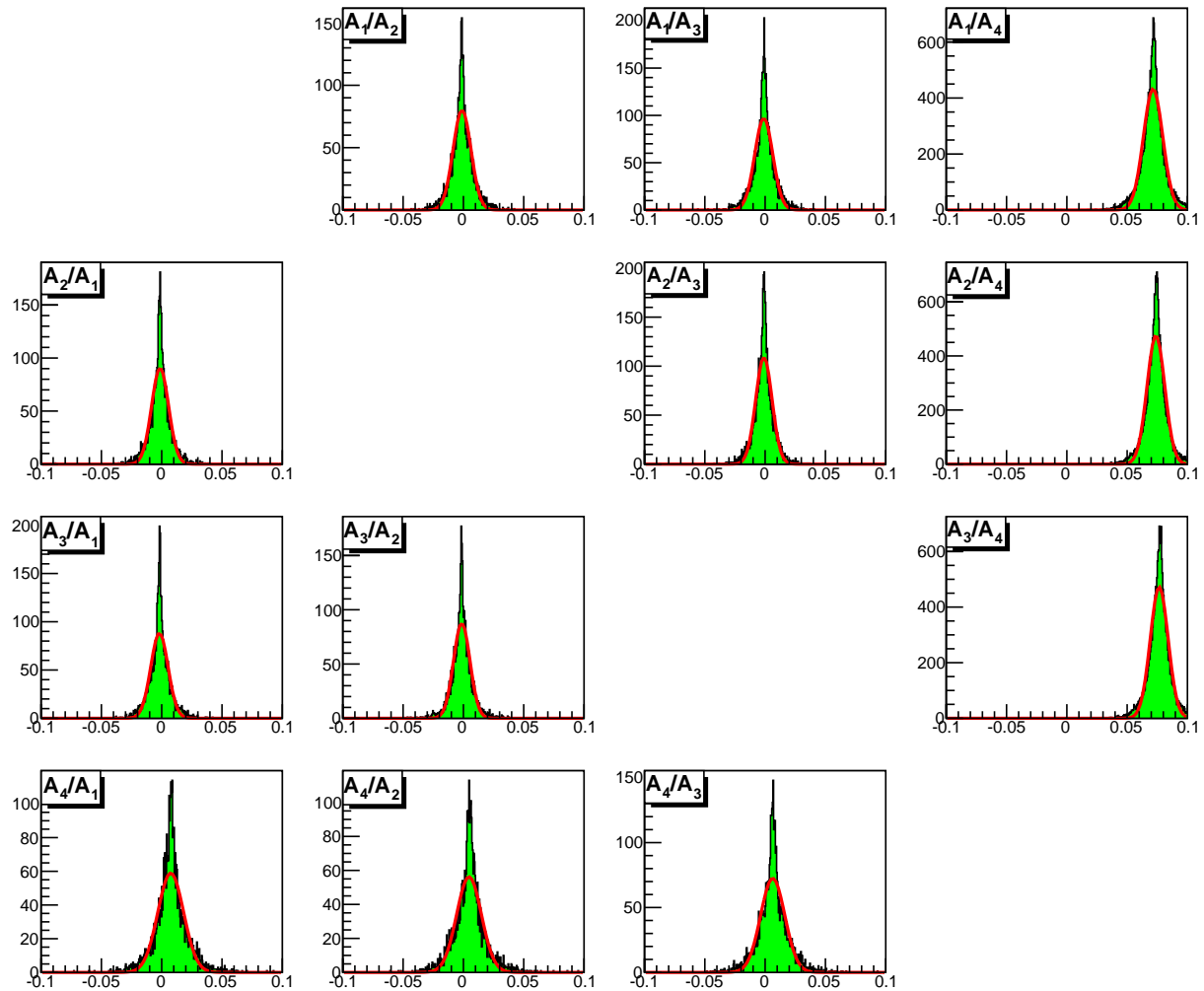
Figure 7.8: A cross-talk matrix at position of (r=25 mm, ϕ=212°) from top scan. The centroids of the fitted Gaussians represents the cross-talk coefficients.
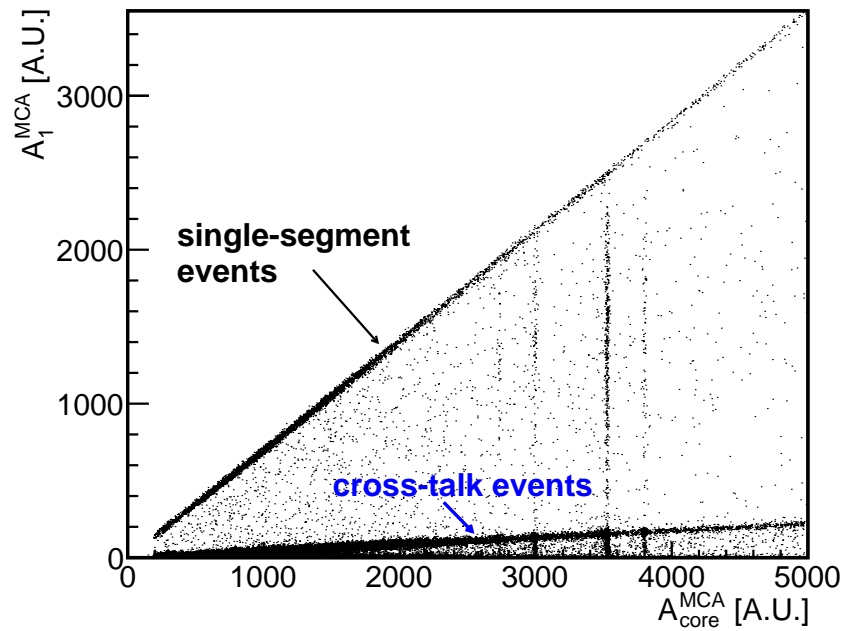
(a)
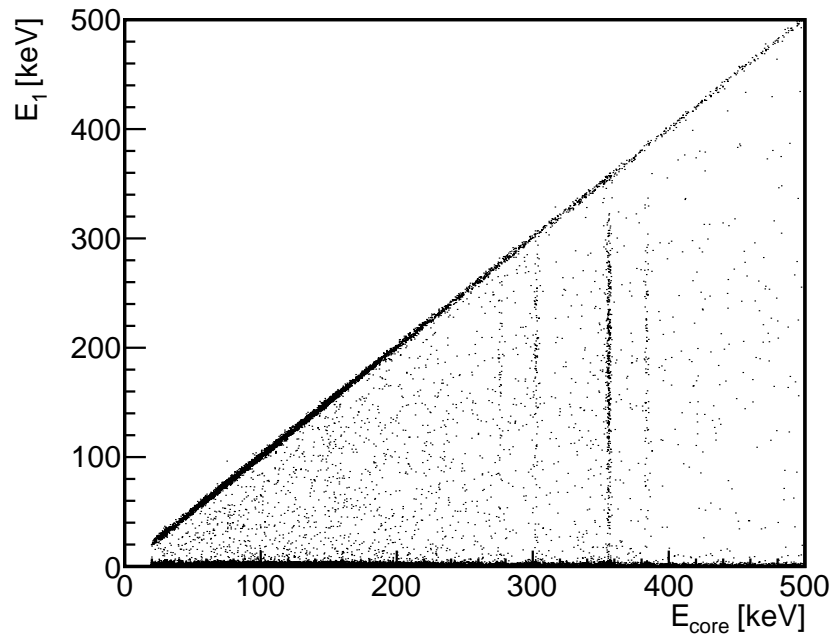
(b)

Figure 7.9: (a) Scatter plot of segment 1 pulse height versus core pulse height. The lower band represents the cross-talk events. (b) Scatter plot of segment 1 energy versus core energy after cross-talk and energy calibration. The scan position is at (r=25 mm, ϕ=212°) from top scan. The source pointed on the mantle.

Validations of the Cross-talk Correction Method

In order to validate the cross-talk correction, the result can be checked by two conditions:

- baselines of cross-talk corrected mirror pulses come back to zero,

- sum of segment energy equals the core energy.

Fig. 7.10 gives an example of a single event with 355.03 keV before and after cross-talk correction (at r=25 mm and ϕ=212°, from top scan). It can be seen that the baselines of the mirror pulses come back to zero.

If the cross-talk procedure is well-defined, the center of distribution of the energy sum (E_{sum}) of multi-segment events minus the core energy should be positioned at zero. Fig. 7.11 shows (E_{sum}-E_{core}) for 2- and 3-segment events. N-segment events require any of the energy deposits of the N segments to be above 10 keV. It can be seen in Fig. 7.11 that a peak is centered at zero, showing that the crosstalk correction is valid. For two segment events there is a tail towards the left ($E_{core} > \sum_j E_j$). This can result from events with energy deposits of $E_j < E_{th}$. Note that these events do not deter the analysis in the following, as the results deal with single segment events only.
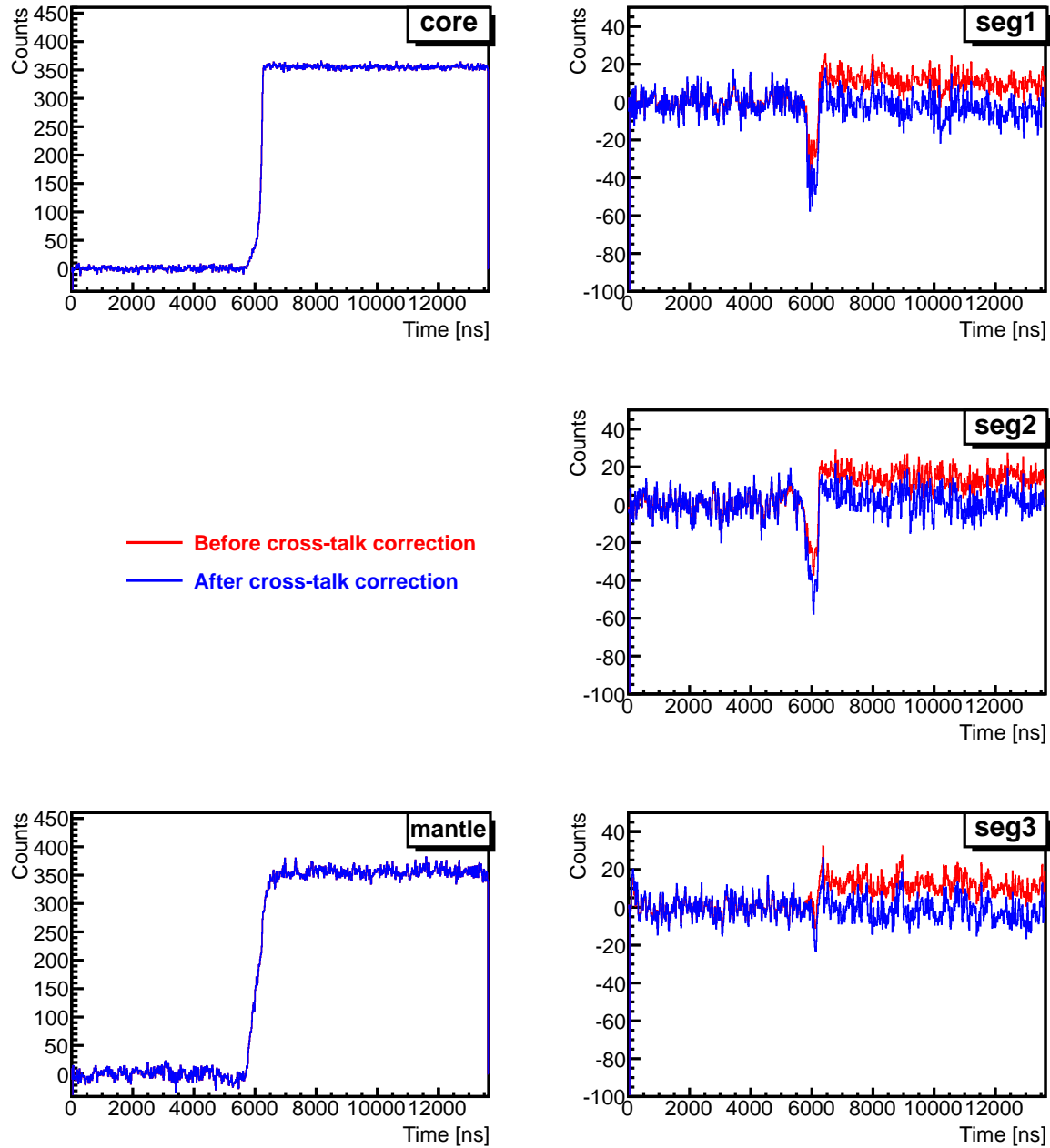
Figure 7.10: A single event before and after cross-talk correction with the source pointed at r=25 mm and ϕ=212° (on the mantle). Charge pules before (red) and after (blue) cross-talk correction are shown. The core energy of this event is 355.03 keV. It can be clearly seen that the baselines of mirror pulses come back to zero after cross-talk correction.
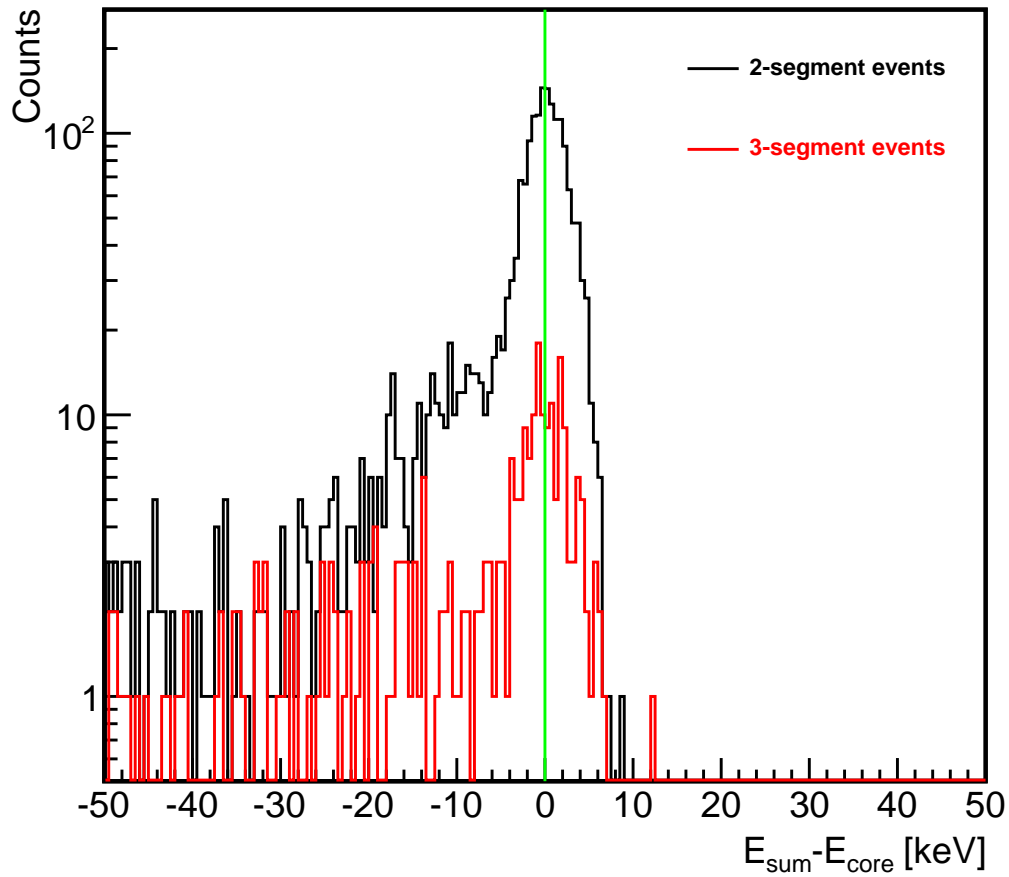
Figure 7.11: E_{sum} minus E_{core} with multi-segment event selections. The black histogram is for 2-segment event selection and the red one for 3-segment event selection.

Energy	Energy resolution (FWHM) [keV]				
[keV]	core	segment 1	segment 2	segment 3	mantle
30.851	1.50±0.02	9.30±0.32	3.33±0.06	6.63±0.18	6.40±0.11
34.987	1.66±0.04	7.78±0.80	3.02±0.14	4.05±0.47	4.01±0.33
80.997	1.62±0.03	8.65±0.18	3.31±0.05	6.20±0.11	6.25±0.13
276.398	1.80±0.08	7.23±0.79	2.78±0.17	5.06±0.44	6.04±0.48
302.853	1.76±0.05	7.59±0.36	3.21±0.09	5.61±0.23	5.77±0.21
356.017	1.80±0.02	8.05±0.18	3.26±0.05	5.74±0.10	6.16±0.11
383.851	1.93±0.09	6.85±0.70	2.97±0.15	4.91±0.48	5.00±0.33

Table 7.4: Measured energy resolutions for all the channels using ^{133}Ba source.

7.2.3 Energy Resolutions

Fig. 7.12 shows a typical energy spectrum of the core, segment 1, segment 2, segment 3, and mantle. The major γ-lines as listed in Table 7.2 are visible. The energy resolutions (FWHM) of the various γ-lines in the core and the segment spectrum are reported in Table 7.4. The low energy γ-lines at 30.851 keV and 34.987 keV of the segments and the mantle can not be resolved due the limited energy resolutions compared to the core signal. The FWHMs of these two γ-lines are derived by fitting double-Gaussian functions to the spectrum.

(a) segment 1 spectra

(b) segment 2 spectra

(c) core spectra

(d) segment 3 spectra
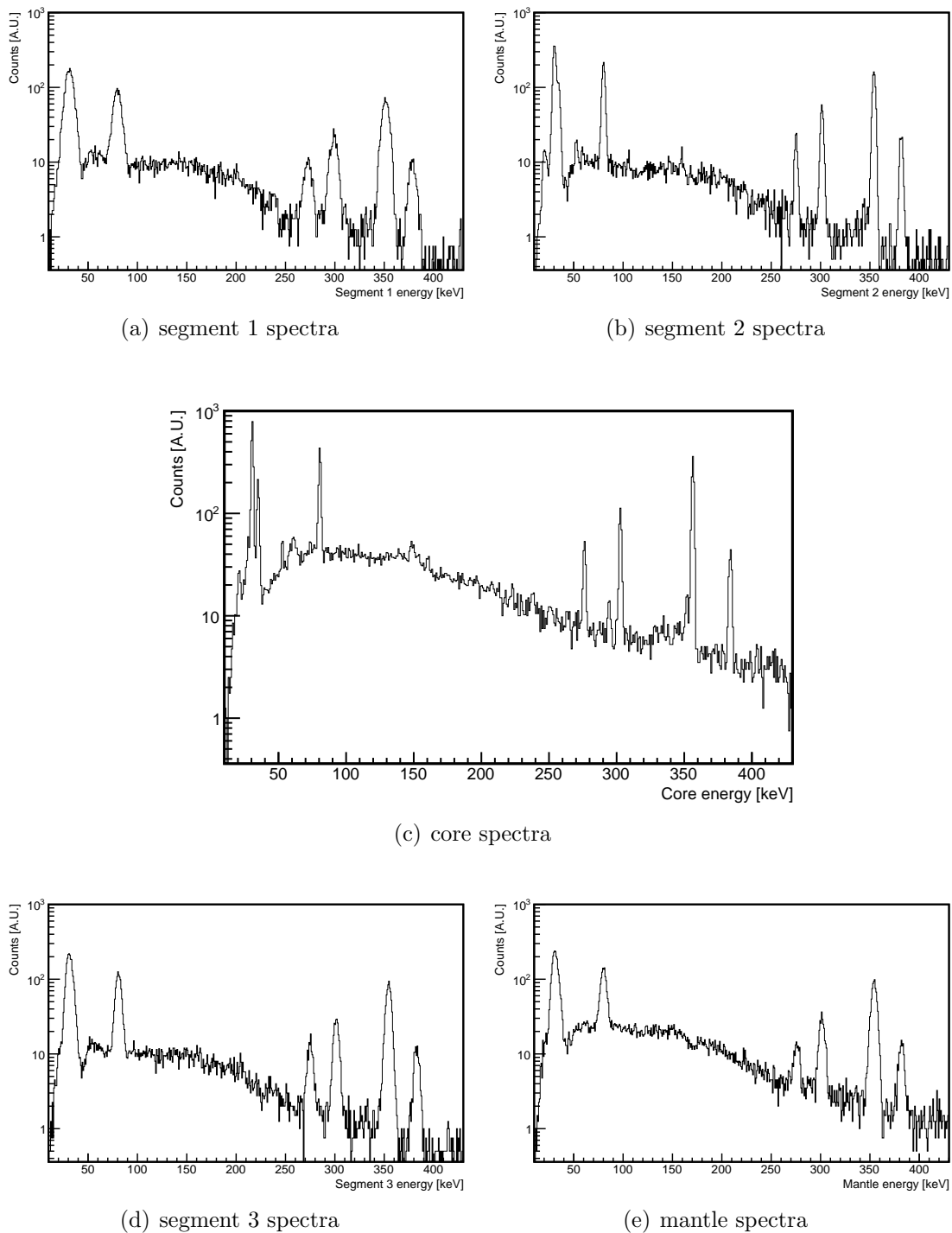
(e) mantle spectra

Figure 7.12: Energy spectra of a calibration measurement with the source pointed on the segments: (a) segment 1, (b) segment 2, (c) core, (d) segment 3, and (e) mantle. The source position was at (r=22 mm, ϕ=149°), (r=28 mm, ϕ=272°), (r=24 mm, ϕ=22°), and (r=27 mm, ϕ=325°) for segment 1, segment 2, segment 3, and mantle, respectively. For the core spectrum, the measurement was taken at r=24 mm and ϕ=22°.

Measurement ID	Source position [mm, deg]	Source orientation [deg]	Δt_{5-95} [ns]/[K]
TM1	(24, 27)	$\phi_{\langle 110 \rangle}$-4°	1.21±0.19
TM2	(22, 160)	$\phi_{\langle 010 \rangle}$-6°	2.55±0.13
TM3	(3, 288)	$\phi_{\langle 110 \rangle}$-13°	1.80±0.11
TM4	(24, 22)	$\phi_{\langle 110 \rangle}$-9°	1.30±0.16
TM5	(22, 70)	$\phi_{\langle 100 \rangle}$-6°	2.45±0.11

Table 7.5: Summary of the temperature dependence measurements. The third column shows the source orientation with respect to the nearby crystallographic axis. The last column summarizes the increasing rate of core rise time (t_{5-95}) with respect to the temperature.

7.3 Temperature dependence of the Core Rise Time

The actual detector temperature affects the length of the rise time of detector pulses [167]. In order to measure the temperature dependence of the rise time, several measurements were performed using a collimated ^{133}Ba source at fixed positions on the top of the end-cap of the K1 cryostat. Five measurements at different positions were performed.

The 81 keV events are grouped together every 30 minutes for the core rise time calculation. Fig. 7.13 shows the core rise time (t_{5-95}) as a function of temperature. It can be seen that the core rise time increases by up to a few ns per K. Also, the temperature response of the core rise time changes with respect to the orientation of crystallographic axes (see Table 7.5). This dependency is expected [167].
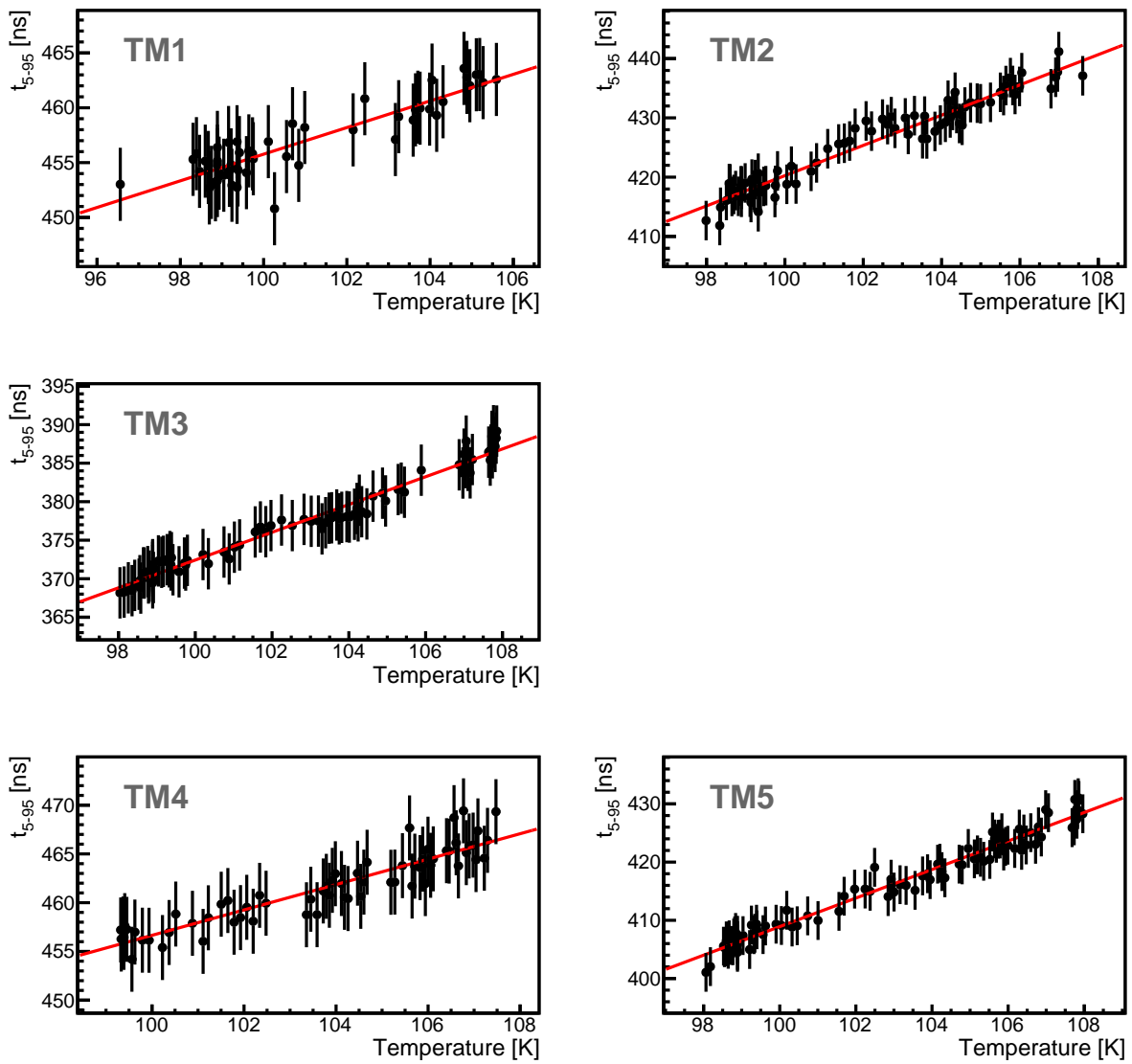
Figure 7.13: Core risetime(t_{5-95}) as a function of temperature measured at different positions.

7.4   Determination of Segment Boundaries

The segment boundaries were determined from the ratio of the count rate of the segments to the count rate of the core, R^{SS}, as a function of azimuthal angle ϕ and radius r. The events in the 81 keV region (E$\pm 3\sigma_E$) were used for the determination of the segment boundaries. This was derived for data taken from top-scans, side-scans, and r-scans.

Fig. 7.14 shows R^{SS} as a function of ϕ for top- and side-scans together with the fit functions for the determination of segment boundaries. The edge of the segment boundary as a function of ϕ can be described by:

$$G(\phi) = \frac{H}{2} \cdot \tanh[\Lambda \cdot (\phi - \phi_{a,b})] + \Gamma. \tag{7.6}$$

where:
H: amplitude of the boundary edge.
Λ: slope of raising/lowering boundary edge.
(>0 for the raising edge; <0 for the lowering edge).
$\phi_{a,b}$: center of the boundary edge.
Γ: offset of the boundary edge.

H, Λ, $\phi_{a,b}$, and Γ are free parameters. The determination of segment boundaries using top- and side-scans are summarized in Table 7.6. The feature of segment boundaries is clearly seen and the segment boundary determination from the two scans are in good agreement with each other. Note that R^{SS} values are not equal to one since the selected data from the given energy region contains background events which are different for core and segments. Fig. 7.15 shows the measurements with fixed ϕ along the radius. The fit results of segment boundaries at different angles are tabulated in Table 7.7. The observed segment boundaries are as expected.

Measurement	segment	ϕ_a [deg]	ϕ_b [deg]	$|\phi_a - \phi_b|$ [deg]
Top-scan				
	1	122.6±0.7	182.0±0.8	59.3±1.0
	2	244.6±0.6	303.4±0.8	58.8±1.0
	3	3.9±0.8	61.3±0.6	57.4±1.0
	4	62.8±0.6	120.8±0.7	58.0±0.9
	4	183.4±0.5	243.0±0.5	59.6±0.7
	4	304.3±0.6	2.2±1.8	57.9±1.9
Side-scan				
	1	120.3±0.7	181.9±0.9	61.6±1.1
	2	242.8±0.6	302.6±0.6	59.9±0.9
	3	1.5±0.7	61.8±0.8	60.3±1.1
	4	61.8±0.8	121.1±0.9	59.2±1.2
	4	182.0±0.8	243.0±0.9	60.9±1.2
	4	303.0±0.7	1.3±0.9	58.3±1.1

Table 7.6: Determination of segment boundaries from the top- and side-scan measurements using the fit function of Eq. (7.6) to derive the center of segment boundaries.

Measured angle [deg]	segment	radius [mm]
170	1	8.2±0.2
170	4	7.8±0.2
258	2	7.9±1.9
258	4	7.8±0.1
26	3	8.3±0.2
26	4	8.8±3.1

Table 7.7: Determination of segment boundaries from the r-scan measurements using the fit function of Eq. (7.6) to derive the center of segment boundaries.
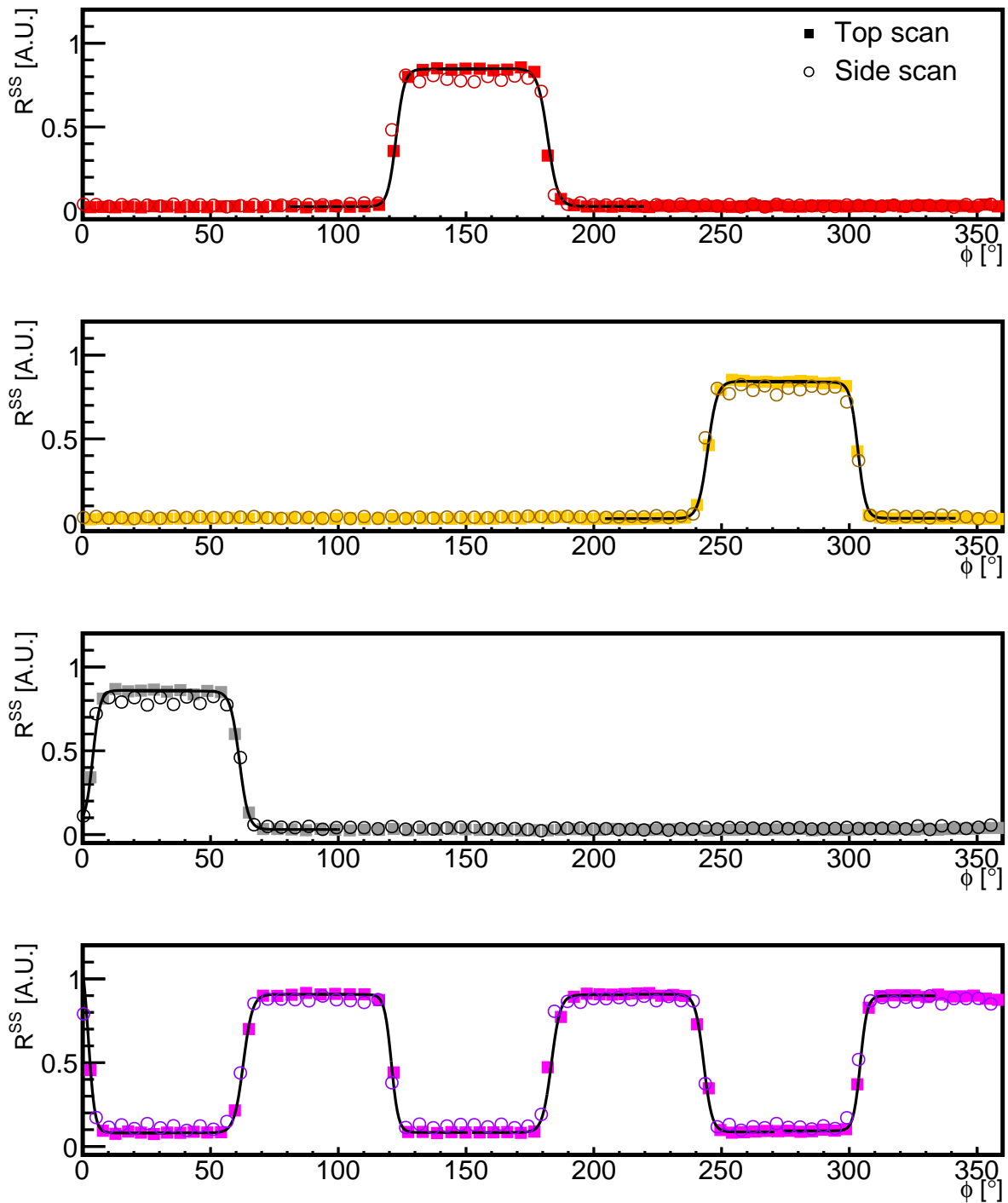
Figure 7.14: R^{SS} as a function of ϕ for the determination of segment boundaries. The determination is performed by using the ratio of the count rate of the segments to the count rate of the core at $81\,\mathrm{keV}$ region. The centers of segment boundaries can be determined using Eq. (7.6) (shown in black, the fits shown in the figures are performed using top-scans.).
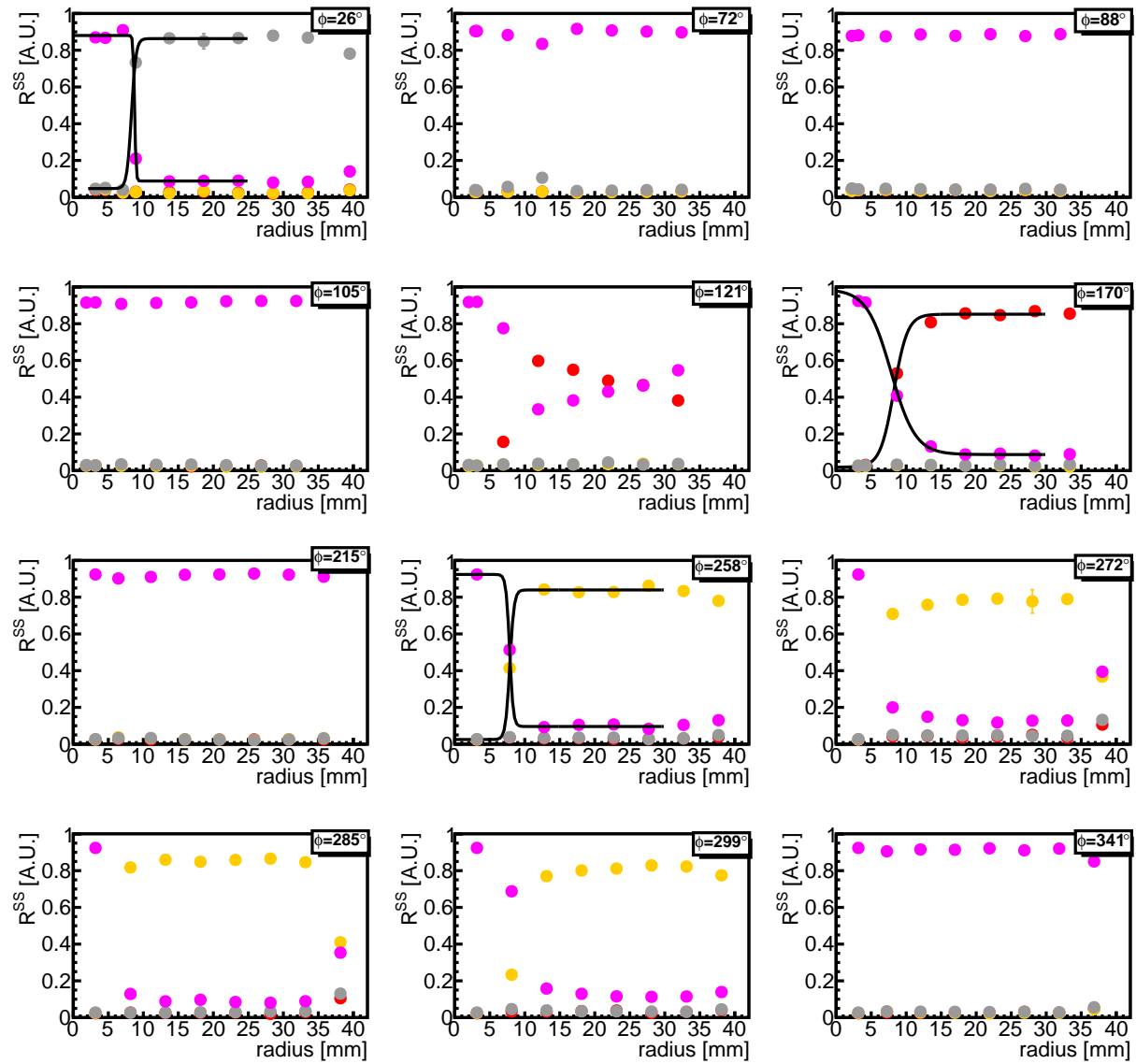
Figure 7.15: R^{SS} against radius for determination of segment boundaries with fixed ϕ. The centroids of segment boundaries are derived using the fit function given in Eq. (7.6).

7.5   Crystal Axes Orientation

The orientation of crystallographic axes is essential when comparing measurements with pulse shape simulation. It is important since the crystallographic axes not only affect charge carrier drift velocities but also their trajectories, as discussed in Section 2.3.2. The $\langle 001 \rangle$-axis is usually aligned with the Z axis of a cylindrical germanium detector after the Czochralski pulling procedure. The $\langle 110 \rangle$-axis is normally not known upon the delivery of the Ge detector. So its orientation has to be extracted experimentally, for example from rise time measurements.

Two sets of measurements, top- and side-scans, were performed to determine the crystallographic axes. The 81 keV γ-line with localized energy depositions close to the detector surface (distance of the averaged energy barycenter is 2.42 mm from the detector surface, see Section 7.1.2) was used. It can keep the unique feature of the pulses, which is important for the rise time calculation.

The core rise time (t_{5-95}) was used to locate the crystallographic axes. For each data point, two rise time calculation methods were performed. One method is to calculate the core rise time event-by-event at 81 keV peak. The rise time distribution is fitted with a Gaussian fit where the centroid of the Gaussian represents the rise time value of the measurement (individual pulse method, called IP method). The other method is to average all the core pulses at 81 keV and calculate the 5-95 % rise time (average pulse method, called AP method).

Fig. 7.16 shows t_{5-95} calculated by the two methods as a function of ϕ for the top and side scans. It can be observed that there is a slight time offset between the IP and AP methods. This is due to noise fluctuations. The AP method has lower noise fluctuations and hence has a larger t_{5-95} value. In order to eliminate the effect due to the noise fluctuations, the core rise time were normalized with respect to the maximum rise time value. The comparisons between the two methods from the top and side scans are shown in the bottom panel of Fig. 7.16. The calculations give consistent result.

The dependence of the core rise time on the azimuth angle was fitted with the function:

$$t_{5-95} = C + A \cdot \sin[\frac{2\pi}{90}(\phi + \phi_{\langle 110 \rangle})], \tag{7.7}$$

where C, A, and $\phi_{\langle 110 \rangle}$ are free parameters. The extracted $\phi_{\langle 110 \rangle}$ angles are summarized in Table 7.8.
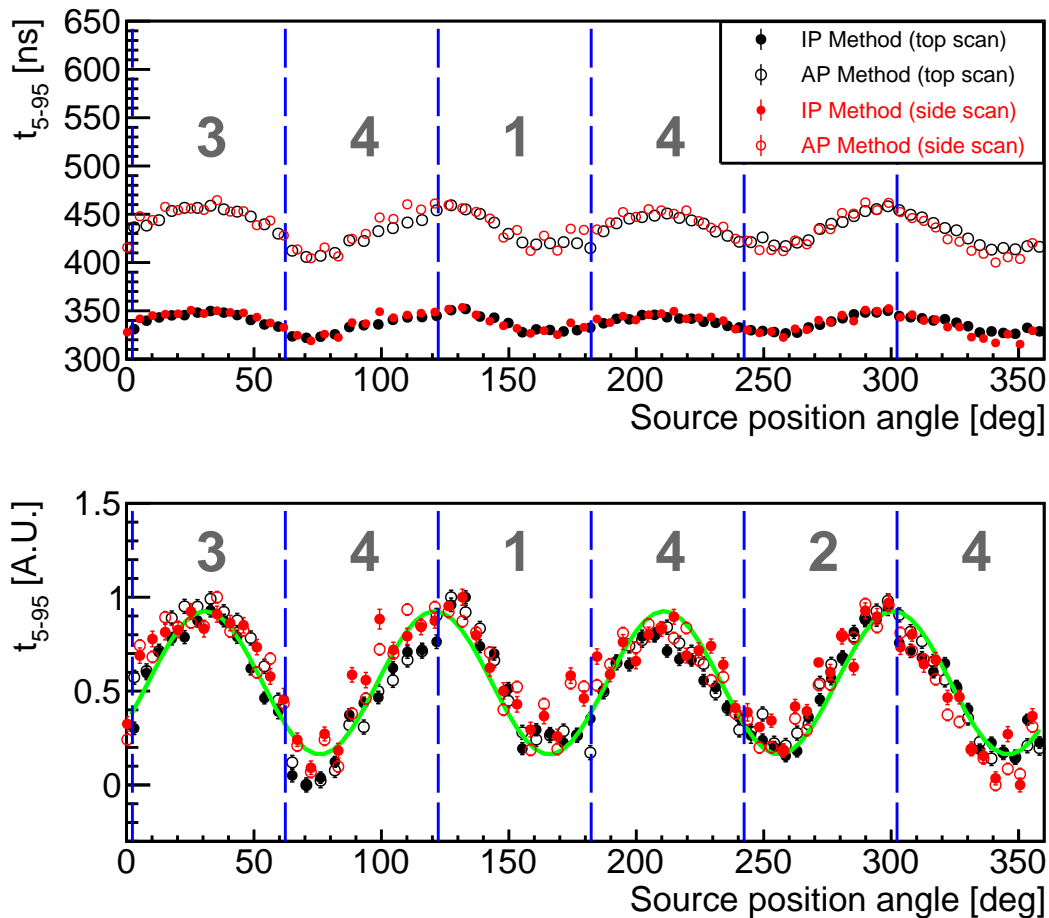
Figure 7.16: Rise time versus ϕ for crystal axes determination. (a) Top panel: Core rise time (5-95 %) as a function of ϕ. (b) bottom panel: Normalized core rise time against ϕ with a sinusoidal function fitted to the top-scan data using the AP method.

Measurement	Rise time calculation method	$\phi_{\langle 110 \rangle}$ [deg]
Top scan	IP method	31.3±0.3
Top scan	AP method	30.6±0.3
Side scan	IP method	32.9±0.3
Side scan	AP method	32.9±0.2

Table 7.8: Best-fit results using different methods and measurements for determining ϕ_{110}-axes.

The contributions of the total uncertainty for determining ϕ_{110} are from:

- statistical uncertainty: $\pm 0.3°$

- uncertainty using different methods: $\pm 2.3°$ (dominant contribution)

- uncertainty due to the temperature dependence of the rise time: $\pm 0.2°$

The statistical uncertainty derived from the measurements is $\pm 0.3°$. The contribution includes the measurement uncertainty of the source position ($\sim 1°$ uncertainty in ϕ). The systematic uncertainty is calculated by the maximum deviation between different methods from the top- and the side-scan measurements. It is the dominant contribution of the total uncertainty. The systematic uncertainty due to the temperature effect is $\pm 0.2°$ [6]. The total uncertainty is the sum of the individual components in quadrature. The determined $\phi_{\langle 110 \rangle}$ is $(31.9 \pm 2.3)°$.

---

[6]The core rise time changes about $2.5\,\mathrm{ns/K}$ during the measurements.

7.6 Pulse Shape Simulation

7.6.1 Framework of Pulse Shape Simulation

Pulse shape simulation is performed using the simulation software MAGE. The procedure of the simulation is described as follows [85]:

1. before simulating charge carrier creation and transportation, calculation of electric field and weighting field,

2. physics process generation,

3. clustering of the hits,

4. calculation of charge carrier drift in the bulk,

5. calculation of induced charge on the electrode (pulse shape),

6. folding in effects of temperature,

7. folding in effects of the electronics,

8. comparison of simulated pulses with the measured pulses.

Before simulating charge carrier creation and transportation, the electric field and the weighting field are calculated. The weighting potential depends only on the geometry of the detector and its electrodes. The weighting potentials of the core and the mantle of the segmented BEGe detector are shown in Fig. 7.17. The range of the weighting potentials is between 0 and 1 (1 for the assigned electrode).

The interactions of particles with germanium are simulated using Geant4 to extract the information of the energy depositions and their positions and the according number of induced electron-hole pairs.

Since the HPGe detector can not resolve the two hits that are within $\sim$1 mm, clustering of individual hits with distance within 1 mm. The new hit position is the energy barycenter of the individual hits and the energy is given by the sum of the energies of the individual hits.

The charge carriers, electrons and holes, drift in the bulk is then simulated. The effects that influence the magnitudes and directions of the carrier velocities are considered, namely, the crystallographic axes and the impurity concentration. Fig. 7.18 shows the electric potential in the segmented BEGe detector and some electron trajectories. For this examples, electrons were generated at r=35 mm and Z=19.9 mm every 3 degree. The mobility anisotropy due to the crystallographic structure of germanium is clearly seen. The impurity level changes the E-field in the bulk as well. Fig. 7.19 shows the simulated pulses of the segmented BEGe detector using different impurity concentrations. The effect on pulses due to different impurity concentrations is substantial. The correct impurity concentration profile is crucial and gradient to fully deplete the HPGe detector. Without

or with too low impurity concentration, the detector can not be fully depleted. Point-like charge carriers are used for the pulse shape simulation in this work. The estimated charge cloud size of electrons is ~ 0.2 mm due to the thermal diffusion [7]. The position sensitivity of a real HPGe detectors is about mm. Hence, the effect due to thermal diffusion is insignificant and can be safely neglected.

Once the mean hit positions in the bulk are determined, the drift velocities and the trajectories of the charge carriers in the bulk are determined. A point-like charge carrier is used for the pulse shape simulation.

The next step is to calculate the induced charges on the electrode as a function of time, the pulse according to the Ramo-Schockley Theorem, as discussed in Section 2.3.3.

The simulated pulse is the superposition of the individual pulses from electrons and the holes. Fig. 7.20 givens an example of describing the procedure from step 2 to step 5.

The drift velocities of the charge carriers in the simulated pulses were at 77 K, whereas most of the measured pulses were at 98-100 K. Hence, the temperature effects on the drift velocities are required to the simulated pulses to stretch in time based on the temperature of the measured pulses. According to the earlier study [167], the rise time at 98-100 K increases 10-20 % compared to the one at 77 K [8] The stretching factor can also be derived by fitting averaged simulated pulses to the averaged measured pulses. The calculated stretching factors for most of the measurements are in a range of 10-20 %, which are in good agreement with the previous study [167]. A global stretching factor in time for all the simulated pulses was set to a value of 1.15 (15 % stretching in time) to take into account the temperature response on the simulated pulses. This setting of global stretching factor is an approximation which assumes that the charge carriers have the same temperature response.

After taking into account the temperature response on the simulated pulses, the preamplifier response functions were folded in for all the channels.

Finally, the simulated pulses can be compared to the real measured pulses.

7.6.2   Settings of Simulation Parameters

The key input parameters used in the pulse shape simulation are:

- $\phi_{\langle 110 \rangle}$=31°,

- charge carrier mobilities: using B. Bruyneel's model (see Table 7.9),

- impurity concentration (head-tail): $(0.19\text{-}0.26) \times 10^{10}$ cm^{-3}.

The settings of the model, i.e. axis orientation, charge carrier mobilities and the impurity concentration were chosen to reproduce measurements shown in Section 7.7. Note that impurity concentrations chosen differs by a factor of 5 from the values provided by the manufacturer.

---

[7]Assuming a typical rise time of $\sim 1\,\mu$s and using Eq. (2.21)

[8]Crystal axes dependent.

(a)

(b)

(c)

(d)
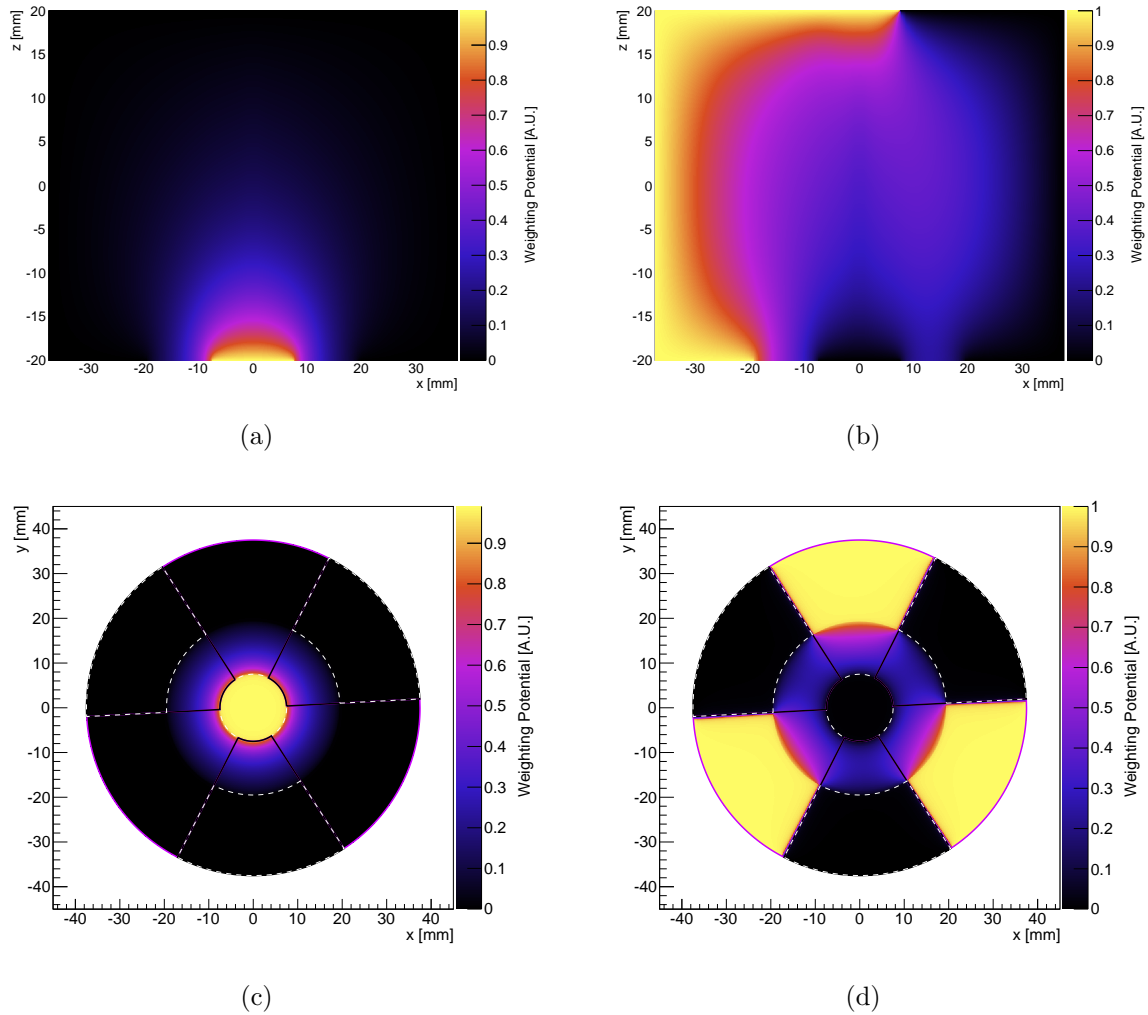
Figure 7.17: Calculated weighting potential of the core: (a) side view and (c) top view. Calculated weighting potential of the mantle: (b) side view and (d) top view.

7.6.3   Response Function

The measurements to derive the pre-amp response functions were performed by injecting square pulses with fixed amplitudes from a fast pulse generator to the test inputs of the pre-amplifiers. A fast pulse generator, HP 8082A module, was used for the measurements.

The settings of the HP 8082A are given as follows:

- frequency=1 kHz

- rise time (t_{10-90})=2 ns

- amplitude of square pulses=15 mV

(a)

(b)

(c)
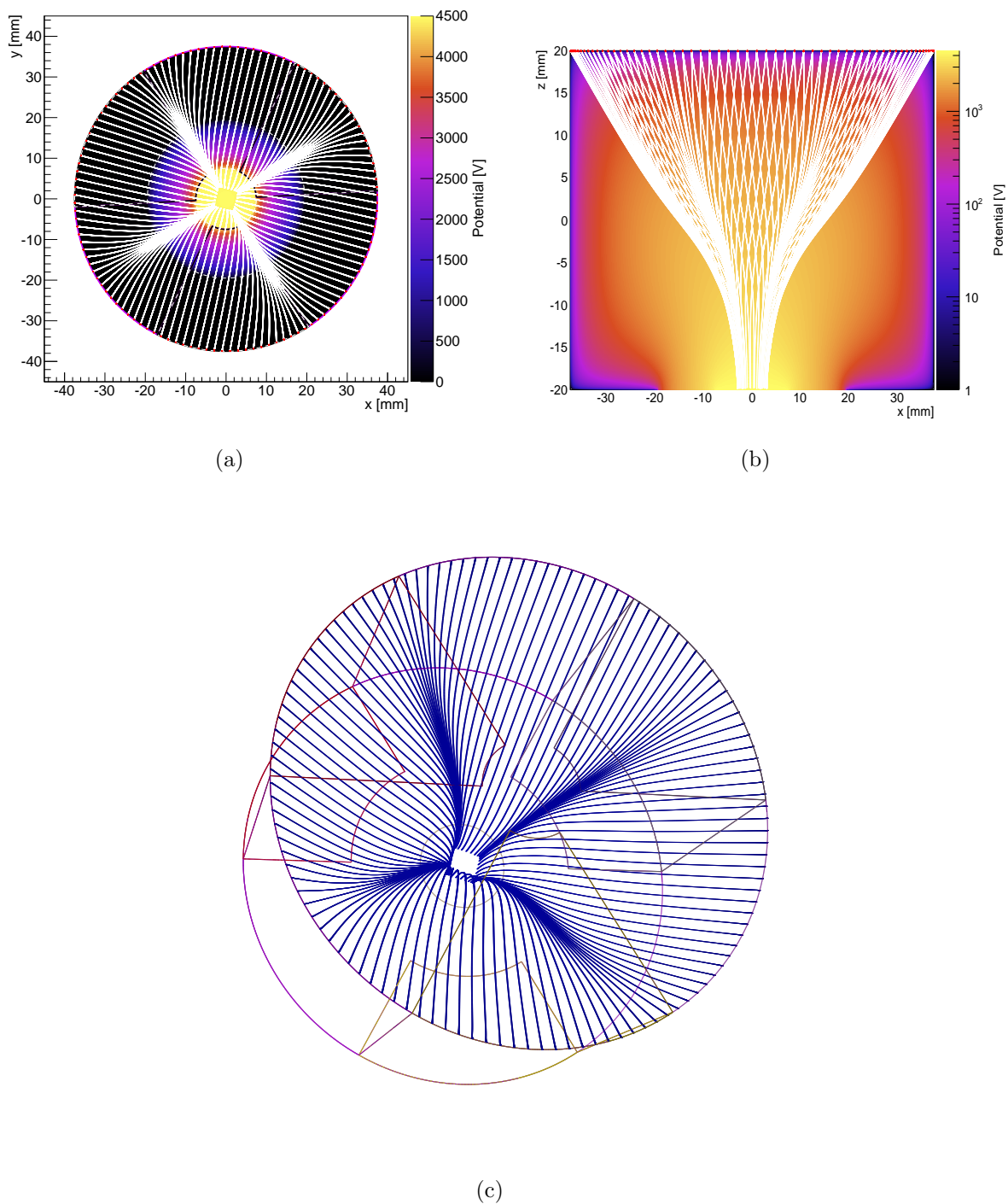
Figure 7.18: Electric potential and electron trajectories (white lines): (a) top view and (b) side view. (c) Electron trajectories (blue lines) in 3D. Electrons trajectories depicted in the figures are generated at r=35 mm and z=19.9 mm. The electron trajectories along $\phi_{\langle 110 \rangle}$-axes (at ϕ=31°, 121°, 211°, and 301°) bent massively.
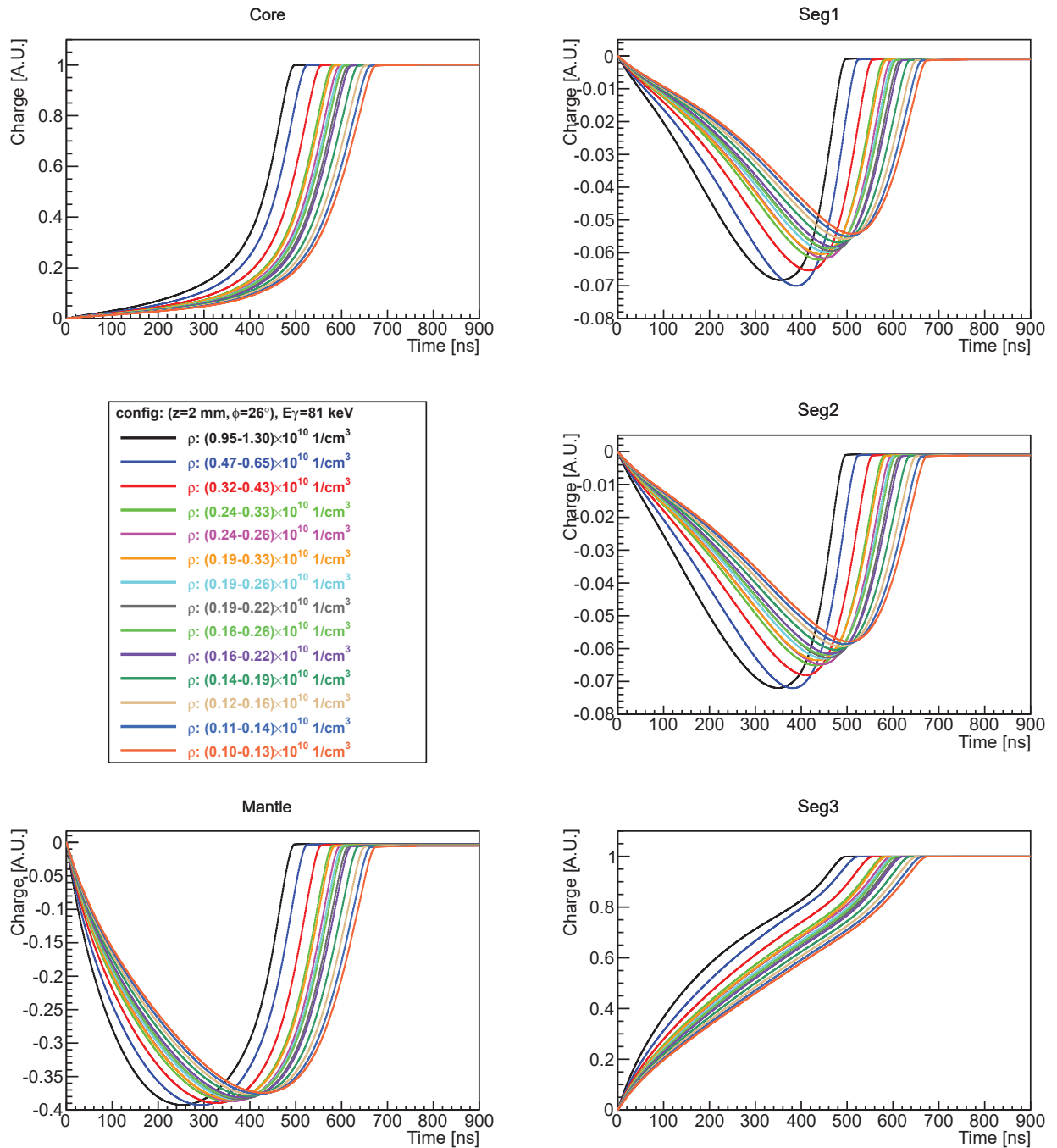
Figure 7.19: Simulated pulses of the segmented BEGe detector with different impurity concentrations. The charge carriers are generated at r=35 mm, ϕ=26°, and Z=2 cm. The impurity density ρ, shows the concentration from head to tail.

The output of the test pulses with 450 mV pulse height were first attenuated to 15 mV. The attenuated pulses went through a four-channel NIM fan-out module. The fan-out
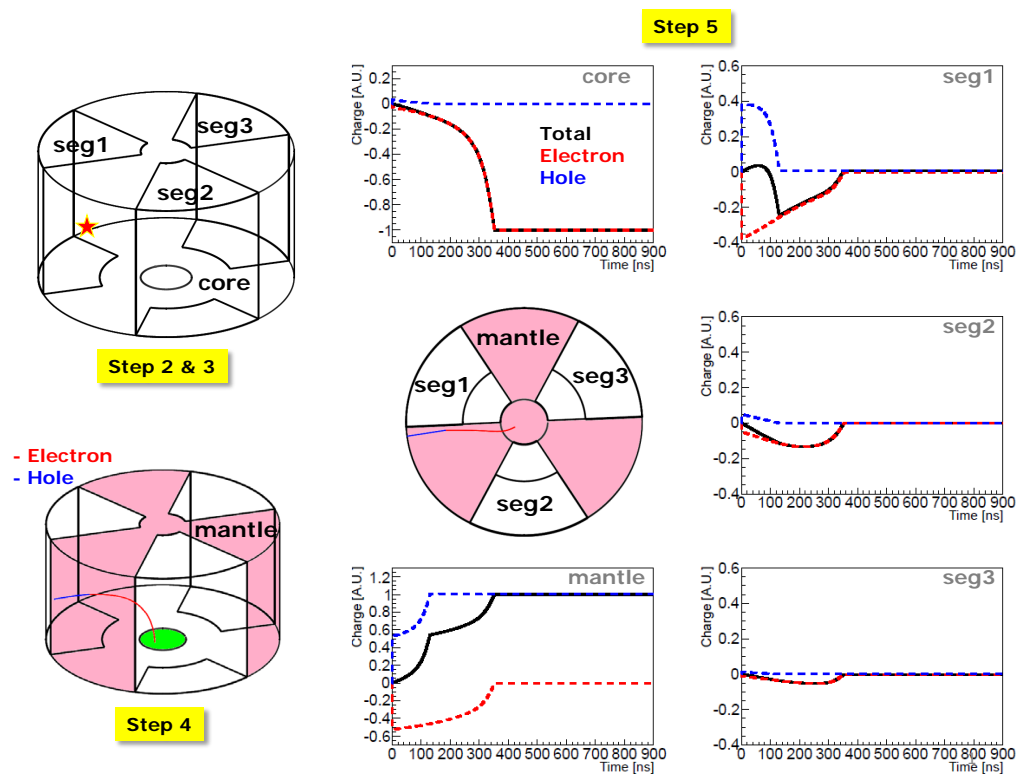
Figure 7.20: An example for the pulse shape simulation of the segmented BEGe detector. In the second and the third step, an energy deposition (star sign) is simulated. The charge carriers drift in the bulk (the trajectory of the electron is shown in red, whereas the one of the hole is shown in blue) is determined. The pulse shapes can then be calculated. The observed pulses (black) are the superposition of the pulses from the electrons (red) and the holes (blue).

pulses subsequently went to the pre-amp test inputs. The pre-amp test outputs were saved by the DAQ.

Fig. 7.21(a) shows the averaged charge pulses from the test outputs of the pre-amplifiers. The measured 2 ns rise time (t_{10-90}) is fast enough with respect to the 13.3 ns sampling rate of DFG PIXIE 4 DAQ. Hence, the response functions can be derived from the differentiation of the recorded template pulses (Refer to Eq.2.26 for more details), as shown in Fig. 7.21(b).

The derived response functions can then be used to convolve with the simulated pulses, as described in Eq.2.25.

Reference	Carrier	Direction	μ_0 $[\mathrm{cm}^2/\mathrm{V} \cdot \mathrm{s}]$	E_0 $[\mathrm{V/mm}]$	β	μ_n $[\mathrm{cm}^2/\mathrm{V} \cdot \mathrm{s}]$
	electrons	$\langle 111 \rangle$	38536	53.8	0.641	510
[82]		$\langle 100 \rangle$	38609	51.1	0.805	-171
	holes	$\langle 111 \rangle$	61215	18.2	0.662	0
		$\langle 100 \rangle$	61824	18.5	0.942	0

Table 7.9: Parametrization for the drift velocities in $\langle 111 \rangle$ and $\langle 100 \rangle$ directions. Table extracted from [85].
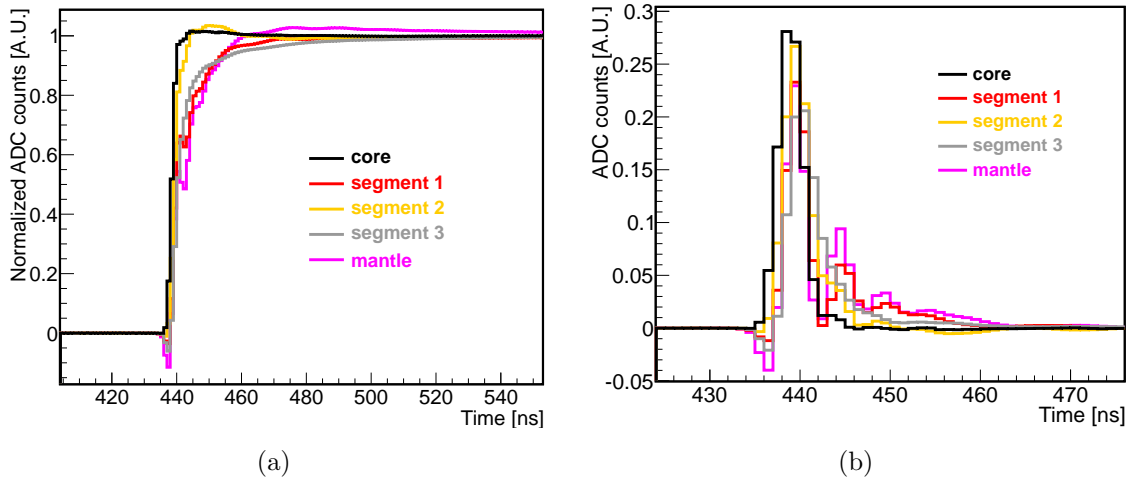
Figure 7.21: (a) Averaged pre-amp output signals from a test pulse generator. (b) The measured pre-amp response functions for all the channels.

7.7   Comparison of Simulated to Measured Pulses

For the top-scan measurements, positions of the 81 keV events are located in a shallow depth of the detector (see Fig. 7.5). Their pulse shapes are well-defined. Hence, they are good samples for the simulation pulses to compare to and to test the validity of the simulation methods.

For each measurement position, the r and ϕ values are known. A pulse shape library based on pulses generated by Monte Carlo simulations with a grid size of Δr=1 mm, $\Delta\phi = 1°$, and Z=17.58 mm was created [9].

The pulse starting time, t_0, can only be derived from the measurements. Five simulated pulses from the core, mantle, and 3 segments were fitted synchronously with a global t_0 parameter, to the individual measured pulses. In order to find the optimal t_0 value to fit best the measured pulses, the values for each time bin in the measured pulses were scanned. For each position in the library, the optimal t_0 value was derived by finding the minimum χ^2/dof value from the fit results among the various t_0 values.

Fig. 7.22 shows a signal-like event, together with the best-fit simulated pulses with temperature effect corrections and folded in pre-amp response functions. By using the scanning measurements it could be shown that the measured pulses can be well reproduced by simulations.

Fig. 7.23 shows the χ^2/dof distributions for the various measured positions. The event position of simulated pulses here corresponds to the position at which the measurement was taken. The χ^2/dof calculation here considers the two segment pulses that were neighboring the event position. The χ^2/dof distributions peak at reasonable values of $\sim$(2.2-2.4) for all positions. Background events can be identified in the tail of the distribution. One such background event is shown in Fig. 7.24.

The simulated pulse shape library in the future can be used for event position reconstruction. This can be done by comparing the calculated pulse shapes in the library to the measured pulse shapes. The most likely event position will be given by the position at which simulated pulse fits best the measured. The event position in the measured data can then be reconstructed.

---

[9]The position of the energy barycenter of 81 keV, see Section 7.1.2.
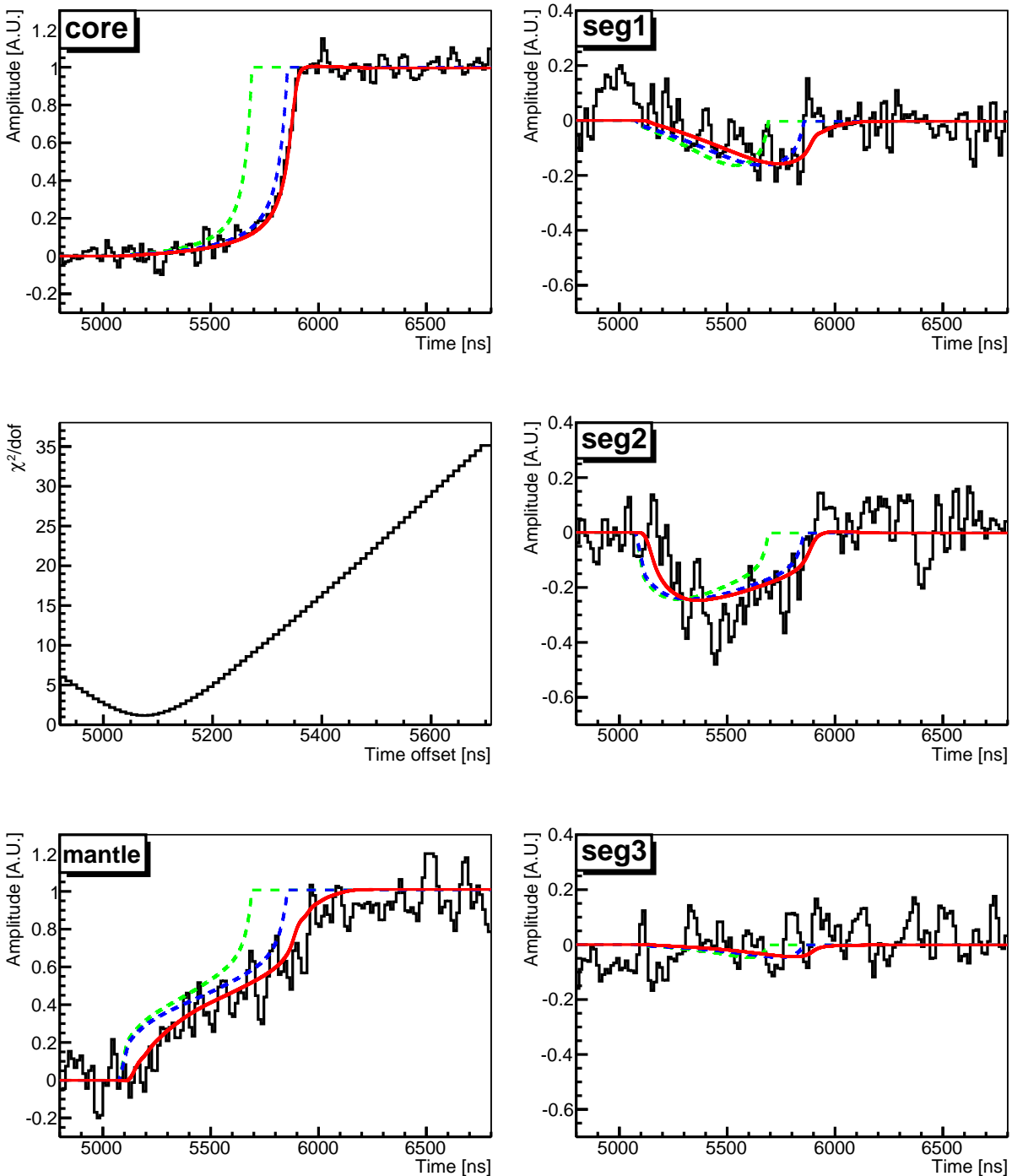
Figure 7.22: A single-like event together with the fitting algorithm. The original simulated pulses at 77 K were shown in green. Simulated pulses after the temperature effect correction and folding in the pre-amp response functions are shown in blue and red, respectively. The middle-left figure shows the best-fit χ^2/dof values in the pulse shape library. The best-fit simulated pulses in the library are shown in red. Refer to the text for more details.
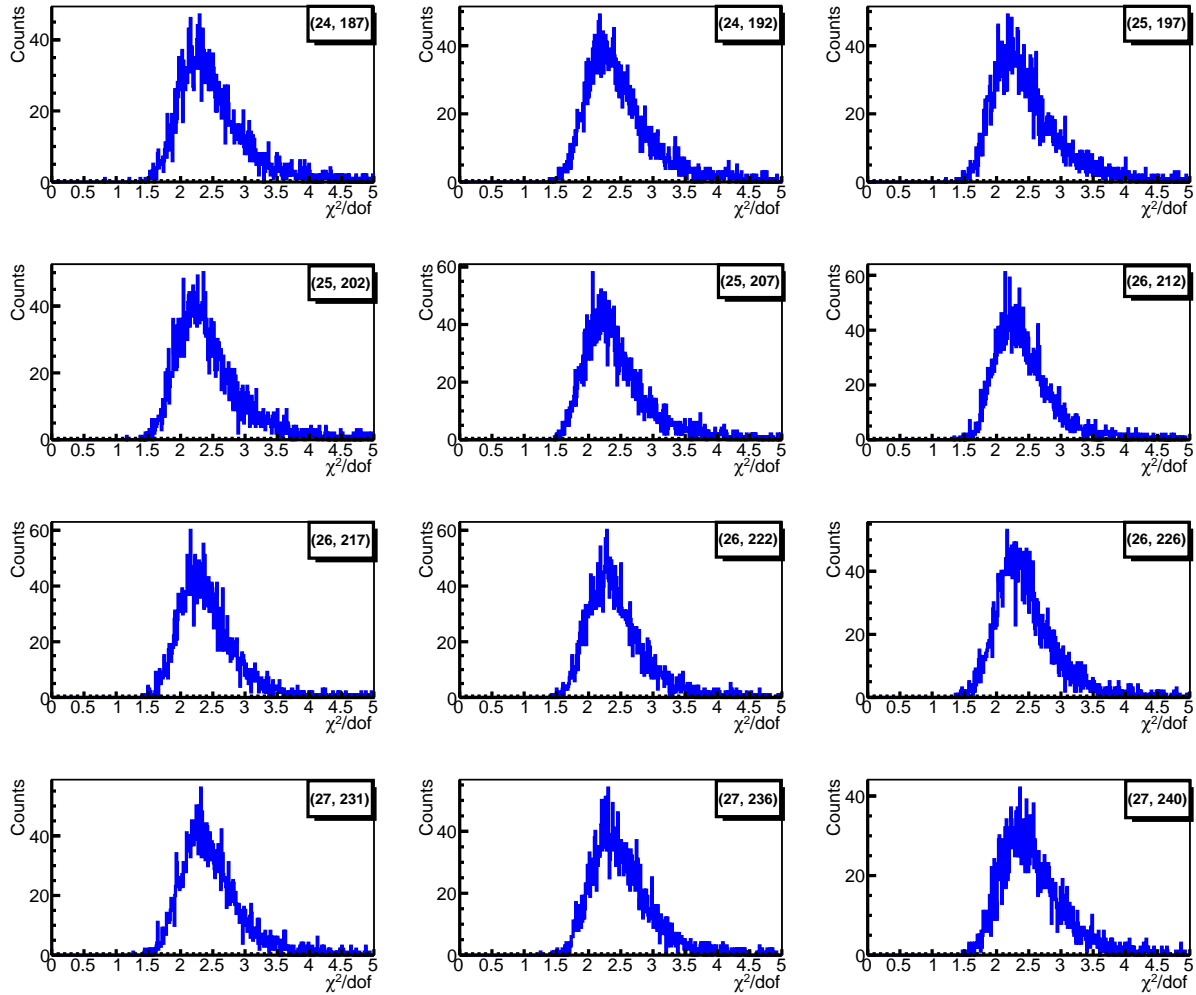
Figure 7.23: χ^2/dof distributions of individual measured positions. For each measurement position the corresponding simulated pulses were fitted to all measured pulses. The χ^2/dof calculation considers the two segment pulses that were neighboring the event position.
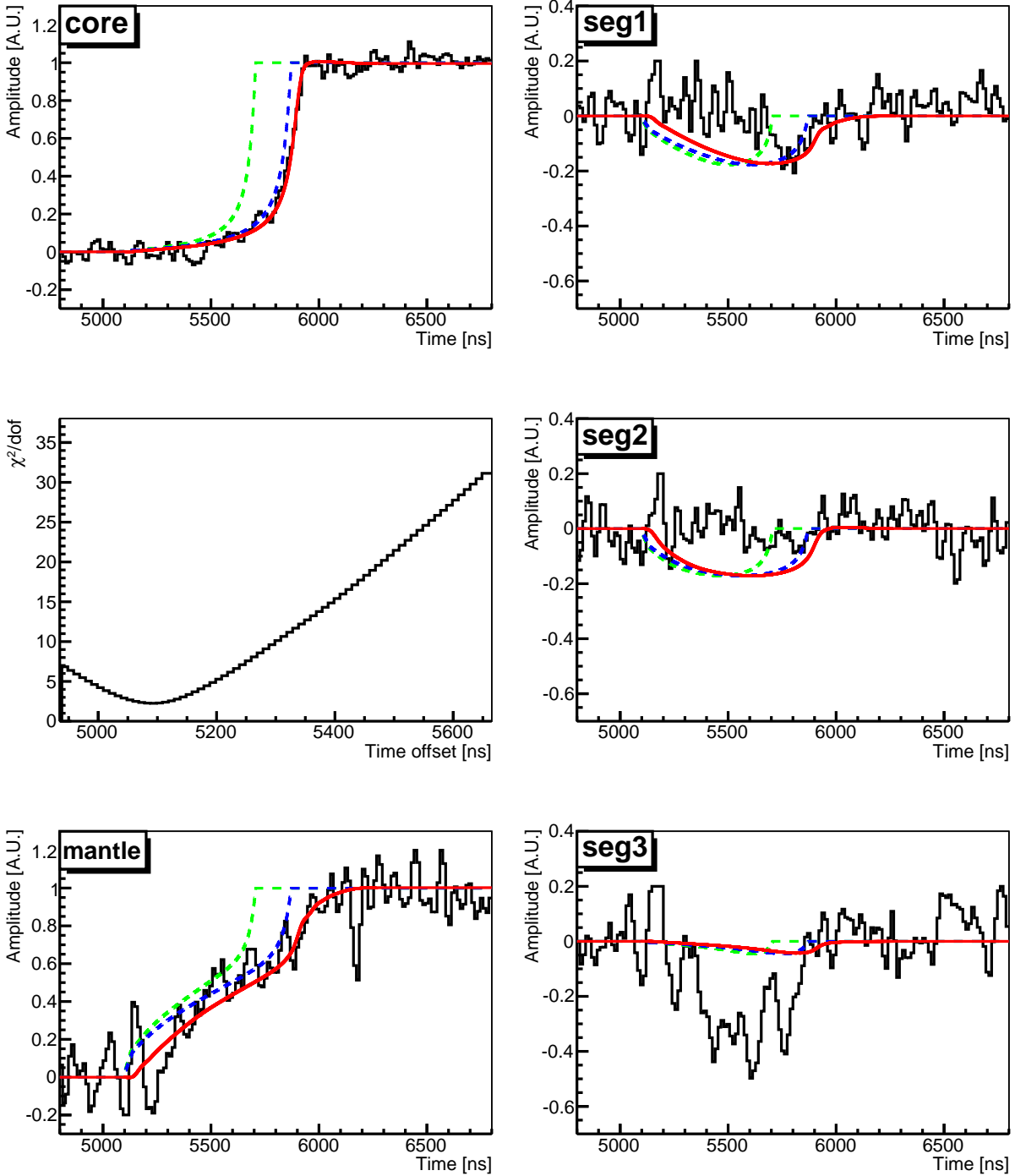
Figure 7.24: An example of a background-like event.

7.8   Summary

The basic detector parameters of the segmented BEGe detector such as energy resolutions, crystal axes, temperature dependence of the core rise times, and the segment boundaries have been determined.

The energy reconstruction was performed off-line. The energy resolution for the core of this detector is $\sim1.6\,\mathrm{keV}$ at $81\,\mathrm{keV}$. A procedure for the cross-talk correction of reconstructed energies and the pulse shapes for the individual segments was developed and tested. The procedure was shown to be effective by checking the baselines of the mirror pulses and the differences between reconstructed total energies determined from the sum of segment entries and core energies, E_{sum} minus E_{core}. The position of segment boundaries were confirmed to coincide with expectations by top-, side-, and r-scans. The temperature dependence of the core rise time was measured. The core rise time (t_{5-95}) increases by up to a few ns per K. The crystal axes are extracted by performing two calculation methods from the top- and side-scan measurements. The determined 110-axis is $31.9°$.

In order to increase the sensitivity of position reconstruction, possible improvements on pulse shape simulations can be achieved by [168]:

- fixing the impurity concentration,

- adjusting the electron mobilities based on the measurements.

The impurity concentration setting in the simulation is a factor of 5 less than the one as provided by the manufacturer. In reality, the Ge detector can not be fully depleted by using the impurity level as adopted in the simulation. Hence, the impurity concentration values used in the simulation is effective but not realistic. However, using the impurity concentration as provided by the manufacturer, the simulated pulse shapes are not similar to the measured pulses most likely the simulated pulses with realistic impurity concentration disagree with measurements due to uncertainties of charge carrier mobilities [82, 83, 84].

Conclusions

This thesis presents analysis of GERDA Phase I BEGe data, Phase II BEGe detectors tested in the HADES underground laboratory, and a novel BEGe detector with four-fold segmentation. The main topic of this thesis is the development of PSD methods for the GERDA experiment to improve the sensitivity for $T_{1/2}^{0\nu}$ of $0\nu\beta\beta$ decay of ^{76}Ge. BEGe detectors have improved background recognition efficiency by pulse shape analysis, exploiting the ratio of the maximum amplitude of the current signal (A) over the calibrated amplitude of charge signal (E) - the A/E parameter. The A/E normalization procedure for Phase I BEGe data was developed to correct time- and energy-dependency of the A/E PSD parameter. With 2.4 kg·yr exposure of GERDA Phase I, the determined $0\nu\beta\beta$ signal detection efficiency after the A/E PSD cut was $(92\pm2)\,\%$. A high background fraction of $\sim80\,\%$ at $Q_{\beta\beta}\pm200$ keV could be rejected thanks to the methods developed. Like this the background index after applying the A/E PSD cut is reduced to $(7^{+4}_{-2})\cdot10^{-3}$ cts/(keV·kg·yr). Further investigations were performed to validate the normalization method used.

Systematic studies for determination of the optimal window size of the moving average filter (MA) used for the current pulses in Phase I background BEGe data were performed. An analysis framework for determination of the optimal window size of the Phase I MA filter was developed. The framework is composed of three parts: derivation of A/E distribution, normalization of A/E distribution, and evaluation of A/E performance. The window size of the MA filter was scanned from 10 ns to 100 ns for both ^{228}Th calibration data and background data. A test statistic algorithm was developed to evaluate the background rejection performance in the single-site event region $(1 - \sigma_{A/E} < \mu_{A/E} < 1 + 2\sigma_{A/E})$. The window sizes with the best signal-to-background ratio were determined to be (49.1 ± 6.1) ns and (61.2 ± 10.9) ns, for the ^{228}Th calibration data and background data, respectively. The results from both calibration and background data sets are in good agreement within $\pm2\sigma$. As a result of the systematic investigation, it can be stated that 50 ns used for Phase I data analysis was a good choice and that the sensitivity of the analysis can not be significantly improved by the further optimization of the window size.

An alternative new de-noising algorithm based on wavelet analysis was developed in order to improve the background rejection efficiency. The de-noising algorithm is based on CDF(4,2) wavelets, a sub-branch of the Cohen-Daubechies-Feauveau (CDF) wavelets. The method was applied to a subset of the Phase I ^{228}Th calibration data. Soft-thresholding was used in this analysis by applying a Sigmoid function to the wavelet coefficients. A global threshold cut with soft-thresholding algorithm was applied to all the wavelet coefficients.

The value of optimal threshold cut was determined by scanning from 0 to 2 with a step size of 0.05. It could be shown that an improvement of background suppression by up to 50 % for the FEP events compared to the results using the standard Phase I MA filter can be achieved.

The 30 newly produced BEGe detectors for Phase II of the GERDA experiment were characterized in the HADES underground laboratory before deploying them into the GERDA cryostat. The characterization for each detector was performed by using a ^{228}Th source ∼8 cm from the top of the end-cap of BEGe cryostat. In the course of this work an analysis was performed to evaluate the PSD performances and the energy resolutions of all BEGe detectors. The results showed that for all 30 BEGes the energy resolution is within specifications, while 29 out of the 30 BEGe detectors have PSD performance according to requirements. The FWHMs at DEP were in a range of 1.76 and 2.08 keV.

In order to study systematic uncertainties of pulse shape analysis and to break angular degeneracies of standard BEGes, a novel BEGe detector with four-fold segmentation was studied. It was characterized by using a collimated ^{133}Ba source. The energy resolution for the core of this detector is ∼1.6 keV at 81 keV. A procedure for the cross-talk correction of reconstructed energies and the pulse shapes for the individual segments was developed. The procedure was shown to be effective by checking the baselines of the mirror pulses and the differences between reconstructed total energies determined from the sum of segment entries and core energies, (E_{sum} minus E_{core}). The position of segment boundaries were confirmed to coincide with expectations by top-, side-, and radius-scans. The temperature dependence of the core rise time was measured. The core rise time (t_{5-95}) increases by up to a few ns per K. The crystal axes are extracted by performing two calculation methods from the top- and side-scan measurements. The determined 110-axis is 31.9°. In order to understand this novel type of detector, pulse shape simulation tools were developed. A full pulse shape library of simulated pulses was created. By using scanning measurements it was shown that the measured pulses can be well reproduced by simulations.

Appendix A

Energy Dependence Correction with MA Filters
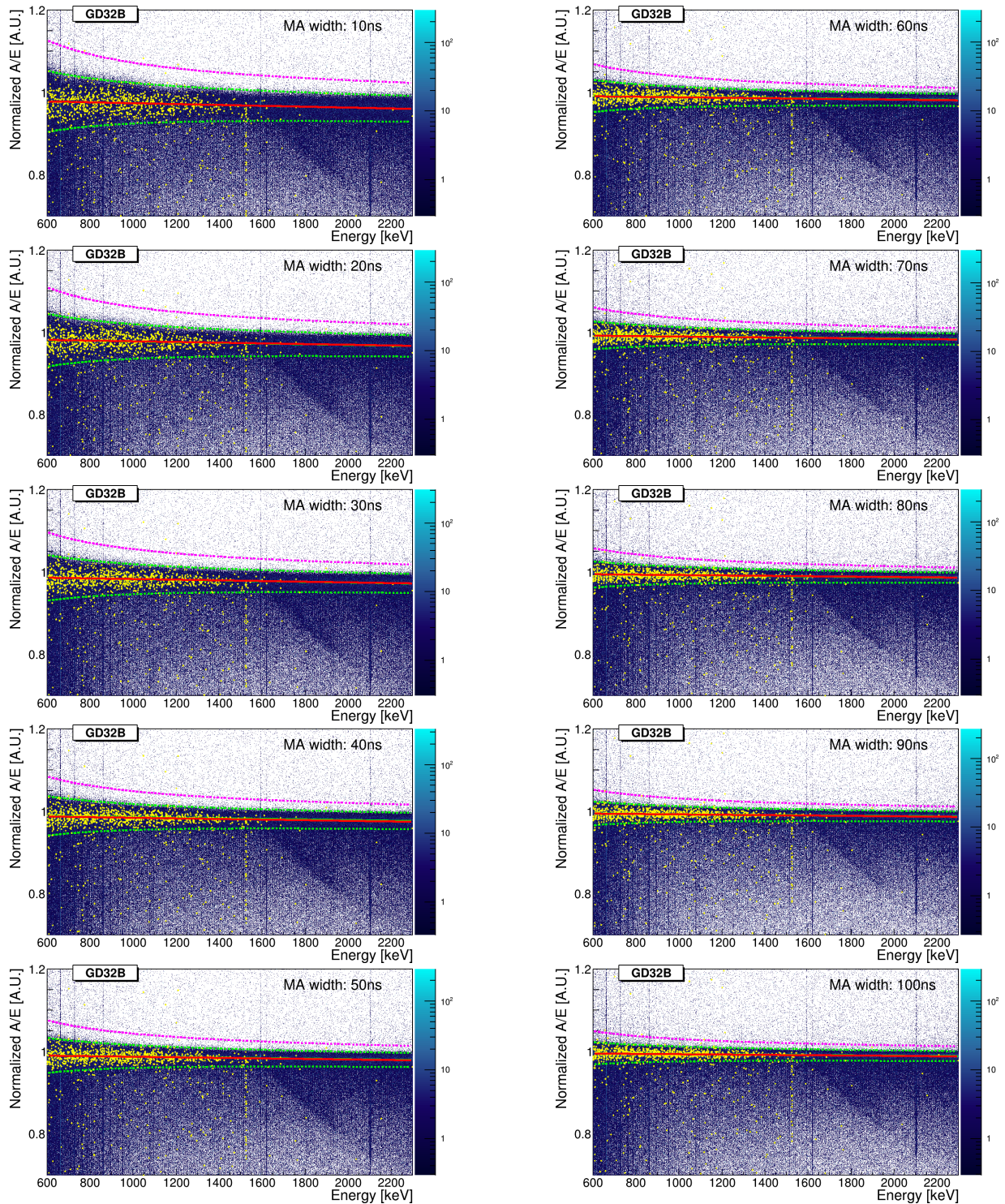
Figure A.1: Scatter plots of the normalized A/E versus E of the GD32B detector after applying MA filters with different lengths. Each figure shows the ^{228}Th calibration data (blue) and the background data (yellow) with the linear fits for the energy dependence correction (green line for calibration data and red line for the background data). The green and pink dash-lines represent the cut values in $\mu_{A/E} \pm 2.6\ \sigma_{A/E}$ and $\mu_{A/E} + 5.2\ \sigma_{A/E}$, respectively.
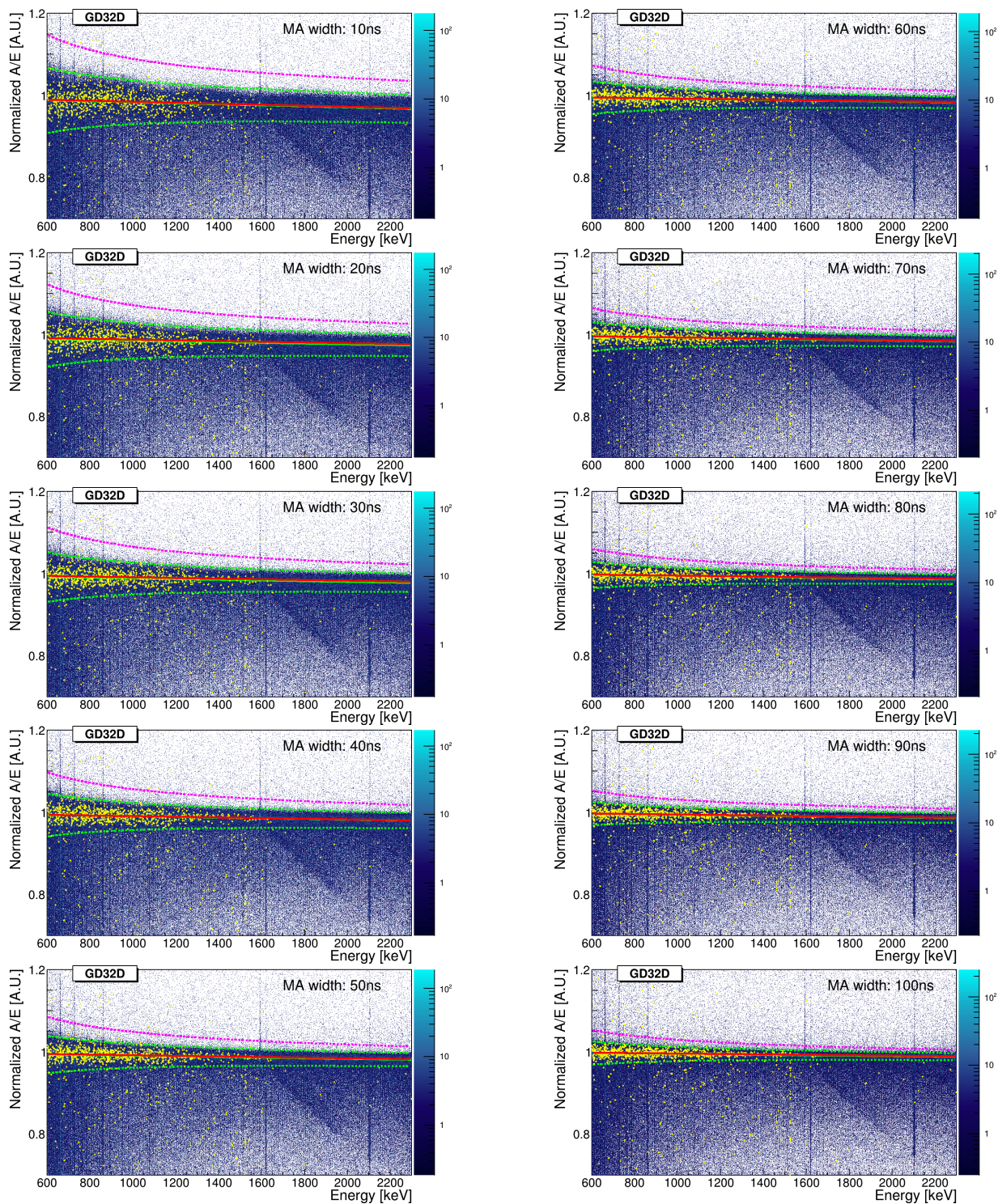
Figure A.2: Scatter plots of the normalized A/E versus E of the GD32D detector after applying MA filters with different lengths. Each figure shows the ^{228}Th calibration data (blue) and the background data (yellow) with the linear fits for the energy dependence correction (green line for calibration data and red line for the background data). The green and pink dash-lines represent the cut values in $\mu_{A/E} \pm 2.6\ \sigma_{A/E}$ and $\mu_{A/E} + 5.2\ \sigma_{A/E}$, respectively.
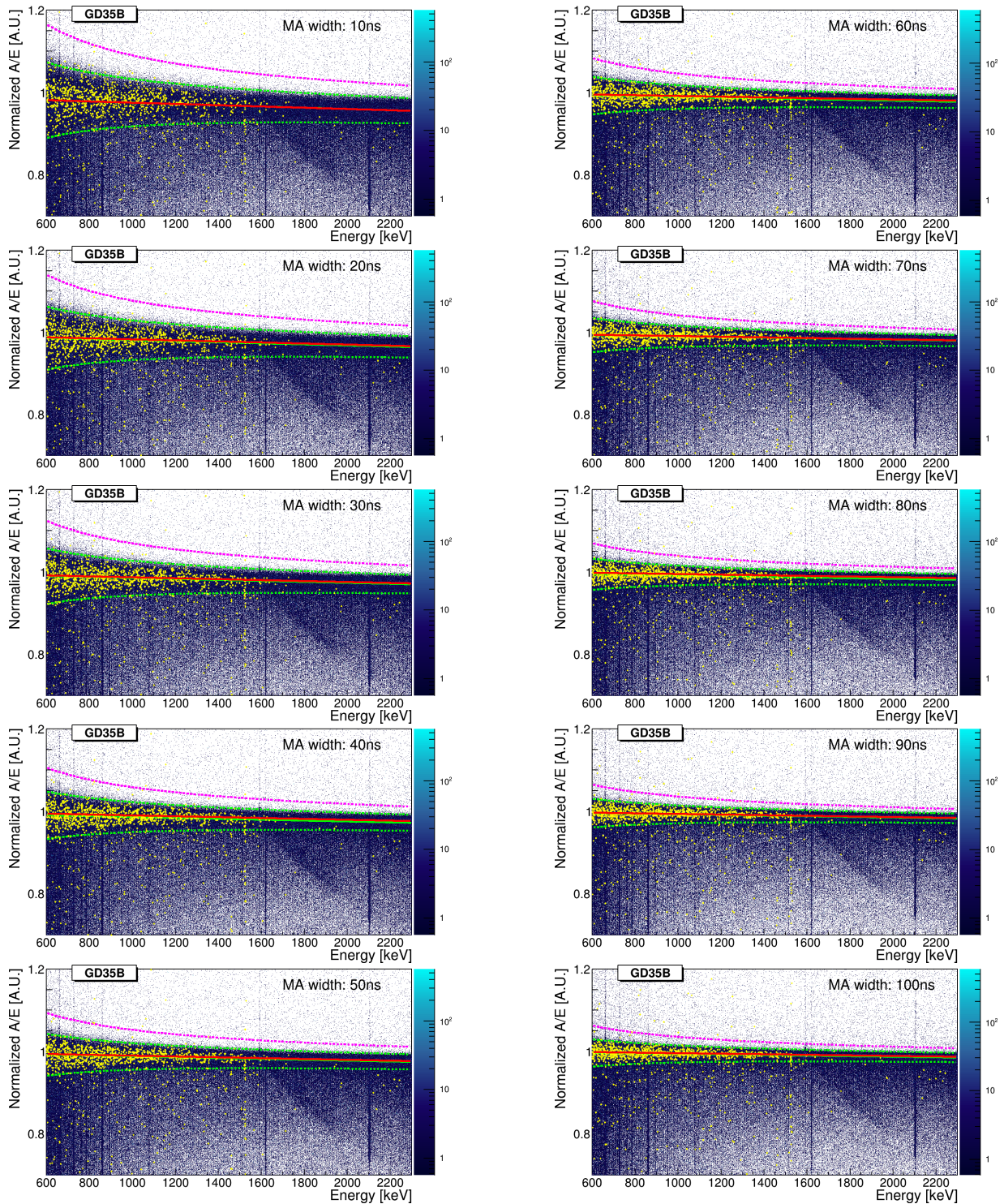
Figure A.3: Scatter plots of the normalized A/E versus E of the GD35B detector after applying MA filters with different lengths. Each figure shows the ^{228}Th calibration data (blue) and the background data (yellow) with the linear fits for the energy dependence correction (green line for calibration data and red line for the background data). The green and pink dash-lines represent the cut values in $\mu_{A/E} \pm 2.6\ \sigma_{A/E}$ and $\mu_{A/E} + 5.2\ \sigma_{A/E}$, respectively.

Appendix B

Pre-amplifier Decay Time Correction

The pre-amp decay time correction can be described in the following way. Assuming B_j is the jth binning without the τ-decay, and A_j is the jth binning after τ-decay correction. The relation between the binning before and after the τ-decay correction can be described as:

$$A_0 = B_0$$
$$...$$
$$A_j = A_{j-1} + B_j - B_{j-1} \times \exp(-t/\tau_c)$$

(B.1)

where t is sampling rate (13.3 ns for DGF Pixie-4 DAQ), and τ_c is the decay constant. In the current setting, the index j is from 1 to the 1023 samples.

The pre-amp decay time constants are calculated for the total 5 channels. For each of the 5 channels, events with energies above 300 keV are selected and the decay time is calculated by fitting the last 416 samples of each pulse with exponential decay function. The Fig. B.1(a)-Fig. B.1(e) show the fitted pre-amp decay time as a function of ϕ for the core, segment 1, ..., and the mantle, respectively. The fitted values of the pre-amp decay time versus ϕ are used for the τ-decay corrections, as summarized in table Table 7.3.

(a)

(b)

(c)

(d)

(e)
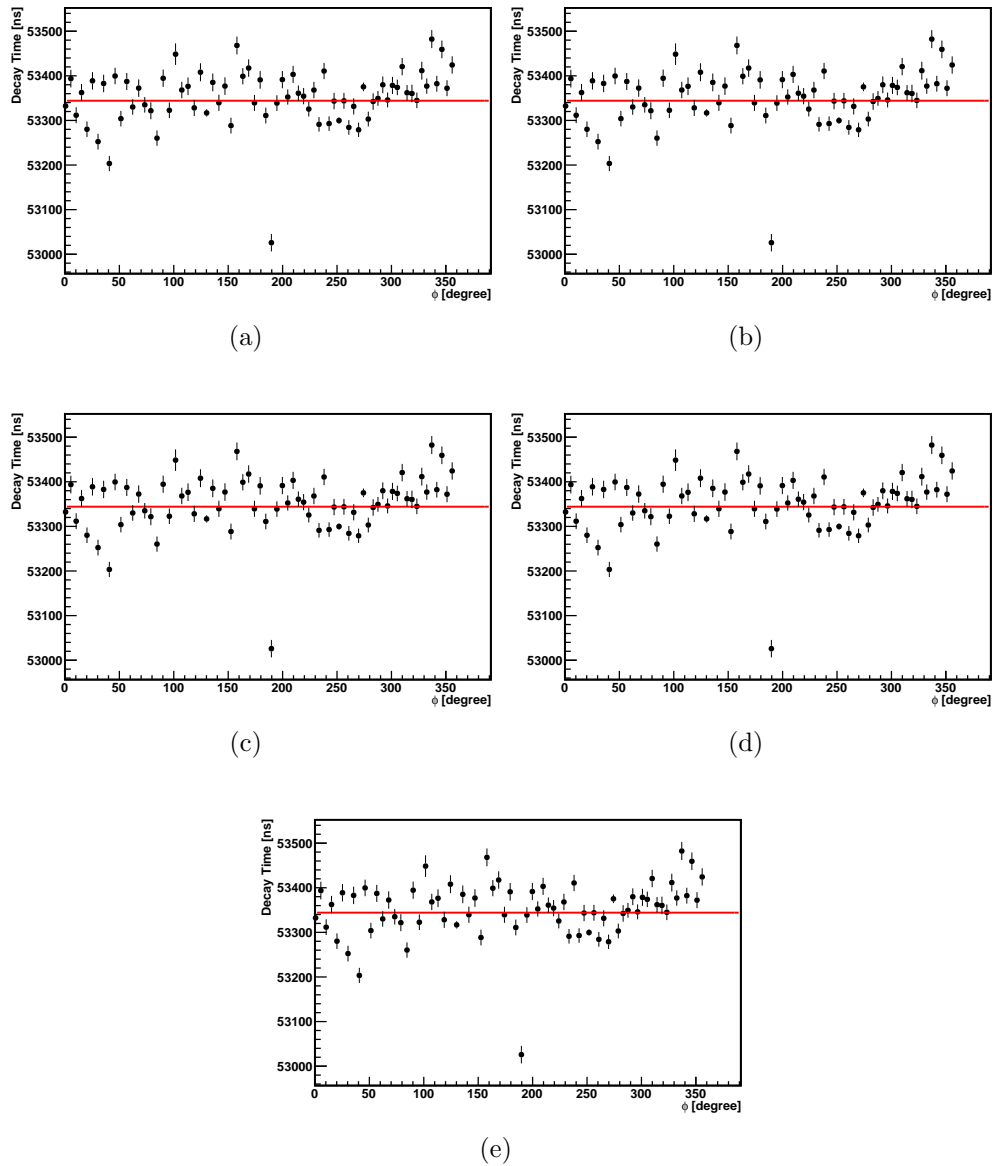
Figure B.1: (a) The mean of the core pre-amp decay time as a function of ϕ. (b), (c), (d), and (e) for the segment 1, 2, 3, and the mantle, respectively. The fitted decay constants are shown in red.

Bibliography

[1] Raymond Davis, Jr., Don S. Harmer, and Kenneth C. Hoffman, "Search for Neutrinos from the Sun", Phys. Rev. Lett. **20**, 1205 (1968)

[2] John N. Bachcall, "Solar Models: An Historical Overview", Nuclear Physics **B 118**, 77-86 (2003)

[3] K. S. Hirata *et al.*, "Observation of ^{8}B solar neutrinos in the Kamiokande-II detector", Phys. Rev. Lett. **63**, 1619 (1989)

[4] A. I. Abazov *et al.*, "Search for neutrinos from the Sun using the reaction ^{71}Ga(ν_e,e$^-$)^{71}Ge", Phys. Rev. Lett. **67**, 3332-3335 (1991)

[5] P Anselmann *et al.*, "Solar neutrinos observed by GALLEX at Gran Sasso", Phys. Lett. **B 285**, 376-389 (1992)

[6] J. Beringer *et al.*, (Particle Data Group), Phys. Rev. **D 86**, 010001 (2012)

[7] B. Pontecorvo, "Inverse beta process and nonconservation of lepton charge", Zh. Eksp. Teor. Fiz. **33**, 549 (1957)

[8] Z. Maki, M. Nakagawa, S. Sakata, Prog. "Remarks on the Unified Model of Elementary Particles" Theor. Phys. **28**, 870 (1962)

[9] L. Wolfenstein, "Neutrino oscillations in matter", Phys. Rev. **D 17**, 2369 (1978)

[10] C. Kraus *et al.*, "Final results from phase II of the Mainz neutrino mass searching tritium β decay", Eur. Phys. J. **C 40**(4), 447468 (2005)

[11] V. N. Aseev *et al.*, "Upper limit on the electron antineutrino mass from the Troitsk experiment", Phys. Rev. **D 84**(11), 112003 (2011)

[12] K. Blaum *et al.*, "The Electron Capture ^{136}Ho Experiment ECHo", arXiv:1306.2655

[13] Planck Collaboration, "Planck 2015 results. XIII. Cosmological parameters", arXiv:1502.01589

[14] R. Laureijs *et al.*, "Euclid Definition Study Report", http://arxiv.org/abs/1110.3193

[15] Andrea Giuliani and Alfredo Poves, "Neutrinoless Double-Beta Decay", Advances in High Energy Physics, Volume **2012**, 857016 (2012)

[16] A. Barabash, "Precise half-life values for two neutrino double beta decay", Phys. Rev. **C 81**, 035501 (2010)

[17] A. Barabash, "Double Beta Decay: Historical Review of 75 Years of Research", Phys. Atom. Nucl. **74**, 603-613 (2011)

[18] A. Barabash, "Review of double beta decay experiments", arXiv:1403.2870

[19] The GERDA Collaboration, "Results on decay with emission of two neutrinos or Majorons in ^{76}Ge from GERDA Phase I", arXiV:1501.02345

[20] E. Majorana, "A symmetric theory of electrons and positrons", Nuovo Cimento **14**, 171184 (1937)

[21] I. Avignone, Frank T., S. R. Elliott, and J. Engel, "Double Beta Decay, Majorana Neutrinos, and Neutrino Mass", Rev.Mod.Phys. **80**, 481-516 (2008)

[22] J. Gomez-Cadenas *et al.*, "The Search for neutrinoless double beta decay", Riv. Nuovo Cim. **35**, 29-98 (2012).

[23] J. Schechter and J. W. F. Valle, "Neutrinoless double-β decay in SU(2)×U(1) theories", Phys. Rev. **D 25**, 2951 (1982)

[24] GERDA collaboration, "Results on Neutrinoless Double-β Decay of ^{76}Ge from Phase I of the GERDA Experiment", Phys. Rev. Lett. **111**, 122503 (2013)

[25] J. B. Albert*et al.*, "Search for Majorana neutrinos with the first two years of EXO-200 data", Nature **510**, 7504, 229-234 (2014)

[26] H.V. Klapdor-Kleingrothaus, A. Dietz, L. Baudis,*et al.*, "Latest results from the HEIDELBERG-MOSCOW double beta decay experiment", Eur. Phys. J. **A 12**, 147-154 (2001)

[27] C. E. Aalseth, F. T. Avignone, III, R. L. Brodzinski*et al.*, "IGEX ^{76}Ge neutrinoless double-beta decay experiment: Prospects for next generation experiments", Phys. Rev. **D 65**, 092007 (2002)

[28] "Search for neutrinoless double beta decay with enriched ^{76}Ge in Gran Sasso 19902003", Physics Letters **B 586**, Issues 34, 198212 (2004)

[29] C. E. Aalseth, A. S. Barabash, F. Böhm*et al.*, "Comments on Evidence for Neutrinoless Double Beta Decay", Modern Physics Letters **A 17**, p. 1475 (2002)

[30] Majorana Collaboration, N. Abgrall*et al.*, "The MAJORANA DEMONSTRATOR Neutrinoless Double-Beta Decay Experiment", Adv.High Energy Phys. **2014**, 365432 (2014) .

[31] A. Gando *et al.*, "Limit on Neutrinoless $\beta\beta$ Decay of ^{136}Xe from the First Phase of KamLAND-Zen and Comparison with the Positive Claim in ^{76}Ge", Phys. Rev. Lett. **110**, 062502 (2013)

[32] A. Gando,*et al.*, "Measurement of the double- decay half-life of KamLAND-Zen experiment", Phys. Rev. **C 85**, 045504 (2012).

[33] M. Auger,*et al.*, "Search for Neutrinoless Double-Beta Decay in ^{136}Xe with EXO-200", Phys. Rev. Lett. **109**, 032505 (2012)

[34] R. G. H. Robertson, "Empirical Survey of Neutrinoless Double Beta Decay Matrix Elements", arXiv:1301.1323

[35] Bernhard Schwingenheuer, "Status and prospects of searches for neutrinoless double beta decay", Annalen der Physik **V 525**, Issue 4, p269280 (2013)

[36] Fedor Šimkovic, Vadim Rodin, Amand Faessler, and Petr Vogel, "$0\nu\beta\beta$ and $2\nu\beta\beta$ nuclear matrix elements, quasiparticle random-phase approximation, and isospin symmetry restoration", Phys. Rev. **C 87**, 045501 (2013)

[37] J. Barea, J. Kotila, and F. Iachello, "$0\nu\beta\beta$ and $2\nu\beta\beta$nuclear matrix elements in the interacting boson model with isospin restoration", Phys. Rev. **C 91**, 034304 (2015)

[38] J. M. Yao, L. S. Song, K. Hagino, P. Ring, and J. Meng, "Systematic study of nuclear matrix elements in neutrinoless double-β decay with a beyond-mean-field covariant density functional theory", Phys. Rev. **C 91**, 024316 (2015)

[39] S. M. Bilenky and C. Giunti, "Neutrinoless Double-Beta Decay: A probe of physics beyond the standard model", Int. J. Mod. Phys. **A 30**, 1530001 (2015)

[40] M. Gunther *et al.*, "Heidelberg - Moscow $\beta\beta$ experiment with ^{76}Ge: Full setup with five detectors", Phys. Rev. **D 55**, 5467 (1997)

[41] A. Morales, "Review on double beta decay experiments and comparison with theory", Nucl.Phys.Proc.Suppl. **77**, 335345 (1999)

[42] H. Klapdor-Kleingrothaus, I. Krivosheina, A. Dietz, and O. Chkvorets, "Search for neutrinoless double beta decay with enriched ^{76}Ge in Gran Sasso 1990-2003", Phys. Lett. **B 586**, 198-212 (2004)

[43] H. Klapdor-Kleingrothaus, L. Baudis, A. Dietz, G. Heusser, B. Majorovits *et al.*, "GENIUS-TF: A Test facility for the GENIUS project", Nucl. Instrum. Methods **A 481**, 149-159 (2002)

[44] M. Barnabé Heider, "Performance and stability tests of bare high purity germanium detectors in liquid argon for the GERDA experiment", Ph.D. Dissertation, University of Heidelberg, Germany (2009)

[45] M. Barnabé Heider, C. Cattadori, O. Chkvorets, A. di Vacri, K. Gusev, S. Schönert and M. Shirchenko, "Performance of bare high-purity germanium detectors in liquid argon for the GERDA experiment", arXiv:0812.1907

[46] GERDA Collaboration, M. Agostini *et al.*, "The background in the $0\nu\beta\beta$ experiment GERDA" Eur. Phys. J. **C 74**, 2764 (2014).

[47] I. Abt *et al.*, "A New ^{76}Ge Double Beta Decay Experiment at LNGS", arXiv:hep-ex/0404039.

[48] Nicola Nosengo, "Gran Sasso: Chamber of physics", Nature web page: http://www.nature.com/news/gran-sasso-chamber-of-physics-1.10696

[49] GERDA web page, https://www.mpi-hd.mpg.de/gerda/

[50] G. Heusser, "Low-radioactivity background techniques", Ann.Rev.Nucl.Part.Sci. **45**, 543590 (1995)

[51] W. Maneschg, M. Laubenstein, D. Budjáš, W. Hampel, G. Heusser, K.T. Knöpfle, B. Schwingenheuer, H. Simgen, "Measurements of extremely low radioactivity levels in stainless steel for GERDA", Nucl. Instrum. Methods **A 593**, 448-453 (2008)

[52] H. Simgen, G. Zuzel, "Analysis of the ^{222}Rn concentration in argon and a purification technique for gaseous and liquid argon", Applied Radiation and Isotopes vol. **67**, Issue 5, p.922-925 (2009)

[53] J. Janicskó Csáthy *et al.*, "Development of an anti-Compton veto for HPGe detectors operated in liquid argon using silicon photo-multipliers", Nucl. Instrum. Methods **A 654**, 225 (2011)

[54] J. Janicskó Csáthy, "A liquid argon scintillation veto for GERDA and LArGe", talk in DPG Spring meeting, "Hadronen und Kerne" (March 2012)

[55] B. Lehnert, "Analysis of Double Beta Decays in Germanium, Palladium and Argon", Diploma thesis, TU Dresden (2011)

[56] L. Pandola, *et al.*, "Monte Carlo evaluation of the muon-induced background in the GERDA double beta decay experiment", Nucl. Instrum. Methods **A 570**, 149-158 (2007)

[57] GERDA Collaboration, I. Abt *et al.*, "The GERmanium Detector Array for the search of neutrinoless $\beta\beta$ decays of ^{76}Ge at LNGS", Proposal to the LNGS P38/04 (2004)

[58] C. O'Shaughnessy, E. Andreotti, D. Budjas, A. Caldwell, A. Gangapshev, *et al.*, "High voltage capacitors for low background experiments", Eur. Phys. J. **C 73**, 2445 (2013)

[59] R. Isocrate, M. Bellato, M. Bettini, R. Venturelli, C. Ur, and D. Bazzacco, "MD2S - Digital sampling electronics for the MARS detector", Laboratori Nazionali di Legnaro, Annual Report (2004)

[60] C. Ur, C. R. Alvarez, C. Rusu, D. Bazzacco, M. Bellato, E. Farnea, and R. Isocrate, "A data acquisition system for the MD2S digital sampling electronics", Laboratori Nazionali di Legnaro, Annual Report (2004)

[61] M. Agostini, L. Pandola, and P Zavarise, "Off-line data processing and analysis for the GERDA experiment", Journal of Physics: Conference Series **368**, 012047 (2012)

[62] L. Pandola, "Parameters and facts for the analysis dataset of the $0\nu\beta\beta$ decay of GERDA Phase I, GERDA Scientific Technical Reports: GSTR-13-012 (2013)

[63] Internal GERDA resources.

[64] A. Caldwell and K. Kröninger, "Signal discovery in sparse spectra: A Bayesian analysis", Phys. Rev. **D 74**, 092003 (2006)

[65] T. Mukoyama, "Range of Electrons and Positrons", Nucl. Instrum. Methods **134**, 125 (1976)

[66] C. Grupen, B. Shwartz., "Particle Detectors", 2nd edition. Cambridge University Press (1996)

[67] H. W. Koch, J. W. Motz , Review of Modern Physics **31**, 920 (1959)

[68] M.J. Berger, J.S. Coursey, M.A. Zucker and J. Chang
The NIST data base: Stopping-Power and Range Tables for Electrons, Protons, and Helium Ions, http://www.nist.gov/pml/data/star/

[69] G. F. Knoll, "Radiation Detection and Measurement", Wiley, 4th edition (2011)

[70] Charles Kittel, "Introduction to Solid State Physics", Wiley, New York, 8th edition (2008)

[71] O. Klein, Y. Nishina, "Über die Streuung von Strahlung durch freie Elektronen nach der neuen relativistischen Quantendynamik von Dirac", Z. Phys. **52**, Issue 11-12, 853 - 868 (1929)

[72] W.S.C. Williams, "Nuclear and Particle Physics", Clarendon Press, Oxford (1991)

[73] C. F. G. Delaney and E. C. Finch, "Radiation Detectors", Oxford University Press (1992)

[74] B. Pratt and F. Friedman, "Diffusion of Lithium into Ge and Si", J. Appl. Phys. **37** no. 4, 1893-1896 (1966)

[75] E. Aguayo *et al.*, "Characteristics of Signals Originating Near the Lithium-Diffused N+ Contact of High Purity Germanium P-Type Point Contact Detectors", Nucl. Instrum. Methods A **701**, 176-185 (2013)

[76] U. Fano, Phys. Rev. **72**, 26-29 (1947)

[77] G. Gilmore and J. Hemingway, "Practical Gamma Ray Spectroscopy", Wiley & Sons (1996)

[78] J. B. Johnson, "Thermal agitation of electricity in conductors", Phys. Rev. **32**(1), 97-109 (1928)

[79] H. Nyquist, "Thermal agitation of electric charge in conductors", Phys. Rev. , **32**(1), 110-113 (1928)

[80] H. G. Reik and H. Risken, "Drift Velocity and Anisotropy of Hot Electrons in n Germanium", Phys. Rev. **126**, 17371746 (1962)

[81] W. Sasaki *et al.*, "Anisotropy of hot electrons in germanium", J. Phys. Chem. Sol. 8, 250256 (1959)

[82] B. Bruyneel , P. Reiter and G. Pascovici, "Characterization of large volume HPGe detectors. Part I: Electron and hole mobility parameterization", Nucl. Instrum. Methods Phys. Res. A, vol. **A 569**, pp. 764-773 (2006)

[83] L. Mihailescu *et al.*, "The influence of anisotropic electron drift velocity on the signal shapes of closed-end HPGe detectors", Nucl. Instrum. Methods **A 447**, 350-360 (2000)

[84] G. Ottaviani *et al.*, IEEE Trans. Nucl. Sci. NS-22, 192 (1975)

[85] J. Liu., "Development of Segmented Germanium Detectors for Neutrinoless Double Beta Decay Experiments.", Ph.D. Dissertation, Technische Universität München, Germany (2009)

[86] A. Einstein, "Über die von der molekularkinetischen Theorie der Wärme geforderte Bewegung von in ruhenden Flüssigkeiten suspendierten Teilchen", Annalen der Physik vol. 322 no. **8**, 549-560 (1905)

[87] C. Jacoboni, F. Nava, C. Canali, and G. Ottaviani *et al.*, "Electron drift velocity and diffusivity in germanium" Phys. Rev. **B 24**, 1014 (1981)

[88] G. Lutz, "Semiconductor Radiation Detectors: Device Physics. ", Springer-Verlag Berlin Heidelberg (2007)

[89] P. Finnerty, "A Direct Dark Matter Search with the MAJORANALow-Background Broad Energy Germanium Detector", Ph.D. Dissertation, University of North Carolina at Chapel Hill (2013)

[90] P. N. Luke *et al.*, "Low capacitance large volume shaped-field Germanium detector", IEEE Trans. Nucl. Sci. Vol. **36**, 926 (1989)

[91] P. S. Barbeau, J. I. Collar, and O. Tench, "Large-mass ultra-low noise germanium detectors: performance and applications in neutrino and astroparticle physics", J. Cosm. Astro. Phys. **0709**, 009 (2007)

[92] CANBERRA Industries, Broad Energy Germanium Detector, http://www.canberra.com

[93] D. Budjáš, M. B. Heider, O. Chkvorets, S. Schoenert, and N. Khanbekov, "Pulse Shape Analysis with a Broad-Energy Germanium Detector for the GERDA experiment", arXiv:0812.1735.

[94] L. Reggiani *et al.*, Hole Drift Velocity in Germanium, Phys. Rev. **B 16**(6), 2781-2791 (1953)

[95] W. Shockley, "Currents to Conductors Induced by a Moving Point Charge", J. Appl. Phys. **9**, 235 (1938)

[96] S. Ramo, "Currents Induced by Electron Motion", Proc. of the I.R.E **27**, 584 (1939)

[97] Z. He, "Review of the ShockleyRamo theorem and its application in semiconductor gamma-ray detectors", Nucl. Instrum. Methods **A 463**, 250 (2000)

[98] Bart Bruyneel, "Characterization of Segmented Large Volume, High Purity Germanium Detectors", Ph.D. Dissertation, Universität zu Köln, Germany (2006)

[99] Michael Christian Schlarb, "Simulation and Real-Time Analysis of Pulse Shapes from segmented HPGe-Detectors", Ph.D. Dissertation, Technische Universität München, Germany (2009)

[100] D. Budjáš, "Germanium detector studies in the framework of the GERDA experiment.", Ph.D. Dissertation, Max Planck Institut für Kernphysik, Heidelberg, May (2009)

[101] D. Budjáš *et al.*, "Pulse shape discrimination studies with a Broad-Energy Germanium detector for signal identification and background suppression in the GERDA double beta decay experiment", JINST 4 P10007 (2009)

[102] D. Budjáš, "Germanium detector studies in the framework of the GERDA experiment", Ph.D. Dissertation, University of Heidelberg (2009)

[103] GERDA collaboration, "Pulse shape discrimination for GERDAPhase I data", Eur. Phys. J. **C 73**, 2583 (2013)

[104] S. Agostinelli *et al.*, "Geant4: a simulation toolkit", Nucl. Instrum. Methods **A 506** no. 3, 250-303 (2003)

[105] M. Boswell *et al.*, "MaGe - a Geant4-Based Monte Carlo Application Framework for Low-Background Germanium Experiments", IEEE Trans. Nucl. Sci. **58** no. 3, 1212-1220 (June, 2011)

[106] M. Agostini *et al.*, "Signal modeling of high-purity Ge detectors with a small read-out electrode and application to neutrinoless double beta decay search in Ge-76", JINST **6** P03005

[107] M. Agostini, "Signal and background studies for the search of neutrinoless double beta decay in GERDA.", Ph.D. Dissertation, Technische Universität München, Germany (2013)

[108] Neslihan Becerici Schmidt, "Results on Neutrinoless Double Beta Decay Search in GERDA: Background Modeling and Limit Setting", Ph.D. Dissertation, Technische Universität München, Germany (2014)

[109] A. Caldwell, F. Cossavella, B. Majorovits, D. Palioselitis, O. Volynets, "Systematic uncertainties of artificial neural-network pulse-shape discrimination for $0\nu\beta\beta$-decay searches using true-coaxial HPGe detectors", Eur. Phys. J. **C 75**, 350 (2015)

[110] GERDA Collaboration, K. H. Ackermann *et al.*, "The GERDA experiment for the search of $0\nu\beta\beta$ decay in ^{76}Ge", Eur. Phys. J. **C 73**, 2330 (2013)

[111] Andrea Lazzaro, "Studies of high-purity Ge detector signals", Andrea Lazzaro, Master's thesis, U. Milano / TUM (2012)

[112] G. Zuzel *et al.*, "Determination of the ^{42}K specific activity in argon by using the LArGe facility", GERDA Scientific Technical Reports GSTR-12-018 (2012)

[113] D. Budjáš *et al.*, "Production of ^{42}Ar for high intensity ^{42}K background studies with LArGe", GERDA Scientific Technical Reports GSTR-12-011 (2012)

[114] G. Zuzel, "LArGe refilling and spiking with ^{42}Ar", Presentation given at the GERDA collaboration meeting, LNGS, November 7-9 (2011)

[115] M. Agostini *et al.*, "Investigation of the 42K background suppression by using bare BEGe detector in LArGe", GERDA Scientific Technical Reports GSTR-12-016 (2012)

[116] M. Agostini *et al.*, "Production, characterization and operation of ^{76}Ge enriched BEGe detectors in GERDA", Eur. Phys. J. **C 75**, 39 (2015)

[117] M. Agostini *et al.*, "Improvement of the Energy Resolution via an Optimized Digital Signal Processing in GERDA Phase I", arXiv:1502.04392

[118] M. Agostini, L. Pandola, P. Zavarise, and O. Volynets, "GELATIO: A General framework for modular digital analysis of high-purity Ge detector signals", JINST **6** P08013 (2011)

[119] M. Agostini, L. Pandola, and P. Zavarise, "Off-line data processing and analysis for the GERDA experiment", J. Phys. Conf. Ser. **368**, 012047 (2012)

[120] P. Zavarise, M. Agostini, A. Machado, L. Pandola, and O. Volynets, "Off-line data quality monitoring for the GERDA experiment", J.Phys.Conf.Ser. **375**, 042028 (2012)

[121] P. Zavarise, "Analysis of the first data of the GERDA experiment at LNGS", Ph.D. Dissertation, UNIVERSITÁ DEGLI STUDI DELL'AQUILA (2013)

[122] L. Pandola, P. Zavarise, "Estimate of the muon-induced background in the GERDA commissioning runs", GERDA Scientific Technical Reports: GSTR-11-007 (2011)

[123] L. Pandola, M. Bauer, K. Kröninger, X. Liu, C. Tomei, S. Belogurov, D. Franco, A. Klimenko, M. Knapp, "Monte Carlo evaluation of the muon-induced background in the GERDA double beta decay experiment" Nucl. Instrum. Methods **A 570**, 149 (2007)

[124] G. Meierhofer *et al.*, Eur. Phys. J. **A 48**, 20 (2012) and references therein.

[125] C. E. Aalseth *et al.*, "Results from a Search for Light-Mass Dark Matter with a p-Type Point Contact Germanium Detector", Phys. Rev. Lett. **106**, 131301 (2011)

[126] MINUIT's User's Guide

[127] High Activity Disposal Experimental Site (*Hades*) of the Belgian Nuclear Research Center SCK·CEN, Boeretang 200, BE-2400 Mol, Belgium.

[128] Richard B. Firestone, Virginia S. Shirley *et al.*, "Table of Isotopes", John Wiley & Sons, Inc., eighth edition (1998)

[129] E. Schönfeld, U. Schötzig, E. Günther, and H. Schrader, "Standardization and decay data of 68Ge/68Ga", Applied Radiation and Isotopes **45** no. 9, 955-961 (1994)

[130] J. A. Bearden and A. F. Burr, "Reevaluation of X-Ray Atomic Energy Levels", Rev. Mod. Phys. **39** no. 1, 125-142 (1967)

[131] F.T. Avignone *et al.*, "Theoretical and experimental investigation of cosmogenic radioisotope production in germanium" Nucl. Phys. B (Proc. Suppl.) 28A, 280 (1992)

[132] I. Barabanov, S. Belogurov, L. B. Bezrukov, A. Denisov, V. Kornoukhov, *et al.*, "Cosmogenic activation of germanium and its reduction for low background experiments", Nucl. Instrum. Methods **B 251**, 115120 (2006)

[133] G. Zuzel and H. Simgen, "High sensitivity radon emanation measurements", Appl. Rad. Isot. **67**, 889 (2009)

[134] D. Lenz, "Pulse Shapes and Surface Effects in Segmented Germanium Detectors", Ph.D. Dissertation, Technische Universität München, Max-Planck-Institut für Physik, Germany (2010)

[135] I. Barabanov, L. Bezrukov, E. Demidova, V. Gurentsov, S. Kianovsky, *et al.*, "Shielding of the GERDA experiment against external gamma background", Nucl. Instrum. Methods **A 606**, 790-794 (2009)

[136] P. Benetti *et al.*, "Measurement of the specific activity of ^{39}Ar in natural argon", Nucl. Instrum. Methods **A 574**, 83 (2007)

[137] H. Primakoff and S. P. Rosen, "Double beta decay", Rep. Prog. Phys. **22**, 121 (1959)

[138] GEANT4, S. Agostinelli *et al.*, GEANT4: A Simulation toolkit, Nucl. Instrum. Methods **A 506**, 250-303 (2003)

[139] M. Salathe, "Computational studies for enrBEGe detectors", Presentation given at the Gerda collaboration meeting, LNGS, November 5-7 (2012)

[140] Andrea Kirsch, "Search for the neutrinoless double β-decay in GERDA Phase I using a Pulse Shape Discrimination technique", Ph.D. Dissertation, Ruperto-Carola University of Heidelberg, Germany (2014).

[141] E. Andreotti, A. Garfagnini, W. Maneschg *et al.*, "HEROICA: an underground facility for the fast screening of germanium detectors", JINST **8** P06012 (2013)

[142] More details in TMultiLayerPerceptron Class Reference,
https://root.cern.ch/doc/master/classTMultiLayerPerceptron.html

[143] S. G. Mallat, "A Theory for Multiresolution Signal Decomposition: A Wavelet Representation", IEEE Transactions on Pattern Analysis and Machine Intelligence, Vol 11, No. 7, (July 1989)

[144] More details in "cubic-spline biorthogonal wavelet"
O. Schulz, Blitzwave wavelet library. http://oschulz.github.io/blitzwave/

[145] O. Schulz, Blitzwave c++ wavelet library, http://oschulz.github.io/blitzwave/

[146] G. Uytternhoeven, D. Roose, and A. Bultheel, "Wavelet Transforms Using the Lifting Scheme", REPORT ITA-WAVELETS-WP1.1, Department of Computer Science. Leuven: Katholieke Universiteit Leuven, 1997.

[147] A. Cohen, I. Daubechies, and J. Feauveau, "Biorthogonal bases of compactly supported wavelets", Communications on Pure and Applied Mathematics, Vol. XLV, 485-560 (1992)

[148] W. Sweldens, "The lifting scheme: A new philosophy in biorthogonal wavelet constructions", Proc. SPIE 2569, Wavelet Applications in Signal and Image Processing III, 68 (September 1, 1995)

[149] G. Uytterhoeven, D. Roose, and A. Bultheel, "Wavelet Transforms Using The Lifting Scheme.", Technical Report ITA-Wavelets-WP1.1, Kath. Univ. Leuven, Dept. C.S. (1997)

[150] Yi, T.H., Li, H.N. and Zhao, X.Y., "Noise Smoothing for Structural Vibration Test Signals Using an Improved Wavelet Thresholding Technique", Sensors **12**(8), 11205-11220 (2012)

[151] Joint Stock Company "Production Association Electrochemical Plant", Pervaya Promyshlennaya 1, 663690 Zelenogorsk, Russia.

[152] PPM Pure Metals GmbH, Am Bahnhof 1, 38685 Langelsheim, Germany.

[153] Canberra Industries Inc., 107 Union Valley Rd, Oak Ridge, TN, USA.

[154] Canberra Semiconductor N.V., Lammerdries 25, 2250 Olen, Belgium.

[155] Canberra Model 2002 CSL

[156] The Canberra Multiport II NIM module, for the ^{228}Th measurements. Multiport II NIM module

[157] Struck SIS3301 VME FADCs

[158] Model PSC-823C, designed by Canberra-France

[159] DGF Pixie-4 module, developed by XIA (X-Ray Instrumentation Associates), http://www.xia.com/DGF_Pixie-4.html

[160] S.Y.F. Chu, L.P. Ekström, R.B. Firestone, "The Lund/LBNL Nuclear Data Search", database 2.0, February (1999)

[161] Björn Lehnert, "Search for $2\nu\beta\beta$ excited state transitions and HPGe characterization for surface events in GERDA Phase II", Ph.D. Dissertation, Technische Universität Dresden, Germany (2016)

[162] Katharina von Sturm, "Confined event samples using Compton coincidence measurements for signal and background studies in the GERDA experiment ", Ph.D. Dissertation, U. Padova, Italy (2016)

[163] Iris Abt *et al.*, "Characterization of the first true coaxial 18-fold segmented n-type prototype HPGe detector for the GERDA project", Nucl. Instrum. Methods **A 570**, 479-486 (2007)

[164] Refer to the official website of AGATA collaboration for more publications. https://www-win.gsi.de/agata/publications.htm

[165] R.J. Cooper, D.C. Radford *et al.*, "A novel HPGe detector for gamma-ray tracking and imaging", Nucl. Instrum. Methods **A 665**, 25 (2012)

[166] I. Abt, A. Caldwell, D. Lenz, J. Liu, X.Liu, B. Majorovits, "Pulse shape simulation for segmented true-coaxial HPGe detectors", Eur. Phys. J. **C 68** issue 3, pp 609-618, August (2010)

[167] I. Abt, A. Caldwell, J. Liu, B. Majorovits, O. Volynets, "Measurement of the temperature dependence of pulse lengths in an n-type germanium detector", Eur. Phys. J. Appl. Phys. **56**, 10104 (2011)

[168] Private discussions with David Radford.

[169] Oleksandr Volynets, "Methods to improve and understand the sensitivity of high purity germanium detectors for searches of rare events", Ph.D. Dissertation, Technische Universität München, Germany (2012)

List of Figures

List of Tables

Acknowledgements

and Sebastian, Alex, and my best baseball teammate, Takeshi.

Finally, I would like thank the most important person, Tzuchun, for being the best support in my life.